Impact of biofuels on the catalytic oxidation system of diesel vehicles

Paola Anguita

N°d'ordre NNT :
2018LYSE1181

THESE de DOCTORAT DE L'UNIVERSITE DE LYON
opérée au sein de
l'Université Claude Bernard Lyon 1

Ecole Doctorale N° 206
(Ecole Doctorale de Chimie de Lyon)

Spécialité de doctorat : Chimie
Discipline : Catalyse

Soutenue publiquement le 08/10/2018, par :
Paola Anguita

Impact des biocarburants sur le système d'oxydation catalytique des véhicules diesel

---

Devant le jury composé de :

Delahay, Gérard	Directeur de Recherche ENSC Montpellier	Rapporteur
Dujardin, Christophe	Professeur des universités ENSC Lille	Rapporteur
Bordes, Claire	Maître de Conférences Université Lyon 1	Examinatrice
Iojoiu, Eduard Emil	Ingénieur Renault Trucks – Volvo	Examinateur
Liotta, Leonarda Francesca	Directrice de Recherche ISMN Palerme, Italie	Examinatrice
Valverde, José Luis	Professeur des universités UCLM, Espagne	Examinateur
Giroir-Fendler, Anne	Professeure des universités Université Lyon 1	Directrice de thèse
Gil Villarino, Sonia	Maître de Conférences Université Lyon 1	Co-directrice de thèse
Courtois, Xavier	Maître de conférences IC2MP Poitiers	Invité
Da Costa, Patrick	Professeur des universités IJLRA Paris	Invité
Tschamber, Valérie	Professeure des universités LGRE Mulhouse	Invitée

UNIVERSITE CLAUDE BERNARD - LYON 1

Président de l'Université	**M. le Professeur Frédéric FLEURY**
Président du Conseil Académique	M. le Professeur Hamda BEN HADID
Vice-président du Conseil d'Administration	M. le Professeur Didier REVEL
Vice-président du Conseil Formation et Vie Universitaire	M. le Professeur Philippe CHEVALIER
Vice-président de la Commission Recherche	M. Fabrice VALLÉE
Directrice Générale des Services	Mme Dominique MARCHAND

COMPOSANTES SANTE

Faculté de Médecine Lyon Est – Claude Bernard	Directeur : M. le Professeur G.RODE
Faculté de Médecine et de Maïeutique Lyon Sud – Charles Mérieux	Directeur : Mme la Professeure C. BURILLON
Faculté d'Odontologie	Directeur : M. le Professeur D. BOURGEOIS
Institut des Sciences Pharmaceutiques et Biologiques	Directeur : Mme la Professeure C. VINCIGUERR
Institut des Sciences et Techniques de la Réadaptation	Directeur : M. X. PERROT
Département de formation et Centre de Recherche en Biologie Humaine	Directeur : Mme la Professeure A-M. SCHOTT

COMPOSANTES ET DEPARTEMENTS DE SCIENCES ET TECHNOLOGIE

Faculté des Sciences et Technologies	Directeur : M. F. DE MARCHI
Département Biologie	Directeur : M. le Professeur F. THEVENARD
Département Chimie Biochimie	Directeur : Mme C. FELIX
Département GEP	Directeur : M. Hassan HAMMOURI
Département Informatique	Directeur : M. le Professeur S. AKKOUCHE
Département Mathématiques	Directeur : M. le Professeur G. TOMANOV
Département Mécanique	Directeur : M. le Professeur H. BEN HADID
Département Physique	Directeur : M. le Professeur J-C PLENET
UFR Sciences et Techniques des Activités Physiques et Sportives	Directeur : M. Y.VANPOULLE
Observatoire des Sciences de l'Univers de Lyon	Directeur : M. B. GUIDERDONI
Polytech Lyon	Directeur : M. le Professeur E.PERRIN
Ecole Supérieure de Chimie Physique Electronique	Directeur : M. G. PIGNAULT
Institut Universitaire de Technologie de Lyon 1	Directeur : M. le Professeur C. VITON
Ecole Supérieure du Professorat et de l'Education	Directeur : M. le Professeur A. MOUGNIOTTE
Institut de Science Financière et d'Assurances	Directeur : M. N. LEBOISNE

Remerciements

Je tiens à tout d'abord remercier l'Agence National de la Recherche (ANR) pour avoir financé le projet AppiBio dans lequel s'inscrit cette thèse. Également merci à tous les partenaires du projet pour leurs conseils et leur aide durant les différentes réunions de projet.

Je souhaite tout particulièrement remercier Catherine Pinel, directrice de l'Institut de Recherches sur la Catalyse et l'Environnement de Lyon (IRCELYON), pour m'avoir permis d'effectuer mes travaux de thèse au sein de son établissement.

Un grand merci à mes directrices de thèse, Anne Giroir-Fendler et Sonia Gil, pour leur encadrement pendant ces trois années. Vraiment merci pour tout le temps que vous m'avez accordé, votre aide et votre soutien.

Merci à Gérard DELAHAY et Christophe DUJARDIN pour avoir accepté d'être les rapporteurs de cette thèse. Je remercie également Leonarda LIOTTA, José Luis VALVERDE, Claire BORDES, Eduard Emil IOJOIU, Xavier COURTOIS, Patrick DA COSTA et Valérie TSCHAMBER pour leur participation à mon jury de thèse.

Merci aux membres du laboratoire, services techniques et services administratifs, pour votre compréhension et aide à une étrangère perdue. Merci aux membres de l'équipe de CAractérisation et REmédiation des polluants dans l'air et l'eau (CARE), pour la bonne ambiance générale et leur implication dans la vie de laboratoire.

Grand merci à mes amis du laboratoire, Géraldine, Marième, Milenna, Thomas, Álvaro, Ángel, Puca, Antonio, Weydong, Vincent, Vargas, Diego… Spécialement merci à Guillaumecito et Ioanna (plus connue comme « the greek »), pour les discussions scientifiques et surtout non scientifiques ! Merci à tous pour votre aide et soutien au quotidien.

Merci à mes collègues de TP, qui m'ont très bien accueilli au sein de la plateforme chimie physique. Merci pour votre bonne humeur, vous m'avez fait apprécier les séances de TP. Merci pour votre patience et votre aide, ainsi que pour m'avoir montré comme maitriser l'hydrogénation des oléfines, je reste invaincue !

Merci à mes besties, Bea et Patri, dans lesquelles j'ai trouvé une famille lyonnaise.

Je me permets de changer à l'espagnol pour dire merci aux personnes plus importantes dans ma vie.

Gracias a la mujer más fuerte que conozco, mi madre Estrella, que me ha enseñado a ver siempre el lado positivo. A Maxi, por cuidarla mientras estoy lejos. A mi hermano David, quien me ha animado a poner todo mi esfuerzo en todo lo que haga. A Soraya, por todo el apoyo que me da siempre con esa alegría tan suya.

Gracias a mis divinas, nuestros audios kilométricos demuestran que la amistad no entiende de distancia. No importa dónde vayamos, nos llevamos en la piel.

Finalement merci à Pierre Alexis, qui m'a montré le charme des montagnes jolies. Merci de me faire sourire tous les jours.

Voici ma thèse, à ceux qui vont la lire : profitez bien ! À ces qui s'arrêtent ici : au revoir que dijo Voltaire.

Merci, thanks, obrigada, ευχαριστώ, **GRACIAS.**

CONTENTS

ABSTRACT

The more restrictive regulations to reduce pollutants emissions, especially CO_2, promote the use of biofuels. However, biodiesel contains inorganic elements (Na, K, Ca and P) that reduce the durability of the after-treatment catalysts. This work aims to evaluate the performance of Diesel Oxidation Catalysts (DOCs, $PtPd/CeZrO_2/La\text{-}Al_2O_3$ reference catalyst). The characterization results have shown that the above-mentioned impurities affect the physico-chemical, redox, surface and catalytic properties. Although the crystalline structure of reference catalyst did not change after impurities incorporation, the specific surface area decreased. The redox ability was also decreased when Na, K and Ca impurities are present due to their low electronegativity, which increased the oxygen interaction. This high interaction seems to be responsible of the enhanced C_3H_6 reaction rate. NO-TPD results evidenced that the high basicity of Na, K and Ca impurities resulted in an increase of NO adsorption strength. Accordingly, DRIFT results showed the presence of NO adsorption intermediates associated to the electrostatic field created by these cations, hindering NO oxidation. CO adsorption was also promoted, enhancing CO reaction rate. The formation of cerium phosphate was also observed, which could stabilize the Ce^{3+} oxidation state (checked by XPS), decreasing NO oxidation due to the blockage of catalytic sites. Nevertheless, CO and C_3H_6 co-oxidations were enhanced by avoiding self-poisoning. After catalyst hydrothermal aging, the effect of impurities was masked by the sintering of Pt/Pd active sites, which decreases the DOC catalytic performances.

Keywords: Diesel Oxidation Catalysts, biodiesel after-treatment impact, alkali-alkaline earth impurities, phosphorus, in-situ DRIFTS, hydrothermal aging.

RESUME

Les normes européennes en vigueur visent à réduire les émissions de polluants, en particulier le CO_2, favorisant l'usage des biocarburants comme le biodiesel. Ce dernier contient des éléments inorganiques comme le Na, K, Ca et P qui affectent la durabilité des systèmes de post-traitement. Dans ce travail, les performances d'un catalyseur d'oxydation diesel de type $PtPd/CeZrO_2/La\text{-}Al_2O_3$ ont été évaluées et des caractérisations physico-chimiques ont permis de relier l'activité catalytique à l'évolution des sites actifs lors de l'accumulation de Na, K, Ca et P à la surface de ce catalyseur de référence. Bien que la structure cristalline du catalyseur de référence ne change pas après l'incorporation des impuretés, la surface spécifique diminue ainsi que les propriétés redox. Ce phénomène s'explique par la faible électronégativité du Na, K ou Ca, qui favorise l'interaction avec l'oxygène et qui augmente la vitesse d'oxydation de C_3H_6. Les résultats NO-TPD confirme que la forte basicité de Na, K ou Ca augmente l'adsorption du NO. Par DRIFT il a été aussi montré que l'adsorption des intermédiaires du NO, associée au champ électrostatique des cations Na, K ou Ca, inhibe l'oxydation de NO. Pour le CO l'adsorption est favorisée, et l'oxydation est favorisée. En présence de phosphore, des phosphates de cérium sont formés stabilisant le cérium à l'état de Ce^{3+} ce qui entraine une faible activité dans l'oxydation de NO. Néanmoins en présence de P, les oxydations de CO et de C_3H_6 s'améliorent avec une limitation de l'auto-empoisonnement. Après vieillissement hydrothermal, la diminution des teneurs en Na, K ou Ca et le frittage des métaux nobles affectent les performances catalytiques.

Mots-clés: Catalyseur d'Oxydation Diesel, système de post-traitement biodiesel, impuretés à basse d'alcalin et d'alcalino-terreux, espèces phosphorées, in-situ DRIFTS, vieillissement hydrothermal.

TABLES AND FIGURES CAPTION

CHAPTER I: Bibliographic study

CHAPTER II: Experimental

CHAPTER III: Effect of Na, K, Ca and P-impurities on diesel oxidation catalysts (DOCs)

CHAPTER IV: In-situ DRIFT study of impurities influence on surface adsorption properties of DOC

CHAPTER V: Effect of hydrothermal treatment on reference and modified-catalysts

Figure V-13. DRIFT spectra in the region 3200-1100 cm^{-1} of HT-PtPd and HT-P-PtPd aged catalysts at 150 ºC (left) and 250 ºC (right) under simulated exhaust conditions. FT-IR chamber feed: 500 ppm NO, 300 ppm CO, 300 ppm C_3H_6, 10% O_2, He as balance. Total flow: 40 ml min^{-1}. Each spectrum has been taken 60 min after the desired temperature reached

LIST OF ABBREVIATIONS

BDDT: Brunauer-Deming-Deming-Teller

BET: Brunauer-Emmet-Teller

BJH: Barnet-Joyner-Haneda

BTX: Benzene-Toluene-Xylene

COP: Conference of Parties

CRT: Continuously Regeneration Trap

DOC: Diesel Oxidation Catalyst

DPF: Diesel Particulate Filter

DRIFTS: Diffuse Reflectance Infrared Fourier Transform Spectroscopy

EDX: Energy Dispersive X-ray analysis

EGR: Exhaust Gas Recirculation

EN: European Normative

EU: European Union

EXAFS: X-Ray Absorption Fine Structure

FAAE: Fatty Acid Alkyl Esters

FFA: Free Fatty Acids

FTIR: Fourier Transform Infrared spectroscopy

GHG: Green House Gas

GHSV: Gas Hourly Space Velocity

HDVs: Heavy Duty Vehicles

HT: Hydrothermal

ICP-OES: Induced Conductivity Plasma-Optical Emission Spectroscopy

IF: Inorganic Fraction

IUPAC: International Union of Pure and Applied Chemistry

NO_x: Nitrogen Oxides

NSR: NO_x Storage Reduction

OBD: On-Board Diagnostic

OSC: Oxygen Storage Capacity

PAHs: Polycyclic Aromatic Hydrocarbons

PGM: Platinum Group Metals

PM: Particulate Matter

PN: Particulate Number

R: Richness

SCR: Selective Catalytic Reduction

SiC: Silicon Carbide

SOF: Solid Organic Fraction

SOI: Start of Injection

SSA: Specific Surface Area

TCD: Temperature Controller Detector

TDS: Temperature Desorption Spectroscopy

TEM: Transmission Electron Microscopy

THC: Total Hydrocarbon

TPD: Temperature Programmed Desorption

TPR: Temperature Programmed Reduction

ULSD: Ultra Low Sulfur Diesel

UNFCCC: United Nations Framework Convention of Climate Change

USA: United States of America

UV: Ultraviolet Vision

VECTO: Vehicle Energy Consumption Calculation Tool

VOCs: Volatile Organic Compounds

WHSC: World Harmonized Stationary Cycle

WHTC: World Harmonized Transient Cycle

XPS: X-Ray Photoelectron Spectroscopy

XRD: X-Ray Diffraction

ZDDP: Zinc Dialkylthiophosphate

Introduction

The impacts of climate change are evident. The members of the states of the European Union, including France, are active in the fight against global warming. Fossil fuels are major contributors to climate change, accounting for the vast majority of greenhouse gas (GHG) emissions. Transportation activities, in particular emissions from diesel heavy-duty vehicles, are considered to be responsible for about 30% of GHG emissions, which directly increases the pollutants levels in the atmosphere.

Diesel engines are widely used due to their high fuel efficiency and low cost. However, it is worth noting that it contains considerable amount of nitrogen oxides (NOx) and particulate matter (PM) that adversely affect the environment as well as human health. In addition, use of fossil energies has led to increase CO_2 levels in atmosphere, which are still climbing as a function of fuel burnt leading to greenhouse effect, acid rains, smog and change of climate world-over.

In this context, the search of alternative fuels has become highly pronounced. Europe has committed to promote the use of biofuels as a substitute for diesel in the transport sector. The Directive 2009/28/EC mandates that at least 10% of all energy in road transport fuels be produced from renewable sources by 2020.

Biodiesel is an alternative fuel that can be produced from vegetable oils and animal fat. It presents calorific values that are greater or equal to those of a fossil fuel. Moreover, biodiesel presents a net removal of CO_2 from the atmosphere, as most of CO_2 emissions are recycled into organic tissues during plant growth. Thus, biodiesel remains a promising renewable fuel that can make it possible to limit the dependence on fossil fuels such as diesel, while limiting the carbon impact of vehicles.

The more restrictive government regulations for exhaust emissions from heavy-duty engines (Euro VI) promoted the continuous improvement of existing after-treatment systems. As a result, automotive makers must introduce a Diesel Oxidation Catalyst (DOC) that processes carbon monoxide (CO), unburned hydrocarbons (HC) and oxidation of NO to NO_2, which heavily influences the effectiveness of other catalytic units. In addition a Diesel Particulate Filter (DPF) and then a Selective Reduction Catalyst (SCR), which targets NOx through the use of urea, were respectively added. Moreover, the durability demanded by the Euro VI standard, in keeping with the typical use of these trucks, attains seven years or 700 000 km.

The intensive use of biodiesel can prove detrimental with regard to the durability of catalytic after-treatment system. Besides European regulations (EN 14214) limits their presence, biodiesel can contain alkali metals (Na, K) coming from the liquid-phase synthesis of biodiesel, or phosphorus (P) from the additive oils.

The ANR project APPIBio (Approche Pluridisciplaire de l'Impact des Biocarburants sur les systèmes de post-traitement diesel, for its acronym in French) aims to study the effects of biodiesel on the durability of the three catalytic units that together compose the Euro VI post-treatment system of biodiesel vehicles, namely the DOC, the SCR catalyst and the DPF, and to identify the reaction mechanisms involved when alternative fuels are used. The consortium of this project has Renault Trucks – Volvo Powertrain as industrial partner, and four university laboratories: the IJLRA (Paris), the IC2MP (Poitiers), LGRE (Mulhouse) and IRCELyon (Lyon). The objective of this Ph.D. thesis is the study of the effect of Na, K, Ca and P-impurities coming from biodiesel on the diesel oxidation catalyst (DOC).

Chapter I

CHAPTER I: Bibliographic study

I. Atmospheric pollution from thermal combustion in diesel engines

Diesel engines have been widely used in the worldwide automotive sector due to their high combustion efficiency, reliability and fuel economy performance [1]. Despite all the great advantages, the downside of diesel combustion engines is evident: their ubiquitousness has created one of the major challenges for society and the environment. Previous studies [2–4] have clearly show that the diesel engine emissions are the most prevalent anthropogenic pollutants worldwide, which profoundly affect human health.

Diesel engines inherently operate lean-burn conditions, which is characterized by excess air in the combustion chamber, leading the formation of CO_2 and H_2O under complete combustion of diesel fuel [5]. However, the features of the diesel fuel itself, and of the diesel engine operating conditions (air-to-fuel ratios, ignition timing, turbulence and temperature in the combustion chamber) lead to the formation of harmful products during the thermal combustion. The most significant harmful products are carbon monoxide (CO), total hydrocarbons (THC), nitrogen oxides (NO_x), and particulate matter (PM). These diesel engine emissions (Figure I-1) may originate from the incomplete combustion of fuel, from operating conditions that favor the formation of particular pollutants, or from the oxidation of nitrogen- and sulfur-containing compounds present in the fuel which are not hydrocarbons. Because diesel engines are lean combustion engines, the concentration of CO and HC is minimal.

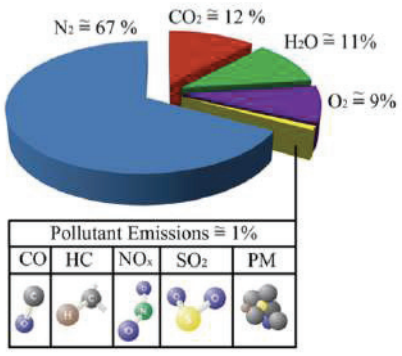

Figure I-1. The compositions of diesel exhaust gas [6].

a. Diesel exhaust pollutants

In this section, the origin and the effects on both health and environment of the four main exhaust pollutants (CO_x, HC, PM and NO_x) from diesel engine will be described.

- ***Carbon oxides (CO_x)***

Carbon monoxide results from the incomplete combustion where the oxidation process does not occur completely. The concentration of CO emitted is largely dependent on air-fuel ratio of the mixture, in the combustion chamber. For a diesel engine combustion happens in excess of air (lean burn conditions) in order to increase the yield and at the same time reduce the fuel consume. Although CO is minimized under lean conditions, a small portion still emitted under lean conditions because of chemical kinetic effects [7].

Carbon monoxide is a colourless, odourless and extremely toxic gas due to its high affinity for blood haemoglobin [8]. Above 0.01% vol., headaches occur and a rate of 0.1% vol. is deadly. In the atmosphere, its life is short, but it contributes to the increase of ozone and methane levels, and contributes to the formation of photochemical smog.

Otherwise, carbon dioxide (CO_2) coming from combustion process, contributes actively to global temperature increase due to its greenhouse gas properties. In addition, it could also participate in ocean acidification, which may lead to the disappearance of some species sensitive to pH.

- ***Nitrogen oxides (NO_x)***

Nitric oxide (NO) and nitrogen dioxide (NO_2) are grouped as NO_x. Nitrous oxide (N_2O) is also included in some cases but its concentration is low in the exhaust gases. The amount of produced NO_x is a function of the maximum temperature in the combustion chamber oxygen concentrations, and residence time [9].

NO is a colorless and odorless gas, while NO_2 is a reddish brown gas with pungent odor [10,11]. Nitrogen oxides emissions from vehicles are responsible for a large amount of health hazard. NO and NO_2 are considered as toxic; but NO_2 has a level of toxicity five times greater than that of NO and it can irritate the lungs and

lower resistance to respiratory infection [8]. However, the principal issue presented by NO_x is compared to the formation of ozone. Indeed, NO_x can react with Volatile Organic Compounds (VOCs), which can react with HC under the influence of UV radiation to form tropospheric ozone [12]. They also participate in the formation of acid rain and/or photochemical smog.

- ***Total hydrocarbons (THC)***

Hydrocarbon emissions are the result of incomplete combustion or evaporation of the fuel before combustion [13,14]. They consist of alkanes, alkenes, aldehydes, alcohols, but also aromatic compounds added to fuels to increase the octane number [15]. These unburned hydrocarbons continue to react in the exhaust if the temperature is above 600 °C and oxygen present [7].

The most known effects of unburned hydrocarbons on human health are neurasthenia, depression and anxiety (due to the depressing effect of THC on the nervous system). The mucous membranes and the skin can also be irritated in case of greater exposure. Chronic and long-term exposure can eventually cause brain degeneration and cancers caused by benzene and aromatic derivatives [16]. Moreover, they play a significant role in the formation of ground-level ozone with other pollutant emissions. Vehicles are responsible for about 50 % of the emissions that form ozone [17,18].

- ***Particulate matter (PM)***

Diesel particles generally consist of a carbon core and agglomerates of several compounds from combustion (average size: 0.1 μm). Diesel particle emissions can be divided into three main components: soot, composed of elemental carbon (31%) that is seen as black smoke; Soluble Organic Fraction (SOF), which consist on heavy hydrocarbons adsorbed or condensed on the soot (7%); and Inorganic Fraction (IF), formed by sulphates, water (14%), and unburned lubricant (40%) as well as traces of metals [19–22].

The formation process of PM is dependent on many factors as the combustion and expansion process, fuel quality (sulphur and ash content), lubrication oil quality and consumption, combustion temperature, exhaust gas cooling [23]. Particulate matters are also resulted from hydrocarbon chains that have not been completely

oxidized [24]. Among them, acetylene and Polycyclic Aromatic Hydrocarbons (PAHs) are recognized as the precursors of diesel soot.

The main risks associated with diesel particulate matters are related to the ability of the finest particles ($PM_{2.5}$ and PM_{10}, particulate matters with 2.5 and 10 µm diameter respectively) to penetrate directly into the pulmonary alveoli when they are inhaled [25]. Moreover PM emissions contribute to pollution of air, water and soil, soiling of buildings, reductions in visibility, impact agriculture productivity and global climate change [26,27].

b. Environmental regulations for atmospheric pollution

European Union (EU) has published emission regulations in order to control the pollutants in automobile exhaust [28]. Note that Roman numerals are used for heavy-duty engines standards (Euro I … VI).

The last European emission standard for heavy good vehicles published, Euro VI, was introduced by Regulation 595/2009 and became effective from 2014. Euro VI standard aims to reduce NO_x emissions by 80% and particulate emissions by 66% compared to Euro V standards (Table I-1). These standards consider not only particulate emissions in bulk (particulate matter, PM) but also in number (particulate number, PN) due to the potential respiratory diseases that could be produced by smaller particles [29]. As a result, vehicle manufacturers must introduce an after-treatment system, which aims to reduce pollutant emissions. Euro VI standard demanded a minimum durability of after-treatment systems equally severe, attaining seven years or 700 000 km.

Table I-1. Heavy-duty engines Euro emission standards evolution.

Stage	Date	Directive	CO	HC	NOx	PM	PN
			g/kWh				1/kWh
Euro 0	01-10-1990	88/77	11.2	2.4	14.4	-	-
Euro I	01-10-1993	91/542 (A)	4.5	1.1	8.0	0.36	
Euro II	10-10-1996	91/542 (B)	4.0	1.1	7.0	0.15	
Euro III	01-10-2001	199/96	2.1	0.66	5.0	0.13	
Euro IV	01-10-2006	199/96	1.5	0.46	3.5	0.02	
Euro V	01-10-2009	199/96	1.5	0.46	2.0	0.02	
Euro VI	31-12-2013	Regulation 595/2009	1.5	0.13	0.4	0.01	$8.0 \cdot 10^{11}$

Parallel to European emission standards, on-board diagnostic (OBD) vehicle test cycles have been developed to control the accomplishment of the established limits. Since Euro VI stage, two representative tests cycles, a transient test cycle (World Harmonized Stationary Cycle, WHSC) that relates the engine speed with the values used in the drive train model, with both cold and hot start requirements, and a hot start steady-state test cycle (World Harmonized Transient Cycle, WHTC) based on the frequency distribution of normalised engine speed and load of the reference transient engine cycle. These tests have been created covering typical driving conditions in the EU, USA, Japan and Australia.

In addition to the European emission standards, the yearly Conference of Parties (COP) of the United Nations Framework Convention of Climate Change (UNFCCC) assesses the progress in dealing with climate change. In the known Paris Climate Conference (COP21, 2015), the Paris Agreement was negotiated, that continues the labour of the Kyoto Protocol to deal with greenhouse emissions, and finance starting in 2020. The Agreement aims to respond to the global climate change threat by keeping a global temperature rise this century below 2 ºC.

Moreover, the agreement states the intent of the European Commission (EC) to move toward regulating CO_2 from HDVs. The EC have developed simulation software, the Vehicle Energy Consumption Calculation Tool (VECTO) that can be used to measure the CO_2 emissions and fuel consumption of HDVs for specific loads, fuels and mission profiles. The Commission has proposed its use on 1st January 2019, using the data collected to report a new draft Commission regulation. On the meantime, Euro VI normative already includes a requirement of measuring CO_2 emissions and fuel consumption to report to the relevant authority as part of the type approval process.

Otherwise, European Directive 2009/33/CE imposed increase the use of biofuels, which contributes to decrease CO_2 emissions. More recently a Directive published on 17th October 2012 (COM(2012) 595) proposed to limit the volume of agriculture-based biofuels to 5% until 2020, while maintaining the objective of 10% renewable fuels in the transport energy mix at this date. The high calorific value of biodiesel makes it a promising renewable fuel that can reduce the dependence on fossil fuels such as conventional diesel fuel emanating from oil, while limiting the

carbon impact of vehicles. Nevertheless, its intensive use can prove detrimental with regard to catalytic after-treatment systems.

c. After-treatment systems

The more stringent emission standards defined in environmental regulations have obliged the vehicle manufacturers to develop new systems for reducing pollutant emission from automobile exhaust. In order to achieve the desired emission levels, vehicles engines must be equipped with complex exhaust after-treatment systems [5,30].

Among all current after-treatment systems to control NOx emissions, Exhaust Gas Recirculation (EGR) is an established and effective technology to control NOx emission for diesel engines [31,32]. In EGR systems, part of the exhaust (with O_2, N_2, H_2O and CO_2) is recirculated back to the combustion chamber and then, mixed with fresh air at intake stroke. In fact, since the heat capacity of CO_2 in the recirculated exhaust gas is about 20–25% higher than that of O_2 and N_2, the energy released from the fuel combustion results in a lower temperature rise, which leads lower NOx levels. Consequently, the combustion temperature will decrease which means a reducing in NOx formations. However, the efficiency of combustion is decreased due to the reduction temperature in the cylinder, leading to the increase of HC and CO emissions [30]. Therefore, this strategy alone is not sufficient to meet the recent environmental regulations.

As a result, vehicle manufacturers must introduce a diesel oxidation catalyst (DOC), which processes carbon monoxide (CO) and unburned hydrocarbons (HC), in addition to a diesel particulate filter (DPF), and to the selective catalytic reduction system (SCR), which targets NO_x through the use of urea. Moreover, the last European standard Euro VI imposed a minimum durability of after-treatment system in keeping with the typical use of these vehicles, equal to seven years or 700 000 km.

The after-treatment system configuration employed in heavy-duty diesel engines consists in diesel oxidation catalyst (DOC), diesel particulate filter (DPF) and finally, selective catalytic reduction (SCR).

i. Diesel Oxidation Catalyst (DOC)

The main function of Diesel Oxidation Catalysts (DOCs) is the oxidation of unburned hydrocarbons, carbon monoxide and nitrogen oxide. Besides, DOC systems lead the reduction of diesel particulate emissions by oxidizing a part of the organic fraction present on the carbon particles [33,34].

The most common DOC catalytic systems are constituted by a ceramic or metallic honeycomb monolith (Figure I-2), which is the structured support for active species that have a specific catalytic activity. The monolith channel density (specified in cpsi: channels per square inch), wall thickness of the individual channels and the external dimensions of monolith (cross-sectional area and length) have a significant role on properties of DOC systems. Channel density and wall thickness determine heat up response, exhaust-gas backpressure, and mechanical stability of the catalytic converter [35].

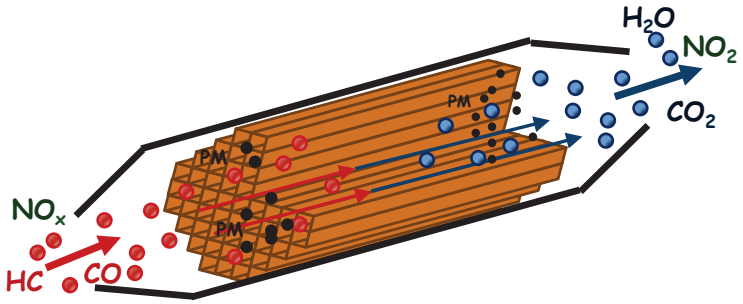

Figure I-2. Diesel oxidation flow through monolith catalyst (modified figure from [36]).

Besides, the monolithic support is coated with an oxide mixture (so-called washcoat) such as Al_2O_3, CeO_2, and ZrO_2, which are principally characterized by a high specific surface (hundreds of m^2/g) and then, the active catalytic metals are deposited within the pores of the washcoat [37,38]. Noble metals such as Pt, Pd, and Rh, are the most popular active phases for heavy-duty vehicles. However, these noble metals catalysts can favor the SO_2 to SO_3 reaction, which consequently react with water and generates sulphates and sulphuric acid compounds. These compounds have quite impact in after-treatment catalytic systems and, as well as harmful environmental and human health effects. There is no technology to prevent and eliminate these forms. Although Ultra Low Sulphur Diesel (ULSD) is used in many countries worldwide, the problem could not be solved completely. Using alternative

fuels as biodiesel can completely reduce or eliminate this pollutant. Besides, it is possible to increase the conversion efficiency of DOC using alternative fuels [39].

Therefore, the exhaust gases flowing into the DOC monolith support diffuse from the bulk of the gas to the washcoat pore structure and down to the catalytic sites, where three main heterogeneous catalytic reactions occur [40].

$$CO + \tfrac{1}{2} O_2 \rightarrow CO_2 \qquad Eq.\ I\text{-}1$$

$$C_3H_6 + \tfrac{9}{2} O_2 \rightarrow 3CO_2 + 3H_2O \qquad Eq.\ I\text{-}2$$

$$OO + \tfrac{1}{2} O_2 \rightarrow OO_2 \qquad Eq.\ I\text{-}3$$

In the oxidising environment (corresponding to so-called "lean-burn conditions" or "lean conditions") of diesel engines, the NO to NO_2 oxidation will be generally assured by the oxygen derivate the incomplete combustion of the fuel in the combustion chamber. NO to NO_2 oxidation is vital to the correct functioning of downstream components, like DPF and SCR. A high NO_2 concentration in the NO_x facilitates passive DPF regenerations, as well as enhances the performance of some SCR reactions. However, the NO oxidation reaction (Eq. I-3) limits the NO_2 concentration due to the equilibrium for the NO oxidation (Figure I-3). NO oxidation reaction is limited either kinetically or thermodynamically in the lean-burn engine after-treatment operating regime. Kinetic limitations, especially at lower temperatures, prevent the reaction from reaching equilibrium. Above 200 ºC and with increasing temperature, lower NO_2 concentrations will be available as thermodynamic limitations become apparent. Also, the amount of available O_2 decreases the thermodynamic boundary shifts to lower temperatures.

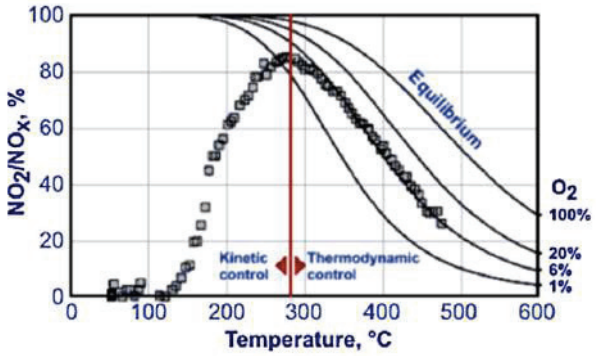

Figure I-3. NO/NO_2 shift in oxidation catalyst [41]. Catalyst: Pt 50 g/ft^3. Gas 270 ppm NO, 6% O_2, 10% H_2O in N_2.

The effectiveness of the DOC in oxidizing CO and HC can be observed at temperatures above ‘‘light-off’’ for the catalytic activity. Light-off temperature is defined as the temperature where the reaction starts in catalyst and varies depending on exhaust composition, flow velocity, and catalyst composition. CO and HC oxidations are limited by their own chemisorption, which produces self-poisoning of the catalysts surface. The oxidation rates increased when temperature reached is enough to overcome kinetic limitations. Moreover, the heat releases by the exothermic oxidation of CO and HC can be used to supports DPF regeneration.

Precious metals represent the usual choice to oxidation reactions due to their unparalleled redox activity. It has been demonstrated that Pt is among the most active elements for NO oxidation. However, the catalytic efficiency of Pt-only automotive catalysts decreases exposure at high temperature under oxidizing conditions [42]. The addition of Pd improves the durability of the catalysts. Thus, Pt/Pd alloy catalysts are preferred due to their higher resistance to sinter phenomena.

ii. Diesel Particulate Filter (DPF)

Diesel particulate filters (DPFs) are a specific technology to remove the PM emissions from the exhaust gas by physical filtration. Filters employed for the trapping of the solid portion are usually made of either cordierite ($2MgO–2Al_2O_3–5SiO_2$) or silicon carbide (SiC) honeycomb structure monolith with the channels blocked at alternate ends, so exhaust gas is forced through the channel walls.

As the filter becomes increasingly saturated with soot, a layer of soot is formed on the surface of the channel walls increasing back pressure across the filter on the engine. It is essential to avoid the excessive PM accumulation, as if the back pressure rise above a predetermined limit many negative effects such as increased fuel consumption, engine failure, and stress in the filter could happen. To prevent these negative effects the DPF needs to be periodically regenerated (cleaned) by soot combustion [43,44]. Unfortunately, the temperature of the diesel exhaust gas is too low (200 – 500 ºC) to initiate and maintain soot oxidation. Thus two types of regeneration processes of DPFs can be used to rise the exhaust gas temperature up to the point that soot oxidation can be self-sustained in the filter (>600 ºC): active and passive regeneration.

- ***Active regeneration***

It takes place when the soot loading reaches a set limit indicated by pressure drop across the DPF. The heat to oxidize PM is supplied from outside sources, such as an electric or microwave heater, flame-based burner, injection of fuel in the exhaust, etc. The large amount of energy for heating increases the cost of system. In addition, the higher temperatures near to the melting point of filter could damage the DPF [45,46]. Due to these negative effects the active regeneration as being out of preference.

- ***Passive regeneration***

The soot regeneration is facilitated by oxidation of carbon at 250-500 ºC with NO_2 formed on the upstream DOC by the following reactions:

$$C + NO_2 \rightarrow CO + NO \qquad \textit{Eq. I-4}$$

$$C + 2NO_2 \rightarrow CO_2 + 2NO \qquad \textit{Eq. I-5}$$

A pre-oxidation step is required to transform the already present NO in the exhaust gas to NO_2, which provides a more effective oxidant than oxygen [47]. This reaction can occur during de DOC step. In order to improve the regeneration efficiency a catalyst can be introduced directly inside the filter. The NO_2 consumed by the soot can be regenerated by Pt catalyst to reoxidize NO to NO_2. This system, named Continuously Regenerating Trap (CRT) is described in Figure I-4 [48]. The advantage of this system is that it requires no attention and it has been developed in many heavy-duty applications.

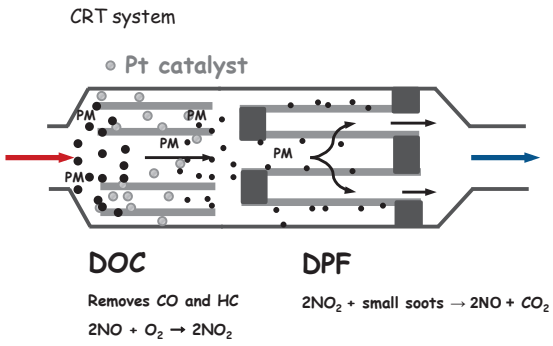

Figure I-4. Continuously Regenerating Trap (CRT) system [36].

iii. Selective Catalytic Reduction (SCR)

The Selective Catalytic Reduction (SCR) of NOx is one of the most prevailing technology to reduce NO_x emissions and especially, for high-duty vehicle engines [49]. SCR systems are used to minimize NO_x emissions in the exhaust gas via Adblue® (precursor of ammonia) injection [50]. This process with urea as reducing agent instead of ammonia is currently considered the best technology for the removal of nitrogen oxides from the exhaust of heavy-duty diesel vehicles, e.g. trucks [51]. In automotive applications, urea is advantageous compared to ammonia, because it is a harmless and environmentally storage compound for ammonia, which is released in the hot exhaust gas (250-450 °C).

In typical diesel exhaust, the nitrogen oxides are mainly composed of NO (> 90%), so that the reaction of NO with NH_3 on the SCR catalyst has to be regarded and therefore called as "standard SCR". The standard SCR follows a 1:1 stoichiometry for ammonia and NO is maintained along with consumption of oxygen (Eq. I-6). When equimolar amounts of NO and NO_2 are present in the feed (1:1 of NO:NO_2 ratio), SCR process is accelerated (reaction rate 10 times higher than standard SCR) and is called as "fast SCR" reaction (Eq. I-7) [52,53]. When only NO_2 is present in the mixture, so the NO is totally converted, the reduction process is called as "NO_2-SCR" (Eq. I-8).

$$4OO + 4NH_3 + O_2 \rightarrow 4O_2 + 6H_2O \qquad \textit{Eq. I-6 (Standard SCR)}$$

$$2OO + 2OO_2 + 4NH_3 \rightarrow 4O_2 + 6H_2O \qquad \textit{Eq. I-7 (Fast SCR)}$$

$$3OO_2 + 4NH_3 \rightarrow \tfrac{7}{2}O_2 + 6H_2O \qquad \textit{Eq. I-8 (NO_2 SCR)}$$

Therefore, the NOx emissions efficiency of SCR system is dependent of NO/NO_2 ratio, in which the efficiency of DOC system is essential.

Among the various types of commercial SCR-NH_3 (noble metals, metal oxides and zeolites) the copper (Cu) and iron (Fe)-exchanged zeolite catalysts are a good choice due to their outstanding deNOx activity and superior thermal durability [54,55], presenting high efficiency at low temperatures. The special features of these materials are their adjustable acidic properties and their ability to stabilize transition metal redox couples such as Cu^+/Cu^{2+}, Fe^{2+}/Fe^{3+} [56–58].

Accordingly to the configuration considered for the after-treatment system of heavy-duty vehicles, one of the challenges presented by these zeolite-based catalysts

is their stability under hydrothermal conditions beyond 900 ºC. In order to improve the stability and efficiency of these zeolites, research efforts are focus on the change of the zeolite structure, as chabazites [59,60]. Recently, some papers relate the use of perovskite catalyst for SCR-NH3 due to their remarkable hydrothermal stability [61–63].

Similarly to the other after-treatment devices, sulfur content of the diesel fuel is an important problem for SCR catalyst. It can accumulate in the active sites of the catalyst, which lowers the catalytic activity. Alternative fuels and fuel additives can prevent the effect of sulphurs on after-treatment technologies. Especially biodiesel is the most used alternative fuel to prevent the sulphur damage, and many researches have been carried out on the use of biodiesel as an alternative fuel to diesel [64].

II. Biodiesel

Biodiesel is a promising alternative diesel fuel derived from a variety of plant and animal feedstock. It presents similar calorific values to those of a traditional diesel fuel that remains a sustainable biofuel that can be used with little or no modification in the engine. Biodiesel thus remains a renewable, nontoxic and eco-friendly fuel that can make it possible to limit the dependence on fossil fuels.

Biodiesel is completely soluble in diesel fuel. Therefore, due to its high viscosity compared with that of conventional diesel fuel, it is blended in any proportion with diesel fuel. Biodiesel is typically used as a diesel blending component at levels of 20 % volume or lower (B20) since it provides a good performance without modification of diesel engines in most cases [65]. Nevertheless, when biodiesel is used, especially B100, the durability of after-treatment systems demanded by Euro VI becomes questionable.

a. Biodiesel synthesis

First step in the production of biodiesel is the choice of feedstock. The feedstocks for biodiesel production are categorized into four main groups:

- ***Vegetable oils***: grouped in edible and non-edible oils [66,67]. The latter have recently been attracting attention due to the potential competition of edible oils with food materials in the long-term.

- ***Animal fats***: which are often priced favourably for conversion into biodiesel, providing an economic advantage, but which high content and various distributions of fatty acids [68] of animal fats difficult biodiesel production.
- ***Used cooking oil***: recycles oil and grease are attractive feedstocks, however, the pre-treatment required due to the large amount of free fatty acids (FFA) and impurities contained, increases the biodiesel production costs.
- ***Algae***: recently it has been demonstrated that microalgae biodiesel has higher yield than non-edible oil production [69,70] and can meet the global demand for transport fuels [71]. However, the main obstacle is the high production cost for high oil yield and effective large-scale bioreactors [72].

The vegetable oils are the main option to biodiesel production. However, it is necessary undergo certain processes and procedures to convert them into biodiesel. Several generally technologies haven been developed to produce a better quality of biodiesel such as direct use and blending to avoid the problems occasioned due to their high viscosity [73]; microemulsions, which consists in mixing the oil with an aqueous phase and a surfactant in order to reduce the high viscosity of vegetable oils [74] or pyrolysis of vegetable oil using thermal cracking reactions [75].

Nevertheless, among all the techniques, transesterification is the most widely used process for industrialized biodiesel production because the conversion efficiency is higher and less expensive [76,77]. It consists in the conversion of an ester into another through a reversible reaction with an alcohol in the presence of base, giving biodiesel (fatty acid alkyl esters, FAAE) as main product and glycerine as by product (Figure I-5) [78].

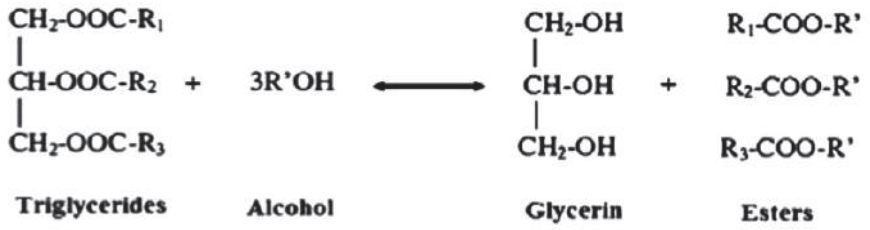

Figure I-5. Transesterification reaction of triglycerides with alcohol [79].

Generally, alcohol and triglycerides (vegetable oil and animal fat) are not miscible to form a single phase of mixture. Hence, due to the poor surface contact between the two reactants a catalyst is used to enhance and improve the reaction rate

and biodiesel yield. Catalysts used in biodiesel production can be: (i) homogenous, if the catalyst remains in the same (liquid) phase to that of the reactants during transesterification; (ii) heterogeneous, when they are in different phase (solid, immiscible liquid or gaseous) to that of the reactants; (iii) enzymatic, which can be used in transesterification of cooking oil as they are sensitive to free fatty acid (FFA) and water content. Alkalis as sodium and potassium hydroxides (NaOH and KOH), and sodium and potassium methoxides (CH_3ONa and CH_3OK) with concentration ranges from 0.5% to 1% by weight for biodiesel production are the most used. They can provide esters with yield from 94% to 99% [80].

At the end of transesterification process, biodiesel crude has to be purified and dried to achieve the European standard (EN14214) and the American standard (ASTM D6751) [81]. The water content, free fatty acid (FFA) level and saturation level of different feedstocks affects to the purification process. Feedstocks with high amount of water and FFAs molecules could result in soaps formation associated with alkaline catalysts (Figure I-6), which increases the biodiesel solubility in glycerol, thereby affecting the purification of crude biodiesel and lowering biodiesel yield [82].

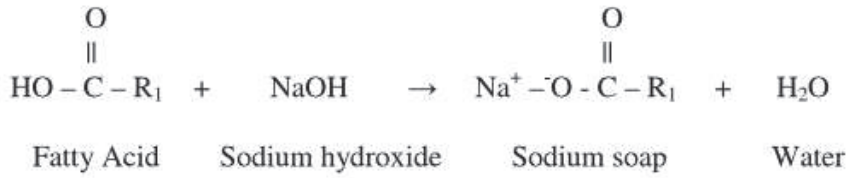

Figure I-6. Soap and water formation.

Biodiesel purification is usually achieved via wet washings, being washing with deionized water the most common technique. The use of water can cause some problems as emulsion formation, preventing the separation of the esters and allowing the formation of free fatty acid and soaps [83]. Thus, organic solvents such as petroleum, or acid solutions (normally with H_3PO_4) are used to neutralize the hydrolysis of the ester and the consequent soap formation.

Furthermore, dry washing technique is commonly employed to purify crude biodiesel through the use of silicates (Magnesol or Trisyl) and ion exchange resins (Amberlite or purolite) that have strong affinity for polar compounds such as methanol, glycerin, glycerides, metals and soap [84]. The use of membrane technology for the purification of crude biodiesel is an emergent area in order to avoid

the operation difficulties of wet and dry washing processes [85], however, higher efforts need to be explore.

b. Influence of biodiesel use in exhaust emissions

Use of biodiesel has an influence in the exhaust emissions when compared to those in diesel fuel. Emissions such as those of unburned hydrocarbons, CO, NO_x, particulate matter and CO_2 are affected by the use of biodiesel and its blends.

i. Particulate matter (PM)

It is a well-known argument that the use of biodiesel instead of diesel causes the PM emissions reduction [86–89]. A small portion of studies found an increase in PM emissions attributed to the higher viscosity of the biodiesel, which decreases fuel atomization [90–93]. However, the increased PM was due to the unburned HC emissions that would increase the SOF percentage in PM [91].

The lower aromatic and sulphur compounds of biodiesel will reduce PM emissions, but the more important factor is the higher oxygen content. Many authors agree with the higher oxygen content causes combustion more complete, and further promote the oxidation of soot, decreasing PM emissions [94]. It should be noted that, the advantage of no sulphur characteristics for biodiesel would disappear as the sulphur content in diesel is becoming fewer and fewer.

The combustion and start of injection of biodiesel are in advance, due to the higher density and viscosity and the lower compressibility [87,95], as well as the higher cetane number [86]. These prolong the residence time of soot particle in the high temperature environment, and thus further promote the oxidation in the presence of oxygen [96]. However, under cold start conditions, PM increases due to the higher kinematic viscosity and lower boiling point of the biodiesel that difficult its atomization and evaporation [97].

ii. Nitrogen oxides (NOx)

The vast majority of literatures reported that NO_x emissions would increase when using biodiesel. It is accepted generally [98] that this increase is mainly due to higher oxygen content for biodiesel, which enhances formation of NO_x. Moreover, the higher cetane number of biodiesel produces the advance start of injection (SOI),

which causes the increase in NO_x emissions [95,99,100]. Nevertheless, the larger content of unsaturated compounds in biodiesel could have a greater impact on NO_x emissions, which would be decreased.

Engine type and its operating conditions have something to do with NO_x emissions of biodiesel. A larger engine load would increase the overall fuel-air ratio, which resulted in an increase in the average gas temperature in the combustion chamber and hence higher NO_x formation would be produced, as it is sensitive to temperature [99,101,102].

The use of EGR will reduce NO_x emissions of biodiesel. EGR rates are optimized to match the operation conditions of diesel. Thus, due to the change of combustion characteristics for biodiesel, EGR rates may not fit well with the same conditions of biodiesel engines.

iii. Carbon monoxide (CO)

According to most of literatures, it is common trend that CO emissions are reduced when diesel is replaced by pure biodiesel due to increasing in oxygen content which promotes CO complete combustion [86,88,90,103]. In addition, the higher cetane number of biodiesel results in the lower possibility of formation of rich fuel zones, and thus reduces CO emissions [86,104,105].

Advance in the injection timing for biodiesel fuel, leads to the advance of ignition timing, decreasing also CO emissions [91,93,106]. It is worth noting that the lower carbon content for biodiesel compared to the diesel diminished CO emissions [104,107].

It was reported in [108] that CO emissions reduced with the increased load of fuel, this trend was explained because the increase in combustion temperature lead to more complete combustion during the higher load. As the result of the better air–fuel mixing process and/or the increased fuel/air equivalence ratio, [88,107] CO emissions for biodiesel decrease with an increase in engine speed.

iv. Total hydrocarbon (THC)

It is predominant viewpoint that THC emissions reduce when pure biodiesel is fueled instead of diesel [86,87,95,109]. However, the lower heating value of the pure

biodiesel increases fuel consumptions that could produce high local fuel-to-air ratios, increasing THC emissions [109].

Biodiesel involves higher oxygen content, which leads to more complete combustion [95,110,111]. Additionally, the higher cetane number of biodiesel could reduce the burning delay, which results in the THC emissions reduction [112,113].

Otherwise, the feedstock of biodiesel and its properties have an effect on THC emissions, especially the increase in chain length or saturation level of biodiesel led to lower THC emissions [114].

Furthermore, the shorter injection and combustion timing will advance for biodiesel compared with diesel would produce lower THC emissions [91,93]. THC emissions of biodiesel decreases at low loads [52,72], although a greater decrease was reported at intermediate load than low and high load [100,116].

v. Carbon dioxide (CO_2)

The potential of biodiesel to reduce the carbon dioxide introduced into the atmosphere as a result of engine combustion has been suggested by several authors [117]. The carbon released by petroleum diesel combustion was fixed from the atmosphere during the formative years of the earth. Nevertheless, carbon dioxide released by biodiesel combustion can be fixed by plants trough the process of photosynthesis in a recent year and will be recycled by the next. So, the use of vegetable oils as biodiesel feedstock could reduce the accumulation of CO_2 in the atmosphere because it comprised a closed carbon cycle [118]. If the effect of biodiesel on global greenhouse gas emissions is evaluated through the life cycle of CO_2 emissions, it can be pointed out that biodiesel will reduce CO_2 emissions in 50-80% compared to fossil diesel fuel [87,106]. In addition, the low carbon to hydrogen ratio of biodiesel than diesel fuel resulted in fewer CO_2 emissions during complete combustion [95,110].

vi. Other non-regulated emissions

Emissions in aromatic and polyaromatic compounds and carbonyl compounds can be also affected by the use of biodiesel fuel and its blends.

- ***Polycyclic aromatic hydrocarbon (PAH) compounds***

  Most of researches [96,111,119,120] reported that the decrease in aromatic and polyaromatic emissions of biodiesel was usually due to the enhanced absorption of PM to these components. The increase of oxygen in the biodiesel improves combustion and promotes the degradation of BTX [111]. In addition, Di et al. [121] detected at higher engine loads and higher exhaust gas temperatures lower benzene emissions, and concluded that benzene could be easily degraded at high exhaust gas temperature.

- ***Carbonyl compounds***

  It is widely accepted that, biodiesel increases these emissions because of higher oxygen content [96,97]. Carbonyl emissions exhibited a strong correlation with the biodiesel content. Acetaldehyde emissions increased sharply with biodiesel–diesel blend [14], which could be caused by a higher free glycerol or total glycerol content of the methyl ester.

III. Diesel Oxidation Catalyst

The role of Diesel Oxidation Catalyst (DOC) is to facilitate the oxidation of unburned hydrocarbons and carbon monoxide through the use of oxygen, thereby producing CO_2. This catalyst is also involved in the oxidation of NO to NO_2, which in turn influences both the passive regeneration of the DPF and the SCR reaction. In addition, it is placed the first in the heavy-duty engines after-treatment system. Thus, the correct functioning of the DOC is key for the effectiveness of the after-treatment system.

Several kinds of materials were tested in early stages of automotive exhaust catalysis since 70s. Metal transition based catalysts as nickel or copper were tried and discarded due to their low thermal stability [122]. It has been long recognized, that noble metals might be enough active to afford the oxidation of the unburned HC and CO on a catalyst placed in the exhaust downstream of the engine. Despite the employment of catalysts based on precious metals, also called platinum group metals (PGM), implies higher economic costs, they are the only ones able to ensure efficient oxidation catalysis.

a. Bimetallic Pt/Pd diesel oxidation catalysts

As previously defined in this chapter, DOC consists on support structure in form of monolith (e.g. ceramic cordierite), which contains a large number of parallel channels. These are coated with a noble metal catalytic active phase supported on a high surface area washcoat.

The primary function of the washcoat is to provide a large surface area for the noble metal, and to slow down catalyst sintering that occurs at high temperatures. Alumina-based materials are widely used as catalysts supports [123–125] due to multiple factors [126]: i) the presence of Lewis acid sites on its surface, which enhance the electron deficiency of noble metals [127,128]; ii) its high thermal stability [129]; iii) the presence of cation vacancies on its structure, facilitating interaction of the active component with the support [130].

For catalytic combustion, γ-Al_2O_3 is usually used as washcoat, as it provides a high, stable surface area for dispersion of the precious metals. The thermal stabilization of alumina support is vital to high temperature applications [123]. During normal running of an engine the catalyst bed can rise to over 1000 ºC, resulting in the phase transformation of γ-Al_2O_3 to the thermodynamically most stable α-Al_2O_3. Sintering precedes the α-Al_2O_3 nucleation, which contributes significantly to the loss of surface area at high temperatures [131,132]. Many cations [131,133–135], such as La^{3+}, Ba^{2+}, Zr^{4+}, Ce^{4+} and Si^{4+}, have positive effects as the inhibitors of these effects.

Previous studies [131–133] have demonstrated the influence of lanthanum on the maintenance of high surface area at over 900 ºC. However, the influence of "purely mechanical mixing" of additive oxides on the loss of surface area of alumina is not considered in most references, especially when the surface area of alumina is low at temperature over 1000 ºC. Nevertheless, La-modified γ-Al_2O_3 by impregnation has demonstrated that the addition of lanthanum delays the surface area loss of alumina. It has been shown [125] that the lanthanum species are located in limited "active sites" of alumina, which are vacancies in the bulk derived from the same valence of the two aluminium ions, which are either tetrahedral or octahedral in nature. These species can interact with the Al_2O_3 forming $LaAlO_3$, which stabilizes these ions in more stable octahedral symmetry. Thus, it mainly retards the loss of surface area by immobilizing the surface aluminium ions into a more stable structure than α-Al_2O_3 structure [136]. In addition, the stabilization of lanthanum species is

related to calcination temperature. Upon calcination at high temperature, the number of "active sites" of alumina will decrease due to the sintering. Therefore, the lanthanum species located in other Al_2O_3 sites would precipitate as La_2O_3.

Besides, a noble metal layer is dispersed on the alumina washcoat as the active phase of diesel oxidation catalysts. The choice of these metals in automotive materials is the result of three factors:

- The size of catalyst that could be accommodated in the available space requires large volumetric flows of the exhaust, which translates in very short residence times. Under these conditions, only precious metals have the necessary activity for the removal pollutants.
- The precious metals have the required resistance to poisoning by residual amounts of sulphur in the exhaust. Sulphur poisoning results in the formation of sulphate species on the support, decreasing the specific surface area [137].
- The interaction between the oxide support and the metals reduce the deactivation at high-temperature.

Currently, Pt, Pd containing catalysts is the most commonly used active phase of diesel oxidation catalysts supported on γ-Al_2O_3.

Platinum has traditionally been the catalyst of choice for diesel oxidation catalysts as is among the most active elements for NO oxidation. However, Pt nanoparticles can sinter when the catalysts are used at high temperature under oxidizing conditions [42]. The mechanism of sintering is Ostwald ripening, which involves interparticle transport of mobile species, with larger particles growing at the expense of smaller due to differences in surface energy.

Sintering catalyst process can be divided in three phases [138]. Firstly, it shows a rapid decay of surface area caused by the disappearance of the smallest particles and the growth in size of the larger ones. During the intermediate stage of catalyst sintering, the decrease of the number of active sites in catalyst surface appeared. However, significant changes are still after long time observations due to the migration of large particles ($\geq$ 10 nm). When these migrating particles encountered other particles on the support, they tended to coalesce and become spheroidal [138]. Finally, at high temperatures, the process of sintering slows down enough to be undetectable over short periods of time. Otherwise, at higher temperatures support

sintering also becomes important. Nevertheless, this phenomenon can be avoided by support stabilization by addition of promoters, as explained before.

Sintering catalysts process results in the loss of active surface area and drop in reactivity after use. Due to the high cost and low abundance of Pt, it is important to develop strategies to slow its rate of sintering and thus, avoid the lost of Pt catalytic efficiency after ageing at high operating temperatures.

Earlier studies have shown that exist some synergetic effects in terms of light-off and thermal stability during interaction of platinum with palladium [139–141]. It has been demonstrated that Pt/Pd alloys sinter more slowly in oxidative atmosphere than pure Pt does. The overall cause of inhibition of Pt sintering by Pd is related to kinetic limitations of Pt volatilization. Pure Pt crystallites have been observed to evaporate as PtO_2 when heated in air above 700 ºC. However, PdO has negligible vapour pressure even at very high temperatures. The vapour pressure of Pd is also considerably lower than that of PtO_2 [142]. Thus, Pd and PdO can be regarded as completely non-volatile under high temperature and oxidant conditions. When Pt and Pd are forming an alloy, there is surface segregation of Pd on the crystallite surface. This could inhibit Pt removal from the crystallite and accordingly, avoid Pt sintering.

The structure of the alumina supported bimetallic Pt/Pd diesel oxidation catalysts have been widely studied [143–145]. Morlang et al. [139], have reported X-ray absorption fine structure (EXAFS) spectra for Pt/Pd bimetallic catalysts after air calcination. Interference between Pd-Pd shell in tetragonal PdO and contributions of Pd-Pt and Pd-Pd metallic phase was observed. Thus, in the bimetallic Pt/Pd catalysts Pd exists in both metallic and oxidised form. Regarding Pt, it is presented in form of Pt-Pt scattering path. The presence of Pd as an additional scatterer increases the metallic coordination shell due to the phase interference between Pt and Pd. So, structure of Pt/Pd bimetallic catalysts consists on a Pt/Pd metallic core enriched of Pt, surrounded by an outer shell of PdO. Similar results were obtained in other studies using XPS and Raman spectroscopy [146–148]. This structure supply to the alloyed system a significant stabilisation against sintering in contrast to monometallic catalysts, as explained above.

b. Oxygen storage complementary phase

Diesel engines can be considered to be learn-burning with respect to the total volume, however the fuel and air are not well mixed before the combustion. Most of the combustion occurs in zones around small droplets of fuel. The presence of an "oxygen storage" component limits the decrease of diesel oxidation catalysts efficiency under lean burn conditions in automotive exhaust.

Since the beginning of the 1980s, the use of CeO_2 in the automotive pollution control has become so broad to represent today the most important application of the rare earth oxides. Addition of CeO_2 limits this disadvantage due to its ability to act as an oxygen buffer by storing/releasing O_2 due to the Ce^{4+}/Ce^{3+} redox couple, which is called the oxygen storage capacity (OSC). The reactions involved in oxygen storage are illustrated in Figure I-7, and make use of the two easily accessible oxidation states of cerium at exhaust gas temperatures.

$$2CeO_2 + CO \rightarrow Ce_2O_3 + CO_2$$

$$Ce_2O_3 + \tfrac{1}{2}\,O_2 \rightarrow 2CeO_2$$

Figure I-7. Reactions involved in cerium oxygen storage [149].

The high OSC is a result of the high reducibility of Ce^{4+}, which is a consequence of the O^{2-} high mobility inside the ceria fluorite type lattice [150,151]. However, the major problem of CeO_2 is the loss of oxygen storage capacity (OSC) due to a reduction in surface area upon sintering produced by thermal treatment. Insertion of zirconia into the cubic CeO_2 framework with formation of a solid solution leads to improvements in oxygen storage capacity of ceria, redox property, thermal resistance, and better catalytic activity at lower temperatures [152–154]. So CeO_2 – ZrO_2 solid solution is widely used for exhaust gas treatment of automobiles [155–157].

The introduction of ZrO_2 intro CeO_2 produces structural modifications of the fluorite type lattice. The CeO_2–ZrO_2 phase diagram [156] below 1200 ºC points to the presence of two tetragonal phases (t' and t'') in the compositional range 10–80% CeO_2, while for ceria contents higher than 80% the cubic phase is formed.

Previous studies [158] have reported that the displacement of the oxygen far from zirconium is responsible for the promoting effects of zirconia on the reduction

behaviour of CeO_2. The lower ionic radius of Zr (0.86 Å) compared to Ce (1.01 Å), decreases the number of neighbouring oxygen around Zr^{4+}. The distance between Zr^{4+} ions and the oxygen increases upon to a non bonding distance, which induces the formation of a pseudo cubic phase with a distorted oxygen sub-lattice [158]. This distortion of the oxygen lattice makes the reduction in the bulk material favourable, improving oxygen storage.

In addition, as Zr^{4+} ion is hardly reducible, the electronic charge transferred during the reduction process would be stabilized via the reduction of tetravalent cerium in the network. The reduction temperature of cerium-zirconium solid solution decreases after first cycle under reductive atmosphere (730 -1050 ºC), and so the subsequent re-oxidation middle temperatures (430 – 600 ºC) [159]. This cycle strongly affects the redox behaviour and dramatically increases oxygen storage capacity.

Otherwise, in contrast with pure CeO_2, surface area does not influence the reduction behaviour of CeO_2 – ZrO_2 solid solutions [153,160]. As reported in the literature [161], the surface area decreases with increasing amounts of ZrO_2. However, the total OSC increases with the amount of ZrO_2, so the actual value of the OSC is influenced by the dependence of the rate on the surface area or grain size.

Moreover, high catalytic activity and stability are found when CeO_2-ZrO_2 solid solutions are used in automotive catalysts. Pt/ceria-zirconia based catalysts present high noble metal dispersion [162], promoted by the metal-support interaction. Previous studies have confirmed by EXAFS the formation of a Pt-Ce alloy that stated as the reason of the properties of redox Pt/ceria-zironia catalysts [163].

In terms of the reaction rate, the Pt interacts with the oxide to enhance the rate of oxygen release. It has been verified [161] that Pt has little effect on the uptake of oxygen. Oxygen surface and bulk diffusivities correlate with the homogeneity of Zr and Ce atom distributions in the oxide framework. However, Pt seems to act as a "gate to remove oxygen from the mixed oxide. Oxygen storage and release reaction in presence of Pt is divided into several reaction steps, namely, reaction on precious metal, surface oxygen diffusion and bulk oxygen diffusion (Figure I-8) [164].

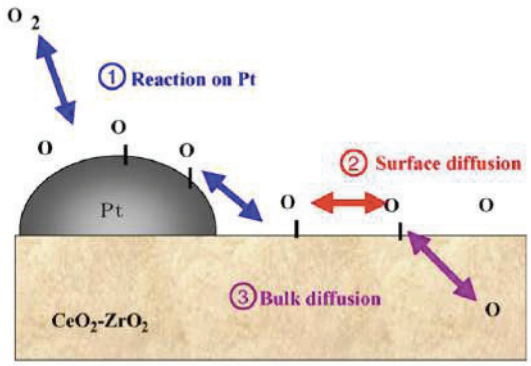

Figure I-8. Steps in oxygen storage/release reaction on Pt/CeO_2-ZrO_2 catalyst [165].

In the case of ceria-zirconia promoted Pd catalysts, the formation of a ceria-zirconia mixed oxide overlayer on Pd particles has been observed [166]. It shows a high interaction between Pd and oxide, which reflects in the higher stability to sinter of the catalyst [167]. Lower reduction temperature was found related to the ability of noble metal to promote the reduction of CeO_2 via spilling H_2 species over the support [168].

On these bases, the use of ceria stabilized in solid solution with zirconia well account to obtain durable diesel oxidation catalysts.

c. Influence of biodiesel and lubricant impurities (Na, K, Ca and P)

Regarding the biodiesel synthesis process, some inorganic compounds can be present on the biofuel, exposing the catalyst to potential poisons. Thus, the use of sodium and potassium alkaline catalysts on biodiesel synthesis via transesterification could difficult the refining process due to the soaps formation [84]. Furthermore, to overcome the problems associated with the separation of the catalyst from the product after completion of transesterification, calcium oxide catalyst is introduced in biodiesel production [169]. Even if it is separated from the reaction mixture by filtration, some traces can stay in biodiesel fuel. Ca catalyst can be found with Mg from dry wash adsorbents or used together from hard water washing [170]. In addition, the burning of the antiwear/antioxidant additive oil zinc di-alkylthiophosphate (ZDDP) might be produced phosphorus species, which can also affect automotive catalyst efficiency [171–173].

Current European (EN 14214 [174]), US and Canadian (ASTM D6751 [175]) regulations, limit the amount of these inorganics compounds in biodiesel fuels (Table I-2).

Table I-2. EN 14214 and ASTM D6751 biodiesel standards [174,175].

Compounds	Na + K	Ca + Mg	P
Biodiesel C_{max} (ppm)	5.0	5.0	4.0

Regardless of the source, these inorganic compounds are converted into oxides, sulphates, hydroxides or carbonates during the combustion process to form an ash that can be deposited onto the exhaust emission control devices.

In spite of the fact that alkali metal has usually been considered promoters since several decades [176], their effective overall role is still debated [177–179]. The low ionisation energy of alkali metals confers them an electropositive (electron donor) behaviour, which increases in moving down a group from Li to Cs. Related to their electron donor characteristics, the adsorption of alkali metals on other metal surface is accompanied by distinctive changes in the work function of the metal. The work function (Φ) of a solid surface is defined as the minimum energy to bring an electron from the Fermi level (E_F) through that surface when it is electrically neutral. Thus, the promotion effect of alkali doping is linked to electronic changes, which allows defining alkali metals as electronic promoters. Generally, electronegative adsorbates (electron acceptor) cause an increase in Φ while electropositive (electron donor) adsorbates, such as alkali metals, decrease the work function.

The promotion effect of alkali doping can manifest in various different ways [180]:

i. Increase the selectivity
ii. Increase the activity
iii. Prolong the lifetime of the catalyst

In general, the selectivity of a doped catalyst passes through a maximum as the quantity of added alkali increases [181]. This is related to the decrease of the work function by doping with alkali metal until a minimum, which is follow of an increase of the work function value. Thus it exists a maximum alkali doping that corresponds to a minimum of the work function. If alkali is doped in excess, then the promotion effect upon the activity decreases. In addition, the selectivity increases doping with

alkali metals with increasing the atomic weight [182]. Thus, the greatest increase activity is usually achieved with cesium and the smallest with lithium. Previous studies [183] found that Na and K alkali metals have a promoting role while Rb and Cs presented a degradation effect in the preferential CO oxidation in H_2-rich gas. This increment of the catalytic activity can be due to the neutralization of acidic centers and creation of basic sites, related to the highly basic properties of alkali compounds.

Although excessive quantities of alkali can be counterproductive, it is worth noting that alkali doping can delay catalyst deactivation due to numerous factors such as sintering or volatility of the active components, phase transformation and coking [184]. Doping is particularly effective against coke deactivation, which is avoided by the formation of alkali metal formats as intermediates in the coke gasification process [185,186].

Otherwise, the modification of the electronic properties of the catalyst surface plays a role in the activity-enhancing effect of alkali upon semiconductor and metallic catalysts. The presence of alkalis may influence the adsorption rate and the strength of the bonds formed between the adsorbed species and the substrate. It has been shown [187] that when an adsorbate is chemically adsorbed on a metal surface, new electronic states are formed. These electronic states consist of bonding and antibonding states, as shown in Figure I-9. When the antibonding states are pushed above the Fermi level, the adsorbate bonds to the metal [188].

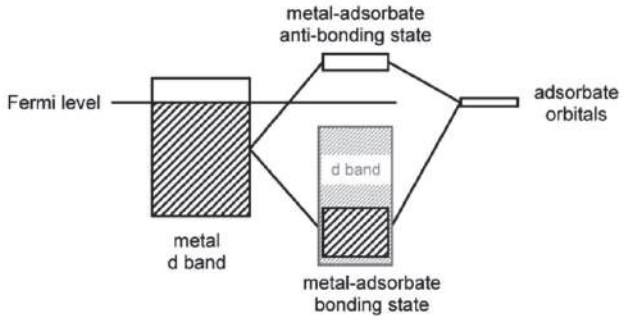

Figure I-9. Simplified scheme describing the electronic states related to the interaction of adsorbate orbitals with the metal d band [187].

As discussed above, alkali metals have a strongly electropositive behaviour. Vayenas et al. [189], demonstrated that alkali metal ions onto the metal catalyst surface present an electron-donor effect from the alkali to the metal, and then to the adsorbates via increased backdonation into the antibonding π^* orbitals of the adsorbed

molecules. These results can be applied to the interaction of adsorbates such as CO and NO, main components in the exhaust gases, with alkali-modified transition metal surfaces like Pt and Pd, principal components on the DOC. Accordingly, alkali addition results in strengthening of the metal-adsorbate NO (or CO) bond, which concomitant weakening of the N-O (or C-O) intramolecular bond, favoring molecular dissociation and subsequent adsorption. This effect is pronounced for transition metal surfaces, such as Pt or Pd, where the backdonation of the metal d-electronic density to the $2\pi^*$ antibonding orbitals of adsorbed NO (or CO) is strong (Figure I-10).

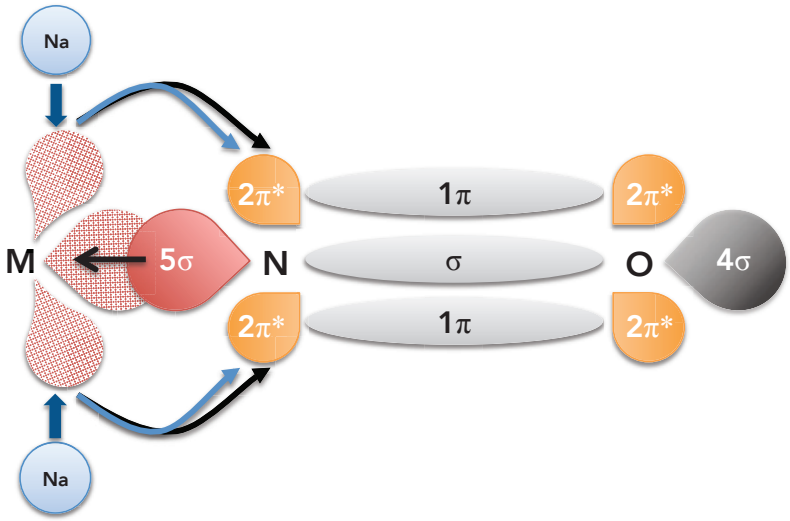

Figure I-10. Scheme describing the electronic transfer related to the interaction of $2\pi^*$ orbital of NO with the metal d-orbitals.

Previous studies have also demonstrated that the doping of the support with alkali or alkaline earth species may affect the catalytic activity of Pt-group metals. Pellegrini et al. [179] suggested that using K as an alkaline dopant may affect the reducibility of PdO. By comparing TPR results of undoped and K-doped catalysts, it was evidenced a strong chemical interaction between potassium and Pd^{2+} species. This interaction can eventually lead to the formation of a mixed compound even at low K content, which decreases the reducibility of the catalyst. Also, it has been revealed that K species may cover a number of the Pt sites. Luo et al. [190] have reported that the decrease in Pt availability with K loading is result from Pt being covered by K. Thus, an excess of K loading results in encapsulation of Pt sites, reducing the efficiency of the catalyst. In addition, because of alkali mobility, K-based catalysts are blamed for low thermal stability, which is associated to several technological problems due to interactions with the monolith support [191].

It is worth noting the role of the alkali metals in de-NOx catalytic chemistry of Pt-group. Previous studies [192–195] have shown that alkali-modified Pt or Pd catalysts exhibit important enhancements in both activity and selectivity towards N_2 production, during NO reduction by CO or C_3H_6. This alkali promotion is due to previously described alkali-induced strengthening of the metal-NO bond, which consequently enhances dissociation of NO molecules adsorbed on the platinum metal component of the catalyst [193].

Otherwise, it is well known that the presence of alkaline metals (and in lower extent of alkaline-earth metals) improves the soot oxidation, either alone or as promoters [196,197]. Several studies [198–200] have suggested that alkali metals may favour soot oxidation through the formation of low melting point compounds. In consequence, the mobility of the active surface species is improved, increasing activity according to a higher contact between catalyst and soot. Thus, the oxidation of soot is promoted by consuming the carbon to form carbonate species during soot combustion. Along this line, some authors have proposed the impregnation of soot with alkaline (Na, K) or alkaline/earth (Ca, Ba) metals [201] in order to increase the contact with the soot. Under these "full contact" conditions, the reactivity in the soot combustion is improved and well correlates with the electropositivity character of the alkali ions [202]. However, the synergetic effects found between platinum and potassium produce that the thermal stability is still not satisfactory [197,202]. In addition, it has been proved that beyond 10 wt% of alkali addition, the beneficial impact on carbon oxidation under is not found anymore [196]. Otherwise, several studies have found higher reactivity to biodiesel soot than diesel soot due to their more amorphous structure , but also to their higher oxygen content and the presence of alkali metals [203,204]. However, the influence of inorganic element on soot oxidation with NO_2 is not widely reported in literature, even NO_2 has a fundamental role as an oxidant agent during passive DPF regeneration. Schobing et al. [205], demonstrated that the impregnation of Na and K on carbon black have a beneficial impact on both active and passive DPF regeneration by increasing the number of surface carbon oxygenated active complex of the reaction.

Furthermore, due to their highly basic properties, alkali and alkaline earth components provide a major contribution to the overall NO_x adsorption capacity of NO_x-storage catalysts. Thermodynamic evaluation and reaction data have

demonstrated that the basicity of the component is directly related to the NO_x trapping performance [206,207]. The addition of different trapping components results in changes in the performance as a function of the temperature. Thereby, based on results of previous studies [208,209], authors suggested that alkali nitrates formed using K, Na and Ca are stables at higher temperatures.

Besides alkali species coming from biodiesel synthesis process, phosphorus impurities coming from lubricants (zinc dialkyldithiophosphate, ZDDP) have also an influence on oxidation catalysts. Chemical deactivation of the precious metals has been verified by adsorption on the active sites, reducing the catalytically active surface [210,211]. It has been suggested that phosphorus continues its accumulation into the catalyst even after adsorption on the active sites. Thus, poisoning elements may disturb the surface diffusion of adsorbed reactants, preventing the oxidation reactions of CO and HCs [212]. In addition, phosphorus compounds may react with the support, changing the composition by forming aluminate phosphates, which would block the catalyst pores, decreasing the specific surface area of the catalyst [213]. In addition, the interaction between phosphorus and the Ce-Zr mixed oxide can lead a layer of Ce phosphate which inhibits the Ce^{4+}/Ce^{3+} reduction and reoxidation steps [214]. Honkanen et al. [215] have verified by TEM analysis that phosphorus poisoning slightly increased the average size of platinum and palladium particles, decreasing the number of active sites. Nevertheless, few studies reveal that phosphorus presents an inhibiting impact on the soot oxidation [216–218]. However, phosphorus presented a catalytic effect for the DPF passive regeneration by NO_2 oxidation when water was present in the gas mixture [205].

IV. Conclusions

The environmental pollution coming from heavy-duty Diesel engine emissions is one of the major problems nowadays. The European Union has published normative each time more restrictive in order to limit these emissions. In addition, automotive makers need to introduce an after-treatment system which consist in diesel oxidation catalyst (DOC), diesel particulate filter (DPF) and finally, selective catalytic reduction (SCR). Moreover, the last European normative published, Euro VI, established that the durability of the after treatment system has to be at least seven years or 700 000 km.

Otherwise, biodiesel depicts like a good alternative to fossil diesel fuel due to its similar calorific power and its better carbon balance, which is in agreement with the objectif of the reduction of CO_2 emissions established in the Paris Agreement. However, impurities coming from biodiesel synthesis (Na, K, Ca) and motor lubricants (P) could influence in the activity and durability of the after-treatment system. As literature review has shown, these impurities can affect the activity of Pt-Pd based catalysts as the employed in the DOC, acting as promoters or poisons depending of different factors.

The present work is focalised in the study of the influence of these impurities in the Diesel Oxidation Catalyst activity. Thus, this manuscript is going to be organised as follows. Firstly, the experimental techniques and set-up employed was resumed in Chapter II. After that, Chapter III aims to describe the influence of Na, K, Ca and P in the catalytic activity of a DOC reference catalyst. To follow, an in-situ DRIFTS study was developed in order to explain the changes found in the DOC catalytic behaviour (Chapter IV). The Chapter V studies the influence of the hydrothermal aging treatment of the DOC catalyst in presence of impurities. Finally, a general conclusion of the results was described in the Chapter VI.

For brevity, some characterization results as well as secondary reactions (reduction of NO_2 by C_3H_6) are presented in Annexe I. In Annexe II, DRIFTS results that present similar tendency than the described during the Chapter IV are depicted.

References:

[1] J.B. Heywood, McGraw-Hill McGraw Hill Ser. Mech. Eng. (1988).
[2] E. Santoyo-Castelazo, A. Azapagic, J. Clean. Prod. 80 (2014) 119–138.
[3] P. Mendoza-Villafuerte, R. Suarez-Bertoa, B. Giechaskiel, F. Riccobono, C. Bulgheroni, C. Astorga, A. Perujo, Sci. Total Environ. 609 (2017) 546–555.
[4] A. Russell, W.S. Epling, Catal. Rev. - Sci. Eng. 53 (2011) 337–423.
[5] R. Prasad, V.R. Bella, Bull. Chem. React. Eng. Catal. 5 (2011) 69–86.
[6] W.A. Majewski, M.K. Khair, SAE Int. (2006) 978–0.
[7] A. Faiz, C.S. Weaver, M. Walsh, S. Gautam, L. Chan, Air Pollution from Motor Vehicles, The World Bank, 1997.
[8] A. Cosseron, (2013).
[9] T. Lee, J. Park, S. Kwon, J. Lee, J. Kim, Sci. Total Environ. 461–462 (2013) 377–385.
[10] J.J. Chong, A. Tsolakis, S.S. Gill, K. Theinnoi, S.E. Golunski, Int. J. Hydrogen Energy 35 (2010) 8723–8732.
[11] S.K. Hoekman, C. Robbins, Fuel Process. Technol. 96 (2012) 237–249.
[12] F. Fajardie, Interaction Métal-Supports Réductibles. Application À La Post-Combustion Automobile, Réaction CO-NO-O2., Université Pierre et Marie Curie, 1996.
[13] D. Demers, G. Walters, (1999).
[14] S. Machado Corrêa, G. Arbilla, Atmos. Environ. 42 (2008) 769–775.
[15] P. Darcy, Modélisation Du Fonctionnement D'un Filtre À Particules Catalysé., Université Pierre et Marie Curie, 2005.
[16] S. Eymerie, Etude Expérimentale Des Décharges Atmosphériques Générées Par Impulsions Nanosecondes - Application Au Traitement Des Particules de Suies Diesel, Université de Rouen, 2003.
[17] D. Diat-Sanchez, Allergy 52 (1997) 52–56.
[18] M. Kryzanowski, B. Kuna-Dibbert, J. Schneider, Health Effects of Transport-Related Air Pollution, 2005.
[19] A.K. Agarwal, Prog. Energy Combust. Sci. 33 (2007) 233–271.
[20] C.J. Tighe, M. V. Twigg, A.N. Hayhurst, J.S. Dennis, Combust. Flame 159 (2012) 77–90.
[21] T.A. Metts, S.A. Batterman, G.I. Fernandes, P. Kalliokoski, Atmos. Environ. 39 (2005) 3343–3354.
[22] B.R. Stanmore, J.F. Brilhac, P. Gilot, Carbon N. Y. 39 (2001) 2247–2268.
[23] H. Burtscher, J. Aerosol Sci. 36 (2005) 896–932.
[24] L. Olsson, E. Fridell, J. Catal. 210 (2002) 340–353.
[25] A.B. Palotas, Enery & Fuels 10 (1996) 254–259.
[26] N. Englert, Toxicol. Lett. 149 (2004) 235–242.
[27] R.A. Michaels, M.T. Kleinman, Aerosol Sci. Technol. 32 (2000) 93–105.
[28] (n.d.).
[29] B. Guan, R. Zhan, H. Lin, Z. Huang, Appl. Therm. Eng. 66 (2014) 395–414.
[30] I.A. Reşitoɨlu, K. Altinişik, A. Keskin, Clean Technol. Environ. Policy 17 (2015) 15–27.
[31] M. Zheng, G.T. Reader, J.G. Hawley, Energy Convers. Manag. 45 (2004) 883–900.
[32] J. Thangaraja, C. Kannan, Appl. Energy 180 (2016) 169–184.
[33] M. Chen, (2003) 1–7.
[34] T.J. Wang, S.W. Baek, (2008) 2528–2537.
[35] E. Zervas, Appl. Therm. Eng. 28 (2008) 962–966.
[36] S. Gil, J.M. Garcia-Vargas, L.F. Liotta, P. Vernoux, A. Giroir-Fendler, Perovskites Relat. Mix. Oxides Concepts Appl. (2015) 797–816.
[37] M.H. Wiebenga, C.H. Kim, S.J. Schmieg, S.H. Oh, D.B. Brown, D.H. Kim, J.H. Lee, C.H.F. Peden, Catal. Today 184 (2012) 197–204.
[38] M. Haneda, K. Suzuki, M. Sasaki, H. Hamada, M. Ozawa, Appl. Catal. A Gen. 475

(2014) 109–115.
[39] L. Zhu, C.S. Cheung, W.G. Zhang, J.H. Fang, Z. Huang, Fuel 113 (2013) 690–696.
[40] M. Zheng, S. Banerjee, Appl. Therm. Eng. 29 (2009) 3021–3035.
[41] K. Johansen, Catal. Today 258 (2015) 2–10.
[42] H. Xiong, E. Peterson, G. Qi, A.K. Datye, Catal. Today 272 (2016) 80–86.
[43] D. Fino, V. Specchia, Powder Technol. 180 (2008) 64–73.
[44] V. Di Sarli, A. Di Benedetto, Chem. Eng. Sci. 137 (2015) 69–78.
[45] M. Belloir, N. Sakushima, H. Lahjaily, SAE Tech. Pap 2007-01–01 (2007).
[46] G. Koltsakis, O. Haralampous, Z. Samaras, L. Kraemer, F. Heimlich, K. Behnk, SAE Tech. Pap 2007-01–11 (2007).
[47] K. Johansen, S. Dahl, G. Mogensen, S. Pehrson, J. Schramm, A. Ivarsson, SAE Int. 2007-01–19 (2007) 330–338.
[48] B.R. Stanmore, V. Tschamber, J.F. Brilhac, Fuel 87 (2008) 131–146.
[49] J. Han, E. Kim, T. Lee, J. Klm, A. N., H. Han, SAE Tech. Pap 2011-01–13 (2011) 6.
[50] M. Stanciulescu, J.P. Charland, J.F. Kelly, Fuel 89 (2010) 2292–2298.
[51] M. Koebel, M. Elsener, M. Kleemann, Catal. Today 59 (2000) 335–345.
[52] C. Scott Sluder, J.M.E. Storey, S. a. Lewis, L. a. Lewis, SAE Tech. Pap. 2005 (2005).
[53] M. Devarakonda, G. Parker, J. Johnson, V. Strots, S. Santhanam, SAE Int. J. Fuels Lubr. 1 (2009) 646–661.
[54] L. Xu, R. McCabe, W. Ruona, G. Cavataio, SAE Tech. Pap 2009-01–02 (2009).
[55] M. Castagnola, J. Caserta, S. Chatterjee, H. Chen, R. Conway, J. Fedeyko, W. Klink, P. Markatou, S. Shah, A. Wlaker, SAE Tech. Pap 2011-01–13 (2011).
[56] J.A. Sullivan, O. Keane, Appl. Catal. B Environ. 61 (2005) 244–252.
[57] M. Colombo, I. Nova, E. Tronconi, Catal. Today 151 (2010) 223–230.
[58] A. Vimont, F. Thibault-Starzyk, M. Daturi, Chem. Soc. Rev. 39 (2010) 4928.
[59] T. Blasco, A. Corma, J. Martínez-Triguero, J. Catal. 237 (2006) 267–277.
[60] M. Kang, J. Mol. Catal. A Chem. 161 (2000) 115–123.
[61] F. Li, Y. Zhang, D. Xiao, D. Wang, X. Pan, X. Yang, ChemCatChem 2 (2010) 1416–1419.
[62] D.Y. Yoon, E. Lim, Y.J. Kim, J.H. Kim, T. Ryu, S. Lee, B.K. Cho, I.-S. Nam, J.W. Choung, S. Yoo, J. Catal. 319 (2014) 182–193.
[63] Y. Luo, X. Wang, Q. Qian, Q. Chen, Int. J. Hydrogen Energy 39 (2014) 15836–15843.
[64] J.H. Ng, H.K. Ng, S. Gan, Clean Technol. Environ. Policy 12 (2010) 459–493.
[65] H. Jung, D.B. Kittelson, M.R. Zachariah, Environ. Sci. Technol. 40 (2006) 4949–4956.
[66] E. V Vega, Int. J. Chem. Environ. Eng. 2 (2011) 2–7.
[67] E.G. Smith, H.H. Janzen, N.K. Newlands, Can. J. Plant Sci. 87 (2007) 793–801.
[68] A. Karmakar, S. Karmakar, S. Mukherjee, Bioresour. Technol. 101 (2010) 7201–7210.
[69] Y. Chisti, Trends Biotechnol. 26 (2008) 126–131.
[70] J.P. Pandey, A. Tiwari, J. Algal Biomass Util. 1 (2010) 20–32.
[71] J.R. Benemann, Microalgae Biofuels A Br. Introd. (2009) 1–13.
[72] P.T. Vasudevan, M. Briggs, J. Ind. Microbiol. Biotechnol. 35 (2008) 421.
[73] M.Y. Koh, T.I. Tinia, Renew. Sustain. Energy Rev. 15 (2011) 2240–2251.
[74] G. Knothe, R.O. Dunn, M.W. Shockley, M.O. Bagby, JAOCS, J. Am. Oil Chem. Soc. 77 (2000) 865–871.
[75] K.D. Maher, D.C. Bressler, Bioresour. Technol. 98 (2007) 2351–2368.
[76] W. Parawira, Sci. Res. Essays 5 (2010) 1796–1808.
[77] L. Yang, M. Takase, M. Zhang, T. Zhao, X. Wu, Renew. Sustain. Energy Rev. 38 (2014) 461–477.
[78] S. Jain, M.P. Sharma, Renew. Sustain. Energy Rev. 14 (2010) 763–771.
[79] A. Abbaszaadeh, B. Ghobadian, M.R. Omidkhah, G. Najafi, Energy Convers. Manag. 63 (2012) 138–148.
[80] A.M.A. Attia, A.E. Hassaneen, Fuel 167 (2016) 316–328.
[81] A. Demirbas, Energy Convers. Manag. 50 (2009) 14–34.

[82] F. Ferella, G. Mazziotti Di Celso, I. De Michelis, V. Stanisci, F. Vegliò, Fuel 89 (2010) 36–42.
[83] M.C. Manique, C.S. Faccini, B. Onorevoli, E.V. Benvenutti, E.B. Caramão, Fuel 92 (2012) 56–61.
[84] I.M. Atadashi, M.K. Aroua, A.R.A. Aziz, N.M.N. Sulaiman, Appl. Energy 88 (2011) 4239–4251.
[85] M.A. Dubé, A.Y. Tremblay, J. Liu, Bioresour. Technol. 98 (2007) 639–647.
[86] H. Kim, B. Choi, Renew. Energy 35 (2010) 157–163.
[87] M. Lapuerta, J.M. Herreros, L.L. Lyons, R. García-Contreras, Y. Briceño, Fuel 87 (2008) 3161–3169.
[88] D.H. Qi, L.M. Geng, H. Chen, Y.Z. Bian, J. Liu, X.C. Ren, Renew. Energy 34 (2009) 2706–2713.
[89] J. Xue, T.E. Grift, A.C. Hansen, Renew. Sustain. Energy Rev. 15 (2011) 1098–1116.
[90] H. Aydin, H. Bayindir, Renew. Energy 35 (2010) 588–592.
[91] O. Armas, K. Yehliu, A.L. Boehman, Fuel 89 (2010) 438–456.
[92] R. Senthil, N. Ravichandiran, R. Silambarasan, Trans. Famena 39 (2015) 87–96.
[93] N.R. Banapurmath, P.G. Tewari, R.S. Hosmath, Renew. Energy 33 (2008) 1982–1988.
[94] P.J.M. Frijters, R.S.G. Baert, Int. J. Veh. Des. 41 (2006) 242.
[95] A.N. Ozsezen, M. Canakci, A. Turkcan, C. Sayin, Fuel 88 (2009) 629–636.
[96] M. Cardone, M. Mazzoncini, S. Menini, V. Rocco, A. Senatore, M. Seggiani, S. Vitolo, Biomass and Bioenergy 25 (2003) 623–636.
[97] O. Armas, J.J. Hernández, M.D. Cárdenas, Fuel 85 (2006) 2427–2438.
[98] G. Labeckas, S. Slavinskas, Energy Convers. Manag. 47 (2006) 1954–1967.
[99] L. Zhu, W. Zhang, W. Liu, Z. Huang, Sci. Total Environ. 408 (2010) 1050–1058.
[100] S. Kalligeros, F. Zannikos, S. Stournas, E. Lois, G. Anastopoulos, C. Teas, F. Sakellaropoulos, Biomass and Bioenergy 24 (2002) 141–149.
[101] S.J. Deshmukh, L.B. Bhuyar, Biomass and Bioenergy 33 (2009) 108–112.
[102] H. Raheman, S. V. Ghadge, Fuel 86 (2007) 2568–2573.
[103] A.S. Ramadhas, C. Muraleedharan, S. Jayaraj, Renew. Energy 30 (2005) 1789–1800.
[104] M. Karabektas, Renew. Energy 34 (2009) 989–993.
[105] X. Shi, Y. Yu, H. He, S. Shuai, J. Wang, R. Li, Fuel 84 (2005) 1543–1549.
[106] C. Carraretto, A. Macor, A. Mirandola, A. Stoppato, S. Tonon, Energy 29 (2004) 2195–2211.
[107] C.Y. Lin, H.A. Lin, Fuel 85 (2006) 298–305.
[108] M.A.R. Nascimento, E.S. Lora, P.S.P. Corrêa, R. V. Andrade, M.A. Rendon, O.J. Venturini, G.A.S. Ramirez, Energy 33 (2008) 233–240.
[109] J.M. Luján, V. Bermúdez, B. Tormos, B. Pla, Biomass and Bioenergy 33 (2009) 948–956.
[110] P.K. Sahoo, L.M. Das, M.K.G. Babu, S.N. Naik, Fuel 86 (2007) 448–454.
[111] C.S. Cheung, L. Zhu, Z. Huang, Atmos. Environ. 43 (2009) 4865–4872.
[112] A. Monyem, J. H. Van Gerpen, M. Canakci, Trans. ASAE 44 (2001) 35–42.
[113] G.H. Abd-Alla, H.A. Soliman, O.A. Badr, M.F. Abd-Rabbo, Energy Convers. Manag. 42 (2001) 1033–1045.
[114] M.S. Graboski, R.L. McCormick, Prog. Energy Combust. Sci. 24 (1998) 125–164.
[115] J.T. Song, C.H. Zhang, Proc. Inst. Mech. Eng. Part D J. Automob. Eng. 222 (2008) 2487–2496.
[116] P. Kwanchareon, A. Luengnaruemitchai, S. Jai-In, Fuel 86 (2007) 1053–1061.
[117] C.L. Peterson, T. Hustrulid, Biomass and Bioenergy 14 (1998) 91–101.
[118] J.M. Dias, M.C.M. Alvim-Ferraz, M.F. Almeida, Fuel 87 (2008) 3572–3578.
[119] L. Turrio-Baldassarri, C.L. Battistelli, L. Conti, R. Crebelli, B. De Berardis, A.L. Iamiceli, M. Gambino, S. Iannaccone, Sci. Total Environ. 327 (2004) 147–162.
[120] N. Yilmaz, S.M. Davis, Fuel 181 (2016) 729–740.
[121] Y. Di, C.S. Cheung, Z. Huang, Sci. Total Environ. 407 (2009) 835–846.
[122] Y.F. Yu Yao, J.T. Kummer, J. Catal. 46 (1977) 388–401.

[123] H. Arai, M. Machida, Appl. Catal. A Gen. 138 (1996) 161–176.
[124] G. Niu, Y. Huang, X. Chen, J. He, Y. Liu, A. He, Appl. Catal. B Environ. 21 (1999) 63–70.
[125] X. Chen, Y. Liu, G. Niu, Z. Yang, M. Bian, A. He, Appl. Catal. A Gen. 205 (2001) 159–172.
[126] C. Morterra, G. Magnacca, Catal. Today 27 (1996) 497–532.
[127] T. ISHIHARA, J. Catal. 136 (1992) 161–169.
[128] A.Y. Stakheev, L.. Kustov, Appl. Catal. A Gen. 188 (1999) 3–35.
[129] C. Bin Wang, H.G. Lee, T.F. Yeh, S.N. Hsu, K.S. Chu, Thermochim. Acta 401 (2003) 209–216.
[130] S.-D. Mo, Y. Xu, W.-Y. Ching, J. Am. Ceram. 80 (1997) 1193–1197.
[131] H. Schaper, E.B.M. Doesburg, L.L. Van Reijen, Appl. Catal. 7 (1983) 211–220.
[132] H. Schaper, E.B.M. Doesburg, P.H.M. De Korte, L.L. Van Reijen, Solid State Ionics 16 (1985) 261–265.
[133] P. Burtin, J.P. Brunelle, M. Pijolat, M. Soustelle, Appl. Catal. 34 (1987) 225–238.
[134] M.F.L. Johnson, J. Catal. 123 (1990) 245–259.
[135] L.A. Xue, I. Chen, J. Mater. Sci. Lett. 11 (1992) 443–445.
[136] B. Béguin, E. Garbowski, M. Primet, Appl. Catal. 75 (1991) 119–132.
[137] T. Kolli, T. Kanerva, M. Huuhtanen, M. Vippola, K. Kallinen, T. Kinnunen, T. Lepistö, J. Lahtinen, R.L. Keiski, Catal. Today 154 (2010) 303–307.
[138] B.B. Hansen, A.D. Jensen, P.A. Jensen, Fuel 106 (2013) 234–240.
[139] A. Morlang, U. Neuhausen, K. V. Klementiev, F.W. Schütze, G. Miehe, H. Fuess, E.S. Lox, Appl. Catal. B Environ. 60 (2005) 191–199.
[140] M. Kaneeda, H. Iizuka, T. Hiratsuka, N. Shinotsuka, M. Arai, Appl. Catal. B Environ. 90 (2009) 564–569.
[141] J.M. Herreros, S.S. Gill, I. Lefort, A. Tsolakis, P. Millington, E. Moss, Appl. Catal. B Environ. 147 (2014) 835–841.
[142] M. Chen, L.D. Schmidt, J. Catal. 56 (1979) 198–218.
[143] N. Toshima, M. Harada, T. Yonezawa, K. Kushihashi, K. Asakura, J. Phys. Chem. 95 (1991) 7448–7453.
[144] P.L. Hansen, A.M. Molenbroek, A. V. Ruban, J. Phys. Chem. B 101 (1997) 1861–1868.
[145] T. Rades, M. Polisset-Thfoin, J. Fraissard, R. Ryoo, C. Pak, Stud. Surf. Sci. Catal. 98 (1995) 65–66.
[146] K. Otto, C.P. Hubbard, W.H. Weber, G.W. Graham, Appl. Catal. B, Environ. 1 (1992) 317–327.
[147] J. Goetz, M.A. Volpe, A.M. Sica, C.E. Gigola, R. Touroude, J. Catal. 153 (1995) 86–93.
[148] V.H. Sandoval, C.E. Gigola, Appl. Catal. A Gen. 148 (1996) 81–96.
[149] M. V. Twigg, Appl. Catal. B Environ. 70 (2007) 2–15.
[150] H.C. Yao, Y.F.Y. Yao, J. Catal. 86 (1984) 254–265.
[151] S. Damyanova, C.A. Perez, M. Schmal, J.M.C. Bueno, Appl. Catal. A Gen. 234 (2002) 271–282.
[152] M. Pijolat, M. Prin, M. Soustelle, O. Touret, P. Nortier, J. Chem. Soc. Faraday Trans. 91 (1995) 3941.
[153] P. Fornasiero, G. Balducci, R. Di Monte, J. Kašpar, V. Sergo, G. Gubitosa, A. Ferrero, M. Graziani, J. Catal. 164 (1996) 173–183.
[154] S. Damyanova, B. Pawelec, K. Arishtirova, M.V.M. Huerta, J.L.G. Fierro, Appl. Catal. A Gen. 337 (2008) 86–96.
[155] R. Di Monte, J. Kaspar, P. Fornasiero, M. Graziani, C. Pazé, G. Gubitosa, Inorganica Chim. Acta 334 (2002) 318–326.
[156] L.F. Liotta, A. Macaluso, A. Longo, G. Pantaleo, A. Martorana, G. Deganello, Appl. Catal. A Gen. 240 (2003) 295–307.
[157] B. Yue, R. Zhou, Y. Wang, X. Han, X. Zheng, Appl. Surf. Sci. 246 (2005) 36–43.

[158] G. Vlaic, R. Di Monte, P. Fornasiero, E. Fonda, J. Kašpar, M. Graziani, J. Catal. 182 (1999) 378–389.
[159] T. Masui, T. Ozaki, K. Machida, G. Adachi, J. Alloys Compd. 303–304 (2000) 49–55.
[160] G. Balducci, P. Fornasiero, R. Di Monte, J. Kaspar, S. Meriani, M. Graziani, Catal. Letters 33 (1995) 193–200.
[161] M. Sugiura, Catal. Surv. from Asia 7 (2003) 77–87.
[162] A. TROVARELLI, Catal. Rev. 38 (1996) 439–520.
[163] P. Fornasiero, E. Fonda, R. Di Monte, G. Vlaic, J. Kaspar, M. Graziani, J. Catal. 187 (1999) 177–185.
[164] H. Shinjoh, J. Alloys Compd. 408–412 (2006) 1061–1064.
[165] T. Tanabe, A. Suda, C. Descorme, D. Duprez, H. Shinjo, M. Sugiura, Stud. Surf. Sci. Catal. 138 (2001) 135.
[166] L.S.F. Feio, C.E. Hori, S. Damyanova, F.B. Noronha, W.H. Cassinelli, C.M.P. Marques, J.M.C. Bueno, Appl. Catal. A Gen. 316 (2007) 107–116.
[167] G.W. Graham, H. Jen, R.W. Mccabe, A.M. Straccia, L.P. Haack, 67 (2000) 99–105.
[168] J. Kašpar, P. Fornasiero, M. Graziani, Catal. Today 50 (1999) 285.
[169] N. Panneerselvam, A. Murugesan, C. Vijayakumar, A. Kumaravel, D. Subramaniam, A. Avinash, Renew. Sustain. Energy Rev. 50 (2015) 17–31.
[170] T.L. Alleman, L. Fouts, G. Chupka, Contract 303 (2013) 275–3000.
[171] M.J. Rokosz, A.E. Chen, C.K. Lowe-Ma, A. V. Kucherov, D. Benson, M.C. Paputa Peck, R.W. McCabe, Appl. Catal. B Environ. 33 (2001) 205–215.
[172] D. Lafyatis, R. Petrow, C. Bennett, SAE Tech. Pap 2002-01–10 (2002).
[173] L. Xu, G. Guo, D. Uy, A.E. O'Neill, W.H. Weber, M.J. Rokosz, R.W. McCabe, Appl. Catal. B Environ. 50 (2004) 113–125.
[174] (2008).
[175] T. Alleman, L. Fouts, G. Chupka, Tech. Rep. NREL (n.d.).
[176] R.B. Anderson, (1956) 1–5.
[177] C. Crisafulli, R. Maggiore, S. Mini, S. Galvagno, Appl. Surf. Sci. 93 (1996) 309–316.
[178] L.F. Liotta, G. a Martin, G. Deganello, J. Catal. 164 (1996) 322–333.
[179] R. Pellegrini, G. Leofanti, G. Agostini, L. Bertinetti, S. Bertarione, E. Groppo, A. Zecchina, C. Lamberti, J. Catal. 267 (2009) 40–49.
[180] W.D. Mross, Catal. Rev.-Sci. Eng. 25 (1983) 591–637.
[181] L.M. Dmitrenko, L.D. Kuznetsov, P.D. Rabina, T.J. Malisheva, M.M. Ivanov, S.S. Mishchenko, V.S. Sobolevski, (1968) 560.
[182] Shell International, (1973) 448, 449.
[183] Y. Minemura, M. Kuriyama, S. ichi Ito, K. Tomishige, K. Kunimori, Catal. Commun. 7 (2006) 623–626.
[184] R. Krabetz, W.D. Mross, Ullmans Enzyklopädie Der Technischen Chemie, 4th ed., n.d.
[185] British Gas, (1975) 634, 541.
[186] P. Royen, F. Erhard, Erdöl Kohle 6 (1953) 195.
[187] J. Singh, R.C. Nelson, B.C. Vicente, S.L. Scott, J.A. Van Bokhoven, Phys. Chem. Chem. Phys. 12 (2010) 5668–5677.
[188] B. Hammer, J.K. Norskov, Adv. Catal. 45 (2000) 71–129.
[189] C.G. Vayenas, S. Brosda, Electrochemical Activation of Catalysis, 2002.
[190] J. Luo, F. Gao, D.H. Kim, C.H.F. Peden, Catal. Today 231 (2014) 164–172.
[191] R. Matarrese, L. Castoldi, N. Artioli, E. Finocchio, G. Busca, L. Lietti, Appl. Catal. B Environ. 144 (2014) 783–791.
[192] M. Konsolakis, N. Macleod, J. Isaac, I. V Yentekakis, R.M. Lambert, J. Catal. 193 (2000) 330–337.
[193] S. Koukiou, M. Konsolakis, R.M. Lambert, I. V. Yentekakis, Appl. Catal. B Environ. 76 (2007) 101–106.
[194] M. Konsolakis, I. V. Yentekakis, Appl. Catal. B Environ. 29 (2001) 103–113.
[195] I. V Yentekakis, R.M. Lambert, M.S. Tikhov, M. Konsolakis, V. Kiousis, J. Catal. 176

(1998) 82–92.
[196] E. Aneggi, C. de Leitenburg, G. Dolcetti, A. Trovarelli, Catal. Today 136 (2008) 3–10.
[197] K. Krishna, M. Makkee, Catal. Today 114 (2006) 48–56.
[198] P. Ciambelli, V. Palma, P. Russo, S. Vaccaro, J. Mol. Catal. A Chem. 204–205 (2003) 673–681.
[199] M.L. Pisarello, V. Milt, M.A. Peralta, C.A. Querini, E.E. Miró, Catal. Today 75 (2002) 465–470.
[200] V.G. Milt, C.A. Querini, E.E. Miró, Thermochim. Acta 404 (2003) 177–186.
[201] L. Castoldi, R. Matarrese, L. Lietti, P. Forzatti, Appl. Catal. B Environ. 90 (2009) 278–285.
[202] L. Castoldi, R. Matarrese, L. Brambilla, A. Serafini, M. Tommasini, L. Lietti, Aerosol Sci. Technol. 50 (2016) 405–415.
[203] J. Song, M. Alam, A.L. Boehman, U. Kim, Combust. Flame 146 (2006) 589–604.
[204] N. Lamharess, C.N. Millet, L. Starck, E. Jeudy, J. Lavy, P. Da Costa, Catal. Today 176 (2011) 219–224.
[205] J. Schobing, V. Tschamber, A. Brillard, G. Leyssens, Appl. Catal. B Environ. 226 (2018) 596–607.
[206] N. Takahashi, H. Shinjoh, T. Iijima, T. Suzuki, K. Yamazaki, K. Yokota, H. Suzuki, N. Miyoshi, S. Matsumoto, T. Tanizawa, T. Tanaka, S. Tateishi, K. Kasahara, Catal. Today 27 (1996) 63–69.
[207] G. Fornasari, F. Trifirò, A. Vaccari, F. Prinetto, G. Ghiotti, G. Centi, Catal. Today 75 (2002) 421–429.
[208] L.J. Gill, P.G. Blakeman, M. V Twigg, A.P. Walker, Top. Catal. 28 (2004) 157–164.
[209] W.S. Epling, L.E. Campbell, A. Yezerets, N.W. Currier, J.E. Parks, Catal. Rev. 46 (2004) 163–245.
[210] T.N. Angelidis, S.A. Sklavounos, Appl. Catal. A Gen. 133 (1995) 121–132.
[211] V. Kröger, T. Kanerva, U. Lassi, K. Rahkamaa-Tolonen, M. Vippola, R.L. Keiski, Top. Catal. 45 (2007) 153–157.
[212] C.H. Bartholomew, Appl. Catal. A Gen. 212 (2001) 17–60.
[213] M. Kärkkäinen, M. Honkanen, V. Viitanen, T. Kolli, A. Valtanen, M. Huuhtanen, K. Kallinen, M. Vippola, T. Lepistö, J. Lahtinen, R.L. Keiski, Top. Catal. 56 (2013) 672–678.
[214] C. Larese, F. Cabello Galisteo, M. López Granados, R. Mariscal, J.L.G. Fierro, M. Furió, R. Fernández Ruiz, Appl. Catal. B Environ. 40 (2003) 305–317.
[215] M. Kärkkäinen, T. Kolli, M. Honkanen, O. Heikkinen, M. Huuhtanen, K. Kallinen, T. Lepistö, J. Lahtinen, M. Vippola, R.L. Keiski, Top. Catal. (2015) 961–970.
[216] M.J. Valero-Romero, F.J. García-Mateos, J. Rodríguez-Mirasol, T. Cordero, Fuel Process. Technol. 157 (2017) 116–126.
[217] X. Wu, L.R. Radovic, Carbon N. Y. 44 (2006) 141–151.
[218] X. Wu, L.R. Radovic, Carbon N. Y. 43 (2005) 333–344.

.

Chapter II

CHAPTER II: Experimental

I. Catalyst preparation

As commented on the introduction, DOCs catalysts are mainly integrated by a high surface support as La-stabilised alumina, doped with oxides such as ceria-zirconia to increase the oxygen storage capacity and with metals like platinum and/or palladium as the catalytic active phase.

The catalyst synthesized as a reference was supported in alumina stabilised by lanthanum (to increase the thermal resistance). A cerium-zirconium oxide phase was added as a complementary phase due to its high oxygen storage capacity owing to the high oxygen mobility produce by the vacancies exist in its structure. Finally, platinum and palladium were chosen as the active phase due to its high activity to oxidation reactions.

To start with the synthesis of the catalyst the alumina support was prepared by calcination of γ-Al_2O_3 (Alfa Aesar) at 650 ºC for 5h under air flow (50 ml min^{-1}) containing 10% water, controlled using the vapour pressure of H_2O at the temperature of the saturator. The calcined alumina was doped with 4 wt% of lanthanum by incipient wetness impregnation, using an aqueous solution of $La(NO_3).6H_2O$ (Sigma Aldrich). Then the support was dried at 100 ºC overnight and calcined at 650 ºC under 10% water and 50 ml min^{-1} of air flow. The alumina-supported ceria-zirconia supports were prepared by co-impregnation of the lanthanum doped alumina with an aqueous solution of cerium (III) nitrate hexahydrate (Sigma Aldrich) and zirconyl nitrate hydrate (Sigma Aldrich) as precursors of cerium and zirconium, respectively. The $CeZrO_2$/Al-La support was prepared with 10 wt% of ceria-zirconia oxides (Ce/Zr weight ratio of 2.5). This material was dried again at 100 ºC overnight and calcined under the same conditions. Finally, the reference catalyst was prepared by incipient wetness impregnation of the support with an aqueous solution of $Pt(NH_3)_4(NO_3)_2$ (Sigma Aldrich) and $Pd(NO_3)_2$ (Sigma Aldrich); drying and calcination conditions after the impregnation were the same as used for the support. In this way, the reference catalyst 0.71 wt% Pt – 0.47 wt% Pd/$CeZrO_2$/La-Al_2O_3 was obtained.

In order to simulate the behaviour of the catalyst after biodiesel use, once the reference catalyst was obtained, alkalis and phosphor were supplemented to the

catalyst. These impurities were incorporated by the same method, incipient wetness impregnation of aqueous solutions of $NaNO_3$ (Sigma Aldrich), KNO_3 (Sigma Aldrich), $Ca(NO_3)_2.4H_2O$ (Sigma Aldrich) or $(NH_4)_2HPO_4$ (Sigma Aldrich). The amount of impurities added was related to real percentage found on DOCs based on biodiesel fuel consumption of 35 L km^{-1} for a truck during 700 000 km. The modified catalysts synthesized were: 1.6 wt% Na-, 0.5 wt% K-, 1.6 wt% Ca- and 5.6 wt% P-PtPd/$CeZrO_2$/La-Al_2O_3 catalysts. Finally, similar amount of impurities combinations were simultaneous impregnated on the reference catalyst. Precursors and calcination method were similar than employed previously.

To better compare the results obtained, reference catalyst was submitted to a second calcination under 10% water and 50 ml min^{-1} of air flow (Aged – PtPd catalyst, Table II-1).

In order to study the influence of aging conditions, reference and modified catalysts were submitted to a hydrothermal aging protocol. The fresh catalysts were aged at 850 ºC during 16 h under 10% water and 50 ml min^{-1} of air flow.

A list of the synthesized catalysts and the names employed during the manuscripts for abbreviation is presented in Table II-1.

Table II-1. List of synthesized catalysts.

Abbreviation	Catalyst
La-Al_2O_3	La-Al_2O_3
$CeZrO_2$/La-Al_2O_3	$CeZrO_2$/La-Al_2O_3
PtPd (reference)	PtPd/$CeZrO_2$/La-Al_2O_3
Aged-PtPd[1]	PtPd/$CeZrO_2$/La-Al_2O_3
Na-PtPd	Na-PtPd/$CeZrO_2$/La-Al_2O_3
K-PtPd	K-PtPd/$CeZrO_2$/La-Al_2O_3
Ca-PtPd	Ca-PtPd/$CeZrO_2$/La-Al_2O_3
P-PtPd	P-PtPd/$CeZrO_2$/La-Al_2O_3
NaK-PtPd	NaK-PtPd/$CeZrO_2$/La-Al_2O_3
NaCa-PtPd	NaCa-PtPd/$CeZrO_2$/La-Al_2O_3
KCa-PtPd	KCa-PtPd/$CeZrO_2$/La-Al_2O_3
PNa-PtPd	PNa-PtPd/$CeZrO_2$/La-Al_2O_3
PCa-PtPd	PCa-PtPd/$CeZrO_2$/La-Al_2O_3
PK-PtPd	PK-PtPd/$CeZrO_2$/La-Al_2O_3
PNaKCa-PtPd	PNaKCa-PtPd/$CeZrO_2$/La-Al_2O_3
HT-PtPd	PtPd/$CeZrO_2$/La-Al_2O_3
HT-Na-PtPd	Na-PtPd/$CeZrO_2$/La-Al_2O_3
HT-K-PtPd	K-PtPd/$CeZrO_2$/La-Al_2O_3
HT-Ca-PtPd	Ca-PtPd/$CeZrO_2$/La-Al_2O_3
HT-P-PtPd	P-PtPd/$CeZrO_2$/La-Al_2O_3

II. Catalyst characterization

a. Inductively Coupled Plasma Optical Emission Spectroscopy (ICP-OES)

The chemical composition of the different catalysts was quantitatively determined using inductively coupled plasma optical emission spectroscopy (ICP-OES). This technique uses the inductively coupled plasma to produce excited atoms and ions that emit electromagnetic radiation at wavelengths characteristic of a particular element. The intensity of the emission is indicative of the concentration of the element within the sample. Before the measurement, the metal oxides were dissolved using a mixture of inorganic acids (H_2SO_4, HNO_3 and HF).

The ICP-OES analyses were done on a flame Perkin Elmer M1100 spectrometer.

b. N_2 adsorption/desorption

The knowledge of specific surface area (SSA) of a catalyst is directly related with its catalytic activity. Nitrogen adsorption at boiling temperature (-196 ºC) represents the most widely used technique to determine catalyst surface area and to characterize its porous texture. Gas molecules close to the solid surface area are attracted by forces arising from solid-surface atoms. In order to measure de adsorption, the quantity of a sensor gas molecule (nitrogen) on the solid surface at different partial pressure at constant temperature (isotherm) is determined. The adsorption isotherm obtained is characteristic of each material and the quantity of gas adsorbed can provide a measure of surface area [1]. According to IUPAC classification [2] six types can be distinguished, but only four are usually found in catalyst characterization (Figure II-1).

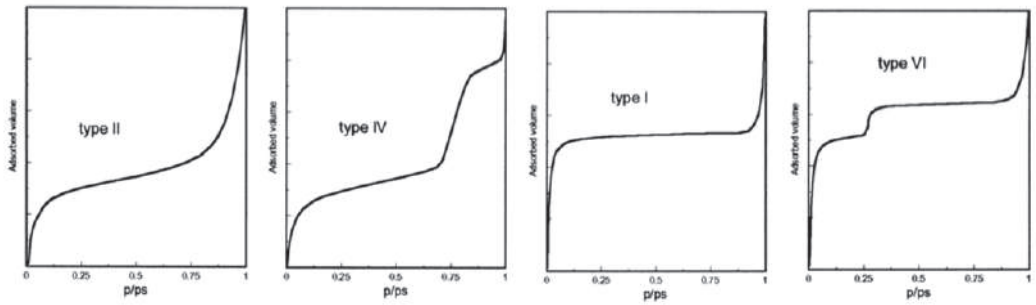

Figure II-1. The four types of adsorption isotherm usually found by nitrogen adsorption [3].

Once saturation is reached, the adsorbate desorption takes place. However, the evaporation usually takes place at a pressure lower than that of capillary condensation giving a hysteresis. This is due to pore shape and four types of hysteresis have been recognized, according to IUPAC classification [2] (Figure II-2).

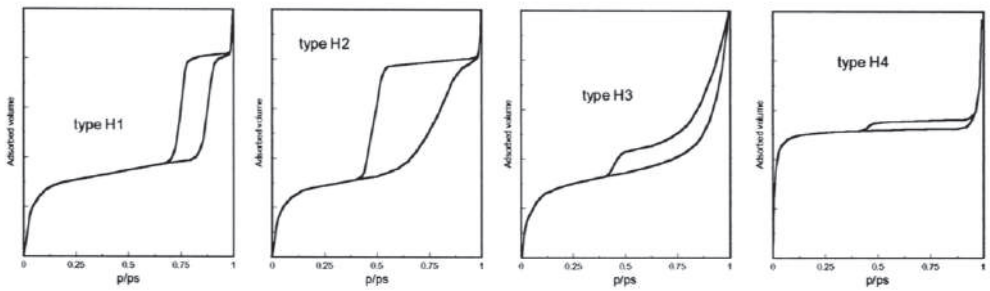

Figure II-2. The four hysteresis shapes of adsorption isotherm usually found by nitrogen adsorption [3].

Nitrogen adsorption and desorption isotherms were measured at -196 ºC on a Micromeritics ASAP 2020 surface area and porosity analyzer. Primary, the catalysts were degassed at 300 ºC for 3 h under vacuum.

The specific surface area of each catalyst was calculated from the linear part using the Brunauer-Emmett-Teller (BET) method. The model developed by Brunauer, Emmet and Teller in 1940s [3], still remains the most used method to determine the specific surface area of a porous material. They defined an equation for multimolecular adsorption using a generalization method of Langmuir's treatment of unimolecular layer [4]. Thus, the specific surface area SSA of solids would be calculated by the following equation:

$$SSA + \frac{V \cdot N_A \cdot \sigma}{V_m \cdot m} \qquad \textit{Eq. II-1}$$

where:

- SSA, specific surface area ($m^2\ g^{-1}$),
- V, volume of N_2 adsorbed (mL),
- N_A, Avogadro number ($6.023 \cdot 10^{23}$ molecules mol^{-1}),
- σ, area covered by one nitrogen molecule (generally 0.162 nm^2),
- V_m, molar volume (mL mol^{-1}),
- m, masse of the analyzed sample.

The commonly called BET equation, involves the assumption of various hypothesis: (i) the adsorption could occur on the solid or on a layer already adsorbed; (ii) adsorption heat is constant and independent of the recovery rate; (iii) when the equilibrium is reached the surface of each layer is constant. This equation is most useful between relative pressures (P/Po) of 0.05 to 0.45 [5].

The porous volume and the pore size distribution were calculated using the Barrett-Joyner-Halenda (BJH) method. The model is based on the fact that each pressure increase causes an increase of the thickness of layer adsorbed on pore walls and capillary condensation in pores. Assuming a geometric model (usually cylindrical or slit shaped), it is possible to calculate the contribution of the thickness of the adsorbed layer to the total adsorption. From these results and the assumed pore geometry, the pore volume and size can be found.

c. *X-ray Diffraction (XRD)*

X-ray powder diffraction (XRD) is a technique primarily used for phase identification of a crystalline material. It is based on the diffracted ray produced by the interaction of monochromatic X-rays generated by a cathode ray tube, and a crystalline sample. The law of Bragg (Eq. II-2) relates the wavelength of electromagnetic radiation to the diffraction angle and the lattice spacing in the crystalline sample.

$$2d_{hkl} \cdot \sin\theta + n \cdot \lambda \qquad \textit{Eq. II-2}$$

where:

- d_{hkl}, lattice spacing,
- θ, angle of incidence (rad),
- n, integer,
- λ, wavelength of the incident X-ray beam (Å).

To identify the phases on the material, the diffraction peaks obtained through a range of 2θ angles, are converted to d-spacing and compared with standard reference patterns.

Powder X-ray diffraction (XRD) patterns of all catalysts were obtained using a Bruker D8 diffractometer (CuKα radiation at 0.154184 nm) equipped with a Ni filter and 1-D fast multistrip detector (LynxEye, 192 channels on 2.95º). The diffractograms were collected at 2θ with steps of 0.02º from 4º to 80º for the total acquisition time of 32 min. Phase identification was carried out using the Diffrac.Eva software (Bruker) and the ICDD-PDF4+ database.

d. *Transmission Electron Microscopy (TEM)*

Transmission electron microscopy (TEM) is a microscopy technique whose goal is observation of the shape and dimensions of solid phases, their porosity and their interfaces. In the case of supported catalysts, the aim of the TEM study is to establish the size of the supported particles and their distribution on the support.

To the formation of images in a conventional TEM, an electron beam from an electron gun illuminates the specimen passing through an illuminating system of condenser lenses. The electron gun can be either a tungsten filament heated at 2500 ºC or a LaB_6 cathode heat at 1600 ºC, which gives an intensity the times higher. The

system of condenser lenses gives a demagnified image of the source on the specimen. The radiation interacts with the specimen and is scattered. The scattered radiation is brought to a focus by the objective lens, which gives a magnified image of the specimen on the image plane. Then, a system of projection lenses magnifies the intermediate image on a fluorescent screen [7].

Complementary to TEM, the chemical analysis system of the energy-dispersive X-ray spectroscopy (EDX) can be used to quantify the chemical composition of the specimen. EDX relies on the counting of X-rays emitted from the beam-illuminated specimen region as a function of the photon energy [8].

To prepare the specimens, all catalysts were ultrasonically dispersed in ethanol and then dried over a copper grid coated with a carbon film. TEM observations of the catalysts were performed on a JEM-2100 microscope with Energy Dispersed X-ray analysis (EDX) detector.

e. X-ray Photoelectron Spectroscopy (XPS)

X-ray photoelectron spectroscopy (XPS) is wide use to determine the chemical state of elements, namely the oxidation state and covalency or ionic types of bondings. The technique consists on the production of a beam of photons of X radiation that hits the sample, which then emits electrons. As the emitted electrons are readily absorbed by any material, the technique requires operation in a high vacuum (10^{-8} - 10^{-11} Torr or 10^{-6} – 10^{-9} Pa) [7]. Thus, the sample emitted electrons are analyzed in terms of numbers and energy. Usually Kα emissions from aluminium (hv = 1486.6 eV) or magnesium (hv = 1253.6 eV) cathodes are used as X-ray sources. The energy conversion principle allows one to write:

$$hv + E_k + E_b + \phi_{sp} \qquad \textit{Eq. II-2}$$

where hv is the incident photon energy; E_k the kinetic energy of the electrons emitted analyzed with an appropriate detector; E_b the binding energy of the electrons in their orbital level; and ϕ_{sp} the work function of the spectrometer. The depth of the electron levels excited, core and valence band electrons, depends upon the energy of the incident beam photons. The obtained XPS spectrum corresponds to the plot of the variations in the numbers of emitted electrons *vs.* their kinetic energy values.

XPS analyses over all catalysts were carried out on a Kratos Analytical AXIS Ultra DLD electron spectrometer using the AlKα (1486.6 eV) radiation source. In

order to compare all the spectra recorded, the Al2p peak from Al_2O_3 present in the catalysts was selected as a binding energy reference, and its value fixed at 74.6 eV.

f. H_2 Temperature Programmed Reduction (H_2-TPR)

In order to characterize the redox properties of the catalysts, the technique of temperature-programmed reduction was employed (TPR). TPR technique is based on the reducibility of species in/on solids by a gas, generally hydrogen, at the same time that the temperature of the system is linearly increased. The gas concentration in the effluent will decrease respect to its initial concentration due to its consumption by the metal reduction. By measuring this decrease, the reduction progress could be follow, obtaining the conditions of species present in/on solids.

A typical TPR apparatus essentially consists of three parts: (i) the gas line for pretreatments and analysis; (ii) the reactor electrically controlled; (iii) the detector for quantitative evaluation of gas-consumption. TCD detectors produced an output signal that is proportional to the concentration of hydrogen in the carrier gas. It works by measuring the difference in thermal conductivity between the pure carrier gas and the mixture of carrier and reactant gas. Due to the difference between thermal conductivities of argon ($45.46 \cdot 10^{-6}$ cal cm^{-1} s^{-1} K^{-1}) or nitrogen ($65.71 \cdot 10^{-6}$ cal cm^{-1} s^{-1} K^{-1}) and hydrogen ($471.11 \cdot 10^{-6}$ cal cm^{-1} s^{-1} K^{-1}), they are preferentially used as carrier gases in TPR. Moreover, the change in thermal conductivity is proportional to the mole fraction of reactant gas in the mixture only at low concentrations of reactant gas.

The reducibility of the catalysts was examined by hydrogen temperature programmed reduction (H_2-TPR) using mass spectrometer detection (Hiden, HPR 20). Prior to the test, the catalyst (about 100 mg) was firstly pre-treated at 600 ºC for 15 min in a synthetic air flow of 50 ml min^{-1} and then cooled down to room temperature in an air flow. It was followed by 5 minutes of purge in an Ar flow, controlled by residual O_2 analysis. 2% H_2/Ar with a flow rate of 50 ml min^{-1} as the reducing gas was introduced and the reactor was heated from 25 to 650 ºC with a rate of 20 ºC min^{-1}. H_2 consumption was quantitatively calculated by time integration of H_2-TPR profiles. Concomitant H_2O evolution was also recorded.

g. NO Temperature Programmed Desorption (NO-TPD)

Temperature-programmed desorption (TPD) is a wide useful technique to know the interaction of reactants with the catalyst surface. The temperature at which species are desorbed from a surface is indicative of the strength of the surface bond: the higher the temperature, the stronger the bond [6]. Therefore, the adsorption of a probe molecule at low temperature and subsequent monitoring of tis desorption characteristics with temperature is a simple way to characterize surface properties of catalysts and adsorbents.

TPD analyses consist in recordering the concentration of desorbing particles in function of a linear increase of the temperature. NO-TPD was used to investigate the effect of impurities (Na, K, Ca and P) in the activity of reference catalyst for NO dissociation, and the formation of N_2O and NO_2.

Temperature-programmed desorption was performed using NO as the adsorbate gas. Samples (ca. 0.1 g) were loaded into a U-shaped quartz tube and pre-treated at 250 ºC for 30 min, under a He flow of 50 ml min^{-1}. Adsorption was carried out at room temperature in a 4000 ppm NO-He flow (50 ml min^{-1}) for 1 h. The catalysts were then exposed to He for 0.5 h at room temperature to remove all the physically adsorbed species before starting the desorption temperature program, which consisted of a ramp of 5 ºC min^{-1} until 600 ºC. Desorbed gases (NO, NO_2, N_2O, CO_2) were analysed by infrared-ultraviolet spectroscopy (EMERSON IR/UV X-STREAM Enhanced XEPG).

III. Catalytic tests

a. Catalytic set-up

Figure II-3 shows a diagram of the setup were the catalytic experiments were carried out. It is constituted by three main parts:

- *Feed system*: it is composed by ten lines to feed different reactants. The gas flow was controlled by BROOKS flowmeters. The water content in the reaction mixture was regulated using the vapour pressure of H_2O at the temperature of the saturator controlled by a heating bath. All lines placed downstream from the saturator were heated above 100 °C to prevent

condensation. By a system of valves it is possible to by-pass the saturator when experiments without water are in progress. In addition, when water is used in the reaction mixture, NO feeding by-pass the saturator in order to avoid the formation of nitrates/nitric acid.

- *Reaction system*: firstly a six-way valve allows choosing between pretreatment gas and gas mixture to feed to the reactor. The catalytic behaviour was tested in a U tubular quartz reactor with the catalyst placed on a fritted quartz place (30 mm in length and 8 mm in internal diameter, Figure II-4). The reactor was heated with a furnace and the temperature measured with a K-type thermocouple (Omega).
- *Analysis part*: gas effluents were analysed with a micro gas chromatograph (SRA % GC-R3000), a FID (Agilent Technologies GC-FID 6850 Network GC) and an infrared-ultraviolet spectroscopy (EMERSON IR/UV X-STREAM Enhanced XEGP).

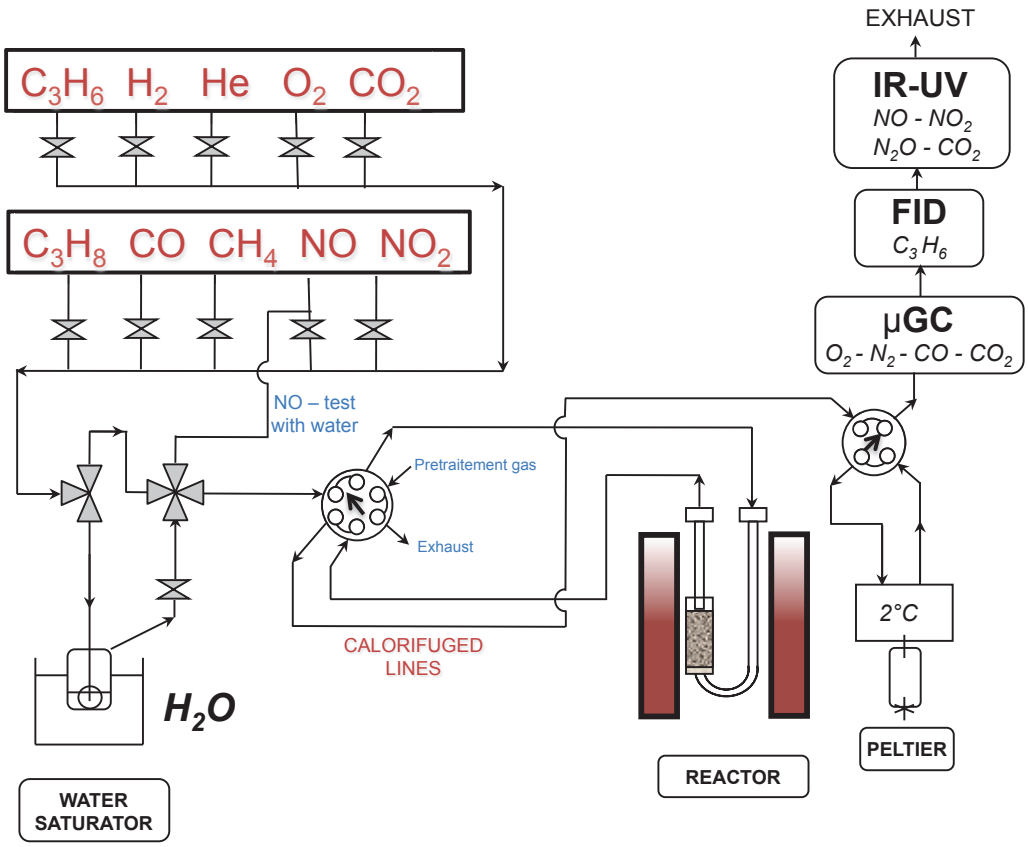

Figure II-3. Experimental set-up.

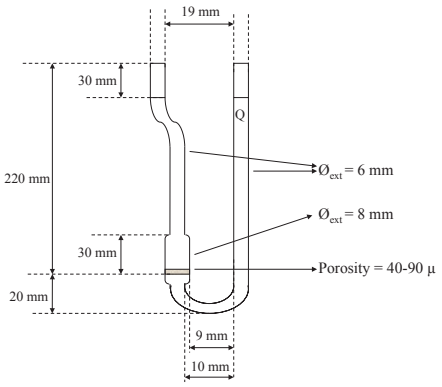

Figure II-4. Quartz reactor dimensions.

b. Operation conditions

Catalytic tests were carried out using 50 mg of catalysts mixed with silicon carbide (SiC) in order to find a gas hourly space velocity (GHSV) on the reactor of 135 000 h^{-1}. Temperature was increased and decreased by a ramp of 5 ºC min^{-1} from 80 ºC up to 600 ºC. Three consecutive catalytic cycles were performed to analyse the catalytic stability.

The reactant mixture contained [NO] ≈ 500 ppm, [CO] ≈ 300 ppm, [C_3H_6] ≈ 300 ppm, [CO_2] ≈ 5 vol.%, [O_2] ≈ 10 vol.%, [H_2O] ≈ 3.5 vol.% and He as the carrier gas, with a total flow of 250 ml min^{-1}. Moreover, experiments varying the reactant mixture were done with the reference catalyst. The concentrations of the gases employed in the different experiments are showed on Table II-2. The total flow stills 250 ml min^{-1} with He as the carrier gas.

Table II-2. Reactant mixtures tested in reference catalyst.

Gas mixture	O_2 (%)	[NO] (ppm)	[CO] (ppm)	[C_3H_6] (ppm)	[NO_2] (ppm)	[H_2O] (%)
O_2+NO	10	500				
O_2+CO	10		300			
O_2+ C_3H_6	10			300		
O_2+NO+CO	10	500	300			
O_2+NO+CO+H_2O	10	500	300			3.5
O_2+NO+C_3H_6	10	500		300		
O_2+NO+C_3H_6+H_2O	10	500		300		3.5
O_2+C_3H_6+NO_2	10			300	500	
O_2+C_3H_6+NO_2+H_2O	10			300	500	3.5
O_2+NO+CO+C_3H_6	10	500	300	300		
O_2+NO+CO+C_3H_6+H_2O	10	500	300	300		3.5

c. *Analysis of the results*

Concentrations of reaction gases and products were measured in ppm. Conversion of NO, CO and propylene were calculated as shown in Eq. II-3, II-4 and II-5 respectively:

$$x_{CO} + \frac{[CO]_0 - [CO]_t}{[CO]_0} \cdot 100 \qquad \textit{Eq. II-3}$$

$$x_{NO} + \frac{[NO]_0 - [NO]_t}{[NO]_0} \cdot 100 \qquad \textit{Eq. II-4}$$

$$x_{C_3H_6} + \frac{[C_3H_6]_0 - [C_3H_6]_t}{[C_3H_6]_0} \cdot 100 \qquad \textit{Eq. II-5}$$

In addition, NO conversion to NO_2 (Eq. II-6) and N_2O (Eq. II-7) were also studied.

$$x_{NO-NO_2} + \frac{[NO_2]_t - [NO_2]_0}{[NO]_0} \cdot 100 \qquad \textit{Eq. II-6}$$

$$x_{NO-N_2O} + \frac{2 \cdot ([N_2O]_t - [N_2O]_0)}{[NO]_0} \cdot 100 \qquad \textit{Eq. II-7}$$

Due to the influence of NO_2 produced in DOC in the effectiveness of SCR and the passive regeneration of DPF, the NO_2/NO_X rate was calculated (Eq. II-8):

$$OO_2/OO_x + \frac{[NO_2]}{[NO]-[NO_2]-[N_2O]-[N_2]} \qquad \textit{Eq. II-8}$$

The amount of N_2 was found by balance (Eq. II-9):

$$O_2\ balance + \frac{([NO]_0 - [NO]_t) - ([NO_2]_0 - [NO_2]_t) - 2 \cdot ([N_2O]_0 - [N_2O]_t))}{2} \qquad \textit{Eq. II-9}$$

Finally, the reaction rate in function of the metal percentage on the catalyst was calculated for NO, CO and propylene (Eq. II-10):

$$r + \frac{P \cdot D \cdot \left(\Delta C/10^6\right)/R \cdot T}{\%\ PGM \cdot g\ catalyst/100}\ (mol \cdot s^{-1} \cdot g_{PGM}^{-1}) \qquad \textit{Eq. II-10}$$

Where:

- P: pressure in atm.
- D: volumetric flow in L s^{-1}.

- ΔC: increment of concentration of the compound whose reaction rate is being calculated in ppm.
- R: ideal gases constant, 0.082 atm L mol^{-1} K^{-1}.
- T: temperature in K.
- % PGM: percentage of precious group metal, so the addition of Pt and Pd amount on the catalyst.

IV. In-situ Diffuse Reflectance Fourier Transform Infrared Spectroscopy (DRIFTS)

To gain further insight into the detail the mechanism of the reactions that take place on DOC catalysts, in-situ DRIFTS experiments were done. Infrared spectroscopy (IR) is a powerful technique for this purpose, as it provides direct information on the nature of the different surface species.

There exist previous IR studies on the NO adsorption on different surfaces. The object of these works is to understand the mechanism of some catalytic reactions involving NO, such as NO decomposition, NO+CO reaction and HC-SCR of NO_x. The main aim of in-situ DRIFTS experiments in the present study is to determine the influence of impurities on the NO involved reactions.

a. Basis

Diffuse reflectance (DRIFTS, Diffuse Reflectance Infrared Fourier Transform Spectroscopy) is applied to analyse powders and rough surface solids. This technique is applied to powders since it relies upon scattering of radiation within the sample.

Typically, diffuse reflectance spectroscopy was used for the study of powders in the UV-visible region, as it seemed that the construction of an integration sphere for collecting the diffuse radiation was too difficult. Finally, to solve this limitation, a spectrometer with elliptic mirrors was designed.

The IR light coming from the source is focused of an ellipse, which is at one focus on the sample (Figure II-5). The IR radiation interacts with the particles and then is reflected by their surfaces, causing the diffusion or dispersion of the light as it moves through the sample. The incident light on a sample may result in multiple reflections from the surface giving rise to diffusely scattered light. The diffuse light is

collected by a combination of mirrors that direct this dispersed energy to the spectrometer detector. The detector records the altered IR beam as an interferogram signal, which generates a spectrum. Collection optics in the DRIFTS accessory are designed to reject the specularly reflected radiation and collect as much of the diffuse reflected light as feasible.

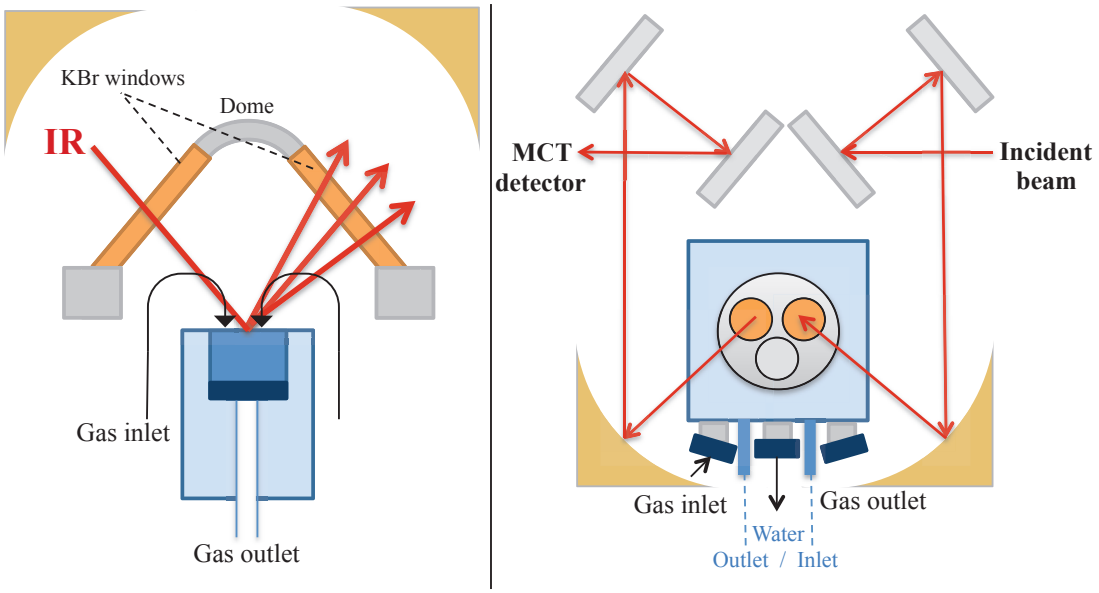

Figure II-5. Cell DRIFTS schema of the front and up views.

b. Operating conditions

In order to identify adsorbed species and reactivity between them and the gas phase, diffuse reflectance IR spectra were performed using a Thermo Scientific Nicolet iS50 spectrometer equipped with a MCT detector and DRIFTS accessory (The Praying Mantis Diffuse Reflection Accessory from Harrick Scientific) designed for in situ sample treatment (Figure II-6). During spectra acquisition the external optics were purged with CO_2-free dry air generated from an air purifier system (Parker Balston, FT-IR purge gas generator). Catalysts samples (~50 mg) in a powder form were loaded into the micro-reactor of the high temperature reaction chamber coupled to the DRIFTS accessory. The chamber is enclosed with a dome with three windows, two in KBr for the spectrometer radiation to enter and exit the camber and the third for viewing, illuminating, or radiating the sample. The catalyst surface was carefully flattened to optimize the intensity of the reflected IR beam. The DRIFTS spectra were collected in the 4000-650 cm^{-1} wavenumber range, accumulating 98

scans at 4 cm^{-1} resolutions. A Temperature Controller (ATC, Harrick Scientific) was connected to the chamber to define temperature profiles.

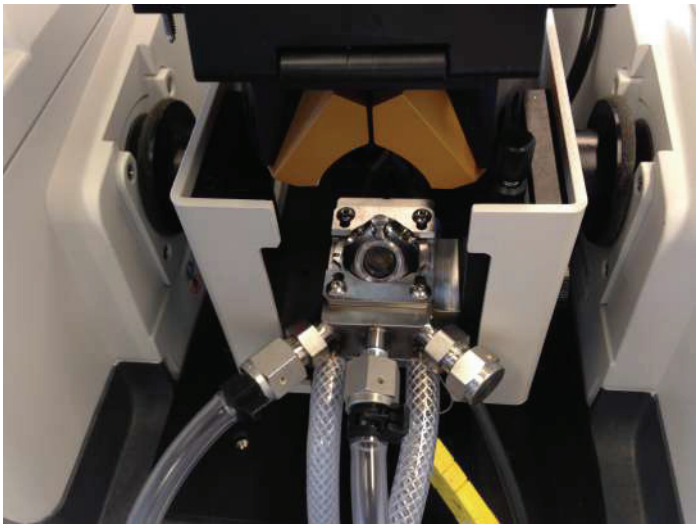

Figure II-6. DRIFTS accessory employed in the reality.

Before experiments, the sample was pre-treated by heating in 40 ml min^{-1} He until 550 ºC, so possible previous adsorbed species were eliminated. This temperature was maintained for 30 min under the same flow of 100% O_2, cooling down to 35 ºC again in He. A background spectrum serie were taken during the cooling down in flowing He to remove any background shift due to temperature and any other temperature effects.

NO-TDS (Thermal Desorption Spectroscopy) experiments were performed as part of the DRIFTS experiments. Pre-treated samples were exposed at 35 ºC to 4000 ppm NO balanced by He. Gases were mixed by BROOKS mass flow controllers and introduced into the DRIFTS reactor at a rate of 40 ml min^{-1}; spectra at different times were recorded during 2 h before the temperature ramp was started. In order to explore the thermal stability of the stored NO_x spectra were also obtained during TDS. The sample was heated at 10 ºC min^{-1} from 35 ºC to 500 ºC, maintaining for 30 min the sample each 100 ºC. A spectrum series was recorded during each plateau.

To characterize the interaction between gas-phase and surface nitrates, transient experiments involving different gas mixture sequences were evaluated at 250 ºC. The catalyst was firstly exposed to 500 ppm of NO with and without 10% O_2 in balance He with a 40 ml min^{-1} total flow for 2 h, followed by an He purge during 30 min. Afterwards, a gas mixture consisted on 300 ppm C_3H_6 or 300 ppm CO in balance He with a 40 ml min^{-1} total flow was introduced.

Finally, steady-state experiments at a constant mixture composition were done at two different temperatures, 150 and 250 ºC, to check changes before and after light-off temperatures. The mixtures tested were: (i) NO, CO, C_3H_6 and O_2; (ii) NO, C_3H_6 and O_2; (iii) NO, CO and O_2.

All DRIFTS chamber feed sequences employed during the simulated exhaust conditions experiments are resumed in Table II-3. Note that all the sequences were tested for the reference, Na-, K-, Ca- and P-PtPd, whereas for the HT-aged catalysts only the NO, CO, C_3H_6 and O_2 gas mixture was verified.

Table II-3. DRIFTS chamber feed sequences defined to simulate exhaust conditions.

DRIFTS chamber feed sequences (40 ml min^{-1})		
500 ppm NO, He balance	He purge	300 ppm C_3H_6, He balance
500 ppm NO, 10% O_2, He balance	He purge	300 ppm C_3H_6, He balance
500 ppm NO, 10% O_2, He balance	He purge	300 ppm CO, He balance
500 ppm NO, 300 ppm CO, 300 ppm C_3H_6, 10% O_2, He balance Temperature = 150ºC	He purge	500 ppm NO, 300 ppm CO, 300 ppm C_3H_6, 10% O_2, He balance Temperature = 250ºC
500 ppm NO, 10% O_2, He balance Temperature = 150ºC	He purge	500 ppm NO, 10% O_2, He balance Temperature = 250ºC
500 ppm NO, 300 ppm CO, 10% O_2, He balance Temperature = 150ºC	He purge	500 ppm NO, 300 ppm CO, 10% O_2, He balance Temperature = 250ºC
500 ppm NO, 300 ppm C_3H_6, 10% O_2, He balance Temperature = 150ºC	He purge	500 ppm NO, 300 ppm C_3H_6, 10% O_2, He balance Temperature = 250ºC

References:

[1] M. Thommes, K. Kaneko, A. V. Neimark, J.P. Olivier, F. Rodriguez-Reinoso, J. Rouquerol, K.S.W. Sing, Pure Appl. Chem. 87 (2015) 1051–1069.
[2] S.J. Gregg, K.S.W. Sing, Acad. Press. London (1982).
[3] G. Leofanti, M. Padovan, G. Tozzola, B. Venturelli, Catal. Today 41 (1998) 207–219.
[4] S. Brunauer, P.H. Emmett, E. Teller, J. Am. Chem. Soc. 60 (1938) 309–319.
[5] D.L. Carter, M.M. Mortland, W.D. Kemper, Methods Soil Anal. Part 1 - Phys. Mineral. Methods 9 (1986) 413–423.
[6] M. Boaro, M. Vicario, C. De Leitenburg, G. Dolcetti, A. Trovarelli, Catal. Today 77 (2003) 407–417.
[7] J. Vedrine, Catalyst Characterization: Physical Techniques for Solid Materials, Plenum Press, New York, 1994.
[8] Z.L. Wang, J. Phys. Chem. B 104 (2000) 1153–1175.

Chapter III

CHAPTER III: Effect of Na, K, Ca and P-impurities on diesel oxidation catalysts (DOCs)

The main aim of this chapter is to study the effect of impurities contain on biofuel on the catalytic activity of the diesel oxidation catalysts (DOCs). Both reference ($PtPd/CeZrO_2/La\text{-}Al_2O_3$) and Na, K, Ca and P modified catalysts were synthesized, characterized by several techniques and tested, concerning their physico-chemical, redox and catalytic properties.

I. Characterization results

a. Chemical composition (ICP) and N_2 adsorption/desorption

The chemical composition and physico-chemical properties of synthesized reference catalyst are listed in Table III-1.

Table III-1. Chemical composition and physical properties of synthesized catalysts.

Samples	Element contents (wt%)[a]					Textural parameters	
	La	Ce	Zr	Pt	Pd	S_{BET} ($m^2\ g^{-1}$)[b]	V_P ($cm^3\ g^{-1}$)[c]
$La\text{-}Al_2O_3$	3.08	-	-	-	-	56	0.22
$CeZrO_2/La\text{-}Al_2O_3$	3.08	5.28	1.98	-	-	60	0.23
$PtPd/CeZrO_2/La\text{-}Al_2O_3$	3.08	5.28	1.98	0.85	0.49	60	0.23

[a] Incertainty in measurement of 3%.
[b] BET surface area.
[c] BJH desorption cumulative volume of pores.

The metal percentage found by chemical analysis corresponded with the expected theoretical one. The La-content was selected taking account the surface area value of alumina final powder. Previous researches [1,2] verified that it exists an optimum La-content for alumina doping. Thus, based on these studies, 4 wt% molar of lanthanum was added by impregnation method (see section I, Chapter II) regarding the alumina thermal stabilization provided by La-doping. Ce/Zr weight ratio was chosen based in literature values [3,4], in order to provide catalyst of a large OSC value.

The N_2-adsorption/desorption analyses showed that the BET specific surface area (SSA) of the support and reference catalyst was evaluated (Table III-1).

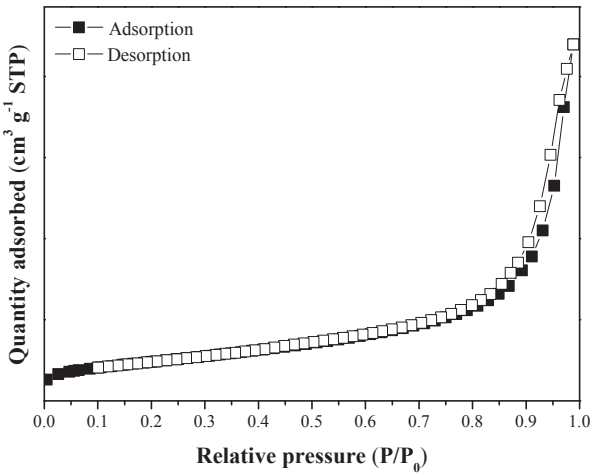

Figure III-1. Adsorption/desorption isotherms of reference catalyst.

Figure III-1 shows the N_2-adsorption/desorption isotherms of the reference catalyst. It exhibited a type IV isotherm based upon the Brunauer-Deming-Deming-Teller (BDDT) classification, which is characteristic of mesoporous materials (2-100 nm) with H3-type of hysteresis [5].

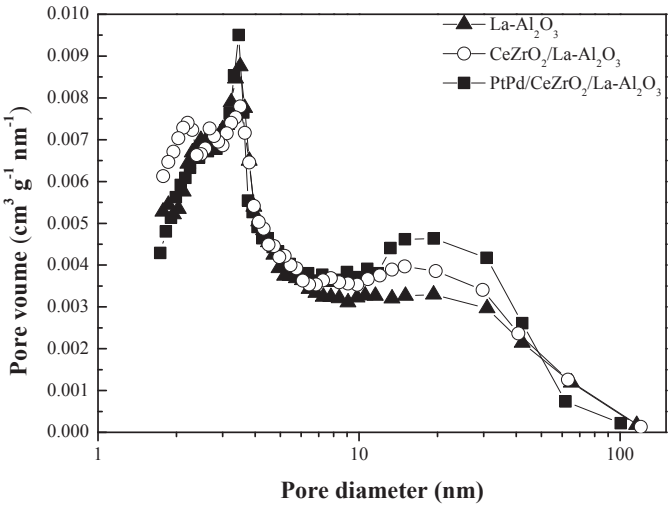

Figure III-2. The BJH pore size distribution curves of the support and reference catalyst.

In addition, Figure III-2 presents the BJH pore size distribution curves for the support and reference catalysts. Support and reference catalyst presented a double pore size distribution: smaller mesopores at around 3-4 nm and larger mesopores with a pore diameter between 30-40 nm. It can be observed that the formation of ceria-zirconia mixed oxide increased the amount of the smaller mesopores (2 and 4 nm, mainly), according to the higher SSA found (Table III-1). The formation of Ce-Zr

mixed oxide is effective in the inhibition of the sintering of ceria, which translates in higher BET surface area [2,6].

After addition of noble metals the smaller mesopores distribution was centred at 4 nm diameters, but also an increase of higher mesopores (30-40 nm) was detected. This phenomenon was in agreement with the maintenance of SSA and total pore volume, after PtPd impregnation (Table III-1).

After analyse of support and reference catalyst, Na, K, Ca and P-modified catalysts were evaluated (Table III-2).

Table III-2. Chemical composition and physical properties of modified catalysts.

Samples	Element contents (wt%)[a]			Textural parameters	
	Pt	Pd	Impurity	S_{BET} ($m^2 g^{-1}$)[b]	V_P ($cm^3 g^{-1}$)[c]
Aged-PtPd[d]	0.33	0.46	-	54	0.40
K-PtPd	0.56	0.48	0.5	57	0.30
Na-PtPd	0.83	0.50	1.6	50	0.41
Ca-PtPd	0.69	0.49	1.6	50	0.31
P-PtPd	0.64	0.46	5.6	33	0.26

[a] Uncertainty in measurement of 3%.
[b] BET surface area.
[c] BJH desorption cumulative volume of pores.
[d] Fresh catalyst calcined twice at 650ºC in presence of 50 ml min^{-1} air and 10% water.

ICP results showed a decrease in platinum amount after impurities addition. In order to verify if this effect was associated with the impact of the second hydrothermal treatment after the impregnation of the additives, a second hydrothermal calcination at 650 ºC was performed to the reference catalyst (aged – PtPd), which presented also a decrease of Pt amount contained. Thus, the lost of Pt is related to the leaching of Pt after the calcination realized after impurities impregnation.

The N_2-adsorption/desorption analyses showed that the BET specific surface area (SSA) of the alkali and alkaline earth containing catalysts slightly decreased in comparison to the reference catalyst. Indeed, the obtained results evidenced that the ageing treatments had an effect on the SSA of this catalyst, which was decreased after treatment, phenomenon also observed by some other authors [7]. However, the decrease of SSA due to phosphorus addition was more severe, that could be attributed to their physical deactivation (pore blocking) by phosphates [8]. Thus, the amount of additives in the catalysts had an important influence on the SSA and pore size

distribution, as the catalyst with higher percentage of additives presented the lower SSA value.

As well as the reference catalyst, the N_2-adsorption/desorption isotherms of the aged catalysts exhibited a type IV isotherm with H3-type of hysteresis (Figure AI-1). The isotherms obtained for all the modified catalysts had the same shape, namely the type IV isotherm corresponding to mesopores distribution, which evidenced that these additives did not modify the type of pores in the catalyst structure.

The BJH pore size distribution curves (Figure AI-2) presented a double pore size distribution: smaller mesopores at around 3-4 nm and larger mesopores with a pore diameter between 30-40 nm. The amount of the smaller mesopores (< 5 nm) slightly decreased after impurities addition, in agreement with the decrease of SSA.

The influence of impurities couple combination on surface area was also studied. In order to simulate the real conditions at which all the impurities would be present, PNaKCa-PtPd modified catalyst was evaluated.

Table III-3. Chemical composition and physical properties of catalysts modified by impurities combination.

Samples	Element contents (wt%)[a]						Textural parameters	
	Pt	Pd	Na	K	Ca	P	S_{BET} ($m^2\ g^{-1}$)[a]	V_P ($cm^3\ g^{-1}$)[b]
NaK-PtPd	0.70	0.48	1.78	0.50	-	-	49	0.35
NaCa-PtPd	0.72	0.46	1.79	-	1.53	-	51	0.36
KCa-PtPd	0.80	0.50	-	0.55	1.37	-	45	0.40
PNa-PtPd	0.51	0.40	1.90	-	-	6.50	26	0.18
PK-PtPd	0.53	0.44	-	<0.1	-	5.20	31	0.15
PCa-PtPd	0.47	0.43	-	-	<0.1	6.10	26	0.08
PNaKCa-PtPd	0.44	0.39	1.57	0.52	1.21	5.59	38	0.13

[a] Uncertainty in measurement of 3%.

The SSA decreased compared with Aged-PtPd catalyst when combination of impurities was employed. Thus, in addition to the influence of the second hydrothermal treatment, the higher amount of impurities present produced a stronger impact. Finally, the results obtained for PNaKCa-PtPd catalyst released a combined effect of alkaline, alkaline earth and phosphorus impurities. The highest amount of impurities is present in this catalyst, decreasing the SSA value when compared with

Aged-PtPd catalyst. However, its surface area still being higher than P- and phosphorus couples modified catalysts. This could be explained by the formation of phosphates that prevents the accumulation of phosphorus on the surface of the catalyst [9].

b. X-ray diffraction (XRD)

Figure III-3 presents the XRD patterns of support and reference catalyst: (A) La-Al_2O_3, (B) $CeZrO_2$/La-Al_2O_3 and (C) PtPd/$CeZrO_2$/La-Al_2O_3, obtained using 2θ positions between 20 and 80º.

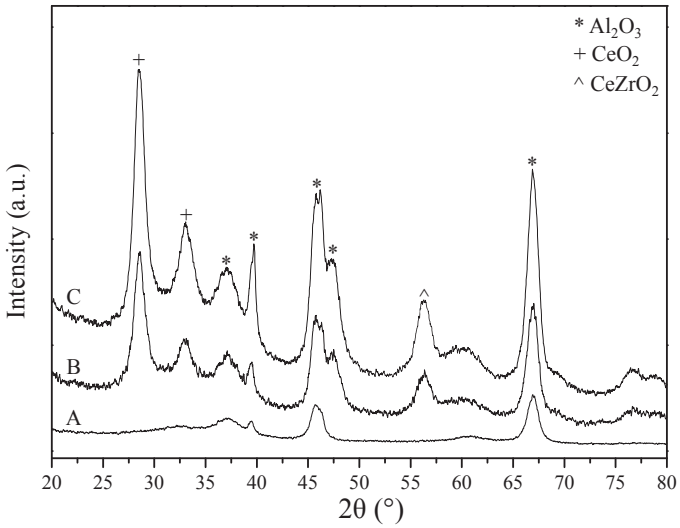

Figure III-3. X-ray diffraction patterns of La-Al_2O_3 (A), $CeZrO_2$/La-Al_2O_3 (B) and PtPd/$CeZrO_2$/La-Al_2O_3 (C).

The La-Al_2O_3 diffraction pattern (Figure III-3, A) presented peaks at 45.8º and 67º, characteristics of γ-alumina, at 39.5º and a broad peak at 37º corresponded to θ-alumina phase. These results evidenced that lanthanum modification retards the alumina phase transformation from γ to α phase upon increasing the temperature. XRD patterns failed to detect any lanthanum containing structure, probably because of its high dispersed state.

The explanation of lanthanum-alumina stabilization might be related to defects on alumina surface that consist in surface reactive aluminium ions. Due to the same valence of the two aluminium ions, there are a lot of vacancies in the bulk, which become very mobile and reactive increasing temperature in presence of water. Then, alumina particles interact with lanthanum, forming $LaAlO_3$ that immobilizes the surface aluminium ions into a stable structure [10].

$CeZrO_2$/La-Al_2O_3 (Figure III-3, B) presented two peaks at 28.8º and 33.1º related to the presence of CeO_2 with a cubic structure [6]. The higher intensity of peak at 28.8º, which is usually found at 28.6º, and the no diffraction peaks related to zirconia phases are an indicative that ceria and zirconia formed a solid solution [11]. An additional peak found at 56.5º associated with ceria-zirconia mixed oxide [4]. This ceria-zirconia mixed oxide could be favoured by the precursors used during catalysis synthesis. Accordingly to [11], the different charge between anionic $Ce(NO_3)_6^{2-}$ and the cationic zirconyl (ZrO^{2+}) could facilitate their interaction, favouring the formation of a solid solution. The shifted observed for ceria phase peak was smaller than reported in literature [4]. Thus, it is possible that not all the zirconium was incorporated into ceria lattice, forming a highly zirconia dispersed phase since it was not detected.

Noble metals (Pt, Pd) were not detected by XRD (Figure III-3, C), which could be attributed to the quite homogeneous distribution on the surface of the support and their low metal-load on the catalysts.

Otherwise, Figure III-4 presents a comparison between the XRD patterns of (C) reference catalyst and modified catalysts (D) Na-, (E) K-, (F) Ca- and (G) P-PtPd catalysts obtained using 2θ positions between 20 and 80º.

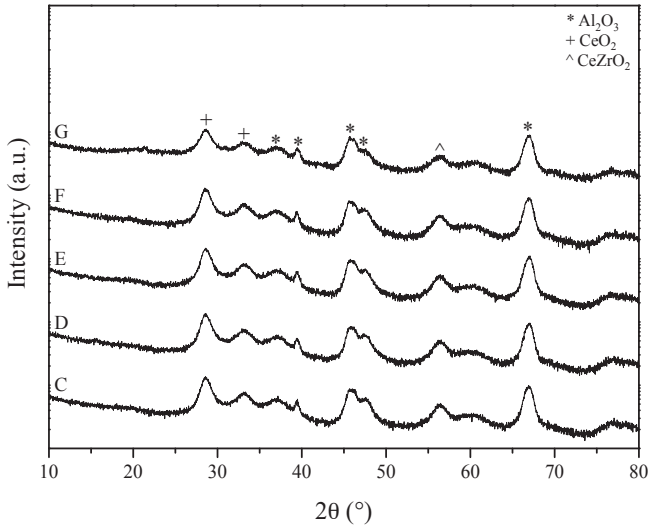

Figure III-4. X-ray diffraction patterns of PtPd (C), Na-PtPd (D), K-PtPd (E), Ca-PtPd (F) and P-PtPd (G).

XRD patterns obtained after impurities addition did not show any peak corresponding to Na, K, Ca or P. These spectra showed only peaks attributable to γ-alumina, cerium oxide and ceria-zirconia mixed oxide. Comparing modified catalysts

spectra with reference one, results suggest that metal addition do not modify the crystal structure of the catalyst.

Moreover, Figure III-5 shows the XRD patterns of (C) PtPd reference catalyst, and the modified by impurities combination catalysts (H) NaK-, (I) NaCa-, (J) KCa-, (K) PNa-, (L) PCa-, (M) PK-PtPd.

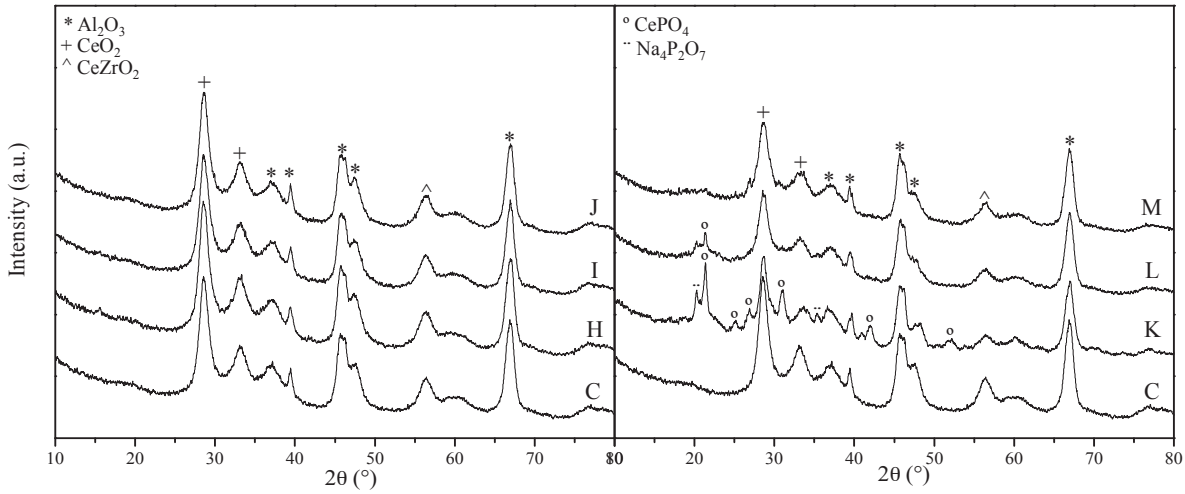

Figure III-5. X-ray diffraction patterns of PtPd (C), NaK-PtPd (H), NaCa-PtPd (I), KCa-PtPd (J), PNa-PtPd (K), PCa-PtPd (L) and PK-PtPd (M).

As it can be seen in Figure III-5, the Na, K and Ca combinations are not visible by XRD, similarly to the modified catalysts with only one impurity. When phosphorus was present in the combinations, it was detected in form of cerium phosphates. In addition, combined with Na it formed sodium phosphates as show in spectra K. Calcium phosphate ($Ca_3(PO_4)_2$) was also formed as demonstrated by N_2 adsorption/desorption results but it was not detected by XRD as it overlaps with cerium phosphate pattern.

c. Transmission electron microscopy (TEM)

Figure III-6 presents TEM analysis results corresponding to: a) PtPd, b) Na-, c) NaK- and c) PNaKCa-PtPd catalysts. These observations were performed to better understand the influence of impurities incorporation on morphological and structural phases in synthesized catalyst.

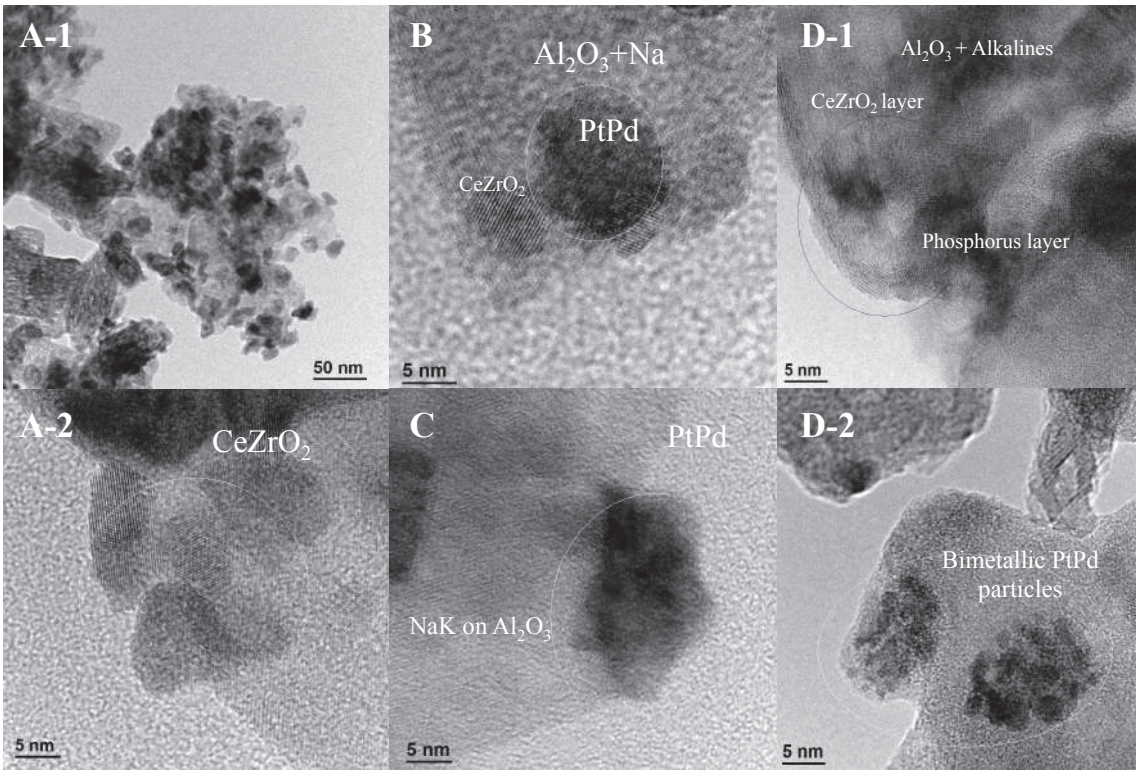

Figure III-6. TEM images of : A) PtPd, B) Na-PtPd, C) NaK-PtPd and D) PNaKCa-PtPd.

Firstly, in Figure III-6 A the alumina support appears as greyish, elongated, partly transparent particles. According to the TEM images, no transition from the γ-phase to the α-phase was evidenced, as expected from the rather moderate ageing temperature used in this study (650ºC). In the support material, EDX analysis showed that dark dots correspond to ceria-zirconia, such as CeO_2 and $CeZrO_2$ mixed oxide, according to XRD results. It could be also observed that the particles of ceria-zirconia formed are uniform in size and covering alumina surface (Figure III-6 A-2). As can be seen on the encircled area in the micrographs, the lattice fringes are clearly visible with a d-spacing of 0.316 nm, which can be assigned to the (111) plane of the cerium oxide [8]. The detection of platinum and palladium was very difficult and no clear evidence of Pt and Pd-particle growth was observed either in the fresh or modified catalysts. In the elemental analyses (EDX), both elements were detected together in different areas of the ceria-zirconia oxides.

In the case of Na- (Figure III-6 B) and NaK- (Figure III-6 C) PtPd catalysts, the TEM images show the same trends. There are no changes in the alumina support or in the platinum or palladium particles size. Again, ceria-zirconia oxides cover the alumina surface with noble metals attached to them as a dispersed phase, according to

the EDX analysis. The presence of alkaline metals was detected by EDX in the alumina support, with no changes in its structure or in the platinum-palladium particles.

Contrary, TEM analyses indicate some structural changes after phosphorus addition. It can be observed in Figure III-6 D-1 that alumina was covered by a phosphorus (P)-containing layer, as well as cerium and zirconium oxides. The phosphorus-containing layer covering cerium oxides could be responsible for the cerium phosphate detected by XRD. In this case, platinum-palladium alloy was visible on the phosphorous-containing layer (Figure III-6 D-2), corresponding to an increased particles size after phosphorus addition.

d. X-ray photoelectron spectroscopy (XPS)

The XPS spectra obtained from the five catalysts studied yielded useful additional information about the oxidation state of the catalysts. Firstly, the peaks corresponding to XPS profiles of the Al 2p (Figure III-7) are centred in the range of 74.4-74.8 eV for all catalysts, corresponding to γ-Al_2O_3, which evidenced that the binding energy (BE) of the alumina was not modified after impurities addition. This fact could be attributed to Al_2O_3-stabilization with lanthanum, which was found as carbonates in a BE range of 834-842 eV [12].

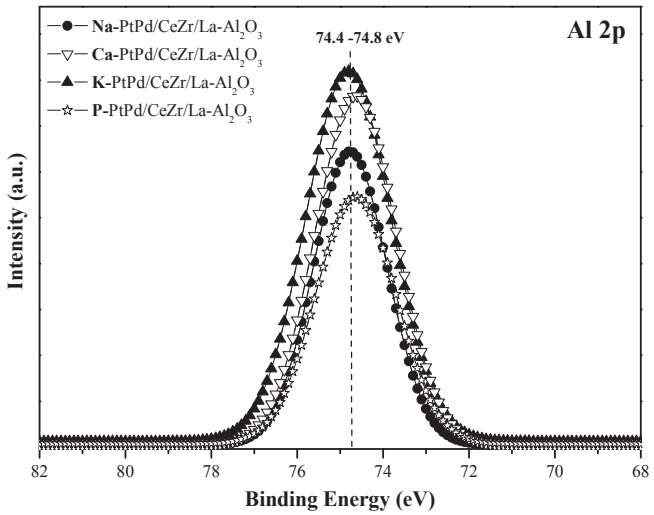

Figure III-7. Al 2p XPS spectra of reference and modified catalysts.

All catalysts presented the same peaks characteristic of pure CeO_2 (not shown), according to the convention established by Burroughs [13,14]. Cerium was detected in two oxidation states, namely Ce^{3+} and Ce^{4+}, with a higher amount of ceria

species in the more oxidized state (Ce^{4+}, see Table III-4), which can be probably associated to the oxidative atmosphere used during the catalyst synthesis. Note that the percentages of the chemical states of cerium (Ce^{3+}/Ce^{4+} ratio) on the surface were calculated by decomposition of Ce 3d spectra associated to these species. Moreover, the highest Ce^{3+}/Ce^{4+} ratio observed in the case of P-PtPd catalyst could be attributed to cerium phosphates formed in this catalyst, according to XRD results. The formation of cerium phosphate is expected to maintain the ceria in the reduced state (Ce^{3+}), decreasing both redox properties and catalytic activity [15]. In addition, Zr 3d (182.1 eV) [16] also detected in two oxidation states, one its oxidation form Zr^{4+} and the other one as some supra oxidized ZrO_x, promoted by the high amount of oxygen and oxidized species around it [17].

Table III-4. Ce^{3+}/Ce^{4+} ratio obtained by XPS.

Samples	$(Ce^{3+}/Ce^{4+})_{XPS}$
PtPd	0.71
Na - PtPd	0.89
K - PtPd	0.79
Ca - PtPd	0.49
P - PtPd	1.19

Moreover, the Figure III-8 shows the palladium chemical state on reference and modified-catalysts. The Pd 3d spectra were characterized by the Pd $3d_{5/2}$ peak at 336.9±0.5 eV, corresponding to Pd^{2+} (bulk PdO). Na and K impurities addition produced a negative shift of the Pd-3d binding energies, which is indicative of an increased electron density on the metal due to the presence of alkali ions [18]. Moreover, XPS profile of K-PtPd catalyst showed a second peak corresponding to Pd^{2+} in contact with the support to form palladium-aluminate structures at 338.1 eV or PdO_2 that induced the formation of new interfacial sites for the oxidation reaction [19]. The lower intensity of these peaks in presence of alkali impurities indicates that palladium is partly covered by the some components of the support, in fact by alkali metal salts [20].

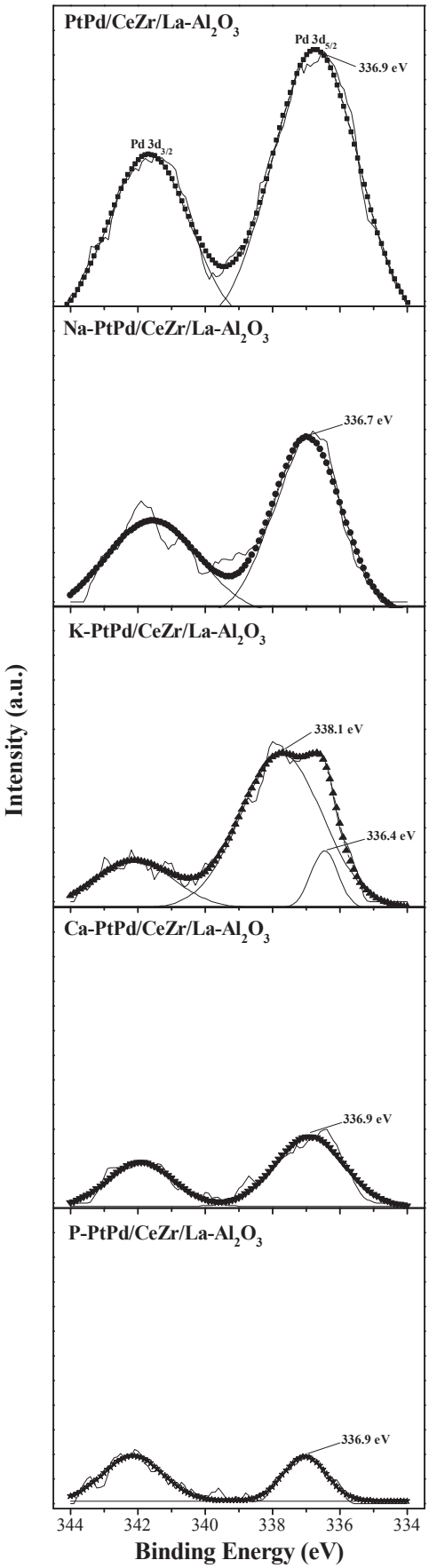

Figure III-8. Pd 3d XPS spectra of fresh and modified catalysts.

Platinum was also detected in an oxidized state, which was not possible to specify exactly due to overlap of their corresponding binding energy with those of zirconium oxides. Otherwise, atomic percentage of platinum and palladium could neither be accurately measured due to the low metal amount presented on catalyst surface.

The Na-PtPd catalyst presented a Na 1s peak with a maximum et 1072.2eV BE [21], which may correspond to sodium carbonate, $NaCO_x$. In the case of Ca-PtPd catalyst, Ca 2p region was overlapped by Zr 3d, so the principal oxidation state could not be detected. However, the secondary state, Ca 2s, showed that calcium appeared also in the form of carbonate, CaCOx, at 439.8eV. The catalyst with potassium additives followed the same trends, K was as $K\text{-}O_x$ with K 2p BE equal to 296.5eV. Finally, P-PtPd behaved differently; phosphorus was found in the form of phosphates, as evidenced by TEM results, being P 2p BE equal to 134.4 eV.

e. H_2 temperature programmed reduction (H_2-TPR)

In order to analyse the influence of the additives on the metal support interaction and reducibility of the catalysts, TPR experiments were carried out from room temperature to 600ºC. The TPR profile of reference catalyst is depicted in Figure III-9.

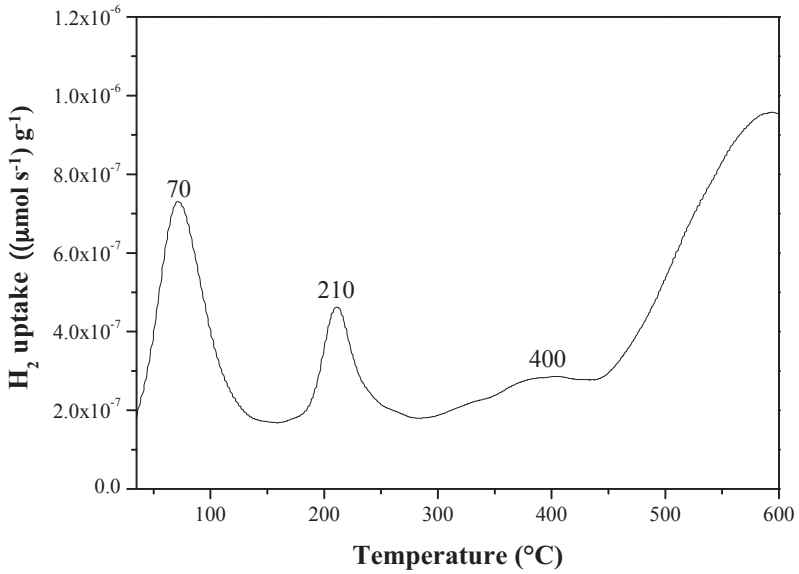

Figure III-9. TPR-H_2 profile of reference catalyst.

The reference catalyst, $PtPd/CeZrO_2/La\text{-}Al_2O_3$, presented two main sharp reduction peaks at low temperature and a broad peak at temperatures higher than 450

ºC. The reduction peak located at 70 ºC could be attributed to the simultaneous reduction of PdO species [22] and surface oxygen of CeO_2 around the Pd species [23]. The reduction peak observed at 220 ºC can be assigned to the reduction of PtO_x species and the superficial cerium oxide reduction, which is in interaction with Pt [24].

The reducibility of the support was also studied by H_2-TPR. No reduction peaks at temperatures lower than 350 ºC were observed. Thus, it seems that platinum and palladium promotes the reduction of surface oxygen. Hydrogen is dissociatively adsorbed on the Pt group metals and may react with an oxide ion in the ceria surface to form a hydroxyl group. Such a hydroxyl group would be adsorbed on platinum or palladium that will catalyse the formation of water, which then leaves the metal surface. As a result, oxygen vacancies are introduced into the ceria lattice at sites near noble metal crystallites [25].

The small broad peak between 350 ºC and 400 ºC can be ascribed to the reduction of superficial CeO_2 that is not interacting with metal. Finally, the broad peak detected at temperatures higher than 450 ºC could be associated with the reduction of bulk ceria promoted by zirconium.

As reported in literature [26], the reduction of ceria occurs in two steps: the bulk reduction occurs at temperatures above 750 ºC while the surface shell reduction takes place at a much lower temperature. Doping zirconium atoms into ceria facilitates the oxygen transport from bulk to surface [27], by increasing the number of oxygen vacancies. Thus, largest mobility of oxygen and favors the reducibility when the cerium-zirconium mixed oxide is formed [6]. It has been reported that reduction of ceria-zirconia solid solution takes place between 450 ºC and 600 ºC, and involves simultaneous surface and bulk reduction [28]. Balducci et al. [29] have carried out calculation which indicate that surface Ce^{4+}/Ce^{3+} reduction energies in the mixed oxides are comparable to bulk values which, in turn, are significantly lower than pure ceria [30].

Similarly to the reference catalyst, the TPR profiles of aged and modified-catalysts are depicted in Figure III-10.

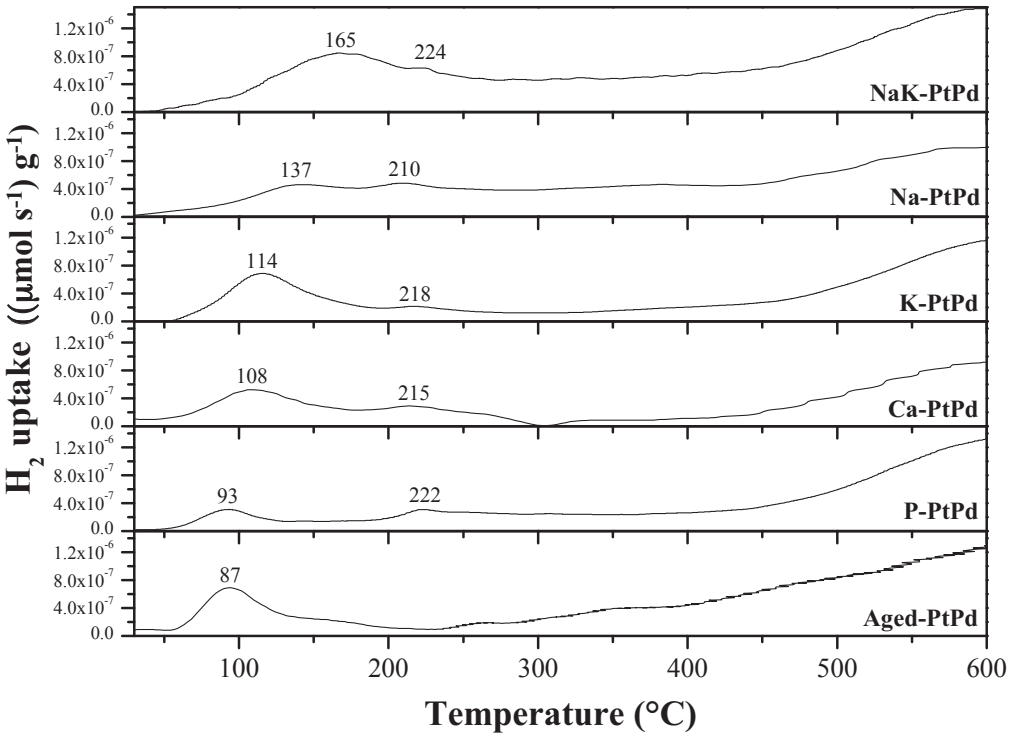

Figure III-10. TPR-H_2 profiles of NaK-PtPd, Na-PtPd, K-PtPd, Ca-PtPd P-PtPd and aged-PtPd catalysts.

The H_2-TPR profile of modified catalysts showed some differences compared to the aged-catalyst. The H_2-TPR profile for the aged-PtPd catalyst presented one peak corresponding to PdO and/or PtO_x reduction at 87ºC. The increase of the temperature reduction can be correlated to the significant deterioration of the surface oxygen mobility after second hydrothermal treatment [31]. In addition, the disappearance of the Pt reduction peak for the aged-PtPd catalyst could be ascribed to its lower amount of Pt, which was leached during hydrothermal aging.

The H_2-TPR profile of modified catalysts showed some differences compared to the reference catalyst. In addition to the decrease of oxygen diffusion after the second hydrothermal treatment, metal-support interaction was increased after additives incorporation, shifting first reduction peak towards higher temperatures, with a stronger effect in the case of Na, K and Ca. This effect could be ascribed to differences in the electronegativity of the additives. The electronegativity of the additives used decreases as follow: Ca > K ≈ Na. Due to the lower electronegativity of the alkali species, a higher interaction of metals with oxygen was produced which increased the reduction temperature. According to this electronegativity tendency, the lowest electronegativity of sodium and potassium species increases the temperature

corresponding to the first reduction peak. However, the higher electronegativy of Ca comparing to that of Na and K compounds, leads to the slightly higher reduction temperature than reference catalyst, with a less marked effect than Na and K.

Otherwise, the second reduction peak became broader after impurities addition. With regard to reduction temperature, alkaline and alkaline-earth presence shifted peak associated with PtO_x to slightly higher temperature than in the case of the reference catalyst. In contrast, the second peak on the P-PtPd catalyst shifted to higher temperature in comparison to the PtPd catalyst. These effects can be ascribed to the lower amount of Pt found after impurities addition, probably due to leaching of Pt during the hydrothermal calcination. The broad reduction peak of bulk ceria appears at temperatures higher than 450 ºC in all the cases.

Moreover, the H_2 consumption of the reference and modified catalysts was calculated in function of the noble metal amount found by ICP for each catalyst (Table III-5).

Table III-5. Reduction temperatures and H_2 consumption observed in the TPR experiments.

Samples	$T_{peak\ 1}$ (ºC)	$T_{peak\ 2}$ (ºC)	$H_{2\ consumed}$ (mol H_2 g^{-1})	$H_{2\ theoretical}$ (mol H_2 g^{-1})
PtPd	70	220	$1.28 \cdot 10^{-4}$	$1.33 \cdot 10^{-4}$
Aged-PtPd	87	-	$1.20 \cdot 10^{-4}$	$7.71 \cdot 10^{-5}$
Na-PtPd	137	210	$1.44 \cdot 10^{-4}$	$1.32 \cdot 10^{-4}$
K-PtPd	114	218	$1.85 \cdot 10^{-4}$	$1.02 \cdot 10^{-4}$
NaK-PtPd	165	224	$2.35 \cdot 10^{-4}$	$1.17 \cdot 10^{-4}$
Ca-PtPd	108	215	$1.49 \cdot 10^{-4}$	$1.17 \cdot 10^{-4}$
P-PtPd	93	222	$5.44 \cdot 10^{-5}$	$1.09 \cdot 10^{-4}$

H_2 consumption of reference catalyst was slightly higher than the theoretical one calculated to Pt and Pd oxides. This could be associated to the existence of a hydrogen spillover phenomenon over Pd and Pt species during the TPR process.

In the case of aged-PtPd catalyst, only one reduction peak was found. The H_2 consumed was similar to the amount of H_2 employed to reduce the reference catalyst. Thus, it seems that the Pt-Pd formed an alloy during the second hydrothermal treatment. In addition, the higher amount of H_2 consumed compared with the theoretical one is in agreement with the spillover phenomenon proposed above.

The H_2 consumption increased by supplying Na, K and Ca additives, especially when Na and K were present combined. However, reduction peaks became broader after alkali addition, being more difficult to integrate accurately. This finding indicates that there might be a hydrogen spillover phenomenon on alkali-modified catalysts during the TPR process, in which H_2 adsorbed on the metal atoms migrates to alkaline oxides in close proximity to them [32]. This promotion effect is closely related to the electron donation property of alkali metals. Ca-PtPd catalyst had a similar effect on the H_2 adsorption, however a weaker promotion effect than the alkali metals was exhibited, according to its higher electronegativity [33]. The consumption of hydrogen measured after P addition was lower than the theoretical one, which could be ascribed to the phosphorus compound layer detected by TEM, which could block and inhibit the reduction process [34].

f. NO temperature programmed desorption (NO-TPD)

NO-TPD was used to investigate the influence of the additives on the NO adsorption capacity, which may be correlated with the NO conversion. Note that NO, NO_2 and N_2O concentration in gas flows were followed by infrared spectroscopy during the desorption ramp.

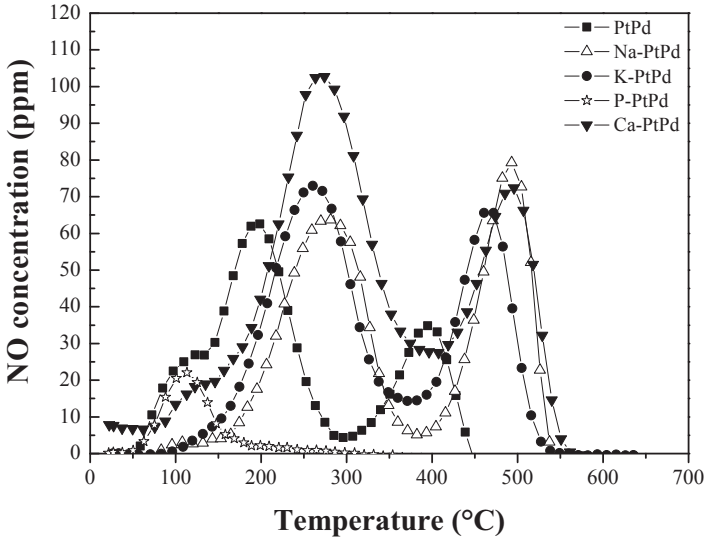

Figure III-11. TPD profiles following NO desorption on the reference catalyst.

NO-TPD study (Figure III-11) showed that only NO was detected in the outlet gases flow under increased temperature for both reference and modified-catalysts. For reference PtPd catalyst, three NO desorption peaks were observed in the 50-

450ºC temperature range, whereas only two desorption peaks were detected for modified-catalysts. The low temperature peak disappeared upon catalyst modification by the additives. In addition, it can be observed that, with additives, desorption peaks are generally more intense and shifted towards higher temperatures. Otherwise, the phosphorus-modified catalyst showed a different behaviour. Contrary to the other catalysts, only one low temperature desorption peak was detected, with an intensity comparable to the one related to the first desorption peak of the reference catalyst.

NO desorption peaks indicated the presence of NO reversibly adsorbed and desorbed within low-temperature region (50-150ºC) as well as in mid (150-350ºC) and high (350-600ºC) temperature regions. The three distinct features in the NO desorption profiles suggest that three types of sites are available for NO adsorption. The first NO feature was associated with the weakly adsorbed NO, while the mid and high temperature desorption peaks have been attributed to more stable NO adsorbed species, as nitrites/nitrates species [35].

Moreover, the total amounts of desorbed NO are presented in Table III-6.

Table III-6. NO amount desorbed (mmol g^{-1}) during NO-TPD experiments.

Samples	$T_{peak\ 1}$ (ºC)	$T_{peak\ 2}$ (ºC)	$T_{peak\ 3}$ (ºC)	NO desorbed (mmol g^{-1})
PtPd	100	188	395	49.89
K - PtPd	-	260	474	41.91
Na - PtPd	-	283	496	43.24
Ca - PtPd	122	263	485	61.36
P - PtPd	112	-	-	4.90

Obtained results showed that the Ca-PtPd catalyst presented higher NO desorbed amount than reference catalyst, while that Na and K-PtPd catalysts presented similar NO desorbed quantities. Finally, in presence of phosphorus, the NO desorbed quantity was the lowest one.

Previous studies showed that the addition of alkaline additives on PtPd causes an increase in the strength of the metal-NO bond, accompanied by a weakening of N-O bond of the adsorbed NO molecules, which facilitate the NO dissociation [36–39]. This fact is ascribed to the low electronegativity of alkali additives, which provides them with an electron donor behaviour, increasing the interaction with NO, which has an electron acceptor character [40]. This is in agreement with the results provided by

NO-TPD experiments, which showed an increase of desorption temperatures in presence of Na, K and Ca additives.

In Figure III-12 is presented the NO desorbed in mmol g^{-1} for each catalyst and the molar percentage and the electronegativity value of each.

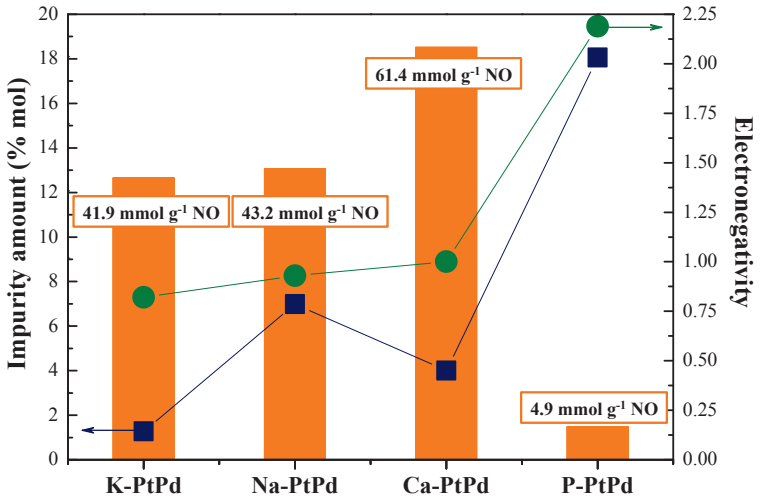

Figure III-12. Relation between the NO desorbed amount (mmol g^{-1}) for modified catalyst and the electronegativity and molar percentage of each impurity.

As discussed before, Ca-PtPd presented the higher NO storage, while in the case of P-PtPd it had the lowest NO desorbed amount. Previous studies [15] have demonstrated that the presence of alkali or alkaline earth in NO_x storage reduction (NSR) catalysts can facilitate the NO_x storage due to their higher basicity. Otherwise, Takahashi et al. [41] related the electronegativity with the basicity, indicating that lower electronegativity translates in stronger basicity, and thus, in higher NO storage. However, the results showed in Figure III-9 presented the contrary tendency, increasing the NO storage with the electronegativity of the impurity presented on the catalyst. This contrary effect could be ascribed to the different impurities mole percentage on the catalysts. The higher amount of Na and Ca could favor the storage more than K, as higher amount of impurity is present. Nevertheless, it is worth noting that Ca-PtPd presented significant higher NO storage than Na-PtPd catalyst. Thus, it could be concluded that it exists an optimum percentage, above which the impurity would start to inhibit the NO storage. In the case of P-PtPd catalyst, the much higher amount of impurity does not allow to compare easily with the other impurities. The low capacity of NO adsorption/desorption was related to the formation of phosphates, according to TEM analysis, which hinder the NO adsorption on the active sites [8]. In

addition, electron transfer from Pt and Pd to ceria in oxidizing atmospheres has been reported [42]. This interaction is expected to increase the strength of NO adsorption (NO electron donor) on oxidized catalysts (Ce^{4+}, electron acceptors; Ce^{3+}, electron donors). However, XPS results evidenced an increase of the percentage of Ce^{3+} in the presence of phosphorus, which disfavoured NO adsorption in the presence of P due to the lower availability of electron acceptor species.

II. Activity test results

a. Catalytic activity of reference catalyst

The catalytic performances of reference catalyst for CO, C_3H_6 and NO conversion (Figure III-13) are going to be discussed.

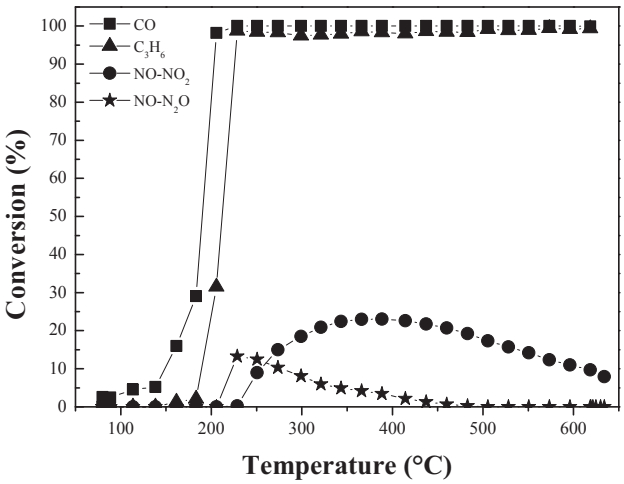

Figure III-13. CO, C_3H_6, NO-NO_2 and NO-N_2O conversion obtained for the reference catalysts during the heating ramp of the first catalytic cycle. Operating conditions: 50 mg, 250 ml min^{-1}, GHSV = 135 000 h^{-1}, 300 ppm CO, 300 ppm C_3H_6, 500 ppm NO, 10% O_2, 5% CO_2, 3.5% H_2O and He as balance.

As it can be seen in Figure III-13, the results obtained for platinum-palladium reference catalyst showed that CO was the first compound to be consumed. The temperature at 50% conversion (T_{50}) was 188ºC and the complete conversion was reached at around 200ºC. Once CO oxidation was almost finished, the C_3H_6 conversion started, reaching a 50% of C_3H_6 conversion quickly at 210ºC and then, the complete conversion was attained. As is well known, in the presence of oxygen and NO, the propene can be consumed by: (i) oxidation with oxygen and (ii) selective

catalytic reduction of NO (SCR). Indeed, platinum based catalysts are known to be active for SCR at low temperature, producing the reduction of NO to N_2O [43]. Thus, propene conversion started at 183ºC and, at a slightly higher temperature, the simultaneous reduction of NO by propene (SCR) and N_2O production at around 225°C take place. The maximum SCR conversion corresponded to the propene conversion very close to 100%. Then, NO-N_2O conversion started to decrease, accompanied by an increase in the NO conversion to NO_2. Finally, the NO conversion to NO_2 attained a maximum of 22% at 370ºC, decreasing at higher temperatures due to limitation by the thermodynamic equilibrium.

b. Experiments varying the reactant mixture

To better understand the reaction mechanism and the influence of each gas reactants over PtPd reference catalyst, several approaches were tested, varying the reaction mixture. Note that in the amounts of different reactants were similar in all catalytic experiments, using He as balance with a total flow equal to 250 ml min^{-1} (see section II-b, Chapter II).

i. Oxidation reactions

The CO, C_3H_6 and NO oxidations were first evaluated (Figure III-14).

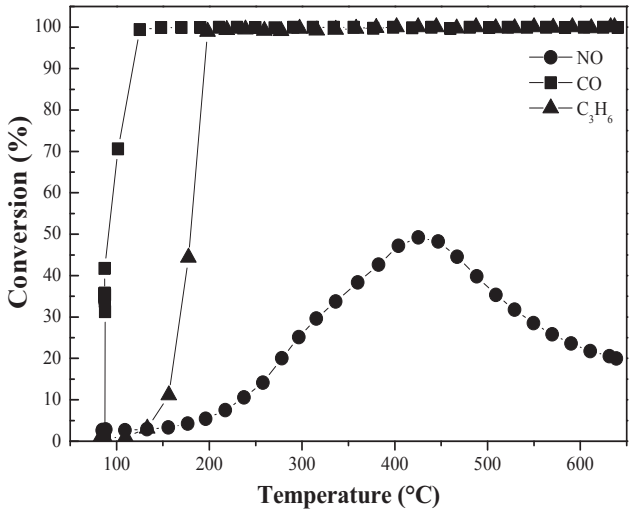

Figure III-14. CO, C_3H_6 and NO conversion in function of the temperature during the heating ramp of the first catalytic cycle. Operating conditions: 50 mg, 250 ml min^{-1}, GHSV = 135 000 h^{-1}, 300 ppm CO or 300 ppm C_3H_6 or 500 ppm NO, 10% O_2 and He as balance.

The first reactive mixture consisted on 300 ppm CO and 10% O_2, in which only the oxidation of CO to CO_2 was detected. The T_{50}, temperature at which conversion is 50%, was found at 90 ºC, and total conversion was quickly reached. The low light-off temperature of CO oxidation can be explained by the ability of CO to strongly adsorb onto the active sites at low temperatures, covering the majority of the catalyst surface [44,45]. The propylene combustion was evaluated using 300 ppm C_3H_6 and 10% O_2. Similarly to CO oxidation, complete conversion was found, however the conversion of 50% was archived a higher temperature (179 ºC). In this case, the strong propylene adsorption onto the active sites of the catalyst was favoured by its double bond [46,47]. Finally, NO to NO_2 oxidation was carried out with 500 ppm NO and 10% O_2. The maximum conversion was equal to 49.3%, with T_{10} value equal to 233 ºC. At high temperatures, NO conversion decreased due to limitation by thermodynamic equilibrium of NO oxidation reaction.

ii. Competition between NO, CO and C_3H_6

It is well known that it exists a competition between NO, CO and C_3H_6 adsorption and subsequent reactions when they are co-feed [48]. Thus, this interaction between the different reactants was studied by varying the total reactive mixture step by step (Figure III-15).

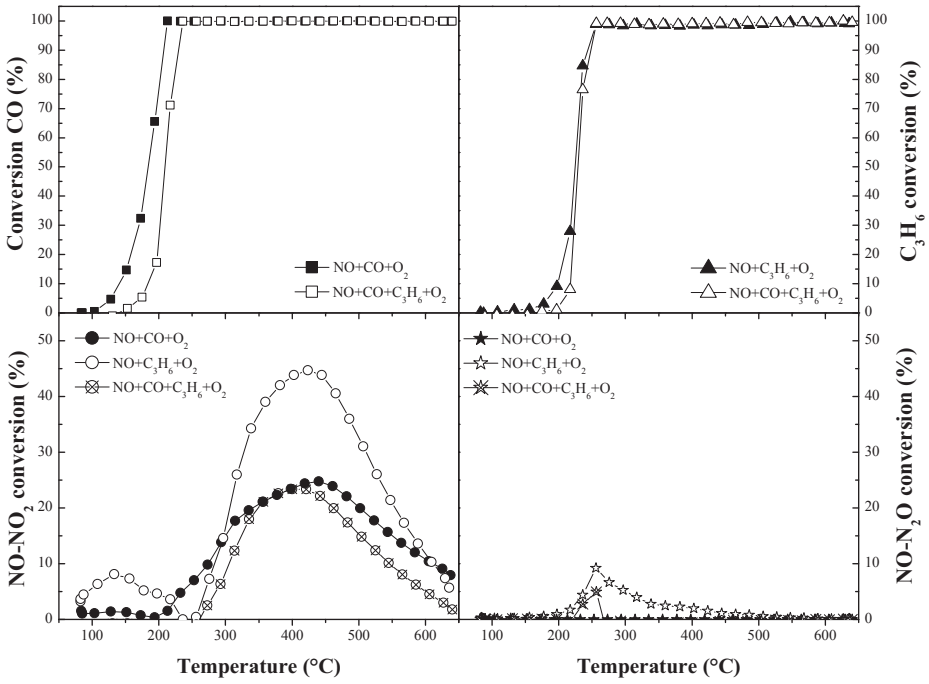

Figure III-15. CO, C_3H_6, NO to NO_2 and NO to N_2O conversion obtained by different mixtures employed during the heating ramp of the first catalytic cycle.

Operating conditions: 50 mg, 250 ml min^{-1}, GHSV = 135 000 h^{-1}, 300 ppm CO and/or 300 ppm C_3H_6, 500 ppm NO, 10% O_2, 5% CO_2 and He as balance.

As shown in Figure III-14, three reactive mixtures were used in order to verify their competition:

- ***500 ppm NO, 300 ppm CO and 10% O_2 (He as balance until 250 ml min^{-1})***

In this first case, total CO conversion was reached (T_{50} value equal to 183 ºC) with a maximum of NO to NO_2 conversion of 24.9% (T_{10} equal to 275 ºC). According to these results, CO complete conversion was achieved at higher temperatures (214 ºC) than in absence of NO (183 ºC). In addition, the presence of NO led to a more gradual increase of CO conversion than in the absence of NO. These data clearly show the inhibition between NO and CO activity by themselves. The adsorption competition of NO_x species with CO can potentially inhibit its oxidation [45,48]. It has been observed in the literature [49,50], that NO can easily adsorb onto Pt and Pd active sites, allowing its further dissociation, which could produce a high coverage of adsorbed nitrogen species and oxygen atoms on the active sites, limiting CO adsorption, although it still adsorbs [45].

- ***500 ppm NO, 300 ppm C_3H_6 and 10% O_2 (He as balance until 250 ml min^{-1})***

The T_{50} and T_{10} of C_3H_6 and NO light-off curves, respectively shifted to higher temperatures when the reactive mixture was constituted by NO and C_3H_6 as reactive gases. Moreover, NO-NO_2 maximum conversion value was decreased from 49.3% to 45%. In presence of both reactants the NO oxidation conversion was lower than in absence of C_3H_6 due to active site competition and the NO reduction via SCR-C_3H_6 (Eq. III-1), which was selective to N_2O instead of N_2:

$$C_3H_6 + 2OO + 4O_2 \rightarrow O_2O + 3CO_2 + 3H_2O \qquad Eq.\ III\text{-}1$$

The oxidation of NO-NO_2 was also detected at temperatures below 200 ºC. However, coinciding with the beginning of C_3H_6 conversion curve at higher temperature, the NO-NO_2 conversion value detected decreased. Shen et al. [51] have shown that at temperatures lower than 250 ºC, adsorbed O_2 facilitates the activation

of C_3H_6, which could favour the formation of oxidised HC intermediates on catalytic sites. Thus, the decrease of NO-NO_2 conversion can be attributed to the reduction of NO_2 back to NO via reaction with C_3H_6 [52]. In addition, these oxidised C_3H_6 intermediates are believed to react preferentially with adsorbed NO, forming N_2O, in agreement with the temperature at which NO reduction started. However, NO reduction decreased when temperature increased due to the combustion of C_3H_6 by O_2 [53].

In order to verify the oxidation of C_3H_6 by NO_2 reduction to NO, a similar experiment was performed using 500 ppm NO_2 instead of NO. As it can be seen in Figure AI-5 (Annexed I), at temperatures below 250 ºC NO_2-NO reduction by C_3H_6 takes place even in oxidizing conditions.

Once the onset of C_3H_6 oxidation was reached, NO can adsorb and react on the active sites. As previously discussed, the double bond of propene favors its strong interaction with metal sites, resulting in a high coverage of catalyst surface by C_3H_6 [54]. Thus, until hydrocarbon species react and lead free catalytic active sites, NO species are not available to react, which means NO reactions are secondary and dependent on reduction of the active sites by C_3H_6 oxidation. These results are in good agreement with H_2-TPR results, in which a reduction peak at 220 ºC was observed, so at similar temperature than T_{50} for C_3H_6 oxidation.

- ***500 ppm NO, 300 ppm CO, 300 ppm C_3H_6 and 10% O_2 (He as balance until 250 ml min^{-1})***

Once the competition between NO and CO or C_3H_6 was verified, a mixture containing NO, CO and C_3H_6 was used in order to study the competition between the three reactants for catalyst active sites. CO and C_3H_6 total conversions still being reached. If T_{50} temperatures are compared with the previous values, in which only NO is present in the reactive mixture, a slight increase of T_{50} temperature was found in the case of C_3H_6 (from 225 ºC to 230 ºC), being even more pronounced in the case of CO (from 183 ºC to 208 ºC). Otherwise, the maximum conversion value of NO to NO_2 oxidation (23.4%) was similar to that obtained in presence of only NO and CO (24.9%). This fact could indicate that the CO and C_3H_6 competition for catalyst active sites affected the NO oxidation. The NO-N_2O conversion still detected due to NO reduction via SCR-C_3H_6. However, the conversion was lower than in the reactive

mixture without CO as a reactant, which could indicate that the CO inhibits all NO reactions (oxidation and reduction), due to the competitive adsorption on catalyst active sites.

Therefore, these catalytic results verified the competitive adsorption at low temperatures between CO, C_3H_6 and NO. However, although both CO and C_3H_6 can strongly adsorb on catalyst active sites, the adsorption of CO is stronger at lower temperature than C_3H_6 and NO adsorption, which inhibits both NO and C_3H_6 oxidation. Once the temperature is high enough to overcome the kinetic limitations the CO oxidation starts, leading some free active sites on which NO and propylene try to adsorb [48,55]. Thus, the results obtained on the previous experiments show that the combined effect of NO and C_3H_6 is accumulative.

iii. Study of water influence

Water is also present in diesel engine exhausts and can play an important role in diesel oxidation catalyst practical operation. Thus, 3.5% of water was added to the previous defined mixtures in order to clarify its influence on the NO, CO and C_3H_6 reactions under oxidation conditions that take place on the reference catalyst (Annexe I, Figure AI-6).

For mixtures in which only CO was present as carbonaceous reactant, 50% conversion was attained at lower temperature when water was added to the mixture. It has been recognized that water enhances CO oxidation by the reduction of the self-poisoning of CO [56]. Otherwise, previous studies [57] have proposed that the CO oxidation barrier could be significantly reduced by the direct reaction of H_2O/OH with CO via COOH intermediates. In addition, CO oxidation via noble metals reduction had also an important contribution. When both C_3H_6 and H_2O are present in the mixture, 50% conversion of propylene and CO were reached at higher temperatures than in absence of water. NO maximum conversion values were also decreased when water was added to the mixture. Thus, the water inhibition is attributed to competitive adsorption with NO, CO and propylene for catalyst active sites [57].

c. Influence of Na, K, Ca and P impurities in catalytic results

The catalytic performances for CO, C_3H_6 and NO oxidation using Na, K, Ca and P-PtPd catalysts (Figure III-16) are discussed and compared with reference catalyst, leading to evaluate the effect of the different impurities on the catalytic conversions.

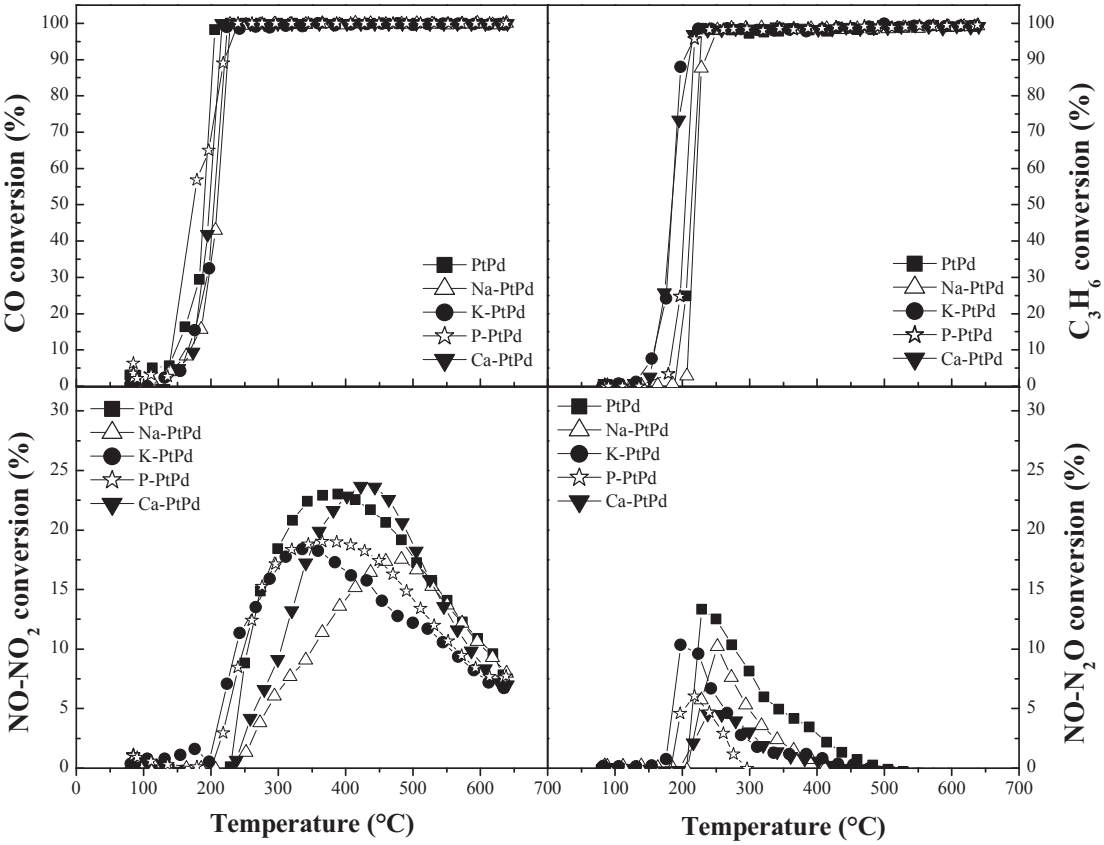

Figure III-16. CO, C_3H_6, NO-NO_2 and NO-N_2O conversion for reference and modified catalysts during the heating ramp of the first cycle. Operating conditions: 50 mg, 250 ml min^{-1}, GHSV = 135 000 h^{-1}, 300 ppm CO, 300 ppm C_3H_6, 500 ppm NO, 10% O_2, 5% CO_2, 3.5% H_2O and He as balance.

Moreover, in order to better explain and compare the different results, reaction rates have been calculated for each catalyst (Table III-7) taking into account its actual metal content.

Table III-7. Catalytic activity results in presence of Na, K, Ca and P impurities for catalytic diesel oxidation reaction.

Catalyst	$^{1}r_{CO}$	$^{1}r_{C3H6}$	$^{1}r_{NO}$	$^{2}NO_2$	$^{2}N_2O$
PtPd	0.912	-	3.191	145	39
Na-PtPd	0.421	0.045	0.736	119	30
K - PtPd	0.504	3.963	4.351	118	31
Ca - PtPd	0.384	4.003	1.036	154	12
P - PtPd	0.994	0.446	3.643	127	25

[1]Reaction rate ((mol s^{-1} g_{PGM}^{-1})·10^5) during the heating at 150, 180 and 230ºC for CO, C_3H_6 and NO, respectively for the first catalytic cycle.
[2]Maximum concentration (ppm) of NO_2 and N_2O for each catalyst during the heating ramp.

Conversely to reference catalyst, CO conversion values obtained with modified catalysts showed the complete conversion in the temperature range of 200-250ºC. Light-off curves shifted towards slightly higher temperatures in presence of Ca, K and Na, showing lower reaction rates calculated at 150°C (Table III-7) than reference catalyst, notably in the case of Ca-PtPd catalyst. As already discussed, CO strongly adsorbs on the active sites of the catalyst at low temperatures, decreasing oxygen adsorption [33]. The use of ceria-zirconia mixed oxide as an "active" support reduced this CO self-inhibition, due to the role of surface oxygen vacancies in oxygen activation [58]. However, the low electronegativity of alkali impurities produces an inhomogeneous electric field, which increase the metal-CO change transfer [40], promoting CO adsorption and the subsequent catalyst surface saturation.

P-PtPd catalyst showed a more different behaviour, probably due to the higher amount of impurities loaded in the catalyst. The light-off of the P-PtPd catalyst started at slightly lower temperatures than that of the reference catalyst. However, the light-off curve was displaced toward higher temperatures when almost complete conversion was attained. As reported in Table III-7, the P-PtPd reaction rate is higher than that of the reference catalyst. This fact could be attributed to the phosphates formed in this catalyst, detected by XRD and XPS, which inhibit CO adsorption, avoiding CO self-poisoning. Moreover, the lower reducibility of Pt-Pd phase in presence of P favoured its oxidation state, which is the active phase for CO oxidation.

Propene oxidation over reference catalyst followed a steady increase until reaching the maximum conversion, in a similar trend than the CO light-off curve. Similarly to reference catalyst, when impurities were present, almost complete conversion was achieved in a range between 200-250 ºC. The catalytic test results

showed that Na-PtPd light-off curve shifted towards higher temperatures, whereas K, Ca and P-PtPd catalysts light-off curves shifted towards lower temperatures compared to the reference catalyst, reaching the highest conversion faster than the reference catalyst. Reaction rates calculated at 180ºC are shown in Table III-7, following this trend: PtPd < Na-PtPd < P-PtPd < K-PtPd < Ca-PtPd. An enhancement of propene reaction rate was noticed for all modified-catalysts, being more pronounced in presence of Ca and K impurities. Note that the reference catalyst showed no conversion at this temperature. The catalytic behaviour of Na- and K-PtPd catalyst for C_3H_6 conversion could be attributed to the electron-donor character of Na and K that could produce an enhancement of oxygen adsorption [59], which could enhance propene oxidation. In the same way, the highest catalytic activity of Ca-PtPd catalyst could be associated to the higher electronegativity of alkaline-earth species compared to that of Na and K species, which decrease the electron-donor effect and, as a consequence, the oxygen interaction. As for CO oxidation, the formation of phosphates avoids C_3H_6 self-inhibition increasing reaction rate of P-PtPd catalyst compared to that of reference catalyst.

In addition, NO-NO_2 conversions obtained for reference and modified catalysts were compared. Although the same trend was found for all catalysts, modified catalysts reached lower maximum conversion values than the reference catalyst. K-PtPd catalyst reached a maximum conversion (18%) at 335 ºC, while Ca and Na-PtPd catalysts accomplished its maximum of NO-NO_2 conversion (~17%) at 430 ºC and 470 ºC respectively. Finally, the P-PtPd catalyst showed its maximum conversion (17%) at 360ºC. NO reaction rates calculated at 230 ºC (Table III-7) showed that K and P-PtPd catalysts had a higher value of reaction rate than the reference catalyst, while Na-PtPd and Ca-PtPd presented a lower value. The decrease in the NO-NO_2 maximum conversion in the presence of alkali impurities could be due to the electron transfer from alkaline to noble metals, which promotes the NO dissociation, increasing the adsorption strength of NO on the catalyst surface. Otherwise, according to NO-TPD analysis the presence of alkaline metal impurities can create the new adsorption sites on these modified catalysts, which are not involved in the reaction but can store NO species [60]. Moreover, the higher reduction temperatures detected by H_2-TPR analysis in the presence of Na, K and Ca additives made more difficult the reduction of Pt and Pd species, diminishing the NO conversion as

metallic Pt and Pd are the active phase for NO oxidation. Finally, the decrease of NO conversion with phosphorus addition could be correlated to the following conclusions: (1) the presence of phosphates detected by TEM and XPS blocked the pores, decreasing the BET specific surface area, which reduces the amount of NO adsorbed; (2) phosphates species on catalysts surface can stabilize the Ce^{3+} oxidation state, according to the higher Ce^{3+}/Ce^{4+} ratio obtained by XPS analysis, decreasing the NO adsorption due to its electron donor character and (3) the amount of NO desorbed obtained by NO-TPD was the lowest, confirming the disfavoured NO adsorption detected by the rest of the characterization methods.

Even in the presence of high amounts of oxygen, as encountered in the present study, NO partial reduction was detected via the SCR-C_3H_6 reaction. N_2O and N_2 to a lesser extent coming from NO partial reduction via C_3H_6-SCR were detected. To complete the NO balance, the undesirable N_2O production was also evaluated for the reference and modified catalysts.

The reference catalyst presented a maximum of NO-N_2O conversion (13%) at 230 ºC (Table III-7), while K-PtPd maximal NO-N_2O conversion (10%) was reached at 198 ºC. Na-PtPd achieved similar maximal conversion than K-PtPd catalyst (10%) but at higher temperature and slightly lower than that of the reference catalyst. However, Ca-PtPd and P-PtPd catalysts presented an almost negligible NO-N_2O conversion of 5% and 8% of maximum conversion, respectively.

The catalytic test results showed that the NO-N_2O conversion started at the light-off temperature of propene combustion, indicating the occupation of NO oxidation active sites by propene [43]. Comparing the results related to modified and reference catalysts, lower NO-N_2O conversion was found for the K-PtPd catalyst than for the reference one. An unexpected fact was the lower temperature at which the maximum conversion was reached, reported to the electron donator role of the K additive. In the case of Na-PtPd, the maximum conversion was found at higher temperature than over the reference and K-PtPd catalysts. As stated before, alkali doping increases the strength of NO chemisorption relative to C_3H_6, which induced a promotion phenomenon of NO reduction. This enhancement follows a volcano type behaviour related to alkali loading. The higher amount of Na compared to K added to the catalyst probably overtook the optimum alkali amount, decreasing the promotion effect related to alkali presence. As shown in Table III-7, the maximum N_2O quantity

produced was similar to that obtained in the case of K-PtPd catalyst, lower than over the PtPd catalyst. In addition, NO to N_2O conversion obtained over the Ca-PtPd catalyst was almost negligible. Finally, the P-PtPd catalyst also disfavour SCR-C_3H_6 reaction, according to the significantly lower NO-N_2O conversion and N_2O formation compared to that of the reference and Na, K and Ca-PtPd catalysts.

d. Impurities combination influence in catalytic results

The catalytic performances obtained when combination of impurities were presented in the catalysts are present in Annexed I (Figures AI-7 and AI-8). The reaction rates were also calculated in order to discuss and compare with the performance of reference catalyst (Table III-8).

Table III-8. Catalytic activity results in presence of Na, K, Ca and P combinations for catalytic diesel oxidation reaction.

Catalyst	$^1r_{CO}$	$^1r_{C3H6}$	$^1r_{NO}$	$^2NO_2$	^2N_2O
PtPd	0.912	1.305	3.191	145	39
NaK-PtPd	0.430	0.145	-	95	11
NaCa - PtPd	0.603	0.073	-	107	13
KCa - PtPd	0.592	0.135	-	117	12
PNa - PtPd	0.802	0.478	0.776	121	23
PCa-PtPd	0.036	0.142	0.332	140	21
PK-PtPd	0.238	-	-	121	23
PNaKCa-PtPd	0.216	0.071	-	107	21

[1]Reaction rate ((mol s^{-1} g_{PGM}^{-1})·10^5) during the heating at 150, 200 and 230ºC for CO, C_3H_6 and NO, respectively for the first catalytic cycle.
[2]Maximum concentration (ppm) of NO_2 and N_2O for each catalyst during the heating ramp.

CO reaction rate decreases as follow when Na, K and Ca combinations are introduced: PtPd > NaCa-PtPd > KCa-PtPd > NaK-PtPd. As previously established, the electronic field produced by alkali impurities is the major factor affecting the catalytic performances of modified catalysts [61], being the NaK-containing catalyst the combination most electropositive. This catalyst presents the highest electron donor character, which should increase the CO adsorption. However, an excess of alkali impurity added can also have a negative role in the CO adsorption [62]. Thus, the lower reaction rate could be ascribed to two contrary effects: (i) surface saturation due to the excessive promotion of CO adsorption, or (ii) avoid of CO adsorption due to the excess of alkali metal over the optimum. The higher amount of impurity present on the catalyst made the second option more suitable. This conclusion will be

corroborated by the in-situ DRIFTS study (Chapter IV). In addition, in the case of catalysts combining with Ca impurities, the higher electronegativity of this alkaline earth compound results in a decrease of the CO reaction rate.

The C_3H_6 light-off curves shifted to higher temperature values due to the higher amount of impurities presented in the catalysts (Figure AI-8 and Table III-8). These results showed that the higher C_3H_6 reaction rate could be related to the low electronegativity of alkaline metals (Na, K and Ca), which enhances the oxygen adsorption, according to the results observed in presence of only one impurity. On the contrary, if the amount of impurity exceeds a certain limit, this promotion can be reverse [62] due to the catalyst surface saturation by O_2 adsorption.

Regarding the NO reaction rate, the combination of alkaline impurities produced the same effect on than when they were presented alone. The reaction rate decreased due to the low electronegativity of these impurities, which will transfer electrons to PtPd, favoring NO dissociation and increasing metal-NO bond strength.

Otherwise, CO and C_3H_6 reaction rates decreased when alkali impurities are combined with phosphorus. The formation of phosphates can avoid the CO and C_3H_6 self-poisoning, however an excess of them reduces the SSA as verified by N_2 adsorption/desorption.

Finally, a catalyst containing all the impurities was synthetized (PNaKCa-PtPd), which shows the combined influence of alkaline impurities and phosphorus (Figure AI-9). The higher content of impurities increased the electronic effect due to the alkali impurities, increasing the temperature at which CO conversion was attained. Propylene conversion also shifted to higher temperature values, but lower difference in temperature between CO and C_3H_6 curves was observed. Indeed, the enhancement of O_2 adsorption was also increased due to the higher amount of impurities, thus C_3H_6 oxidation was also enhanced. Finally, the lower NO adsorption due to the blockage of catalytic active sites by phosphates decreased the catalytic activity.

III. Conclusions

The impact of alkali and alkaline earth metals (Na, K and Ca) or phosphorus species (P), on PtPd/$CeZrO_2$/La-Al_2O_3 diesel oxidation catalysts physico-chemical, redox and catalytic properties was evaluated. The catalytic test results for modified catalysts concerning CO, C_3H_6 and NO oxidation reactions have shown that the presence of inorganic elements originating from biodiesel have a significant impact on the performance of a DOC catalyst. Thus, the inhomogeneous electric field produced around Na, K and Ca species increase the oxygen interaction, according to H_2-TPR analysis. This fact results in a negative effect on the CO catalytic oxidation due to the electron donor character of CO, which promotes its adsorption saturating the catalyst surface. However, the reaction between propene and oxygen is enhanced in presence of these inorganic elements due to this higher oxygen interaction, improving the C_3H_6, oxidation activity. In presence of P species, both CO and C_3H_6 oxidation were improved. These results could be related to the presence of phosphates species that inhibited the catalyst surface saturation, avoiding CO and C_3H_6 self-poisoning. In addition, the lower noble metals reducibility as well as to their higher oxidized state promotes their co-oxidation. Na, K and Ca-PtPd catalysts also presented lower NO catalytic activity than reference catalyst. These results could be attributed to the electro-donor character of these additives, which increase the metal-NO bond strength, according to the higher NO desorption temperature. Phosphates formation inhibited NO adsorption, decreasing the catalytic activity.

References:

[1] M. Ozawa, Y. Nishio, J. Alloys Compd. 374 (2004) 397–400.
[2] M. Ozawa, J. Alloys Compd. 408–412 (2006) 1090–1095.
[3] G.W. Graham, H. Jen, R.W. Mccabe, A.M. Straccia, L.P. Haack, 67 (2000) 99–105.
[4] C.E. Hori, H. Permana, K.Y.S. Ng, A. Brenner, K. More, K.M. Rahmoeller, D. Belton, Appl. Catal. B-Environmental 16 (1998) 105–117.
[5] G. Leofanti, M. Padovan, G. Tozzola, B. Venturelli, Catal. Today 41 (1998) 207–219.
[6] F.A. Silva, D.S. Martinez, J.A.C. Ruiz, L. V. Mattos, C.E. Hori, F.B. Noronha, Appl. Catal. A Gen. 335 (2008) 145–152.
[7] V. Kröger, T. Kanerva, U. Lassi, K. Rahkamaa-Tolonen, M. Vippola, R.L. Keiski, Top. Catal. 45 (2007) 153–157.
[8] S.Y. Christou, H. Birgersson, A.M. Efstathiou, Appl. Catal. B Environ. 71 (2007) 185–198.
[9] V. Kröger, M. Hietikko, U. Lassi, J. Ahola, K. Kallinen, R. Laitinen, R.L. Keiski, Top. Catal. 30–31 (2004) 469–474.
[10] B. Béguin, E. Garbowski, M. Primet, Appl. Catal. 75 (1991) 119–132.
[11] P.P. Silva, F.A. Silva, H.P. Souza, A.G. Lobo, L. V. Mattos, F.B. Noronha, C.E. Hori, Catal. Today 101 (2005) 31–37.
[12] X. Chen, Y. Liu, G. Niu, Z. Yang, M. Bian, A. He, Appl. Catal. A Gen. 205 (2001) 159–172.
[13] A. Pfau, K.-D. Schierbaum, Surf. Sci. 6028 (1994).
[14] J.C.S. Dalton, B.P. Burroughs, A. Hamnett, A.F. Orchard, G. Thornton, (1975).
[15] A. Trovarelli, G.J. Hutchings Catal. Sci. Ser. 2 (2002).
[16] S. Damyanova, B. Pawelec, K. Arishtirova, M.V.M. Huerta, J.L.G. Fierro, Appl. Catal. A Gen. 337 (2008) 86–96.
[17] C. Morant, J.M. Sanz, L. Galán, L. Soriano, F. Rueda, Surf. Sci. 218 (1989) 331–345.
[18] L.F. Liotta, G. a Martin, G. Deganello, J. Catal. 164 (1996) 322–333.
[19] S. Gil, J. Garcia-Vargas, L. Liotta, G. Pantaleo, M. Ousmane, L. Retailleau, A. Giroir-Fendler, Catalysts 5 (2015) 671–689.
[20] V. Pitchon, M. Guenin, H. Praliaud, Appl. Catal. 63 (1990) 333–343.
[21] N.C. Filkin, M.S. Tikhov, A. Palermo, R.M. Lambert, J. Phys. Chem. A 103 (1999) 2680–2687.
[22] L. Ma, M.F. Luo, L.-F. Han, S.-Y. Chen, React. Kinet. Catal. Lett. 70 (2000) 357–362.
[23] Z. Hu, X. Liu, D. Meng, Y. Guo, Y. Guo, G. Lu, ACS Catal. 6 (2016) 2265–2279.
[24] A.C.S.F. Santos, S. Damyanova, G.N.R. Teixeira, L. V. Mattos, F.B. Noronha, F.B. Passos, J.M.C. Bueno, Appl. Catal. A Gen. 290 (2005) 123–132.
[25] B.B. Harrison, a F. Diwell, C. Hallett, Platin. Met. Rev. (1988) 73–83.
[26] H.C. Yao, Y.F.Y. Yao, J. Catal. 86 (1984) 254–265.
[27] S. Ricote, G. Jacobs, M. Milling, Y. Ji, P.M. Patterson, B.H. Davis, Appl. Catal. A Gen. 303 (2006) 35–47.
[28] H.-W. Jen, G.. Graham, W. Chun, R.. McCabe, J.-P. Cuif, S.. Deutsch, O. Touret, Catal. Today 50 (1999) 309–328.
[29] G. Balducci, J. Kašpar, P. Fornasiero, M. Graziani, M.S. Islam, J. Phys. Chem. B 102 (1998) 557–561.
[30] G. Balducci, J. Kaspar, P. Fornasiero, M. Graziani, M.S. Islamm, J.D. Gale, J. Phys. Chem. B 101 (1997) 1750–1753.
[31] J. Gong, D. Wang, J. Li, K. Kamasamudram, N. Currier, A. Yezerets, Catal. Today (2018) 0–1.
[32] C.-H. Lee, Y.-W. Chen, Ind. Eng. Chem. Res. 36 (1997) 1498–1506.
[33] L. Xue, H. He, C. Liu, C. Zhang, B. Zhang, M. About, T. Article, 43 (2009) 890–895.
[34] C. Larese, F. Cabello Galisteo, M. López Granados, R. Mariscal, J.L.G. Fierro, M. Furió, R. Fernández Ruiz, Appl. Catal. B Environ. 40 (2003) 305–317.

[35] S. Koukiou, M. Konsolakis, R.M. Lambert, I. V. Yentekakis, Appl. Catal. B Environ. 76 (2007) 101–106.
[36] I. V. Yentekakis, M. Konsolakis, R.M. Lambert, N. MacLeod, L. Nalbantian, Appl. Catal. B Environ. 22 (1999) 123–133.
[37] M. Konsolakis, J. Catal. 198 (2001) 142–150.
[38] M. Konsolakis, I. V. Yentekakis, Appl. Catal. B Environ. 29 (2001) 103–113.
[39] M. Konsolakis, N. Macleod, J. Isaac, I. V Yentekakis, R.M. Lambert, J. Catal. 193 (2000) 330–337.
[40] N.D. Lang, S. Holloway, J.K. Nørskov, Surf. Sci. 150 (1985) 24–38.
[41] N. Takahashi, H. Shinjoh, T. Iijima, T. Suzuki, K. Yamazaki, K. Yokota, H. Suzuki, N. Miyoshi, S. Matsumoto, T. Tanizawa, T. Tanaka, S. Tateishi, K. Kasahara, Catal. Today 27 (1996) 63–69.
[42] F. Le Normand, L. Hilaire, K. Kili, G. Krill, G. Maire, J. Phys. Chem. 92 (1988) 2561–2568.
[43] X. Auvray, L. Olsson, Appl. Catal. B Environ. 168–169 (2015) 342–352.
[44] Y. Yu Yao, J. Catal. 87 (1984) 152–162.
[45] S.E. Voltz, C.R. Morgan, D. Liederman, S.M. Jacob, Ind. Eng. Chem. Prod. Res. Dev. 12 (1973) 294–301.
[46] F. Diehl, J. Barbier, D. Duprez, I. Guibard, G. Mabilon, Appl. Catal. B Environ. 95 (2010) 217–227.
[47] F. Mittendorfer, C. Thomazeau, P. Raybaud, H. Toulhoat, J. Phys. Chem. B 107 (2003) 12287–12295.
[48] M. Al-Harbi, R. Hayes, M. Votsmeier, W.S. Epling, Can. J. Chem. Eng. 90 (2012) 1527–1538.
[49] T. Watling, M. Ahmadlnejad, M. Tutulano, A. Johansson, M. Paterson, SAE Int. J. Engines 5 (2012) 23.
[50] G. Zheng, E.I. Altman, Surf. Sci. 462 (2000) 151–168.
[51] S.C. Shen, S. Kawi, Appl. Catal. B Environ. 45 (2003) 63–76.
[52] K. Irani, W.S. Epling, R. Blint, Appl. Catal. B Environ. 92 (2009) 422–428.
[53] R. Burch, D. Ottery, Appl. Catal. B Environ. 9 (1996) 19–24.
[54] R. Burch, T.C. Watling, Catal. Letters 43 (1997) 19–23.
[55] I. Lefort, J.M. Herreros, A. Tsolakis, Environ. Sci. Technol. 48 (2014) 2361–2367.
[56] H.J. Kwon, J.H. Baik, Y.T. Kwon, I.S. Nam, S.H. Oh, Chem. Eng. J. 141 (2008) 194–203.
[57] R. Caporali, S. Chansai, R. Burch, J.J. Delgado, A. Goguet, C. Hardacre, L. Mantarosie, D. Thompsett, Appl. Catal. B Environ. 147 (2014) 764–769.
[58] C. Bozo, N. Guilhaume, J.-M. Herrmann, J. Catal. 203 (2001) 393–406.
[59] I. V. Yentekakis, V. Tellou, G. Botzolaki, I.A. Rapakousios, Appl. Catal. B Environ. 56 (2005) 229–239.
[60] W.S. Epling, L.E. Campbell, A. Yezerets, N.W. Currier, J.E. Parks, Catal. Rev. 46 (2004) 163–245.
[61] W.D. Mross, Catal. Rev.-Sci. Eng. 25 (1983) 591–637.
[62] Y. Minemura, M. Kuriyama, S. ichi Ito, K. Tomishige, K. Kunimori, Catal. Commun. 7 (2006) 623–626.

Chapter IV

CHAPTER IV: In-situ DRIFT study of impurities influence on surface adsorption properties of DOC

In the previous chapter the effects of Na, K, Ca and P impurities on a reference DOC catalyst, PtPd/$CeZrO_2$/La-Al_2O_3, were evaluated. It has been shown that, depending of the impurity, these effects were different for each reaction studied.

Regarding the state of the art, several studies have shown that the NO is mainly oxidised on metal sites and subsequent storage on adjacent sites in the form of nitrates occurred [1–3]. Typically alkali or alkaline earth metals, such as barium, are used as storage component on NO_x Storage-reduction (NSR) catalysts. Furthermore, Westerberg et al. [4] proposed that Al_2O_3 could play an important role as storage site at temperatures below 300 ºC. In the present chapter, alkalis were added to the reference catalyst in order to simulate the storage of alkaline species present in biofuels, after long period time of biodiesel combustion. Thus, the modification of adsorption sites on the catalyst surface due to these impurities and its influence on the CO, HC and NO reaction pathways remains uncertain.

Therefore, in this chapter some results related to the Diffuse Reflectance Infrared Fourier Transform Spectroscopy (DRIFTS) data for NO adsorption/desorption on the surface of PtPd reference and Na, K, Ca, P-modified catalysts will be reported in order to give some light to these important questions. In-situ DRIFTS under different sequences of NO_x, CO and C_3H_6 gas mixtures was mainly used in this chapter to gain important insights into the reaction intermediates involved in oxidation reactions and to better understand the relationship between impurities and catalytic activity at the surface of DOC catalysts.

The principal bands observed and the corresponding assignments are summarized in Table IV-1.

Table IV-1. Bands position and the corresponding assignments of surface species in DRIFT spectra.

Surface species		Peak position (cm^{-1})	Infrared vibration	Reference
Bridging nitrites	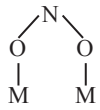	1314-1266	$\nu_{as}(NO_2)$	[5]
		1230-1276	$\nu_{s}(NO_2)$	
Monodentate nitrites	O-N-O-M	1470-1375	ν(N=O)	[6]
		1206-1065	ν(N-O)	
Bidentate nitrites	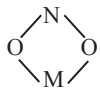	1375-1314	$\nu_{s}(NO_2)$	
		1203-1176	$\nu_{as}(NO_2)$	
Bridging nitrates	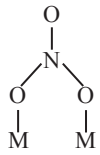	1600-1650	$\nu_{s}(NO_2)$	[4,6–11]
		1200-300	$\nu_{as}(NO_2)$	
Bidentate nitrates	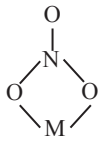	1590-1550	$\nu_{s}(NO_2)$	
		1200-1300	$\nu_{as}(NO_2)$	
Monodentate nitrates	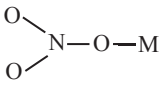	1510-1508	$\nu_{as}(NO_2)$	[2]
		1275-1250	$\nu_{s}(NO_2)$	
Linear or bent NO on Pt	$(NO)^-$	1680-1780	ν(N-O)	[5,7,12,13]
P-OH	$(HO)^-$	3670	ν(O-H)	[14]
Free OH	$(HO)^-$	3684		
Formates	$(HCOO)^-$	1373	$\nu_{s}(COO^-)$	[15–21]
		1410-1390	δ(CH)	
		1585	$\nu_{as}(COO^-)$	
Adsorbed hydrocarbon fragments	$(HC)^-$	2965, 2938	ν_{as}(CH)	
		2910, 2908	ν_{s}(CH)	
Acetates	$(CH_3\text{-}(C{=}O)\text{-}O)^-$	1460-1440	$\nu_{s}(COO^-)$	
		1555-1545	$\nu_{as}(COO^-)$	
Carbonates	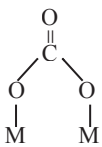	1645	$\nu_{as}(COO^-)$	[21–23]
		1350-1345	$\nu_{s}(COO^-)$	
Carbonyls on partially oxidized Pt	(>C=O)	2113, 2120	ν(CO)	[15,16,21,24]
Cyanide	$(N{+}C)^-$	2155 2141	ν(C+N)	[15,25,26]
Isocyanates	$(N{=}C{=}O)^-$	2205 2170	ν(N=C=O)	[21,27–29]

I. NO adsorption and thermal desorption spectroscopy (TDS)

a. NO adsorption on PtPd and Na, K, Ca and P-modified catalysts

In order to identify the surface species formed on reference and modified catalysts, DRIFTS measurements were firstly conducted during NO adsorption at 35 ºC. For comparison, the NO adsorption on the support alone (La-Al_2O_3 and $CeZrO_2$/La-Al_2O_3) was firstly evaluated and compared to reference catalyst containing Pd/Pt active phases. Figure IV-1 shows the adsorption bands detected after exposition of support and PdPt reference catalyst to NO/He at 35 ºC until surface saturation.

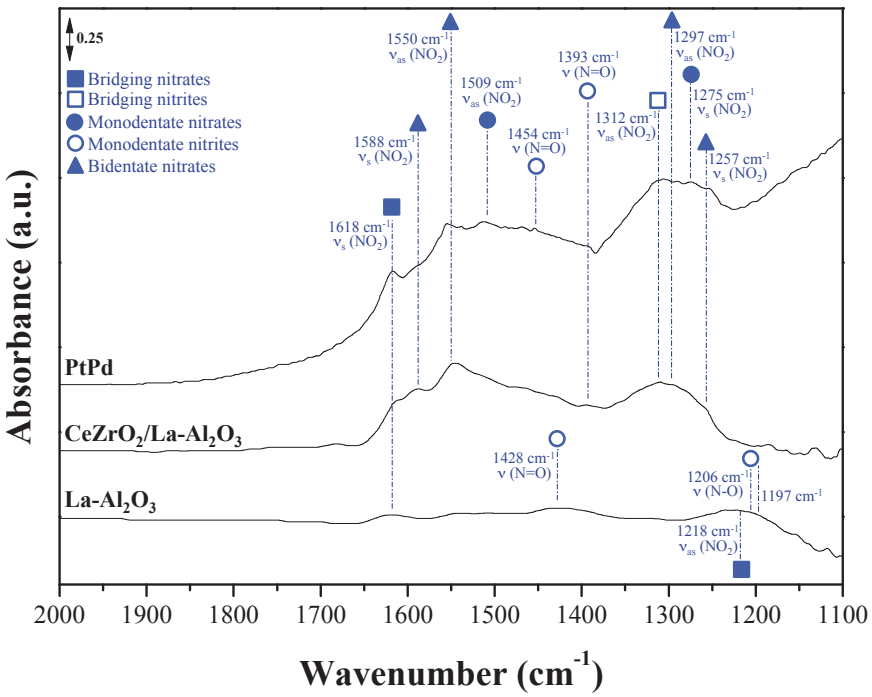

Figure IV-1. DRIFT spectra in the region 2000-1100 cm^{-1} of support and PtPd-reference catalyst after 120 min exposure to NO at 35 ºC.

Firstly, current bands assigned to nitrites and nitrates were detected after NO adsorption on La-doped Al_2O_3. The bands assigned to bridging bidentate nitrates were observed in the 1650-1600 and 1300-1200 cm^{-1} region (peaks at 1618, $\nu_s(NO_2)$, and 1218 cm^{-1}, $\nu_{as}(NO_2)$) [30]. Bands corresponding to monodentate nitrites adsorbed on Al_2O_3 were also detected at 1428 cm^{-1}, ν(N=O), and 1206 cm^{-1}, ν(N-O). Finally, the

peak at 1197 cm^{-1} could be associated to NO^- ions adsorbed on lanthanum phase according to the literature, in which the bands assigned to NO adsorbed on a La_2O_3/Al_2O_3 sample or bulk La_2O_3, as NO^- are detected at 1195 cm^{-1} [31].

The infrared spectra of La-doped Al_2O_3 support promoted with $CeZrO_2$ is also presented in Figure IV-1. The bands previously assigned to bridging nitrates on Al_2O_3 (1618 cm^{-1}, $\nu(NO_2)$ and 1218 cm^{-1}, $\nu_{as}(NO_2)$) were also observed on $CeZrO_2/Al_2O_3$ support, with a more pronounced intensity. This higher intensity could be related to the multi-contribution to the NO_x-adsorption due to the overlapping of these bands with that of the bidentate nitrates on ceria phase (at 1588 cm^{-1}, $\nu_s(NO_2)$ and 1297 cm^{-1}, $\nu_{as}(NO_2)$; 1550 cm^{-1}, $\nu_{as}(NO_2)$, and 1257 cm^{-1}, $\nu_s(NO_2)$) [2]. Moreover, additional bands assigned to the nitrito monodentate species manifest stretches at 1470-1375 cm^{-1} (band at 1393 cm^{-1}, $\nu(N=O)$) and at 1206-1065 cm^{-1} (band at 1206 cm^{-1}, $\nu(N-O)$). Otherwise, bands corresponding to bridging nitrites groups are observed at 1312 cm^{-1} ($\nu_{as}(NO_2)$) and at 1276 cm^{-1} ($\nu_s(NO_2)$) [6].

An increase of nitrites/nitrates bands intensity was observed in $CeZrO_2/La$-Al_2O_3 spectrum. This increase could indicate a significant enhancement of NO_x adsorption due to the oxygen vacancies formed upon the introduction of Zr^{4+} on CeO_2 structure [32] as well as the electron transfer between CeO_2 and the adsorbed NO_x, as had been suggested by Martínez-Arias et al. [33]. Previous studies [32,34–36] have demonstrated that such vacancies are clearly implicated in NO_x storage, e.g.:

$$Ce^{3+}\text{-}\square + NO \rightarrow Ce^{4+}\text{-}NO^- \qquad \textit{Eq. IV-1}$$

$$Ce^{4+}\text{-}NO^- + Ce^{4+}\text{-}O^* \rightarrow Ce^{4+}\text{-}NO_2^- + Ce^{3+}\text{-}\square \qquad \textit{Eq. IV-2}$$

Where $\square$ represents an oxygen vacancy. Eq. IV-1 represents the transfer of an unpaired electron from the NO to the ceria surface; Eq. IV-2 shows the formation of nitrite species by additional electrons transfer between ad-NO_x species and ceria or by improved N-containing species adsorption at the CeO_2 and La-Al_2O_3 interface.

Moreover, all the bands previously assigned to surface NO_x-containing species such as nitrites and nitrates for $CeZrO_2/Al_2O_3$ support were also identified after NO_x adsorption on PtPd-reference catalysts, nevertheless, these bands had more intensity. In addition, new bands associated monodentate nitrites (1454 cm^{-1} ($\nu(N=O)$) and 1206 cm^{-1} ($\nu(N-O)$)) and monodentate nitrates on the Al_2O_3 phase (1509 cm^{-1}, $\nu_{as}(NO_2)$, and 1275 cm^{-1}, $\nu_s(NO_2)$) were found on PtPd-catalyst. Against this background, it

seems evident the promoting effect of the precious metals. On the one hand, Pt and Pd sites can adsorb NO, which spillover onto the support surface with subsequent formation of nitrites/nitrates. On the other hand, the formation of highly interfacial sites at the metal/oxide boundary could promote NO oxidation to NO_2, which can react with the ceria surface to form nitrites/nitrates via Eqs. IV-3 and IV-4.

$$Ce^{3-} + \square + OO_2 \rightarrow Ce^{4-} + OOO^- \qquad \textit{Eq. IV-3}$$

$$Ce^{4-} + OOO^- + OO_2 \rightarrow Ce^{4-} + OO_3^- + OO \qquad \textit{Eq. IV-4}$$

Comparing the infrared adsorption spectra during exposure of both support and PtPd-reference catalyst to NO/He, it is possible to conclude that the NO_x adsorption on these materials was made via the so-called "nitrate (or NO_2) route" [37], which means that both nitrites and nitrates are simultaneously formed on the surface of studied materials.

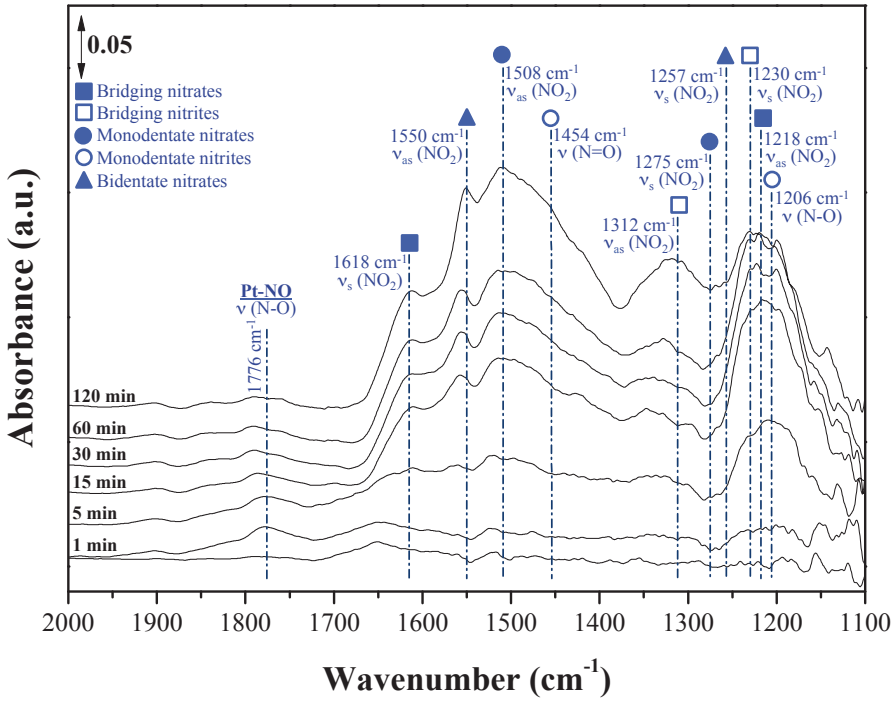

Figure IV-2. PtPd DRIFT spectra collected during exposition to 4000 ppm NO/He (40 ml min^{-1}) at 35 ºC vs time until catalyst surface saturation.

The evolution of NO adsorption with time is shown in Figure IV-2. Increasing the exposition time, it can be seen the presence of nitrates (bridging (1618 cm^{-1}, $\nu_s(NO_2)$ and 1218 cm^{-1}, $\nu_{as}(NO_2)$), bidentate (1550 cm^{-1}, $\nu_{as}(NO_2)$ and 1257 $\nu_s(NO_2)$) and monodentate (1508 cm^{-1}, $\nu_{as}(NO_2)$ and 1275 cm^{-1}, $\nu_s(NO_2)$), as well as nitrites

(bidentate (1312 cm^{-1}, $\nu_{as}(NO_2)$ and 1230 $\nu_s(NO_2)$) and monodentate (1454 cm^{-1}, ν(N=O) and 1206 cm^{-1}, ν(N-O)). Moreover, a band at 1776 cm^{-1} related to NO adsorption on the metal phase [5,7,12,13] was found at low time exposition, which can be ascribed to NO chemisorption on Pt or Pd via a donor-acceptor mechanism, involving electron transfer from the NO-5σ molecular orbit to the metal and back-donation of metal d-electrons to the 2π* level [38]. At higher exposition times, the intensity of this band decreases until it disappears, while the nitrates bands intensities increase. Ji et al. [32] proposed a Pt-assisted NO_x adsorption, which involves the adsorption of NO_x on Pt at low temperatures, followed by spillover of either NO or NO_2 onto the support surface. Thus, we can postulate that the NO_x was effectively adsorbed at 35 ºC and subsequently oxidized to form at first nitrite ad-species and progressively transformed into nitrates ad-species (presumably adsorbed at a support site in proximity of a Pt site or directly on Pt surface sites). Note that between 15 and 120 min the same species were found, increasing only the band intensities due to the saturation of the catalyst surface.

Figure IV-3 shows corresponding IR spectra between 2000-800 cm^{-1} under identical conditions for PtPd-reference and Na-PtPd and K-PtPd modified catalysts to NO/He exposure at 35 ºC.

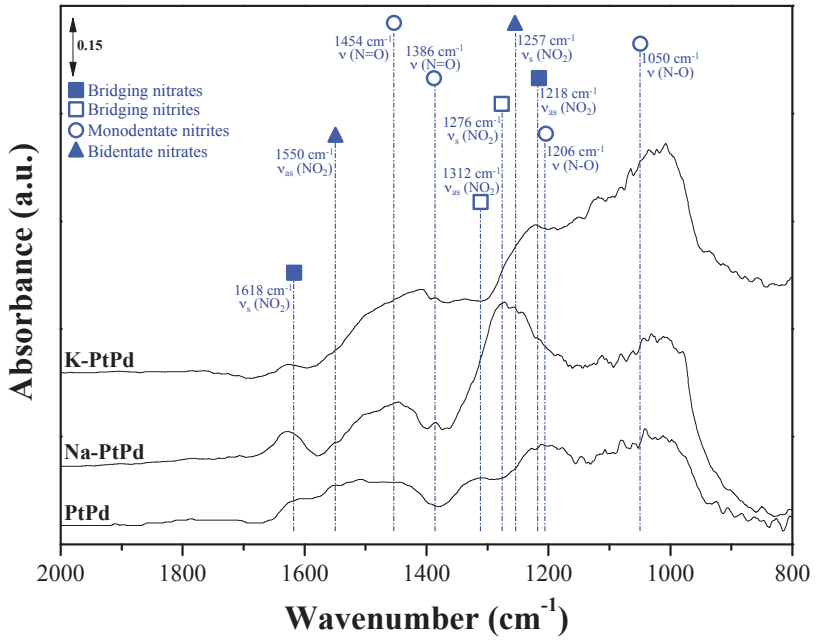

Figure IV-3. DRIFT spectra in the region 2000-800 cm^{-1} of PtPd-reference, Na-PtPd and K-PtPd catalysts after NO surface saturation at 35 ºC.

All the features assigned to nitrites and nitrates formed on PtPd-reference

catalyst were also observed in presence of alkali impurities. However, the bands assigned previously to bridging nitrates (1618 cm^{-1}, $\nu_s(NO_2)$ and 1218 cm^{-1}, $\nu_{as}(NO_2)$) and monodentate (1454 cm^{-1}, ν(N=O) and 1206 cm^{-1}, ν(N-O)) and bridging nitrites (1312 cm^{-1}, $\nu_{as}(NO_2)$ and 1276, $\nu_s(NO_2)$), were more pronounced for Na- and K-PtPd modified catalysts. This higher adsorption of adsorbates such as NO_x and oxygen, could be attributed to a promotion effect of alkali added species, as has been demonstrated in literature [5,21,33,39–41]. M. Konsolakis et al. [40,42] had reported that alkali species can increase the strength of NO adsorption and weaken the N-O bond in adsorbed molecule, favoring the surface coverage and the NO dissociation. This phenomena was ascribed to the effect of the inhomogeneous electrostatic field related to alkali cations [5,40], which enhances the chemisorption of electron acceptors (electronegative adsorbates such as NO) and its dissociation.

$$NO(g) \rightarrow NO(ads) \quad (enhanced\ by\ alkali\ addition) \qquad Eq.\ IV\text{-}5$$

$$NO(ads) \rightarrow N(ads) + O\ (ads) \quad (enhanced\ by\ alkali\ addition) \qquad Eq.\ IV\text{-}6$$

This conclusion can be also discussed in terms of the rigorous model developed by Lang et al. [39]. Thus, the electron transfer between an electropositive adsorbate (such as an alkali cation) and the antibonding π^* orbital of an electron-acceptor adsorbate (NO) is favoured, weakening the N-O bond and promoting the formation of metal-N bond [41], so its adsorption and dissociation (see Chapter I, section III-c in introduction part).

Figure IV-4 displays the absorption bands detected on Ca-PtPd catalyst. Similar IR bands to that of the PtPd-reference catalyst were observed in presence of Ca impurities, however a higher intensity of the bands assigned to bridging nitrates (1618 cm^{-1}, $\nu_s(NO_2)$ and 1218 cm^{-1}, $\nu_{as}(NO_2)$) and monodentate nitrites (1454, 1386 ν(N=O) and 1206, 1050 cm^{-1} ν(N-O)) was found. These more pronounced intensities could be attributed to the higher basicity of Ca species, which has been directly related to the NO_x adsorption [1]. Particularly, Takahashi et al. [43] showed that stronger basicity of the NO_x storage sites leads to higher amounts of adsorbed NO_x. Thus, more stable nitrates could be formed related to the stronger basicity of the NO_x storage species, such as alkaline earth compounds (Ba, Ca, etc.). Therefore, high amount of nitrites ad-species will be formed in presence of Ca impurities due to its higher basicity, which will be simultaneously oxidized to nitrate on Pt sites.

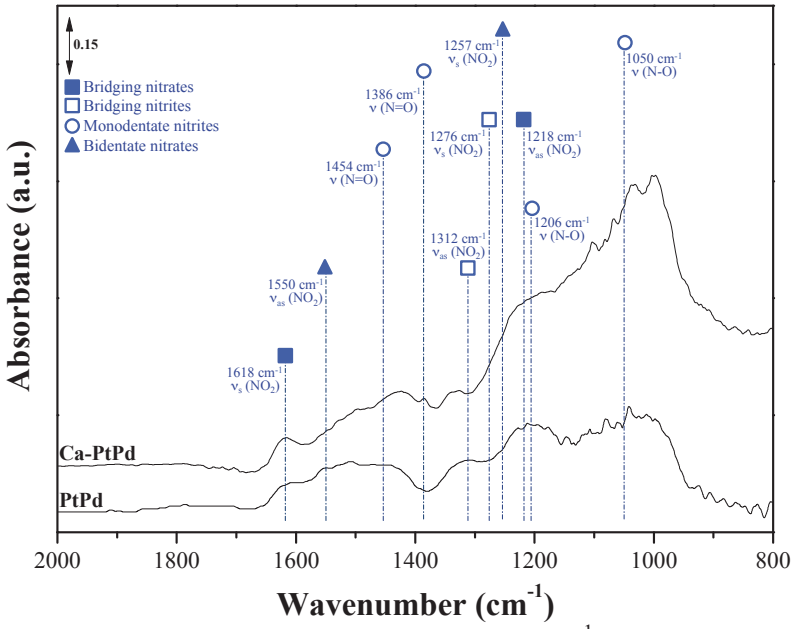

Figure IV-4. DRIFT spectra in the region 2000-800 cm^{-1} of PtPd-reference and Ca-PtPd catalyst after NO surface saturation at 35 ºC.

Finally, the effect of phosphorus species on surface reaction over PtPd catalyst was evaluated (Figure IV-5). The NO_x adsorption on P-PtPd catalyst was almost suppressed, which demonstrated the clear poisoning effect of phosphates species. In the region 1800-1200 cm^{-1}, only the band assigned to bridging nitrates (1618 cm^{-1}, $\nu_s(NO_2)$ and 1218 cm^{-1}, $\nu_{as}(NO_2)$) was clearly observed. This decrease in NO_x adsorption could be attributed to high electronegativity of P species, which gives rise to a positive electrostatic potential outside the catalyst surface [39], resulting in a repulsive effect towards the NO_x molecules. Moreover, two bands corresponded to OH^- (3684 cm^{-1}) and P-OH bonds (3670 cm^{-1}) were observed (Figure IV-5). The perturbation of the –OH band can be ascribed to weak NO-interaction with the P-PtPd catalyst surface, probably through a hydrogen bond with the surface OH's [44]. Otherwise, as discussed in Chapter III, the high phosphorus concentration added to the reference catalyst resulted in a uniform layer throughout the catalyst [45]. This could explain the presence of these new bands, based on the interaction between the phosphorus and superficial OH on alumina support. Previous studies have shown direct evidence of phosphate-OH exchange by infrared spectroscopic characterization of the mineral surface [46]. Phosphate is specifically adsorbed on inorganic materials by a ligand-exchange mechanism with a reactive surface hydroxyl ion. Hingston et al. [47] proposed that the formation of the ligand is associated to the anion exchange

between phosphates and surface hydroxyls on the catalyst surface. These authors showed that protons released from dissociation of protonated anions such as phosphates could react with surface hydroxyls to form water molecules, which can be readily replaced by the phosphates anions.

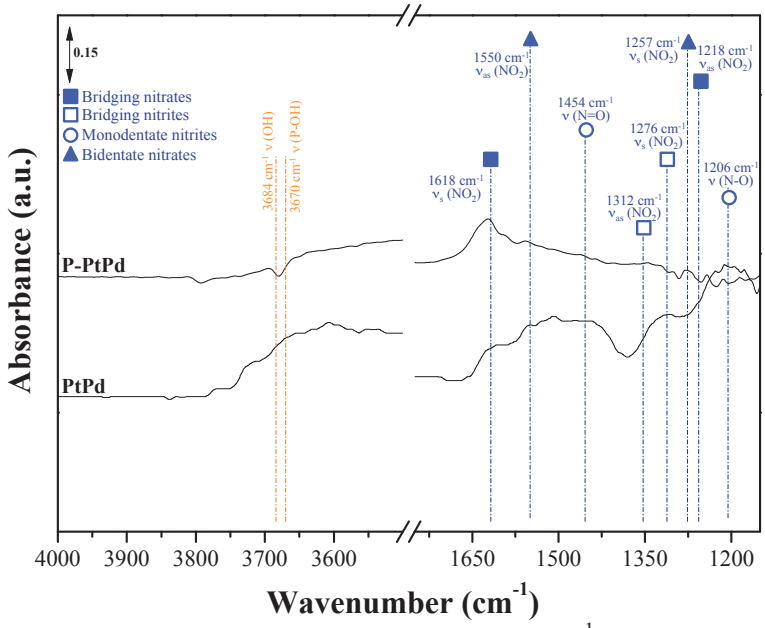

Figure IV-5. DRIFT spectra in the region 4000-1200 cm^{-1} of PtPd-reference and P-PtPd catalyst after NO surface saturation at 35 ºC.

b. NO thermal desorption spectroscopy (NO-TDS)

After NO adsorption until saturation at 35 °C, DRIFT spectra of adsorbed species present on the surface of PtPd reference and modified catalysts were recorded at different temperatures in the interval of 35-500 °C under He flow. According to NO-TPD experiments (see Chapter III), three sites of NO adsorption are mainly presented on PtPd-reference and modified catalysts at 50-150 ºC, 150-350 ºC and 350-600 ºC temperature regions. We assumed that the active sites depend on the different degrees of cerium oxidation states as well as the proximity to impurities present in the alumina phase (verified by EDX/TEM, see Chapter III).

Figure IV-6 shows DRIFT spectra recorded during NO-TPD under He flow, after adsorption of NO/He at 35 ºC on PtPd reference catalyst.

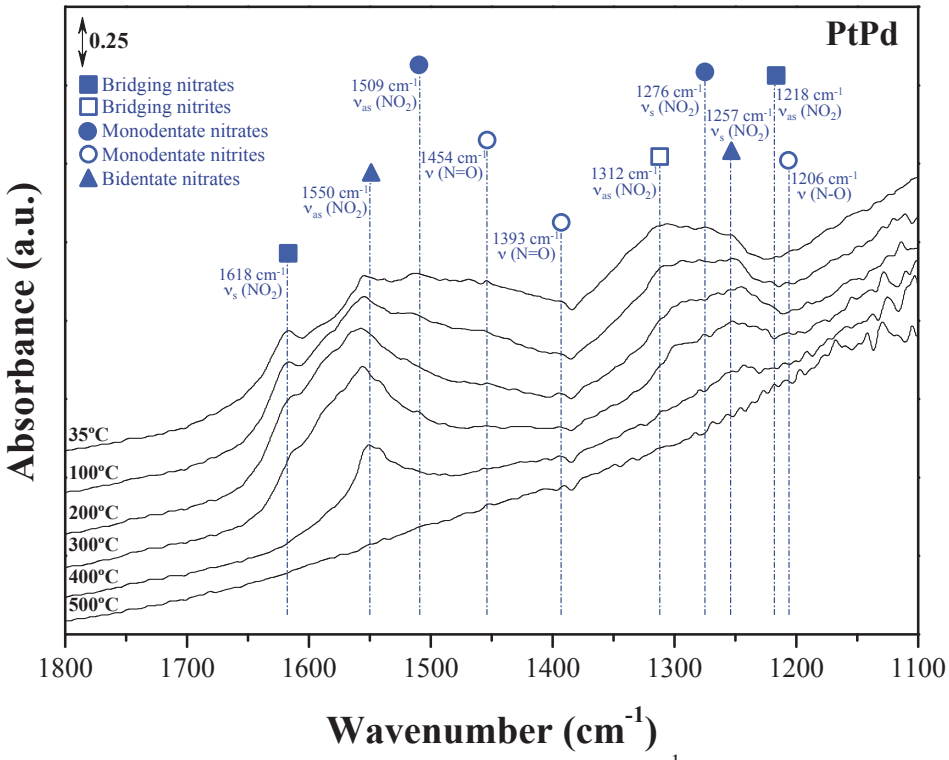

Figure IV-6. DRIFT spectra in the region 1800-1100 cm^{-1} of PtPd-reference catalyst during NO desorption at temperatures in the interval of 35-500°C. Operating conditions: 40 ml min^{-1} He; NO stored at 35 ºC until saturation and subsequently NO-TPD.

The principal bands assigned to surface NO-containing species such as nitrites and nitrates were identified. However, at 100 °C the weak band at 1454 cm^{-1} disappeared, which could be correlated to the first desorption peak of NO observed during NO-TPD (50-150 ºC region). Thus, the amount of NO desorbed measured in the gas phase probably comes from the partial decomposition of nitrites, as follows:

$$3OO_2^- \rightarrow OO_3^- + O^{2-} + 2OO \qquad \textit{Eq. IV-7}$$

As a consequence, only NO was observed in the gas phase (TPD) and an attenuation of nitrites with the simultaneous formation of nitrates bands is occurred. Increasing temperature until 200 ºC involves the disappearance of the band assigned to monodentate (1312 cm^{-1}) and bridging nitrites (1393 cm^{-1}), which could be associated to the transformation of nitrites into nitrates. Also, this temperature corresponded to the maximal temperature found on the second desorption peak during temperature programmed desorption experiments. No significant changes were achieved at elevated temperatures (300ºC), and no NO was detected in the gas phase.

It seems that nitrites are transformed to nitrates as temperature increased, according to reaction:

$$OO_2^- + O^{2-} \rightarrow OO_3^- + 2e^- \qquad \textit{Eq. IV-8}$$

Finally, the entire nitrate assigned bands started to disappear at 300ºC and any band was detected at 500 ºC. At high temperatures, nitrates decomposition to NO_2 was produced, but it was no detected in the gas phase, which can be explained by the thermodynamic equilibrium. Thus, NO_2 formed is immediately reduced, in the presence of ceria-zirconia, to NO:

$$2OO_{2(g)} + 2OO_{(g)} + O_{2(g)} \qquad \textit{Eq. IV-9}$$

Similarly to reference catalyst, the temperature dependence of the DRIFT spectra for Na-, K- and Ca-PtPd catalyst was recorded increasing temperature under He flow (Figures AII-2, AII-3 and AII-4 in Annexe II). Contrary to PtPd reference catalyst, in presence of Na, K and Ca impurities current bands still present until 300 ºC. Below this temperature, nitrites to nitrates transformation was evidenced by simultaneous decrease and increase of nitrite and nitrates bands intensities, respectively. However, the intensity of nitrates bands at 300 ºC was decreased and only nitrites bands still present at 400 °C. No adsorbed species were detected at 500 °C. These tendencies are in agreement with the higher desorption temperatures found by NO-TPD associated to the electronic effect of alkali impurities and high basicity of Ca (see section I-f, Chapter III).

Finally, P-PtPd spectrum (Figure AII-5) only presented a broad peak at 1622 cm^{-1} associated to bridging nitrates that disappeared at temperatures higher than 100 ºC, corresponding to the desorption temperature found by NO-TPD. However, at high temperatures the –OH band (3684 cm^{-1}) increased its intensity (negative peak) at the same time than the P-OH band (3670 cm^{-1}). As established above, adsorbed NO can weakly interact with the OH groups on the surface. Thus, NO desorption could leave –OH available that will interact with phosphorus species, increasing the P-OH band intensity.

II. Steady state in-situ DRIFTS experiments under simulated automotive exhaust conditions

The effect of impurities on catalytic activity in flow reactor was extensively evaluated in Chapter III. Nevertheless, the impurities influence on catalytic activity could be better understandable in terms of impurities effects on the adsorption of reactant species. For this purpose, in the present section, the nature and relative populations of adsorbed species formed on the surface of PtPd-reference and modified catalysts were investigated by in-situ DRIFTS measurements under simulated automotive exhaust conditions. Thus, catalysts were exposed firstly to a mixture of NO + CO + C_3H_6 + O_2 and, subsequently to a simplified mixtures (NO + O_2; NO + O_2 + CO; NO + O_2 + C_3H_6) in order to better ascribe the effect of each reactant on the catalyst surface. This study will be helpful to elucidate the adsorption reactants competition and to better understand the effect of impurities (Na, K, Ca and P), coming from the use of biodiesel or lubricants, in the formation of intermediates species on available catalyst sites.

a. Total exhaust gases reaction mixture (NO + CO + C_3H_6 + O_2)

Figure IV-7 depicts the IR spectra of adsorbed species on the surface of PtPd, Na-PtPd and K-PtPd catalysts exposure of NO + CO + C_3H_6 + O_2 mixture at 150 ºC and 250 ºC.

In order to facilitate the identification of the bands, symbols have been assigned to each species, as shown in Table IV-2.

Table IV-2. Symbol and wavenumber corresponding to identified species.

Symbol	Surface species	Peak position (cm^{-1})
◆	**HC fragments**	2965 (ν_s (CH)), 2908 (ν_{as} (CH))
◌	**Pt-NO**	1776, 1692 (ν (N-O))
■	**Bridging nitrates**	1622 (ν_s (NO_2)), 1218 (ν_{as} (NO_2))
●	**Monodentate nitrates**	1509 (ν_{as} (NO_2)), 1250 (ν_s (NO_2))
□	**Bridging nitrites**	1308 (ν_{as} (NO_2)), 1276 (ν_{as} (NO_2))
○	**Monodentate nitrites**	1465 (ν (N=O)), 1195 (ν (N-O))
△	**Acetates**	1555 (ν_{as} (COO^-)), 1460 (ν_s (COO^-))
◇	**Formates**	1585 (ν_{as} (COO^-)), 1407 (δ (CH)), 1373 (ν_s (COO^-))
▲	**Carbonates**	1645, 1650 (ν_{as} (COO^-)), 1350 (ν_s (COO^-))
★	**Pt-CO**	2120 (ν (CO))
☆	**Cyanides**	2155 (ν (CN)

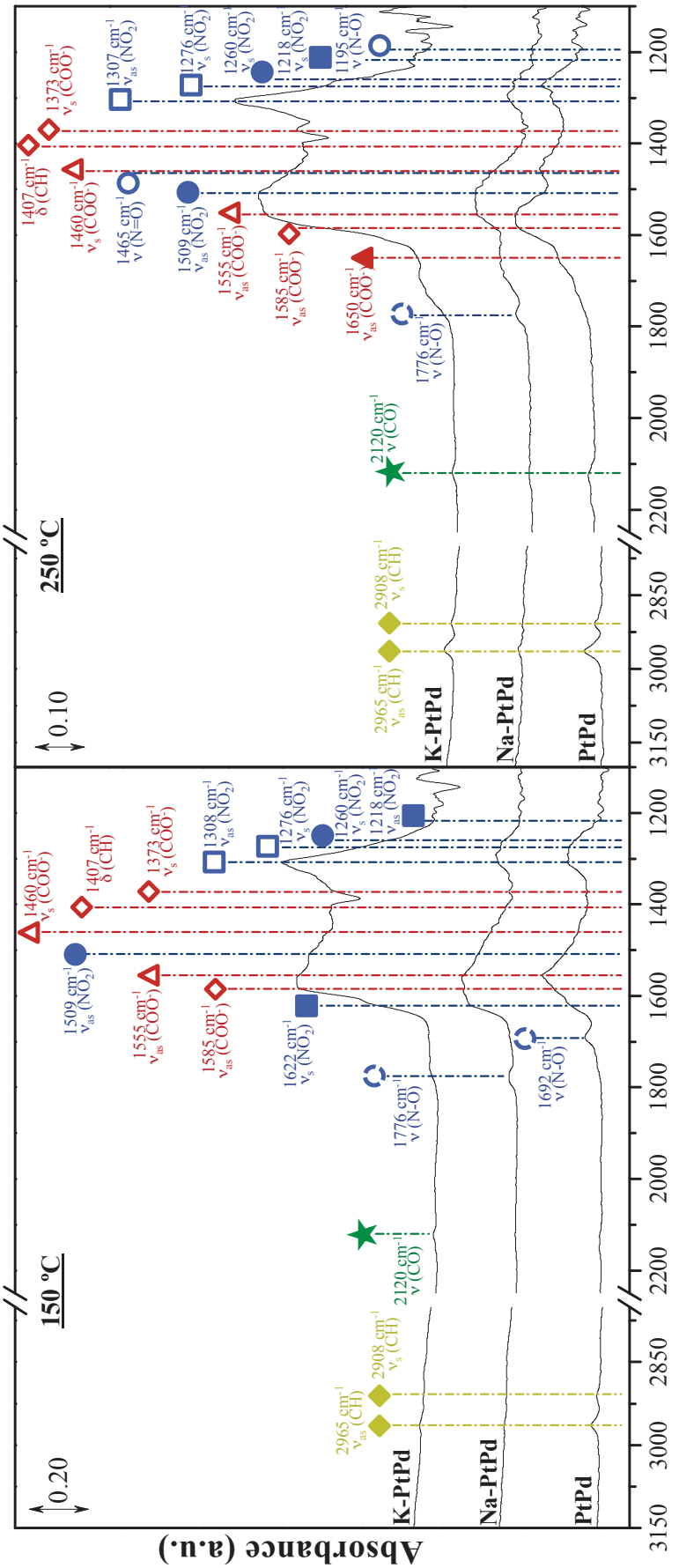

Figure IV-7. DRIFT spectra of PtPd reference, Na-PtPd and K-PtPd catalysts at 150 °C (left) and 250 °C (right) after 60 min under simulated exhaust conditions. FT-IR chamber feed: 500 ppm NO, 300 ppm CO, 300 ppm C_3H_6, 10% O_2, He as balance; 40 ml min^{-1}.

See correspondence between symbols and species in Table IV-2.

The features attributed to nitroxy species (empty dashed circle, full and empty squares, full and empty circles in blue) and to carbonate and/or carboxylate species (empty diamond, empty and full triangles in red) were observed for all catalysts. In addition, the 2300-1800 cm^{-1} region (empty and full stars in green) was assigned to the adsorbed species on Pt sites [7,12] and/or to the adsorbed species for which its formation require the existence of both active metal and support material (i.e. the species that are initially formed on metal active sites and then migrated to the support) [21,48]. Finally, the last observed bands (diamond in yellow) are ascribed to adsorbed HC fragments from propene or from alkyl groups associated with carboxylate species [15,16,27].

At 150 ºC similar adsorption bands were observed on reference and Na, K-modified catalysts, however the intensity of bridging nitrates assigned bands at 1622 cm^{-1} were more pronounced on alkali containing catalysts. Moreover, the presence of Na or K impurities resulted in an additional band at 1776 cm^{-1}, which is attributed to N-O stretch of linear or bent molecular NO species adsorbed on Pt sites [5]. As already discussed, the effect of electrostatic field of alkali impurities promoted NO dissociation (Eqs. IV-5 and IV-6). In addition, more intense bands at 1585, 1407 and 1373 cm^{-1} assigned to formates on Al_2O_3 [15–17,19] ($\nu_s(COO^-)$, $\delta(CH)$ and $\nu_{as}(COO^-)$, respectively) and at 1555 and 1460 cm^{-1}, corresponding to acetates on Al_2O_3 [15–17,20] ($\nu_{as}(COO^-)$ and $\nu_s(COO^-)$ stretches, respectively) were found on K-PtPd catalyst. The appearance of these carboxylate species on K-PtPd catalyst at low temperature, which are considered the reaction intermediates in propene oxidation [16,17], seems to indicate that the propene activation via adsorbed oxygen is promoted by alkali impurities. This result is in agreement with the activity results, which showed higher C_3H_6 reaction rate on PtPd-modified catalysts than on PtPd-reference catalyst (section II-c, Chapter III). In the case of K-modified catalyst, another additional band at 2120 cm^{-1} was also found comparing to the reference catalyst, which could be ascribed to relatively unreactive CO species adsorbed on partially positively charged Pt sites ($Pt^{\delta+}$) [24]. The appearance of this band indicates that under the prevailing conditions the Pt component is mainly in its oxidized form, as previously shown by XPS measurements (section I-d, Chapter III). Otherwise, the absence of terminal and bridged CO species, which are the active species for the CO oxidation, on the catalysts surface could indicate that at 150 ºC the reaction between

CO and oxygen was already started [24]. This is in good agreement with the catalytic activity results obtained in flow reactor, in which the total oxidation of CO complete was reached at temperatures ranging from 150 ºC to 200 ºC.

At 250 ºC (Figure IV-7, right), a significant attenuation of nitrate bands at 1622 cm^{-1} was observed, reflecting the reactivity of the nitro/nitrite species. A weak band at 1650 cm^{-1} associated with carbonates species ($\nu_{as}(COO^-)$; 1350 cm^{-1}, $\nu_s(COO^-$ [1]) appeared when the temperature was increased, due to the CO_2 adsorption produced during CO and C_3H_6 co-oxidations. The weak band at 2120 cm^{-1} assigned to unreactive CO species progressively appeared for the three catalysts, which indicates the consumption of CO active intermediates. So, only the species that are non-involved in CO oxidation reaction still presented. At elevated temperature, the band assigned to monodentate nitrites at 1509 cm^{-1}, $\nu_{as}(NO_2)$, was increased on alkali-modified catalysts. An additional band at 1465 cm^{-1} appeared in PtPd-reference spectrum, which can be attributed to the formation of linear nitrites [21,25] resulting from the reduction of nitrates ad-species by C_3H_6 or the oxidation of C_3H_6, respectively. The nitrate bands were attenuated at the same time that band at 1465 cm^{-1} appeared, which evidence the formation of these new species. Thus, we can associate this band to linear nitrites and suppose that it is overlapping to the band assigned to acetates (1460 cm^{-1}, [49]). Otherwise, the increase of carboxylate bands intensity with temperature is consistent with the higher intensity of C-H corresponding bands in the region of 2900 - 3000 cm^{-1} (at 2965, $\nu_{as}(CH)$, and 2908 cm^{-1}, $\nu_s(CH)$). So, carboxylate bands principally remained at this temperature, indicating that propene replaced almost all nitrate species [27,49], i.e. that the reactions involving C_3H_6 became more significant at 250 °C.

Similar tendencies in nature and relative populations of adsorbed species formed on Ca-PtPd and P-PtPd modified catalysts were found under the identical exhaust conditions, Figure IV-8 and IV-9. However, only in the case of Ca-PtPd modified catalyst, the band assigned to cyanide species (bridged species intermediates) on Al^{3+} sites (2155 cm^{-1}) [50] was observed, which means that the oxidation of isocyanide species was faster on reference and Na, K and P-modified catalysts surface. Otherwise, the addition of Ca increased the basicity of the support, inducing the adsorption of CO_2 coming from the oxidation of CO and C_3H_6 oxidations. This is evidenced by the presence of carbonates (1645 cm^{-1}, $\nu_{as}(COO^-)$ and

1350 cm^{-1}, $\nu_s(COO^-)$) on Ca-PtPd spectra. The weak intensities found on P-PtPd catalyst was associated to the blocking of adsorption sites by phosphates formation.

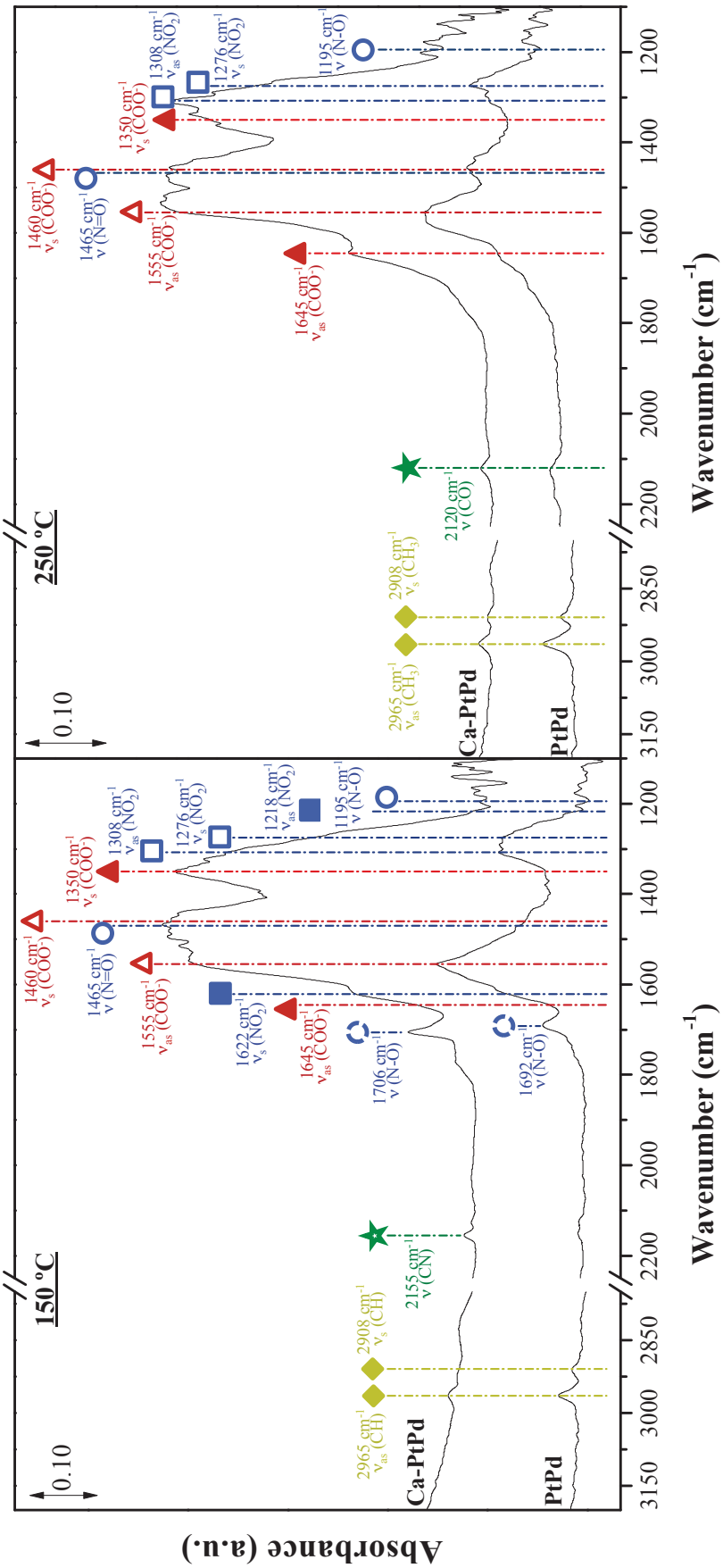

Figure IV-8. DRIFT spectra of PtPd reference and Ca-PtPd catalysts at 150 °C (left) and 250 °C (right) after 60 min under simulated exhaust conditions. FT-IR chamber feed: 500 ppm NO, 300 ppm CO, 300 ppm C_3H_6, 10% O_2, He as balance; 40 ml min^{-1}.

See correspondence between symbols and species in Table IV-2.

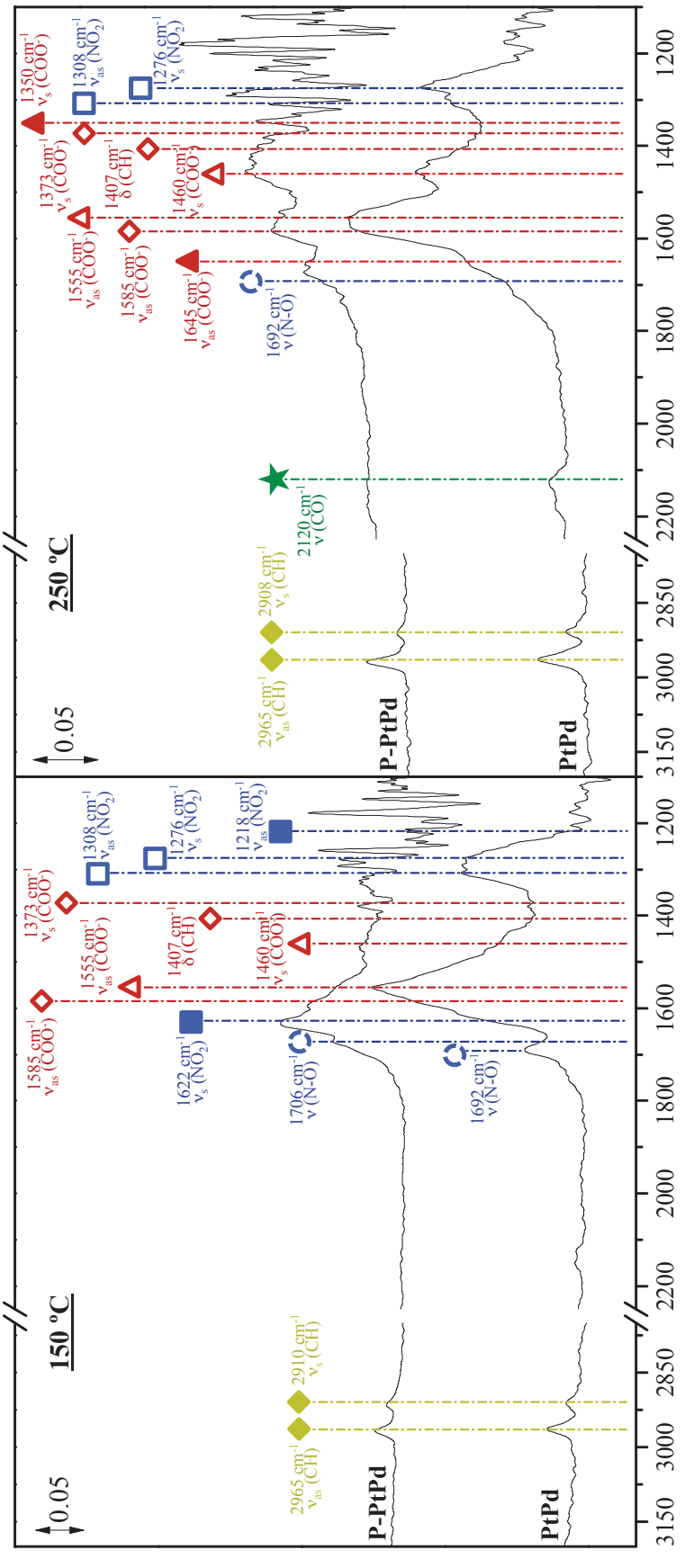

Figure IV-9. DRIFT spectra of PtPd reference and P-PtPd catalysts at 150 °C (left) and 250 °C (right) after 60 min under simulated exhaust conditions. FT-IR chamber feed: 500 ppm NO, 300 ppm CO, 300 ppm C_3H_6, 10% O_2, He as balance; 40 ml min^{-1}.

See correspondence between symbols and species in Table IV-2.

These DRIFTS studies evidenced the formation of species involving both NO, C_3H_6 and CO such as nitroxy and carboxylate species. However, it was difficult to discriminate the influence of impurities in NO, CO and C_3H_6 adsorption competition and to realize the involved reaction intermediates. Therefore, additional DRIFTS measurements using a sequential approach, with different reactive mixtures such as NO + O_2, NO + CO + O_2 and NO + C_3H_6 + O_2, were conducted in order to better correlate the catalytic results and the adsorption of reactant species as a function of studied impurity.

b. Simplified gas mixture (NO + O_2, NO + CO + O_2 and NO + C_3H_6 + O_2)

The reference and modified catalysts were firstly exposed to NO + O_2 gas mixture. The IR adsorption spectra, the principal bands observed and the corresponding assignment are summarized in Figures IV-10, 11 and 12 and in Table IV-1.

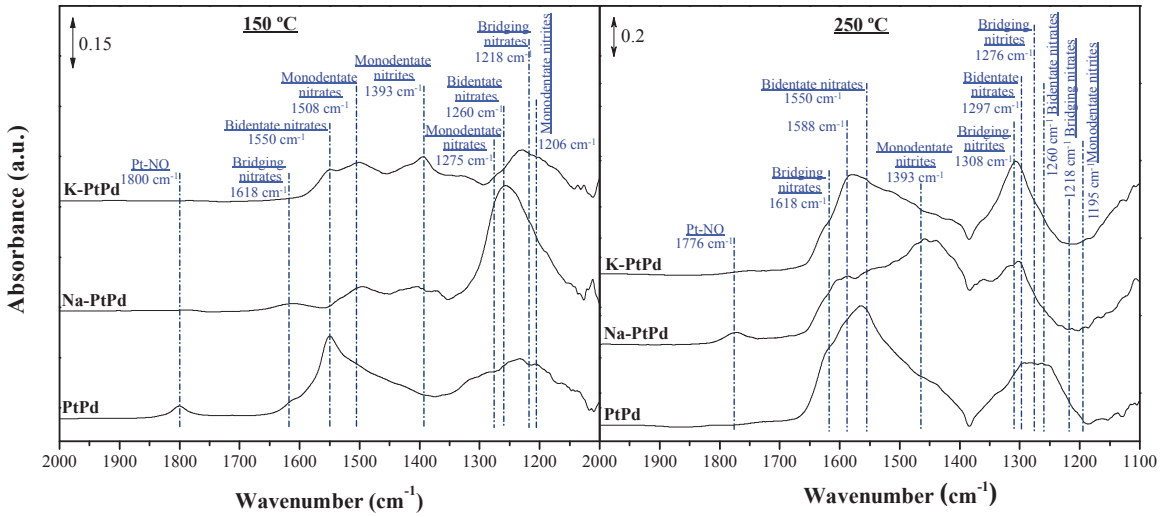

Figure IV-10. DRIFT spectra of PtPd-reference and Na- and K-PtPd catalysts at 150ºC (left) and 250ºC (right) after 60 min under simulated exhaust conditions. FT-IR chamber feed: 500 ppm NO, 10% O_2, He as balance; 40 ml min^{-1}.

Bands appearing in the 1650-1200 cm^{-1} region may be assigned to nitrite/nitrate species on the support (see NO adsorption, [4,6,7,9–11]). At 150 ºC, several bands at 1618, 1550 and 1508 cm^{-1} assigned to nitrates adsorbed species (bridging, bidentate and monodentate) and a band at 1393 cm^{-1} corresponding to monodentate nitrite, were detected. It is worth noting the appearance of a band at

1800 cm^{-1} in the case of the reference catalyst, which could be associated with the interaction between NO and Pt sites. Increasing the temperature until 250 ºC, new bands at 1588 and 1308 cm^{-1} assigned to bidentate nitrates and bridging nitrite, respectively were appeared [4,6,7,9–11]. The band at 1800 cm^{-1} on the reference catalyst disappeared, while a band at 1776 cm^{-1} was only observed in the case of Na-PtPd catalyst, which is assigned to N-O stretch of NO species adsorbed on Pt oxidized sites [5]. Moreover, the bands at 1618 and 1550 cm^{-1}, assigned to bridging and bidentate nitrates adsorbed on the support, still presented at 250 °C[5,6,9].

Thus, the amount of nitrates adsorbed species increases in presence of oxygen (NO and O_2 in the gas mixture), which could be attributed to NO_2 formation via NO oxidation on Pt active sites at temperatures above 150 ºC, as has been demonstrated in the literature [4]. This means that the NO oxidation is a key step for the storage of nitrate species, which is in good agreement with the obtained results. NO adsorbed species at 150 ºC were detected on metal sites (band at 1800 cm^{-1}), however after increasing temperature, these species are oxidized to nitrates and then migrate and adsorb on the support. Moreover, the presence of surface nitrites seems to play an important role as an initial step in the adsorption and subsequent storage processes. The increasing concentration of nitrates species with increasing time exposure (Figure AII-6) could result from an oxidation of nitrites by the gas phase. Thus, the sorption process started with nitrites adsorption via dissociative adsorption of NO, which were subsequently oxidized by gas phase or adjacent adsorbed oxygen. Finally, after extended exposure, nitrates were the main adsorbed species.

In presence of alkali impurities, the bands presented higher intensity (Figure IV-10) related to the enhanced NO dissociation due to the electronic effects produced by Na and K impurities. Although at 150 ºC alkali-modified catalysts did not present any adsorption on metal active sites, at 250 ºC the interaction between Pt and NO was evidenced for the Na-PtPd catalyst. At low temperature, the promoted dissociation could be eventually poisoning the catalyst surface by oxygen adsorption. Increasing the temperature, the dipole-dipole coupling between NO chemisorbed molecules would decrease with decreasing coverage. In addition, the electron donating effect of alkali impurities would decrease the N-O bond order, thus shifting the Pt-NO wavenumber towards lower values.

Figure IV-11, presents the results obtained after exposition of Ca-PtPd catalyst to NO + O_2, in comparison with reference catalyst spectrum.

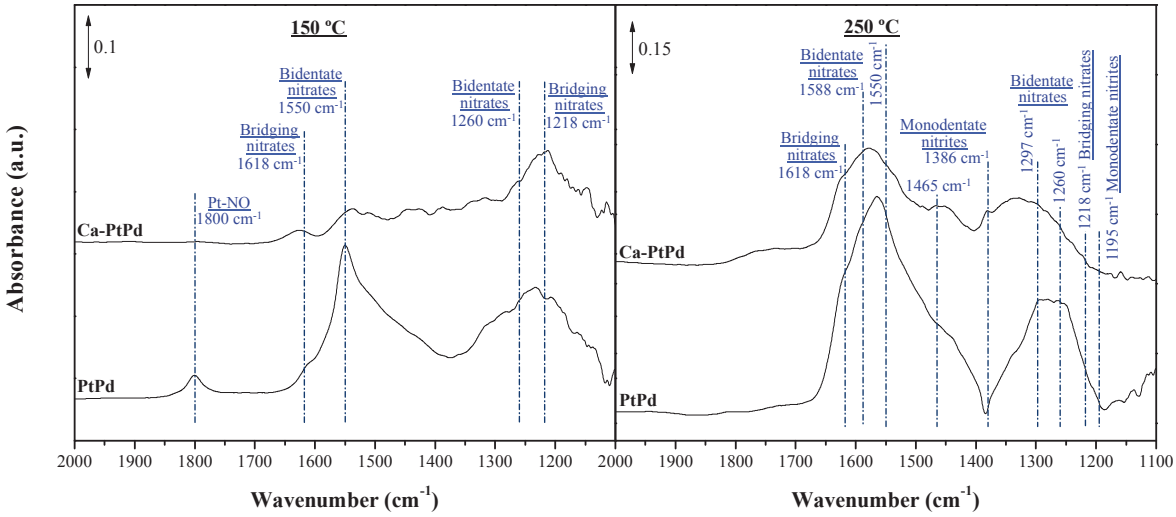

Figure IV-11. DRIFT spectra of PtPd-reference and Ca-PtPd catalysts at 150ºC (left) and 250ºC (right) after 60 min under simulated exhaust conditions. FT-IR chamber feed: 500 ppm NO, 10% O_2, He as balance; 40 ml min^{-1}.

After exposure at 150 ºC (Figure IV-11, left), Ca-PtPd presented associated with bridging nitrates (1618, 1218 cm^{-1}) and bidentate nitrates (1550, 1260 cm^{-1}). When increasing the temperature until 250 ºC, bands corresponding to bidentate nitrates (1550 cm^{-1}) and monodentate nitrites (1465 and 1386 cm^{-1}) appeared also on the Ca-PtPd spectrum. Previous characterization results (see XPS, section I-d, Chapter III) proved that Ca impurities were in form of carbonates. Thus, at 150 ºC, almost no adsorption was produced as the surface was saturated with carbonates. Increasing the temperature, carbonates could be oxidized by adsorbed oxygen and/or lattice oxygen coming from the oxidized support, allowing the adsorption of nitrates species, which will be stored on the basic sites proportionated by the Ca impurities.

Finally, in the case of P-PtPd catalyst (Figure AII-7), nitrite/nitrate species were observed at both temperatures, but no significant changes were noticed. That could be ascribed to the phosphates formed on the catalyst surface, which blocked the adsorption sites.

Once nitrates/nitrites were identified, the competition between NO and CO species was also evaluated. Figure IV-12 shows spectra of PtPd, Na-PtPd and K-PtPd catalysts after treatment in NO + CO + O_2 flow at 150 ºC (left) and 250 ºC (right).

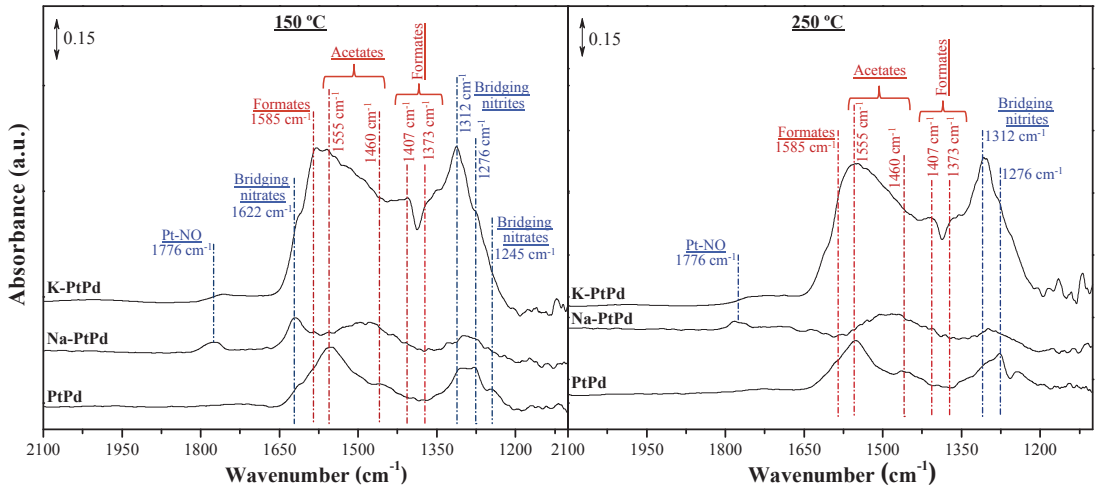

Figure IV-12. DRIFT spectra of PtPd-reference and Na- and K-PtPd catalysts at 150ºC (left) and 250ºC (right) after 60 min under simulated exhaust conditions. FT-IR chamber feed: 300 ppm CO, 500 ppm NO, 10% O_2, He as balance; 40 ml min^{-1}.

When CO was present in the mixture, bands corresponding to acetates (1555 and 1460 cm^{-1}) and formates (1585, 1407 and 1373 cm^{-1}) appeared at 150 ºC. Nitrites (1312 and 1276 cm^{-1}) and nitrates (1622 and 1245 cm^{-1}) bands also depicted in the obtained spectra. In addition, the interaction between NO and the metallic phase was evidenced at 1776 cm^{-1} in the case of Na-PtPd catalyst. At 250 ºC, nitrates species were totally replaced on PtPd catalyst surface, while some nitrates/nitrites species were still present on Na and K-PtPd catalyst along with formates and acetates.

The higher intensity of bands observed in presence of Na and K impurities can be related to the enhanced adsorption due to their electronic effect. Lang et al. [39] established that the electron transfer between an adsorbing molecule and a metal atom is a consequence of a competition between an electron donation from the occupied molecular orbitals and the electron acceptor function of the initially unoccupied, antibonding molecular orbitals. Thus, the inhomogeneous electric field associated with alkali ions (such as Na and K), decreases the energy of the antibonding π^* orbital of electron-accepting co-adsorbates (CO, NO) below the metal Fermi level [51]. Thereby, the charge transfer from metal to adsorbate acts to weaken the C-O and N-O bond, enhancing its adsorption and consequent dissociation.

$$OO(ads) \rightarrow O(ads) + O(ads) \qquad \textit{Eq. IV-10}$$

$$CO(ads) \rightarrow C(ads) + O(ads) \qquad \textit{Eq. IV-11}$$

The promoted adsorption/dissociation is in agreement with the increase of relative populations of NO and CO adsorbed intermediates in presence of alkali ions, being superior in the case of K-containing catalyst, which means that the influence of alkali cations is depending of different factors:

i. On the one hand, the higher amount of Na (6.99 mol %) than K (1.28 mol %) incorporated to the catalyst could partially cover the adsorption sites [52]. Otherwise, it has to take account the amount of alkali that is in direct contact with the metal. Besides the higher Na loading, it could be accumulated on the support and do not play an important role on the promotional phenomena [53].

ii. On the other hand, the impurity effect is strongly influenced by the atomic weight of alkali metal ions. The heavier alkalis (K) are somewhat more effective than the lighter alkalis (Na) (Figure IV-13). Lang et al. [39] observed that the electrostatic potential depth increases with the atomic number of alkalis. It means that even in the case of similar amount of charge transferred from alkalis ions to the metal, the large valence shell of the heavier ions would increase the transferred charge. Therefore, the greater electric field produced by the heavier K cations, would favour the co-adsorption/dissociation of NO and CO molecules, according to the higher intensity peaks of NO and CO intermediates species on K-containing catalyst.

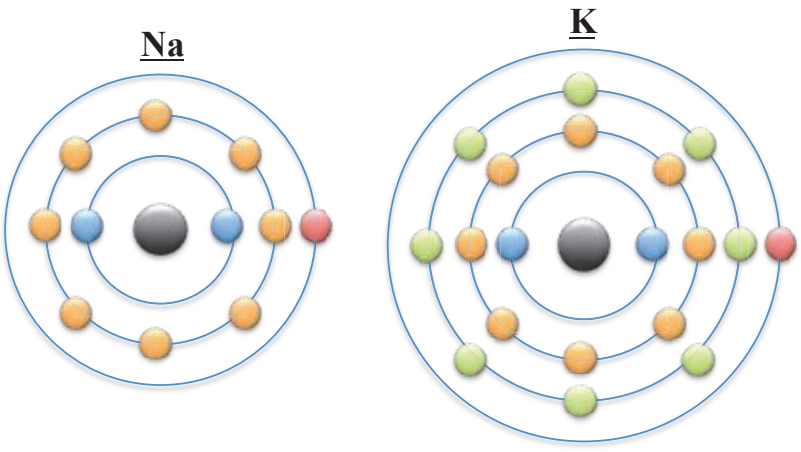

Figure IV-13. Electron configuration of sodium and potassium.

Similarly, Figure IV-14 shows spectra of PtPd and Ca-PtPd catalysts after treatment in NO + CO + O_2 flow at 150 ºC (left) and 250 ºC (right).

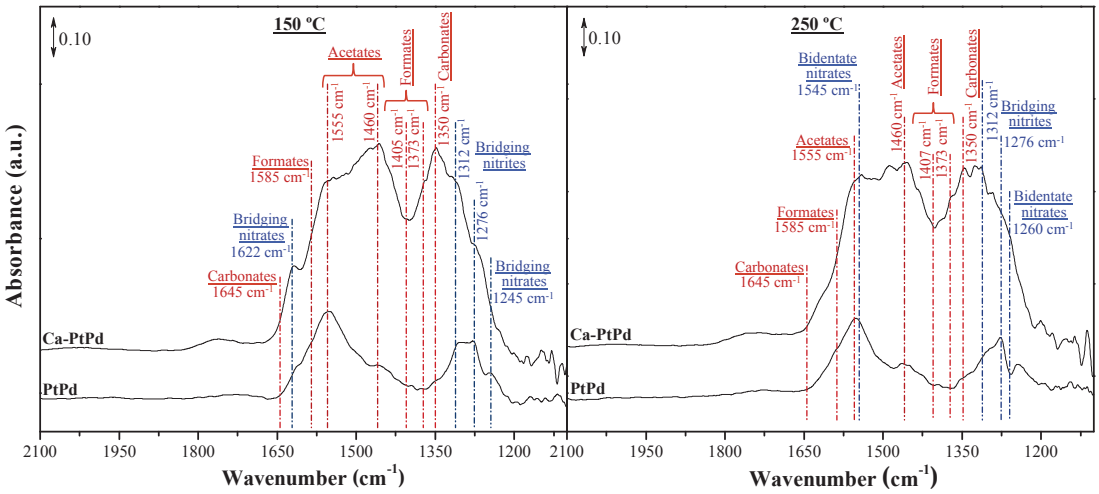

Figure IV-14. DRIFT spectra of PtPd-reference and Ca-PtPd catalysts at 150ºC (left) and 250ºC (right) after 60 min under simulated exhaust conditions. FT-IR chamber feed: 300 ppm CO, 500 ppm NO, 10% O_2, He as balance; 40 ml min^{-1}.

In presence of calcium impurities, bridging nitrites (1312 and 1276 cm^{-1}) and bridging nitrates (1622 and 1245 cm^{-1}) bands were observed at 150 ºC. Moreover, acetates (1555 and 1460 cm^{-1}) and formates (1585, 1407, 1373 cm^{-1}) were also depicted on Ca-PtPd spectrum at 150 ºC. Increasing the temperature until 250 ºC, acetates bands intensity increased, whereas nitrate band at 1622 cm^{-1} disappeared. In addition, new bands related with carbonates at 1645 and 1350 cm^{-1} appeared at both temperatures.

As previously discussed, Ca impurities increased the basicity of the catalyst. Hattori et al. [54] studied alkaline-earth metals basicity by CO_2-TPD and concluded that CaO possessed the higher number of basic sites per unit weight that can retain carbon dioxide under their adsorption conditions. This is in agreement with the appearance of carbonates bands, which are related with CO_2 adsorption coming from CO oxidation. Moreover, the high basicity of calcium impurities provides the catalyst of larger NO adsorption, according to the NO-TPD previous results (section I-f, Chapter III), in which Ca-PtPd catalyst showed the highest amount of desorbed NO. However, it seems that the new basic adsorption sites would be further from the metal particles, as evidenced by the presence of nitrites that were not oxidized to nitrates at high temperature.

Figure IV-15 presents a comparison between PtPd and P-PtPd spectra obtained after exposition to NO + CO + O_2 flow at 150 ºC (left) and 250 ºC (right).

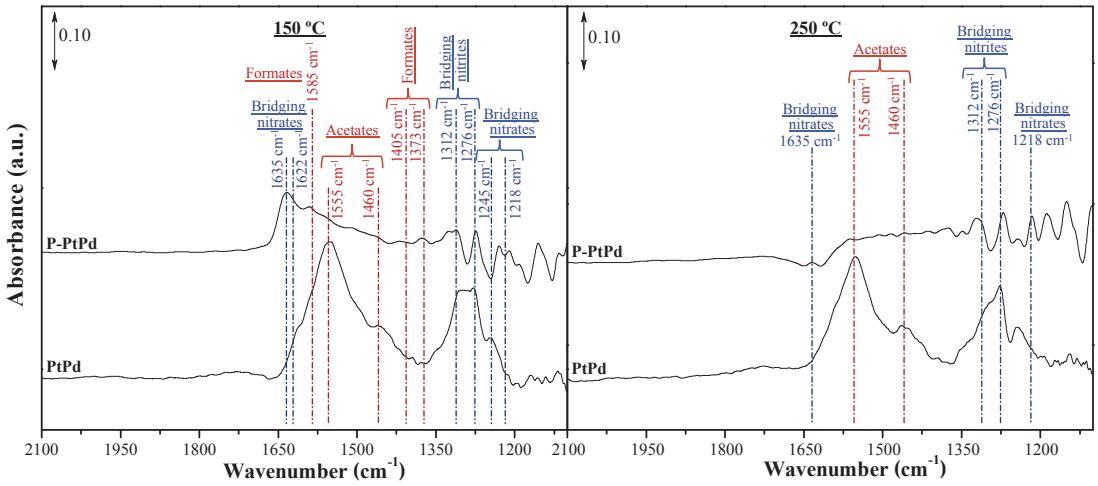

Figure IV-15. DRIFT spectra of PtPd-reference and P-PtPd catalysts at 150ºC (left) and 250ºC (right) after 60 min under simulated exhaust conditions. FT-IR chamber feed: 300 ppm CO, 500 ppm NO, 10% O_2, He as balance; 40 ml min^{-1}.

At 150 ºC nitrates (1635 cm^{-1}) and a broad peak corresponding to formates (1585 cm^{-1}) were evidenced on the P-PtPd catalyst. Increasing the temperature until 250 ºC, almost no adsorbed species were detected on the modified-catalyst surface. These effects can be ascribed to two factors: (i) the high amount of impurity that produced the formation of phosphates that would block the adsorption sites (see section I, Chapter III); and (ii) the positive electrostatic potential around phosphorus impurities due to its high electronegativity, which produces repulsive interaction with NO and CO co-adsorbates. The inhibition of CO adsorption is in agreement with the higher CO reaction rate obtained, as it would inhibit the CO self-poisoning effect on the catalyst surface.

Experiments feeding C_3H_6 instead of CO are also performed. Figure IV-16 presents spectra of PtPd, Na-PtPd and K-PtPd catalysts after treatment in NO + C_3H_6 + O_2 flow at 150 ºC (left) and 250 ºC (right).

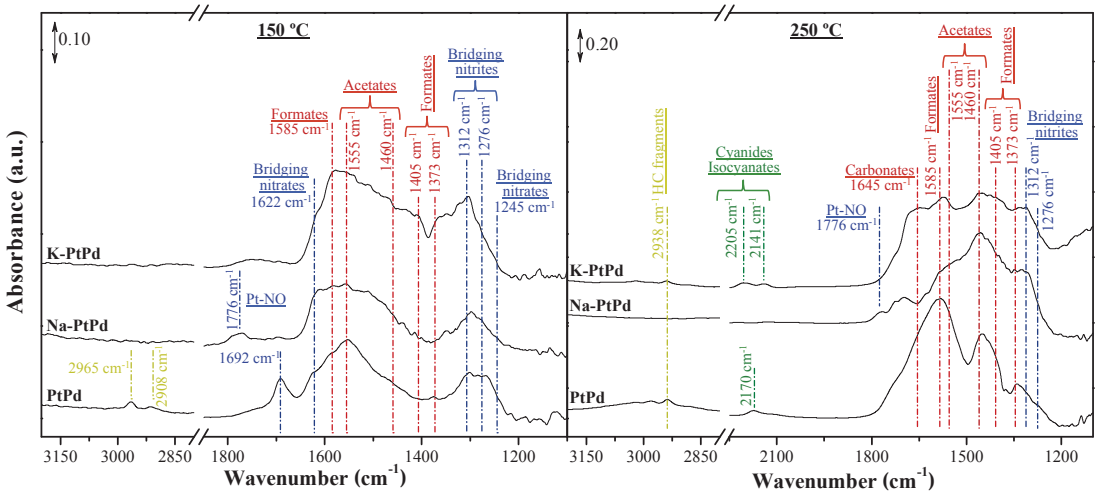

Figure IV-16. DRIFT spectra of PtPd-reference and Na- and K-PtPd catalysts at 150ºC (left) and 250ºC (right) after 60 min under simulated exhaust conditions. FT-IR chamber feed: 300 ppm C_3H_6, 500 ppm NO, 10% O_2, He as balance; 40 ml min^{-1}.

At 150 ºC nitrites (1312 and 1276 cm^{-1}), nitrates (1692, 1622 and 1245 cm^{-1}), acetates (1555 and 1460 cm^{-1}) and formates (1585, 1407 and 1373 cm^{-1}) bands were observed. The lower nitrate formation observed in the spectra can be ascribed to the relatively high concentration of C_3H_6 (300 ppm), based on stoichiometry, compared to NOx (500 ppm) in the feed [49]. In addition, bands corresponding to HC fragments due to C_3H_6 adsorption were presented for PtPd catalyst in the 3000 - 2900 cm^{-1} region. The enhanced NO adsorption on Na and K-PtPd surface catalysts was evidenced by the higher intensity of 1622 cm^{-1} band and the appearance of a new peak at 1776 cm^{-1}, which correspond to the adsorption of NO on the metal phase. At higher temperature (250 ºC), two mainly peaks were observed for reference catalyst spectrum: one at 1585 cm^{-1} corresponding to formate species with contribution of nitrate species (1692 cm^{-1}), and a second one at 1460 cm^{-1}, attributed to acetate species, overlapped with formate species at 1405 and 1373 cm^{-1}. Moreover, nitrite species could contribute to the band at 1460 cm^{-1}, especially in the case of alkali-modified catalysts, in which more intense broad peaks were detected. The appearance of the band at 1460 cm^{-1} at the same time that nitrate band (1697 cm^{-1}) intensity diminished, can be associated to the reduction of nitrate to nitrite (1465 cm^{-1}) by C_3H_6 when temperature increased. Isocyanates (2170 and 2205 cm^{-1}) and cyanide species (2141 cm^{-1}) were also observed on the reference and K-PtPd catalyst spectra. Although similar behaviour was observed for the alkali-modified and reference catalysts, some nitrate species still adsorbed on the former. This effect was less

marked for Na than K-PtPd, which could be ascribed to the larger shell of K ions, increasing its electronic effect and enhancing NO adsorption. Therefore, the strengthening of the metal-NO bond in presence of alkali impurities increases the coverage of surface catalysts by NO molecules. Otherwise, the repulsion effect between electropositive impurities and propene (electron-donor) decreases the competitive adsorption of the reactants. In addition, the adsorbed oxygen on the surface would be also enhanced due to the alkali-promoted NO dissociation. Thus, the higher amount of oxygen available on the catalyst surface could explain the higher propylene reaction rate values obtained for K-PtPd and Na-PtPd catalysts (section II-c, Chapter III).

$$OO(ads) \rightarrow O(ads) + O(ads) \qquad \textit{Eq. IV-6}$$

$$O(ads) + HC\ (ads) \rightarrow CO_2(g) + H_2O(g) \qquad \textit{Eq. IV-8}$$

Besides, isocyanates species are known to be intermediate species in the NOx reduction by propylene [17,50]. The contribution of nitrite bands at 1465 cm^{-1} (not marked) to acetate bands at 1460 cm^{-1}proved the reduction of nitrates by propylene [49]. Thus, the presence of surface isocyanates is in agreement with the NO-N_2O conversion results found in previous catalytic results (see section II, Chapter III).

Figure IV-17 depicts the obtained PtPd and Ca-PtPd catalysts spectra after treatment in NO + C_3H_6 + O_2 flow at 150 ºC (left) and 250 ºC (right). Ca-PtPd catalyst presented higher amount of nitrates (1700, 1692, 1622 and 1245 cm^{-1}) and nitrites (1312 and 1276 cm^{-1}), as well as higher adsorption of acetates/formates species than reference catalyst. When temperature increased until 250 ºC, only carbonates at 1645 cm^{-1} were presented, with acetates (1585 cm^{-1}) and nitrates (1622cm^{-1}) band contribution. The significant increase of carbonaceous intensity bands can be attributed to the high basicity of calcium, which provides the catalyst larger adsorption sites, promoting CO_2 adsorption. The band at 1622 cm^{-1} (not marked) could be attributed to stored nitrates further away from the active metal sites, which will act like spectators and are not involved in the reaction pathway [55].

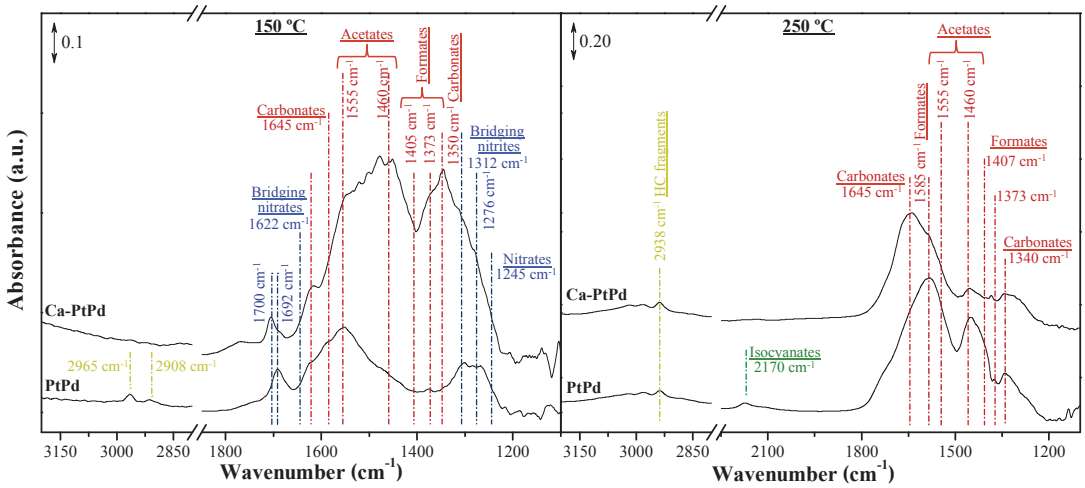

Figure IV-17. DRIFT spectra of PtPd-reference and Ca-PtPd catalysts at 150ºC (left) and 250ºC (right) after 60 min under simulated exhaust conditions. FT-IR chamber feed: 300 ppm C_3H_6, 500 ppm NO, 10% O_2, He as balance; 40 ml min^{-1}.

Finally, Figure IV-18 shows the spectra of PtPd and P-PtPd catalysts after treatment in NO + C_3H_6 + O_2 flow at 150 ºC (left) and 250 ºC (right).

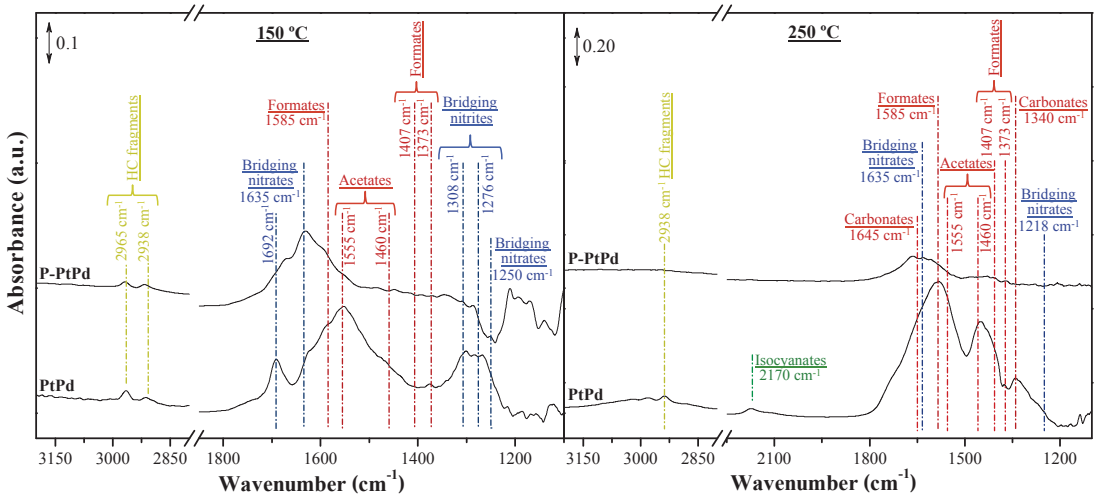

Figure IV-18. DRIFT spectra of PtPd-reference and P-PtPd catalysts at 150ºC (left) and 250ºC (right) after 60 min under simulated exhaust conditions. FT-IR chamber feed: 300 ppm C_3H_6, 500 ppm NO, 10% O_2, He as balance; 40 ml min^{-1}.

Similarly, in presence of phosphorus impurities, the adsorption is disfavoured. Only nitrates species bands were significantly presented at both temperatures.

III. Reaction between adsorbed surface species and the gas phase

The adsorbed species formed on catalyst surface of reference and modified-catalysts as a function of gas reaction mixture was evaluated in previous sections. It has been evidenced the adsorption competition between the different reactants and mainly explained the C_3H_6 and CO oxidation activities obtained in a flux gas reactor. In addition, it has been shown that the impurities could modify the adsorption pathways of the different species.

Previous studies [49] have demonstrated that NO adsorbed species (nitrites/nitrates) can act as oxidants, which could significantly modify the C_3H_6 and CO oxidation activities. Therefore, in order to elucidate the role of surface nitroxy species in C_3H_6 and CO oxidation reactions, reference and modified-catalysts were exposed to different sequences of NO_x and C_3H_6/CO.

Figure IV-19 shows spectra obtained with the reference catalyst after treatment in NO/He flow at 250 ºC for 120 min, followed by switching to C_3H_6 flow at the same temperature.

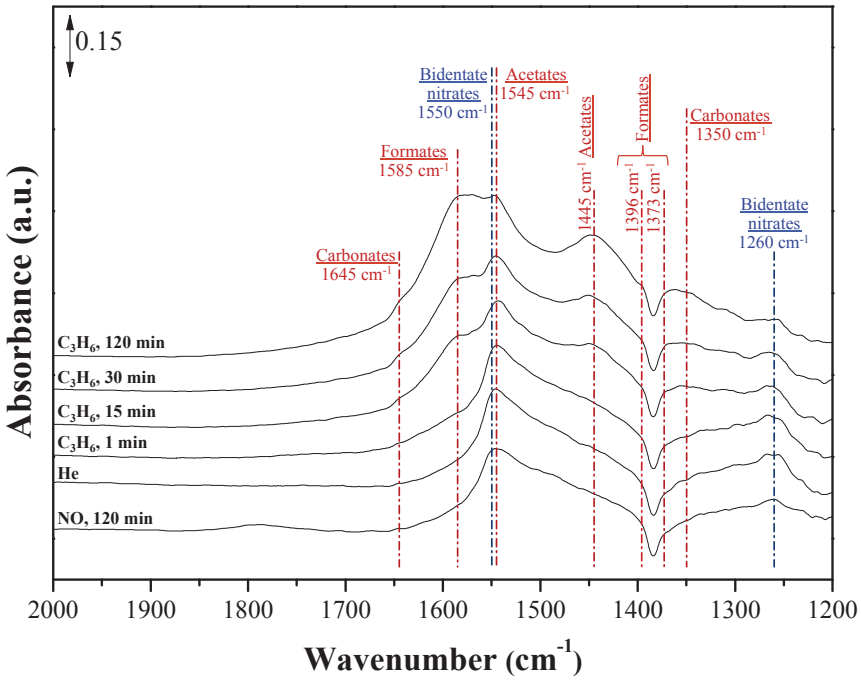

Figure IV-19. DRIFT spectra of PtPd-reference at 250ºC under NO/He/C_3H_6 after 120 min. FT-IR chamber feed: 500 ppm NO, He as balance; He purge; 300 ppm C_3H_6, He as balance; total flow 40 ml min^{-1}.

First, it is evidenced that catalyst surface exposed to NO gas feed results in the formation of significant amounts of bidentate nitrates species (1550 cm^{-1}, $\nu_{as}(NO_2)$ and 1260 cm^{-1}, $\nu_s(NO_2)$), which still present after C_3H_6 exposure. Switching to C_3H_6, several bands assigned to formates and acetates were appeared at 1585 ($\nu_{as}(COO^-)$), 1396 ($\delta(CH)$), 1373 cm^{-1} ($\nu_s(COO^-)$) and at 1545 ($\nu_{as}(COO^-)$) and 1445 cm^{-1} ($\nu_s(COO^-)$), respectively. A band at 1545 cm^{-1} associated to acetate species that overlapped with previously detected bidentate nitrate bands could be also identified as well as a broad peak found at 1645 cm^{-1}, which was associated with carbonates ($\nu_{as}(COO^-)$). The intensity of the new bands increased with C_3H_6 expose time until saturation, whereas the intensity of bands associated to NO_x surface species still unchanged, demonstrating that nitrate adsorbed species were stable at 250 ºC. The presence of nitrate adsorbed species after C_3H_6 exposition could indicate that they are not involved in propylene oxidation reaction. Moreover, the formation of these intermediates species without oxygen in the mixture feed could indicate that the catalyst provide the oxygen needed to NO and propylene oxidations. Note that an oxidation step during the catalyst pre-treatment was carried out, so based on previous characterizations (see section I, Chapter III), it can be assumed that the catalyst is in its oxidized state and the bands corresponding to adsorption on the metal sites were not detected. Moreover, as previously reported (NO adsorption over the bare support $CeZrO_2/La\text{-}Al_2O_3$), the adsorption mainly occurs on the ceria phase, which is known as a reducible oxide [11], and can acts as an oxygen source. Thus, adsorbed species could be produced via NO/C_3H_6 oxidation over surface or lattice ceria oxygen.

For comparison propose, the catalyst was also exposed to a mixture of NO + O_2 instead of NO, followed again by C_3H_6 exposure (Figure IV- 20).

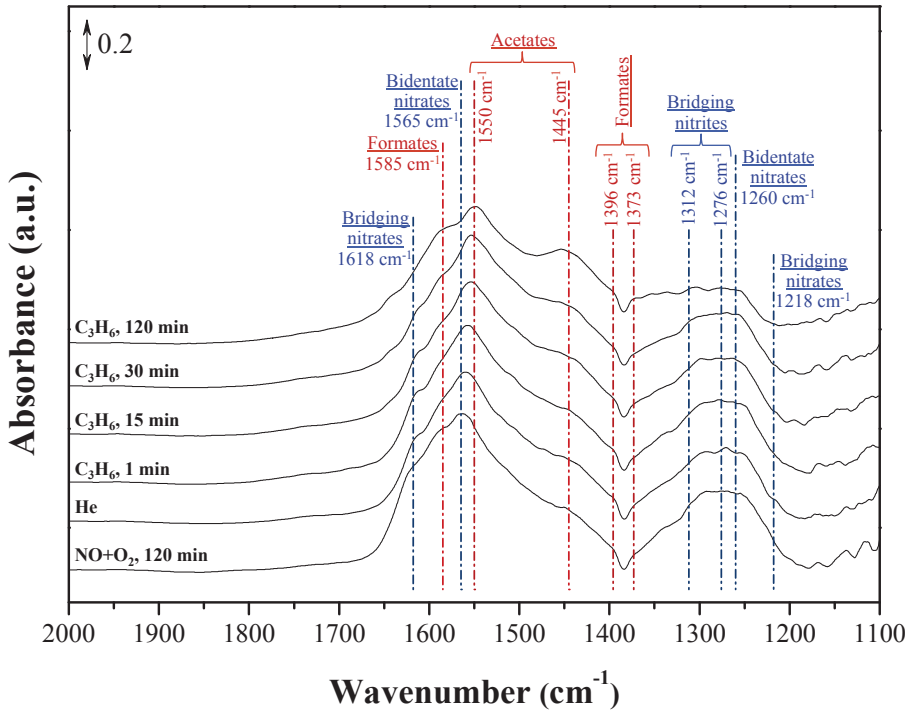

Figure IV-20. DRIFT spectra of PtPd-reference at 250ºC under NO + O_2 /He/C_3H_6 after 120 min. FT-IR chamber feed: 500 ppm NO, 10% O_2, He as balance; He purge; 300 ppm C_3H_6, He as balance; total flow 40 ml min^{-1}.

As it can be seen in Figure IV-20, higher amount of nitrates was formed on the catalyst surface when oxygen was present in the feed gas mixture. This is in agreement with results showed previously, which indicated that the formation of NO_2 in the gas phase enhances the NO_x adsorption. After exposition to C_3H_6, bands at 1550 cm^{-1} (ν_{as} COO^-) and 1445 cm^{-1} (ν_s COO^-) corresponding to acetate species appeared. Contrary to previous study, the intensity of nitrate bands at 1565 cm^{-1} decreases after C_3H_6 adsorption, which evidenced the reaction between propene and nitroxy species adsorbed on the catalyst surface.

The presence of oxygen in the mixture enhanced the NO_2 formation, which would be adsorbed in form of nitrates. These adsorbed nitrate species present a strong oxidant character, and can oxidize the C_3H_6, according to the lower intensity of nitrates bands. Thus, C_3H_6 could be oxidized by the oxygen contained on the support as well as by adsorbed nitrates. These results demonstrated that the pre-adsorbed NOx species had an important influence in adsorption/oxidation reaction pathways, which could be modified in presence of alkali impurities. In order to verify this hypothesis, the modified-catalysts were also studied.

As an example, Na-PtPd results will be discussed below (Figures IV-21 and 22), knowing that similar tendencies and conclusions were obtained for K and Ca-modified catalysts (Figures AII-8 and AII-9).

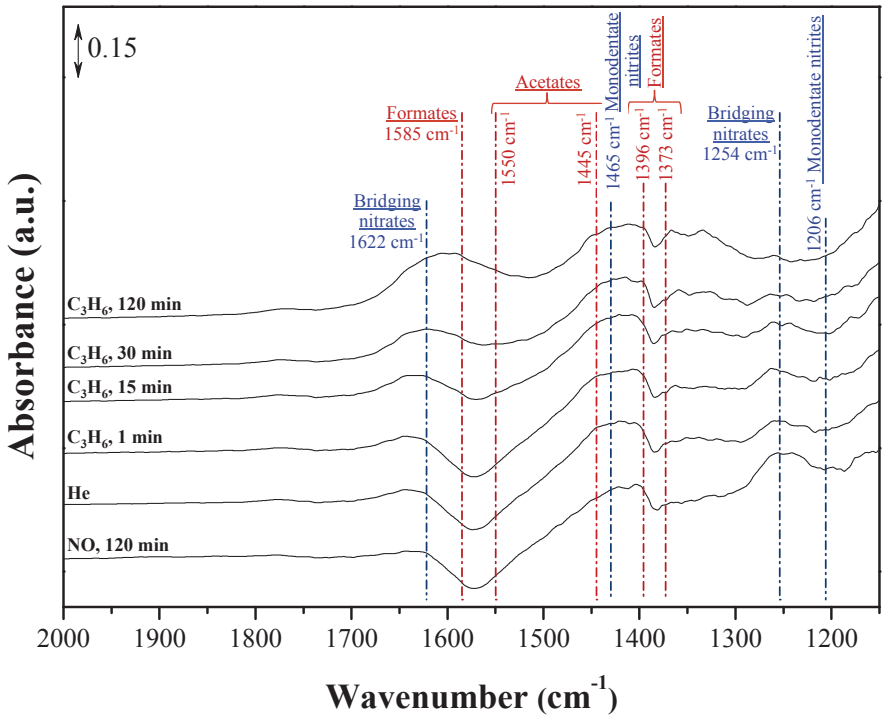

Figure IV-21. DRIFT spectra of Na-PtPd at 250ºC under NO/He/C_3H_6 after 120 min. FT-IR chamber feed: 500 ppm NO, He as balance; He purge; 300 ppm C_3H_6, He as balance; total flow 40 ml min^{-1}.

Firstly, after NO exposure, Na- modified catalyst presented higher amount of nitrites/nitrates than the reference catalyst due to the enhanced NO dissociation as have already been discussed in the previous sections. Switching to C_3H_6, nitrates bands still present, which reflects the high stability of adsorbed nitrates.

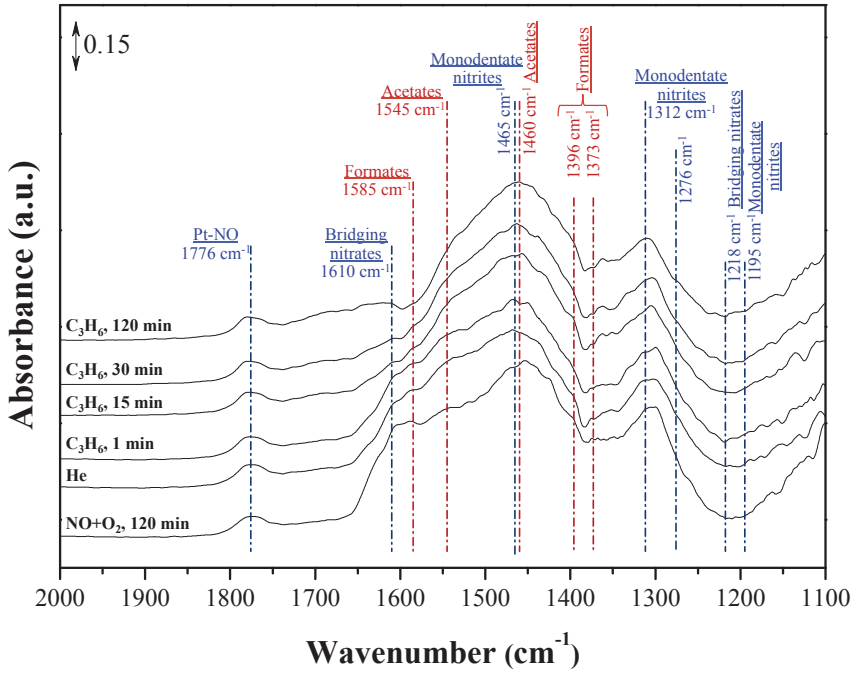

Figure IV-22. DRIFT spectra of Na-PtPd at 250ºC under NO + O_2 /He/C_3H_6 after 120 min. FT-IR chamber feed: 500 ppm NO, 10% O_2, He balance; He purge; 300 ppm C_3H_6, He balance; total flow 40 ml min^{-1}.

Nevertheless, the presence of NO + O_2 in gas feed at 250 ºC (Figure IV-22), results in a significant increase in the amount of nitrates/nitrites adsorbed species. The alkali promotion effect was evidenced by the presence of Pt-NO interaction band at 1776 cm^{-1}. Switching to C_3H_6, the nitrate bands at 1610 cm^{-1} was absent, while nitrite bands at 1465 cm^{-1} presented higher intensity, which is related to the nitrates reduction by C_3H_6. This feature evidenced that alkali impurities enhanced the reaction between C_3H_6 and nitroxy adsorbed species. Previous studies [54] confirmed that the adsorption strength of the atomic oxygen on the catalyst surface is enhanced by Na addition. The authors consider that O is a much stronger electron acceptor than NO, so O adsorption may be favoured compared to NO adsorption. Considering that O adsorption is stronger than NO adsorbed species strength, it seems presumable that reaction between propylene and nitroxy species would be easier than between propylene and oxygen strongly adsorbed. Thus, the oxidation of C_3H_6 by nitrates could produce the reduction of NO to N_2O, which would explain the previous catalytic results (section II-c, Chapter III). Otherwise, band at 1776 cm^{-1} still present after exposition to C_3H_6, which proves the increase of metal-NO bond strength produced by addition of Na.

In the case of P-PtPd catalyst (Figure IV-23), only nitrites species were found after exposure to NO and some nitrates if exposition to NO + O_2. After flowing C_3H_6, nitrates disappeared, but nitrites still present in both cases, which could be explained for the inhibition of adsorption on the catalyst surface produced by phosphate coverage of the support. Thus, the reaction takes place between the gas phase and the metal active sites, but the species do not stay adsorbed. No changes on the OH and P-OH bands corresponding to alumina support were detected during the experiments.

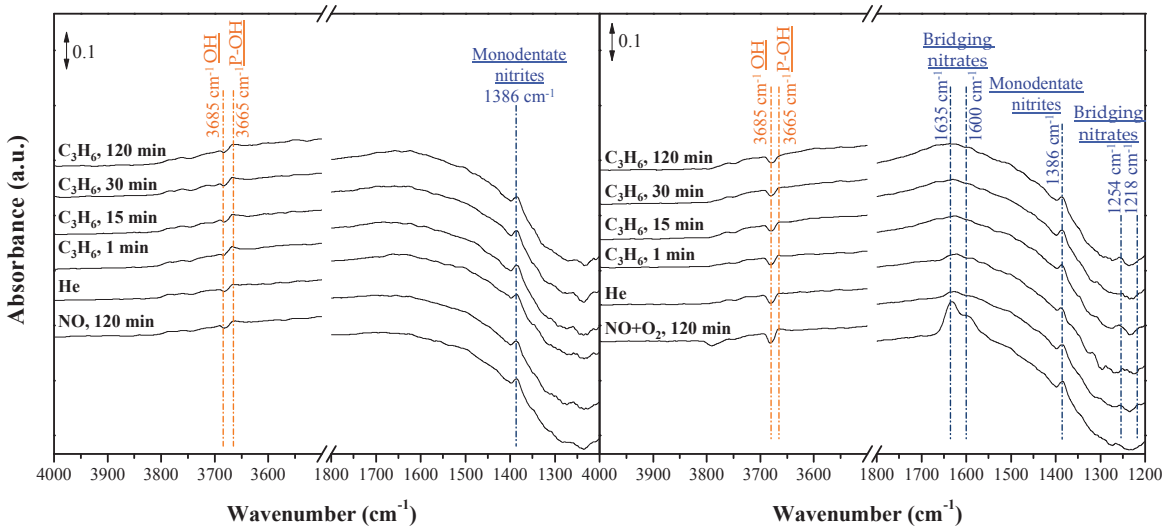

Figure IV-23. DRIFT spectra of P-PtPd at 250ºC under NO (left) and NO + O_2 (right)/He/C_3H_6 after 120 min. FT-IR chamber feed: 500 ppm NO, (10% O_2), He as balance; He purge; 300 ppm C_3H_6, He as balance; total flow 40 ml min^{-1}.

As these experiments have shown, more significant changes were evidenced after NO + O_2 exposition than with only NO. Thus, only experiments switching to from NO + O_2 to CO at 250 ºC were developed. However, when CO is employed instead of C_3H_6, no significant changes were detected. As an example, Figure IV-24 shows the results obtained with PtPd reference and Na-PtPd catalysts. In Annexe II (Figures AII-10 to 12) results obtained for K-, Ca- and P-PtPd are showed.

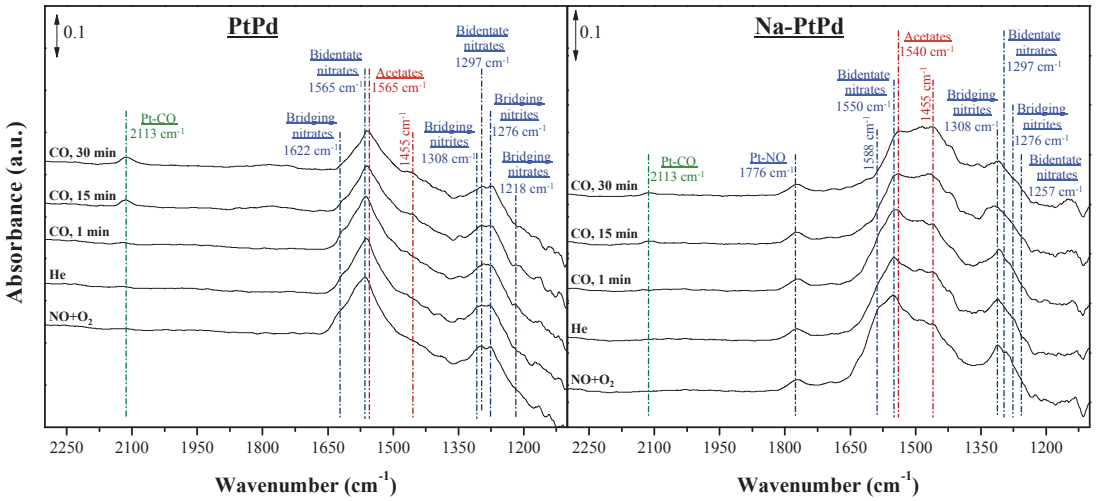

Figure IV-24. DRIFT spectra of PtPd (left) and Na-PtPd (right) at 250ºC under $NO+O_2$/He/CO after 120 min. FT-IR chamber feed: 500 ppm NO, (10% O_2), He as balance; He purge; 300 ppm CO, He as balance; total flow 40 ml min^{-1}.

As in previous experiments, nitrites/nitrates species were formed under NO + O_2 flow, appearing bands attributed to acetates species when switch to CO. Similarly to C_3H_6, the decrease of nitrates bands intensities evidenced the reactivity between CO and nitrosyl species. In addition, a small peak at 2113 cm^{-1} was detected. It can be associated to carbonyls (>C=O) adsorbed on partially oxidized Pt. It is worth noting that in presence of impurities, the band attributed to Pt-NO interaction still presented even after CO exposure, which proves the stability and high strength of Pt-NO interaction. Thus, less adsorption sites were available for CO adsorption, even if its dissociation is also enhanced in presence of alkalis.

IV. Conclusions

A detailed in-situ DRIFTS study was carried out in order to elucidate the competition for the adsorption sites between the main reactants presented in the exhaust gas. In addition, the influence of Na, K, Ca and P impurities on the reactant adsorption and the reaction pathways between the adsorbed species and the gas phase were also evaluated.

Firstly, NO adsorption on the reference catalyst evidenced the formation of nitrites/nitrates notably on the ceria-zirconia oxide phase. The role of noble metals was to enhance the NO oxidation to NO_2 that would be adsorbed as nitrites/nitrates. In agreement, when NO and O_2 were co-fed in the gas mixture, the oxygen promoted the formation of NO_2 as well as the oxidation of nitrites, whose adsorption in form of nitrates was favored.

The electrostatic field associated with Na and K impurities, promoted the charge transfer between metal and electro-donor adsorbates (NO, CO, O_2). Thus, two phenomena were detected: (i) adsorption on metal particles partially oxidized; and (ii) stabilization of antibonding π^* orbital of NO and CO molecules, enhancing its adsorption and subsequent dissociation.

In addition, the strengthening of oxygen adsorption produced in presence of alkali impurities, increased the reaction with the adjacent gas and/or adsorbed species, in agreement with the higher C_3H_6 and CO reaction rates found previously. Nevertheless, only K-modified catalyst presented promotion effect related to NO reaction rate, due to its lower amount and higher atomic number that increased the electrostatic potential.

The higher basicity of the catalyst in presence of Ca impurities promoted also the NO storage. Thus, due to the strengthening of NO adsorption, the reaction rate was diminished.

Finally, it was demonstrated that the saturation of catalyst surface by phosphates formation inhibited the NO adsorption. Moreover, the high electronegativity of P avoided the CO adsorption, which has electron-donor behaviour, having a positive influence in term of C_3H_6 and CO catalytic oxidation because of the inhibition of the self-poisoning phenomenon.

References:

[1] W.S. Epling, L.E. Campbell, A. Yezerets, N.W. Currier, J.E. Parks, Catal. Rev. - Sci. Eng. 46 (2004) 163–245.
[2] J.Y. Luo, W.S. Epling, G. Qi, W. Li, Catal. Letters 142 (2012) 946–958.
[3] C. Sedlmair, K. Seshan, A. Jentys, J.A. Lercher, J. Catal. 214 (2003) 308–316.
[4] B. Westerberg, E. Fridell, J. Mol. Catal. A Chem. 165 (2001) 249–263.
[5] S. Koukiou, M. Konsolakis, R.M. Lambert, I. V. Yentekakis, Appl. Catal. B Environ. 76 (2007) 101–106.
[6] K.I. Hadjiivanov, Catal. Rev. Sci. Eng. 42 (2000) 71–144.
[7] A. Bourane, O. Dulaurent, S. Salasc, C. Sarda, C. Bouly, D. Bianchi, J. Catal. 204 (2001) 77–88.
[8] P. Granger, H. Praliaud, J. Billy, L. Leclercq, G. Leclercq, Surf. Interface Anal. 34 (2002) 92–96.
[9] S.J. Huang, A.B. Walters, M.A. Vannice, Appl. Catal. B Environ. 26 (2000) 101–118.
[10] Y. Su, M.D. Amiridis, Catal. Today 96 (2004) 31–41.
[11] A. Kotsifa, D.I. Kondarides, X.E. Verykios, Appl. Catal. B Environ. 72 (2007) 136–148.
[12] R.F. Van Slooten, B.E. Nieuwenhuys, J. Catal. 122 (1990) 429–437.
[13] M. Primet, J.M. Basset, E. Garbowski, M. V Mathieu, J. Am. Chem. Soc. (1972) 3655–3659.
[14] G. Socrates, Infrared and Raman Characteristic Group Frequencies, 2004.
[15] D.K. Captain, M.D. Amiridis, 389 (1999) 377–389.
[16] W. Schießer, H. Vinek, A. Jentys, Appl. Catal. 33 (2001) 263–274.
[17] M. Haneda, N. Bion, M. Daturi, J. Saussey, J.C. Lavalley, D. Duprez, H. Hamada, J. Catal. 206 (2002) 114–124.
[18] G. Bamwenda, a Ogata, a Obuchi, J. Oi, K. Mizuno, J. Skrzypek, Appl. Catal. B Environ. 6 (1995) 311–323.
[19] M. Huuhtanen, T. Kolli, T. Maunula, R.L. Keiski, Catal. Today 75 (2002) 379–384.
[20] K. Shimizu, H. Kawabata, A. Satsuma, T. Hattori, J. Phys. Chem. B 103 (1999) 5240–5245.
[21] V. Matsouka, M. Konsolakis, R.M. Lambert, I. V. Yentekakis, Appl. Catal. B Environ. 84 (2008) 715–722.
[22] C. Morterra, G. Magnacca, Catal. Today 27 (1996) 497–532.
[23] K. ichi Shimizu, J. Shibata, H. Yoshida, A. Satsuma, T. Hattori, Appl. Catal. B Environ. 30 (2001) 151–162.
[24] O.S. Alexeev, S.Y. Chin, M.H. Engelhard, L. Ortiz-Soto, M.D. Amiridis, J. Phys. Chem. B 109 (2005) 23430–23443.
[25] F.C. Meunier, V. Zuzaniuk, J.P. Breen, M. Olsson, J.R.H. Ross, Catal. Today 59 (2000) 287–304.
[26] N. Bion, J. Saussey, M. Haneda, M. Daturi, J. Catal. 217 (2003) 47–58.
[27] X. Auvray, L. Olsson, Appl. Catal. B Environ. 168–169 (2015) 342–352.
[28] A.A. Davydov, S. Branch, 54 (1991) 287–291.
[29] H.Y. Huang, R.Q. Long, R.T. Yang, Energy & Fuels 15 (2001) 205–213.
[30] M. Adamowska, A. Krztoń, M. Najbar, P. Da Costa, G. Djéga-Mariadassou, Catal. Today 137 (2008) 288–291.
[31] S. Huang, a B. Walters, M. a Vannice, Appl. Catal. B Environ. 17 (1998) 19–33.
[32] Y. Ji, D. Xu, S. Bai, U. Graham, M. Crocker, B. Chen, C. Shi, D. Harris, D. Scapens, J. Darab, Ind. Eng. Chem. Res. 56 (2017) 111–125.
[33] A. Martínez Arias, J. Soria, J.C. Conesa, X.L. Seoane, A. Arcoya, R. Cataluña, J. Chem. Soc. Trans. 91 (1995) 1679–1687.
[34] J. Yu, Z. Si, L. Chen, X. Wu, D. Weng, Appl. Catal. B Environ. 163 (2015) 223–232.
[35] B. Levasseur, A.M. Ebrahim, T.J. Bandosz, Langmuir 27 (2011) 9379–9386.
[36] N. Le Phuc, E.C. Corbos, X. Courtois, F. Can, P. Marecot, D. Duprez, Appl. Catal. B Environ. 93 (2009) 12–21.

[37] I. Nova, L. Castoldi, L. Lietti, E. Tronconi, P. Forzatti, F. Prinetto, G. Ghiotti, J. Catal. 222 (2004) 377–388.
[38] H. Conrad, G. Ertl, J. Küppers, E.E. Latta, Surf. Sci. 65 (1977) 245–260.
[39] N.D. Lang, S. Holloway, J.K. Nørskov, Surf. Sci. 150 (1985) 24–38.
[40] M. Konsolakis, N. Macleod, J. Isaac, I. V Yentekakis, R.M. Lambert, J. Catal. 193 (2000) 330–337.
[41] I. V. Yentekakis, M. Konsolakis, R.M. Lambert, N. MacLeod, L. Nalbantian, Appl. Catal. B Environ. 22 (1999) 123–133.
[42] M. Konsolakis, I. V. Yentekakis, Appl. Catal. B Environ. 29 (2001) 103–113.
[43] N. Takahashi, H. Shinjoh, T. Iijima, T. Suzuki, K. Yamazaki, K. Yokota, H. Suzuki, N. Miyoshi, S. Matsumoto, T. Tanizawa, T. Tanaka, S. Tateishi, K. Kasahara, Catal. Today 27 (1996) 63–69.
[44] F. Kapteijn, L. Singoredjo, M. van Driel, A. Aendrïni, J.A. Moulijn, G. Ramis, G. Busca, J. Catal. 150 (1994) 105–116.
[45] P. Anguita, J.M. García-Vargas, F. Gaillard, E. Iojoiu, S. Gil, A. Giroir-Fendler, Chem. Eng. J. 352 (2018) 333–342.
[46] S. Goldberg, G. Sposito, Commun. Soil Sci. Plant Anal. 16 (1985) 801–821.
[47] F.J. Hingston, A.M. Posner, J.P. Quirk, J. Soil Sci. 23 (1972) 177–192.
[48] E. Fridell, A. Amberntsson, L. Olsson, Top. Catal. 2004 (2004) 143–146.
[49] H. Oh, J. Luo, W.S. Epling, Catal. Letters 141 (2011) 1746–1751.
[50] N. Bion, J. Saussey, M. Haneda, M. Daturi, J. Catal. 217 (2003) 47–58.
[51] C.G. Vayenas, S. Brosda, Electrochemical Activation of Catalysis, 2002.
[52] Y. Minemura, M. Kuriyama, S. ichi Ito, K. Tomishige, K. Kunimori, Catal. Commun. 7 (2006) 623–626.
[53] I. V. Yentekakis, V. Tellou, G. Botzolaki, I.A. Rapakousios, Appl. Catal. B Environ. 56 (2005) 229–239.
[54] H. Hattori, Chem. Rev. 95 (1995) 537–558.
[55] W.S. Epling, L.E. Campbell, A. Yezerets, N.W. Currier, J.E. Parks, Catal. Rev. 46 (2004) 163–245.
[56] P. Vernoux, A.Y. Leinekugel-Le-Cocq, F. Gaillard, J. Catal. 219 (2003) 247–257.

Chapter V

CHAPTER V: Effect of hydrothermal aging on Na, K, Ca and P-modified diesel oxidation catalysts (DOCs)

The influence of Na, K, Ca and P impurities coming from biodiesel and automotive lubricants on DOCs activity has been detailed in previous chapters. Additionally, to the effects produced by impurities, related to the configuration used in heavy-duty after-treatment systems, in which DOC is placed next to DPF, the former often experience very high temperatures up to 750 ºC (i.e. during active DPF regeneration [1]). At this high temperature, precious-metal catalyst can sinter into larger particles, losing their original high activity [2,3]. It is known that the sintering rate depends on the temperature, but the ageing atmosphere is also important. Oxidant medium are more critical to the sintering process; in particular, water vapour accelerates the crystallization and structural change in oxide supports [4].

In this chapter, PtPd reference and Na-, K-, Ca-, P-modified catalysts were hydrothermally aged (HT-PtPd, HT-Na-PtPd, HT-K-PtPd, HT-Ca-PtPd, HT-P-PtPd) under 3 l h^{-1} air flow and 10% H_2O at 850 ºC during 16 h. The effect on the structure and activity of the HT-aged catalysts was investigated. Finally, the catalysts surface properties were evaluated under simulated automotive exhaust by in-situ DRIFTS.

I. Characterization results

a. Chemical composition (ICP) and N_2 adsorption/desorption

The chemical composition and physico-chemical properties of hydrothermally aged catalyst are listed in Table V-1.

Table V-1. Chemical composition and physical properties of HT-aged catalysts.

Samples	Element contents (wt%)						S_{BET} (m^2 g^{-1})	
	Pt		Pd		Impurity			
	Stabilized	HT aged	Stabilized	HT aged	Stabilized	HT aged	Stabilized	HT aged
PtPd	0.85	0.69	0.49	0.49	-	-	60	38
K-PtPd	0.56	0.57	0.48	0.48	0.50	0.39	57	39
Na-PtPd	0.83	0.70	0.50	0.50	1.60	0.20	50	31
Ca-PtPd	0.69	0.67	0.49	0.49	1.60	1.41	50	63
P-PtPd	0.64	0.54	0.46	0.43	5.60	5.45	33	22

ICP results showed a decrease in platinum amount after hydrothermal aged treatment, associated with the leaching of Pt. In addition, the impurities contain decreased also after the aging, especially in the case of alkaline impurities (Na, K). Although modified catalysts were also stabilized in presence of water, the leaching effect was more evident after HT-aging as verified by the lower content on impurities, especially in the case of HT-Na-PtPd catalyst. This could be explained by the variation of the rate of leaching with the time. As higher temperature and longer exposition time under hydrothermal conditions were used during the aging, it increased the alkali leaching. In order to verify this assumption, the pH of the output during the HT-aging process was measured, evidencing that it became more basic increasing the aging time [5].

The specific surface area (SSA) of HT-aged samples was determined by N_2 adsorption/desorption (Table V-1). The obtained values after hydrothermal aging were lower than the SSA found for stabilized catalysts. The isotherms of the HT-aged samples (Figure AIII-1) were ascribed to type IV isotherms with H3-type of hysteresis [6], according to the BDDT classification. Although the HT-catalysts still being associated with mesoporous materials, the BJH pore size distribution curves showed that mesopores distribution was mainly centred at 30 nm. The increase of pore size comparing with mesopores presented in stabilized catalysts (Chapter III) is in agreement with the lower SSA values found.

The changes in surface area can be ascribed to sintering process of the catalyst. The catalyst sintering generally takes place at high temperatures and the reaction atmosphere also influences it. In particular, water vapour accelerates the crystallization and structural change in oxide supports. It has been shown [7] that hydrothermal treatment on alumina supports decreases the surface area and shifts the pore distribution to larger pore size. The decrease of SSA is related to the closure of the pores occasioned by the elimination of the water on the support. The condensation of hydroxyl groups on alumina surface produced the formation of Al-O-Al bonds, which bring more hydroxyls into adjacency and in such way results in the closing of the pores [4].

Alkali metals affect the thermal properties of the support and can accelerate the sintering process by interaction with acid sites of the alumina [8]. Although the

weaker amount of alkalis due to leaching, it slightly increases the sintering process, and thus the loss of SSA.

Otherwise, the amount of Ca barely decreased after hydrothermal aging for the HT-Ca-PtPd catalyst. Accordingly, the higher SSA value found could be related to the presence of calcium oxides, which formed thermally stable spinel phases with alumina, retarding sintering [8].

Moreover, in presence of phosphorus impurities, the SSA also decreased probably due to the pore blocking produced by the formation of phosphates [9].

b. X-ray diffraction (XRD)

Figure V-1 presents a comparison between the XRD patterns of PtPd and HT-PtPd catalysts, obtained using 2θ positions between 20 and 80º.

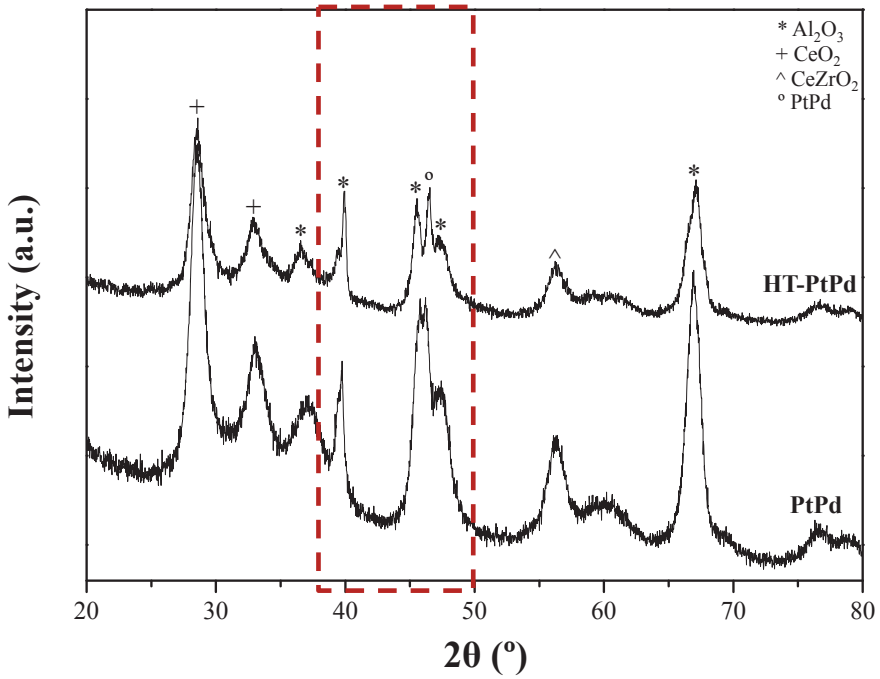

Figure V-1. X-ray diffraction patterns of PtPd and HT-PtPd catalysts.

It can be seen that after hydrothermal aging peaks at 28.8 and 33.1º corresponding to CeO_2 with cubic structure, and peak at 56.5º attributed to ceria-zirconia mixed oxide, still present. Peaks related to Al_2O_3 phase at 37º and 67º did not change. However, some differences can be observed in the 38-50º region. In order to observe these differences a zoom of this spectra region is showed on the Figure V-2.

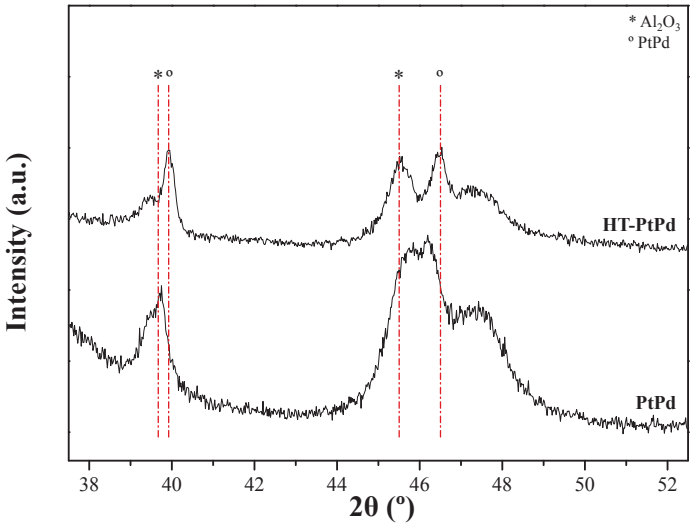

Figure V-2. Zoom of X-ray diffraction patterns of PtPd and HT-PtPd catalysts between 38 and 50º.

Firstly, peak at 39.5º attributed to alumina became a shoulder of a more intense peak at 40º in the case of HT-PtPd catalyst. Otherwise, the broad peak centred at 45.8º related to γ-alumina, was divided in two peaks at 45.5º and 46.5º after the hydrothermal aging. The shoulder at 39.5 and peak at 45.5º were related with the alumina phase. Otherwise, peaks at 40 and 46.5º can be attributed to platinum and/or palladium. The presence of these peaks evidenced the sintering of noble metals after hydrothermal aging.

The XRD patterns of hydrothermally aged modified catalysts are present in Figure V-3.

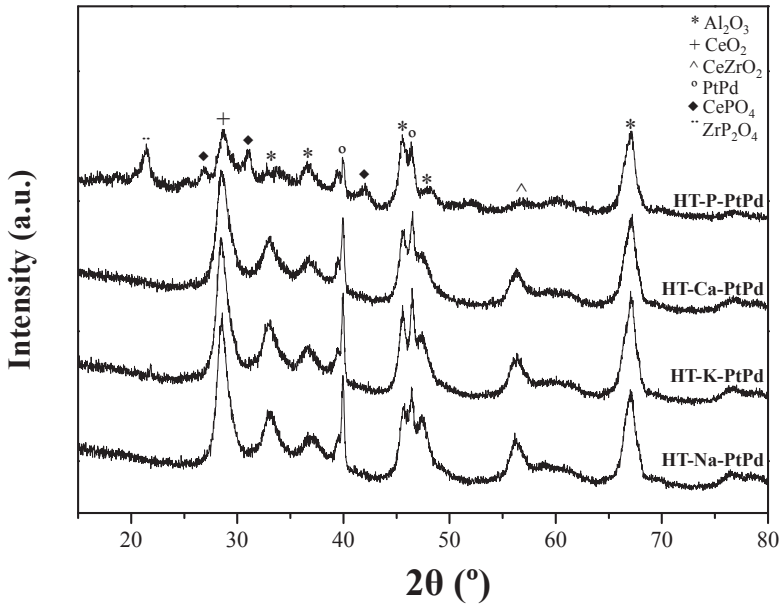

Figure V-3. X-ray diffraction patterns of HT-aged Na-, K-, Ca- and P-PtPd catalysts.

In presence of Na, K and Ca impurities, XRD patterns are similar to the one of HT-PtPd catalyst. Nevertheless, HT-P-PtPd presented some differences when compared with the only P-PtPd catalyst. Peaks corresponding to $CePO_4$ (27.1º, 31.2º and 41.9º) and to ZrP_2O_4 (21.5º) were found. The peak at 56.5º attributed to ceria-zirconia mixed oxide was not present, probably due to the lower amount of Ce and Zr available, as they were forming phosphates.

c. Transmission electron microscopy (TEM)

Figure V-4 presents TEM analysis results corresponding to: a) HT-PtPd, b) HT-Na-, and c) HT-P-PtPd catalysts. The aim of this analysis was to verify the influence of hydrothermal aging on catalysts structural characteristics.

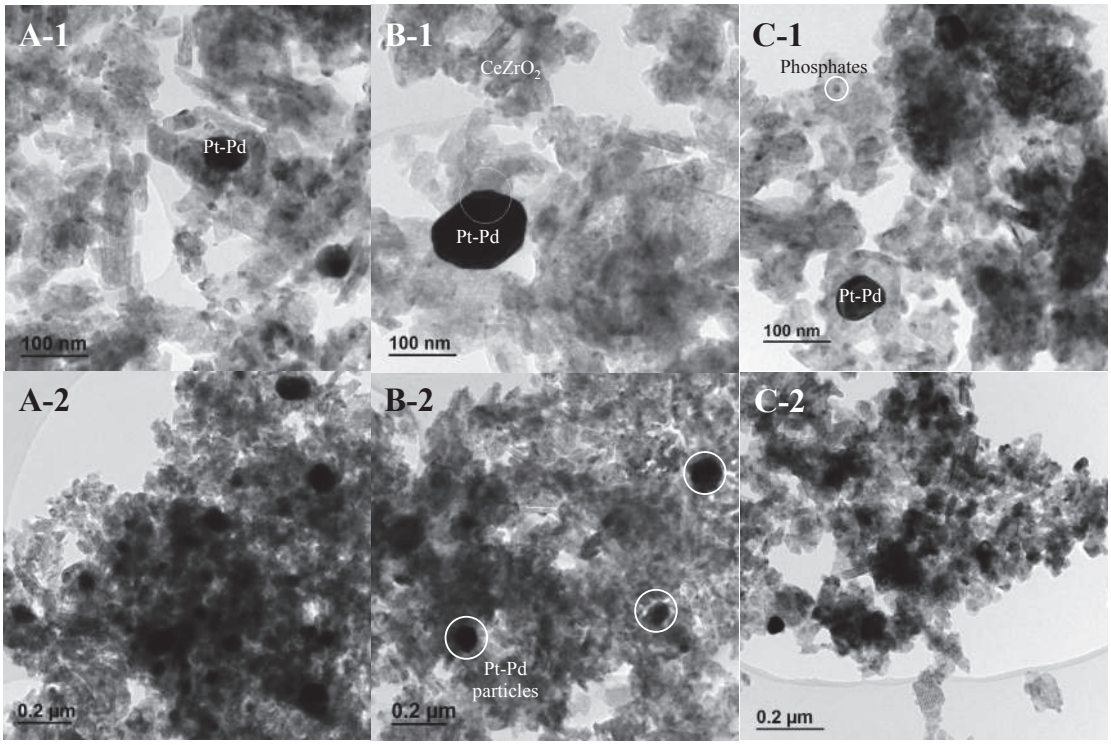

Figure V-4. TEM images of the synthesized: A) HT-PtPd, B) HT-Na-PtPd, and C) HT-P-PtPd.

Based on TEM results, no significant changes were observed in the alumina-based washcoat after the aging, even in the presence of impurities. This fact reveals the thermal stabilization effect produced by doping with lanthanum [10,11]. Ceria-zirconia phase remained in form of mixed oxide, well distributed along all the support.

Adversely to PtPd reference catalyst, HT-PtPd (Figure V-4 A-1) TEM results evidenced an increasing of metallic particles size. After aging at 850 ºC, Pt-Pd particles were visible, which proved the sintering of noble metal particles already discussed in XRD analysis. Although, it can be seen that the metallic particles still well dispersed on the catalyst with a homogeneous particle size around 50 nm (Figure V-4 A-2). The results of EDX analysis indicated that in all the aged bimetallic catalysts the noble metal particles contained both platinum and palladium. The results of aged-PtPd by H_2-TPR (section I-e, Chapter III) verified that after a second hydrothermal treatment at 650 ºC platinum-palladium metals were present as bimetallic particles. Thus, under harsher hydrothermal conditions it seems evident that the metal particles were forming bimetallic particles, which confirm the XRD previous results.

Nano-diffraction experiment was made to the particles observed on HT-PtPd catalyst. However, the crystallographic structures of Pt (0.392 nm), Pd (0.389 nm) and the PtPd (0.390 nm) were almost similar, thus it could not be possible to differentiate if the bimetallic particles were forming an alloy.

Similar results were found in the case of HT-Na-PtPd (Figure V-4 B-2). The noble metal particles presented higher size and were found forming bimetallic particles. The ceria-zirconia phase stayed covering the alumina surface as a dispersed phase (Figure V-4 B-1). The alkaline impurities were analysed by EDX, and found well dispersed in the alumina support.

In difference to P-PtPd, HT-P-PtPd phosphorus was not present forming a layer. It was detected dispersed forming phosphates as previously demonstrated by XRD (Figure V-4 C-1). The bimetallic platinum-palladium particles showed higher particle size, similarly than results obtained with the other hydrothermally aged catalysts.

d. X-ray photoelectron spectroscopy (XPS)

HT-PtPd, HT-Na-PtPd and HT-P-PtPd were analysed by XPS. In this case, only the effect of Na and P impurities were studied after HT-aging, as alkali impurities presented similar effects, while the behaviour of P was different, probably related to the higher amount of this impurity added to the catalyst.

Firstly, the peak corresponding to XPS profiles of the Al 2p (Figure V-5) are centred at the same range (74.6±0.2 eV) for all catalysts, similar than the one found in

fresh catalyst spectra. This BE corresponded to γ-Al_2O_3, which evidenced that no alumina-phase transition was produced after hydrothermal aging. The chemical state of platinum cannot be determined, as the most intensive Pt 4f peak interferes with Al 2p peak.

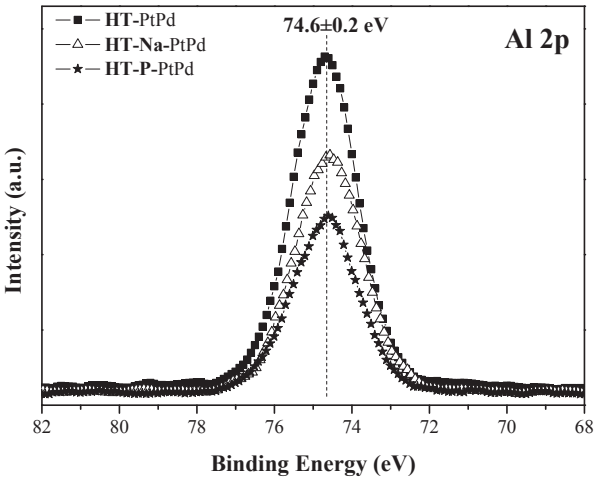

Figure V-5. Al 2p XPS spectra of HT-PtPd, HT-Na-PtPd and HT-P-PtPd catalysts.

Figure V-6 shows the Ce 3d obtained spectra, where all the samples presented the peaks characteristics of CeO_2 according to the convention established by Burroughs [12,13].

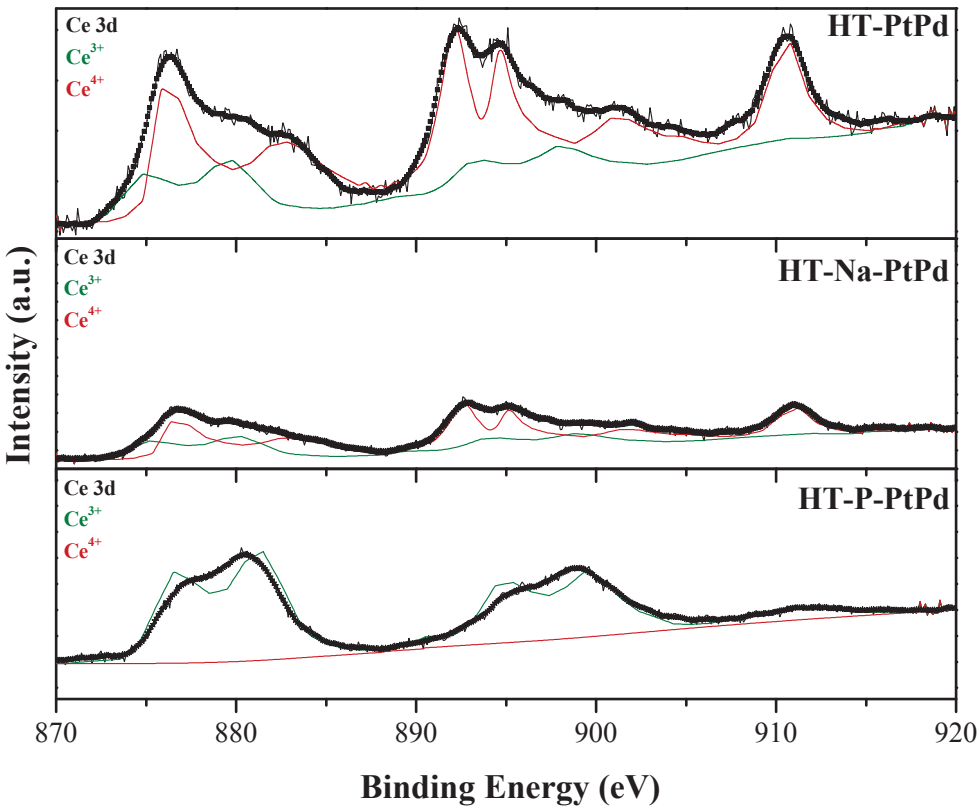

Figure V-6. Ce 3d spectra of HT-PtPd, HT-Na-PtPd and HT-P-PtPd catalysts.

Cerium was found as Ce^{3+} and Ce^{4+} oxidation states, presenting HT-PtPd and HT-Na-PtPd similar results. Nevertheless, the HT-PtPd catalyst showed slightly higher percentage of the oxidized state (Table V-2). It is worth noting that in the spectrum of HT-P-PtPd only was visible the reduced state (Ce^{3+}). It was evidenced by XPS analysis of P-PtPd catalyst that phosphorus impurities could stabilize the ceria in its reduced state [14]. This fact confirms that after hydrothermal treatment, the reduced Ce^{3+} was bounded forming the $CePO_4$ compound.

Table V-2. Binding energies (BEs) and percentage of the chemical states of cerium (Ce^{3+} and Ce^{4+}) on the surface obtained from XPS analyses.

Catalyst	PtPd		Na-PtPd		P-PtPd	
	Stabilized	**HT-aged**	**Stabilized**	**HT-aged**	**Stabilized**	**HT-aged**
BE Ce $3d_{5/2}$ (eV)	884.4	884.2	884.5	884.2	885.0	884.5
Ce^{4+} (%)	58.5%	88.0%	52.9%	84.2%	45.7%	0.0%
Ce^{3+} (%)	41.5%	12.0%	47.1%	15.8%	54.3%	100%

The impurities were found at 1072±0.2 eV in the case of Na 1s, similarly than Na-PtPd fresh catalyst, thus no changes in the chemical state were produced after hydrothermal aging. In the case of phosphorus, a broad peak depicted at 135.2±0.3 eV corresponding to phosphates, in agreement with the results found by XRD and previous hypothesis of stabilization of ceria in its reduced state.

e. H_2 temperature programmed reduction (H_2-TPR)

In order to analyse the influence of hydrothermal aging on the reducibility of the catalysts, H_2 temperature programmed reduction experiments were carried out from room temperature to 650 ºC. The TPR profiles of HT-PtPd, HT-Na-PtPd and HT-P-PtPd samples are shown in Figure V-7. Similar results were found for HT-K-PtPd and HT-Ca-PtPd (Annex III).

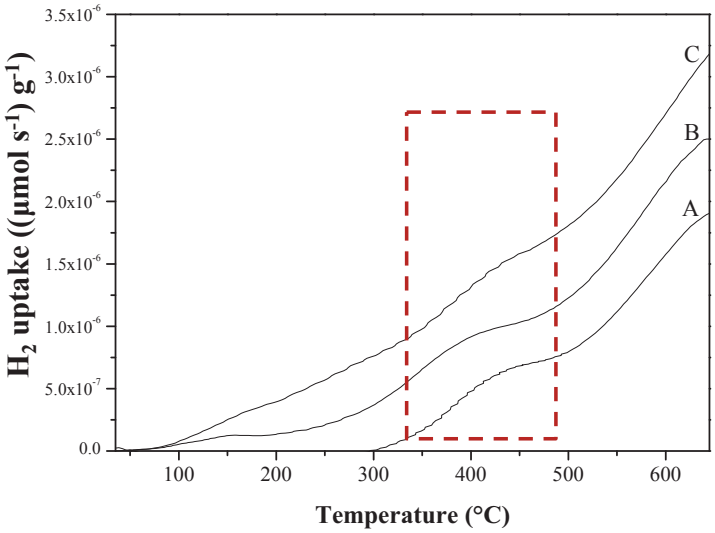

Figure V-7. TPR-H_2 profiles of (A) HT-PtPd, (B) HT-Na-PtPd and (C) HT-P-PtPd catalysts.

Similarly than stabilized catalysts H_2-TPR results, the reduction profiles of HT-aged catalysts present a small broad peak was found between 350 -450 ºC. This peak could be attributed to the reduction of superficial CeO_2 that is not interacting with metal. However, it seems that the peak presents slightly higher intensity after HT-aging. In agreement with the lost of SSA due to the sintering of the support, lower amount of ceria would be in contact with the metal. In addition, as discussed in Chapter III, the hydrothermal aging could produce a deterioration of the surface oxygen mobility capacity increasing the reduction temperature [15]. Thus higher amount of ceria than in the case of stabilized samples would be reduced at higher temperatures. Finally, a broad peak at temperatures higher than 450 ºC was associated with the reduction of bulk ceria promoted by zirconium [16,17].

It is worth noting that after HT-aging treatment the peaks corresponding to the reduction of palladium and platinum disappeared. Previous H_2-TPR results obtained for aged-catalyst (section I-e, Chapter III), presented only one reduction peak. Under the light of characterization results of HT-aged catalysts (XRD, TEM), it has been proved the sintering of Pt-Pd particles. Thus, the loss of reducibility can be ascribed to the formation of bigger Pt-Pd bimetallic particles after exposition to harsh hydrothermal aging conditions.

Tao et al. [18] studied the structure of Pt-Pd bimetallic catalysts, and proposed that the structure of these particles consists on a platinum core and a palladium shell. They did not observed structural changes upon exposition of Pt-Pd catalyst to oxidizing and reducing conditions, with palladium remaining at the bimetallic particle

surface. Thus, the lost of reducibility after HT-aging could be ascribed to the inhibition of metal reduction by palladium on the catalyst surface. Previous studies results [19,20] found also lower H_2 consumption for aged bimetallic catalyst. In agreement with the discussed results, they considered that the metal sintering would limit the re-oxidation of the catalysts, thus decreasing the subsequent reduction. The presence of cerium near to the noble metal particles on the catalyst surface may facilitate the charge transfer between them, resulting in higher oxidation state in the noble metal particles. However, the sintering of the catalyst decreased the metal-support interaction, inhibiting the effect of cerium on the noble metal phase.

II. Activity test results

The catalytic results obtained for CO, C_3H_6 and NO using HT-aged catalysts are going to be discussed. A comparison with stabilized catalysts data was done in order to evaluate the influence of the HT-aging process in presence of impurities.

Figure V-8 presents a comparison between the CO and C_3H_6 conversion curves of stabilized and hydrothermally aged catalysts.

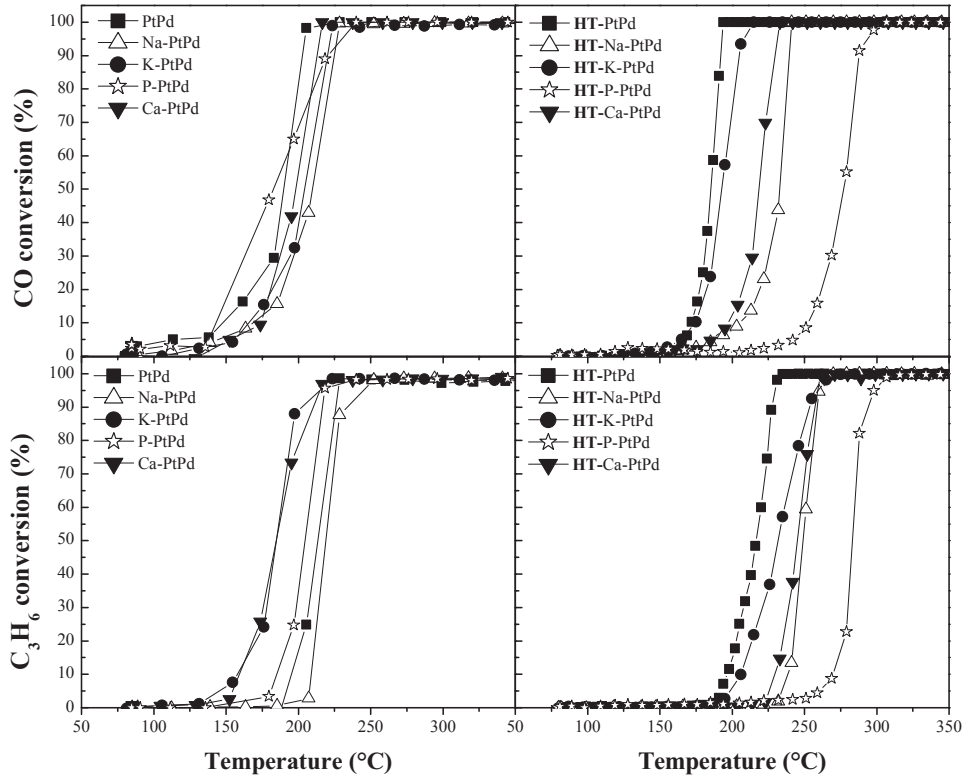

Figure V-8. Comparison of CO and C_3H_6 conversion curves of stabilized (left) and HT-aged (right) catalysts in function of the temperature during the heating ramp.

Operating conditions: 50 mg, 250 ml min^{-1}, GHSV = 135 000 h^{-1}; 300 ppm CO, 300 ppm C_3H_6, 500 ppm NO, 10% O_2, 5% CO_2, 3.5% H_2O and He as balance.

As it can be shown in Figure V-8, all catalysts maintained a high activity after hydrothermal aging. The lower SSA induced by aging did not greatly affect catalyst activity. Thus, the sintering process was produced by occlusion of small internal pores of the support, where only small amounts of ceria or noble metals would be deposited. Although the HT-aged catalysts still attained CO and C_3H_6 complete conversions as the stabilized catalysts, the former reached 100% conversion at higher temperatures. In agreement with Adamowska et al. [21], this result could be ascribed to the sintering of PtPd particles, which would hinder optimal catalytic activity.

In the same way, Figure V-9 presents the NO-NO_2 conversion curves obtained for the stabilized and HT-aged catalysts.

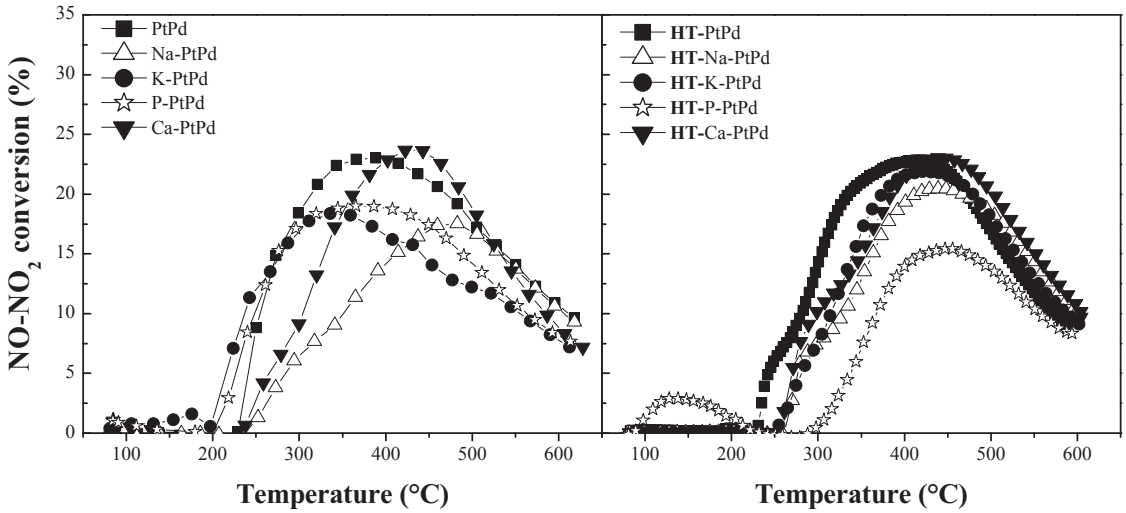

Figure V-9. Comparison of NO-NO_2 conversion curves of stabilized (left) and HT-aged (right) catalysts in function of the temperature during the heating ramp. Operating conditions: 50 mg, 250 ml min^{-1}, GHSV = 135 000 h^{-1}; 300 ppm CO, 300 ppm C_3H_6, 500 ppm NO, 10% O_2, 5% CO_2, 3.5% H_2O and He as balance.

The NO-NO_2 conversion curves shifted towards higher temperatures in general. This could be related to the leaching of the metal after HT-aging treatment. In addition, the increment of T_{50} values of CO and C_3H_6 would delay NO conversion due to the competitive adsorption between the reactants.

The NO-NO_2 conversion curves of HT-aged catalysts in presence of impurities exhibited similar shape. Thus, impurities presented lower influence for HT-aged than for stabilized catalysts. This might be ascribed to the leaching of impurities

occasioned by the HT-aging. It is worth noting that the maximum conversion values are higher after HT-aging for all the samples except HT-P-PtPd catalyst. This is in agreement with the literature, as the size increase of PtPd particles due to the sintering may favors NO oxidation [22].

In the case of HT-P-PtPd, the maximum conversion is lower after the HT-aging. As the characterization results have shown, higher amount of phosphates were formed after the HT-aging, as well as a significant lower SSA was produced, which could decrease the catalytic activity. Nevertheless, note that HT-P-PtPd catalyst presented a slightly conversion increment in the 100 – 200 ºC range, that decreased before the start of mainly conversion curve due to the reduction of NO_2 to NO by C_3H_6 (Chapter III, section II-b-ii). The NO-NO_2 conversion found at low temperatures for HT-P-PtPd, could be attributed to the presence of Ce^{3+} species, as verified by XPS, which promotes NO decomposition [23].

Finally, less pronounced NO-N_2O conversion was also found at low temperatures comparing with stabilized catalyst (Figure V-10). In agreement with the displacement of C_3H_6 curves, NO to N_2O reduction was produced at higher temperature.

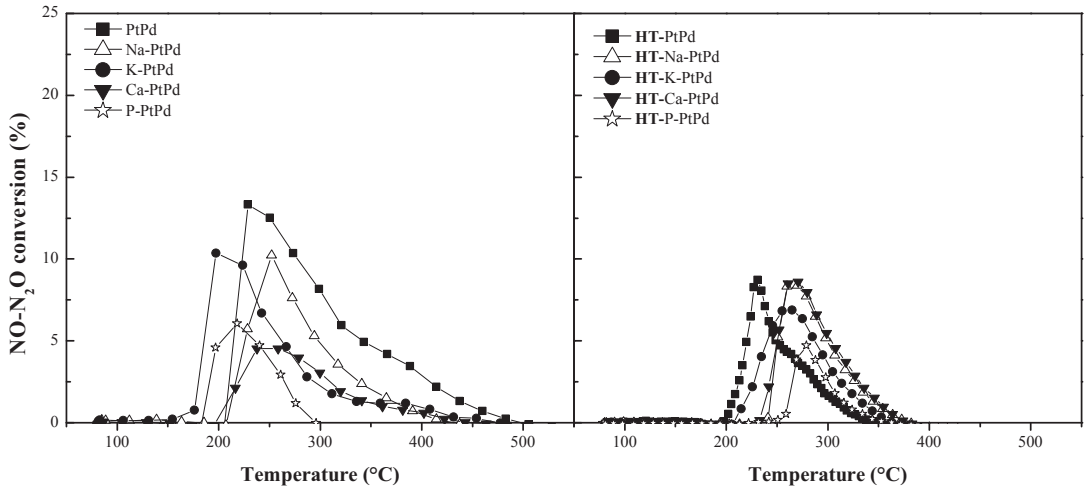

Figure V-10. Comparison of NO-N_2O conversion curves of stabilized (left) and HT-aged (right) catalysts in function of the temperature during the heating ramp. Operating conditions: 50 mg, 250 ml min^{-1}, GHSV = 135 000 h^{-1}; 300 ppm CO, 300 ppm C_3H_6, 500 ppm NO, 10% O_2, 5% CO_2, 3.5% H_2O and He as balance.

The reaction rates calculated at conversions lower than 10% are shown in Table V-3 in order to compare the influence of impurities on catalytic activity after hydrothermal aging.

Table V-3. Catalytic activity results in presence of Na, K, Ca and P impurities after HT-aging treatment for catalytic diesel oxidation reaction.

Catalyst	$^{1}r_{CO}$ (150ºC)		$^{1}r_{C3H6}$ (180ºC)		$^{1}r_{NO}$ (230ºC)	
	Stabilized	HT-Aged	Stabilized	HT-Aged	Stabilized	HT-Aged
PtPd	0.912	0.081	-	0.075	3.191	1.893
Na-PtPd	0.421	0.084	0.045	0.033	0.736	-
K - PtPd	0.504	0.199	3.963	0.034	4.351	0.552
Ca - PtPd	0.384	0.018	4.003	0.024	1.036	0.201
P - PtPd	0.994	0.256	0.446	0.144	3.643	-

[1]Reaction rate ((mol s^{-1} g_{PGM}^{-1})·10^{5}) during the heating at 150, 180 and 230ºC for CO, C_3H_6 and NO, respectively for the first catalytic cycle.

HT-aged catalysts present in general lower CO reaction rate than stabilized ones. However, when comparing the HT-aged catalysts between them, higher reaction rate values for CO at 150 ºC were found in presence of Na, K and P impurities (Table V-3).

As previously discussed, it is well known that CO strongly adsorbs on the catalyst surface [24], producing "self-inhibition" and decreasing the catalytic activity. The use of ceria as a complementary phase on the support promotes the oxidation of the CO, avoiding the saturation of the catalyst surface. However, the hydrothermal aging decreased the redox capacities of the catalysts, thus inhibiting the cyclic change between the oxidation states of metals, as verified by H_2-TPR [25]. This would decrease the capacity of ceria to change its oxidation state, diminishing the oxygen activation on the catalyst and subsequently the reaction rate of CO (Table V-3). Until the temperature was not enough to CO could desorb, the oxygen would not be available to start the reaction.

The low electronegativity of alkali impurities produces an inhomogeneous electric field that promotes the adsorption of CO. Nevertheless, the electronic effect produced by sodium and potassium would be attenuated due to the catalyst sintering, which decreased the metal-support interaction producing lower metal-CO charge transfer [26]. Subsequently the saturation of the catalyst surface by CO adsorption was avoided, increasing the reaction rate for HT-Na-PtPd and HT-K-PtPd in comparison with HT-PtPd catalyst. Due to the higher amount of impurities, electronic effect still produced for HT-Ca-PtPd, favoring CO adsorption. Finally, the phosphates formation verified by TEM, XRD and XPS analyses inhibited CO catalyst saturation for HT-P-PtPd catalyst, increasing the reaction rate.

In general, the C_3H_6 reaction rate calculated at 180 ºC, presented lower values for HT-aged catalysts than the stabilized ones due to their lower redox capacity. In the case of HT-PtPd the obtained C_3H_6 reaction rate was higher than for PtPd catalyst. This higher value could probably due to the promotion of NO reduction to N_2O via C_3H_6-SCR. Previous studies [27] have shown that the higher size of bimetallic particles enhances NO reduction to N_2O. Thus, the sintering of Pt-Pd bimetallic particles after HT-aging would increase the C_3H_6 reaction rate. Comparing with HT-PtPd, the presence of Na, K and Ca impurities decreased the reaction rate, while higher value was found for HT-P-PtPd catalyst. As discussed above, due to the catalyst sintering the promotion effect of the alkaline impurities was decreased. The induced strengthening of electron-accepting adsorbates such as O_2 produced by the electron donor behaviour of these impurities would be inhibited. Consequently the O_2 adsorption will be disfavored, decreasing the C_3H_6 conversion [28]. On the other hand, similarly than for CO and before HT-aging, the formation of phosphates avoid the propylene adsorption, inhibiting its self-poisoning.

The reaction rate of NO at 230 ºC was also lower after HT-aging than the one obtained with the stabilized catalysts. This might be due to the leaching of Pt, as well as to the decrease of the amount of active sites related to the noble metal sintering. Otherwise, the sintering of the catalyst decreased the electron transfer from alkalis to noble metals. Thus, the interaction with NO decreased and subsequently, the promoted NO adsorption by alkali impurities [28,29] was suppressed. In the case of HT-P-PtPd, the blockage of catalytic active sites by the higher amount of phosphates and the formation of phosphates oxides decreased the reaction rate.

III. In-situ DRIFTS study

Once the influence of HT-aging on the catalytic activity was verified, direct spectroscopy evidenced by in-situ Diffuse Reflectance Infrared Fourier Transform Spectroscopy (DRIFTS) were pursued by exposition to NO + CO + C_3H_6 + O_2 at 150 ºC and 250 ºC.

Figure V-11 shows IR spectra of adsorbed species on the surface of HT-PtPd, HT-Na-PtPd and HT-K-PtPd catalysts under NO + CO + C_3H_6 + O_2 gas mixture at 150 ºC (left) and 250 ºC (right).

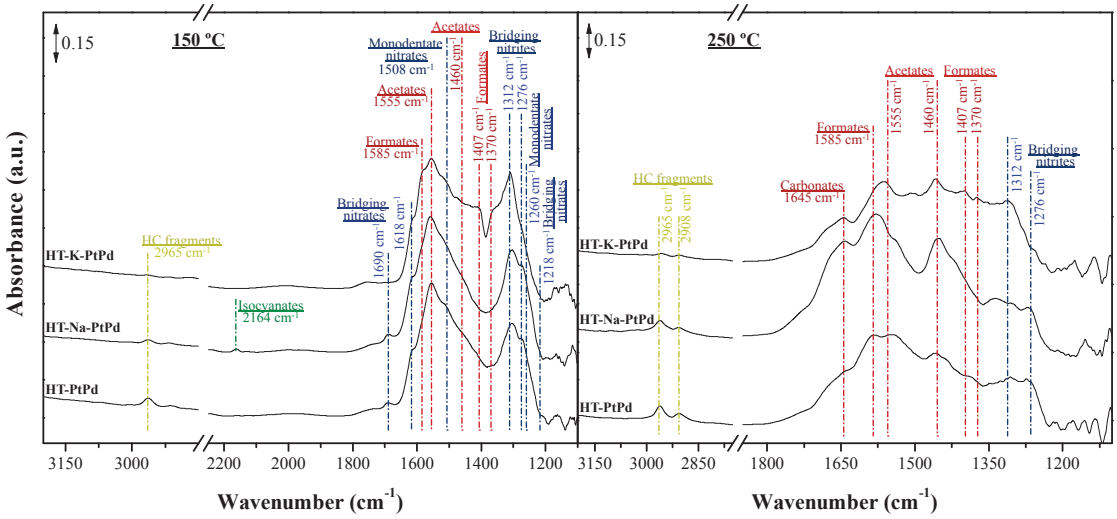

Figure V-11. DRIFT spectra in the region 3200-1100 cm^{-1} of HT-PtPd, HT-Na-PtPd and HT-K-PtPd aged catalysts at 150 ºC (left) and 250 ºC (right) under simulated exhaust conditions. FT-IR chamber feed: 500 ppm NO, 300 ppm CO, 300 ppm C_3H_6, 10% O_2, He as balance. Total flow: 40 ml min^{-1}. Each spectrum has been taken 60 min after the desired temperature reached.

At 150 ºC (Figure V-11, left), HT-PtPd, HT-Na-PtPd and HT-K-PtPd catalysts showed similar bands. The mainly peaks corresponded to acetates species (1555 cm^{-1}, $\nu_{as}(COO^-)$ and 1460 cm^{-1}, $\nu_s(COO^-)$), monodentate nitrates (1508 cm^{-1}, $\nu(N=O)$; 1260 cm^{-1}, $\nu(N-O)$) and bridging nitrites (1312 cm^{-1}, $\nu_{as}(NO_2)$; 1276 cm^{-1}, ν_s (NO_2)). Formates at 1585 cm^{-1} ($\nu_s(COO^-)$; 1407 cm^{-1}, $\delta(CH)$ and 1307 cm^{-1}, $\nu_{as}(COO^-)$) and bridging nitrates at 1618 cm^{-1} ($\nu_s(NO_2)$, 1218 cm^{-1} $\nu_{as}(NO_2)$) were also present in all catalysts. In addition, a band at 1690 cm^{-1} corresponding to linear or bent NO on Pt ($\nu(N-O)$) depicted in HT-PtPd and HT-Na-PtPd spectra. Slightly peak at 2965 cm^{-1} were found in the region of HC fragments, as a consequence of propene adsorption. It is worth noting that in the case of HT-K-PtPd, the bands corresponding to formate species presented higher intensities probably due to the higher basicity of the potassium, which would enhance the activity of CO oxidation (Table V-3) [30].

Moreover, a small peak attributed to isocyanates at 2164 cm^{-1}, $\nu(NCO)$, was detected for HT-Na-PtPd catalyst. The formation of isocyanate is preceded by the dissociation of NO followed by the interaction of N(ads) with CO(ads) (or CO(g)) on active metal centres. Accordingly to characterization results (H_2-TPR), platinum was present in reduced state. In addition, sodium impurities electronically enhanced the

dissociation of NO on the metal sites. Thus, it seems that isocyanates formation would be promoted due to electron enrichment of Pt sites after HT-aging.

When the temperature was increased until 250 ºC the spectra evolved (Figure V-11, right). Nitroxy species almost disappeared, remaining only slightly peaks associated with nitrites at 1312 cm^{-1} ($\nu_{as}(NO_2)$) and 1276 cm^{-1} ($\nu_s(NO_2)$). Moreover, a broad peak at 1645 cm^{-1} attributed to carbonates ($\nu_{as}(COO^-)$; 1350 cm^{-1}, $\nu_s(COO^-)$), appeared for the three catalysts, related with the adsorption of CO_2 produced during CO and C_3H_6 oxidations. Carbonates bands presented higher intensity in presence of Na and K due to the increase of the catalyst basicity related with these impurities. Acetates at 1555 cm^{-1} ($\nu_{as}(COO^-)$) and 1455 cm^{-1} ($\nu_s(COO^-)$), as well as formates at 1585 ($\nu_{as}(COO^-)$), 1393 cm^{-1} ($\delta(CH)$) and 1373 cm^{-1} ($\nu_s(COO^-)$), dominated the obtained spectra. Slightly higher intensity of HC fragments (2965 and 2908 cm^{-1}) corresponding bands, were also found.

In agreement with the similar bands observed for all HT-aged catalysts, it seems that alkali effects were attenuated after HT-aging. This could be ascribed to two facts: (i) the loss of impurity amount associated with alkali leaching during HT-aging, and (ii) the loss of effective contact between alkalis and metal phase [28]. Due to the metal sintering, lower contact with alkalis would be produced, decreasing their electronic influence on the catalytic activity.

IR spectra of adsorbed species on the surface of HT-PtPd and HT-Ca-PtPd catalysts under the same conditions are shown in Figure V-12.

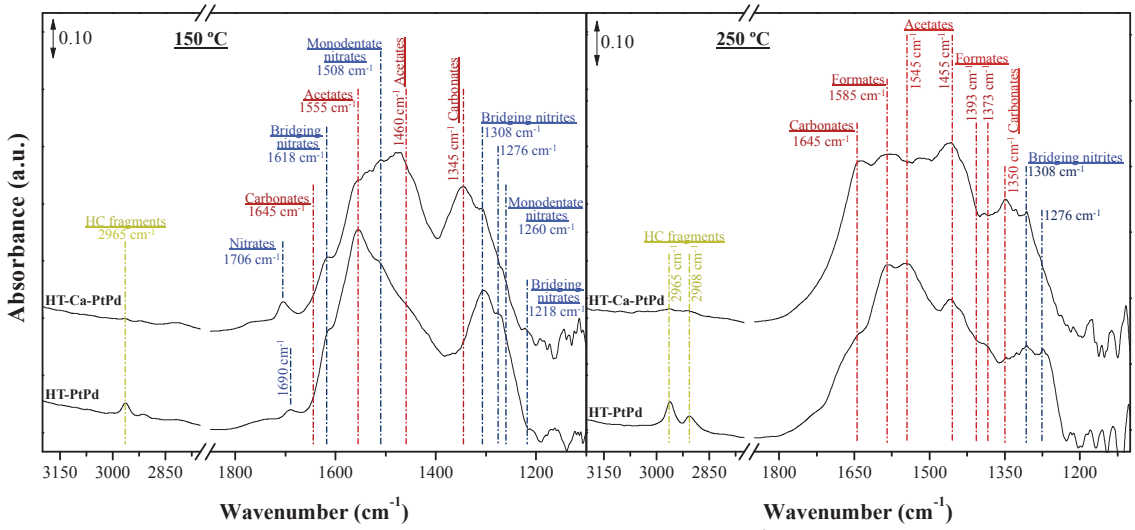

Figure V-12. DRIFT spectra in the region 3200-1100 cm^{-1} of HT-PtPd and HT-Ca-PtPd aged catalysts at 150 ºC (left) and 250 ºC (right) under simulated exhaust conditions. FT-IR chamber feed: 500 ppm NO, 300 ppm CO, 300 ppm C_3H_6, 10% O_2,

He as balance. Total flow: 40 ml min^{-1}. Each spectrum has been taken 60 min after the desired temperature reached.

Comparing HT-PtPd and HT-Ca-PtPd at 150 ºC (Figure V-12, left), some differences were evidenced. An intense peak at 1460 cm^{-1} corresponding to linear acetates ($\nu_s(COO^-)$; 1555 cm^{-1} (ν_{as} (COO^-)) was depicted for HT-Ca-PtPd. In addition, some carbonates were also detected at 1345 cm^{-1} ($\nu_s(COO^-)$; 1645 cm^{-1}, $\nu_{as}(COO^-)$). As well as in the case of HT-PtPd, linear or bent NO on Pt species were presented at slightly higher wavenumber in presence of Ca impurities (1706 cm^{-1}, ν(N-O)). Although in both spectra acetates and carbonates bands intensity increased at 250 ºC (Figure V-12, right), higher peaks intensities were observed on HT-Ca-PtPd spectra.

As discussed in Chapter IV, Ca impurities possess strong basic sites. Minemura et al. [30] shown that alkali metals with strong basicity could increase the activity of the CO oxidation. In addition, Ca-based catalysts can be easily poisoned by H_2O and CO_2 [31]. Thus, the higher intensity bands of HT-Ca-PtPd could be ascribed to the high basicity of Ca impurities.

Finally, HT-aged phosphorus-modified catalyst was compared with HT-PtPd catalyst spectra in Figure V-13.

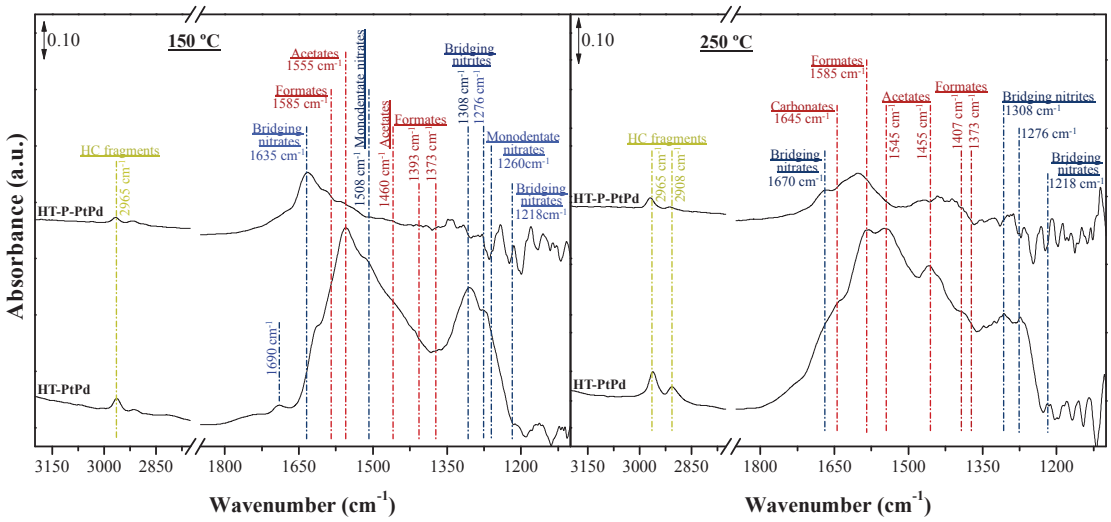

Figure V-13. DRIFT spectra in the region 3200-1100 cm^{-1} of HT-PtPd and HT-P-PtPd aged catalysts at 150 ºC (left) and 250 ºC (right) under simulated exhaust conditions. FT-IR chamber feed: 500 ppm NO, 300 ppm CO, 300 ppm C_3H_6, 10% O_2, He as balance. Total flow: 40 ml min^{-1}. Each spectrum has been taken 60 min after the desired temperature reached.

In the same way than the corresponded stabilized sample, HT-P-PtPd presented weak adsorption bands. At 150 ºC (Figure V-13, left), band attributed to bridging nitrates at 1635 cm^{-1} ($\nu_s(NO_2)$; 1218 cm^{-1}, $\nu_{as}(NO_2)$) was detected. Slightly broad peaks corresponding to formates (1585 cm^{-1}, $\nu_{as}(COO^-)$; 1393 cm^{-1}, $\delta(CH)$; 1373 cm^{-1}, $\nu_s(COO^-)$) and acetates (1545 cm^{-1}, $\nu_{as}(COO^-)$; 1460 cm^{-1}, $\nu_s(COO^-)$), were also observed. However, their intensities were negligible comparing with the intensities of the peaks found on the HT-PtPd spectra.

At higher temperature (250 ºC, Figure V-13, right), bands corresponding to formates (1585 cm^{-1}, $\nu_{as}(COO^-)$, 1407 cm^{-1}, $\delta(CH)$ and 1373 cm^{-1}, $\nu_s(COO^-)$) and carbonates (1645 cm^{-1}, $\nu_{as}(COO^-)$; 1345 cm^{-1} ($\nu_s(COO^-)$) species appeared, but with much lower intensity than HT-PtPd catalyst.

The weaker adsorption in presence of phosphorus could be attributed to the formation of phosphates, which would block the adsorption sites, as verified by the lower SSA values found. Moreover, the adsorption of NO instead of CO and/or C_3H_6 could be attributed to the presence of Ce^{3+} species, as verified by XPS, which promote NO decomposition [23].

The CO and C_3H_6 reaction rates presented higher values for HT-P-PtPd than HT-PtPd. Relating with the low adsorption evidenced by in-situ DRIFTS, it was verified that formation of phosphates avoid the adsorption of CO and C_3H_6, and consequently, the saturation of the active sites. In the case of NO, the reaction rate obtained was lower than HT-PtPd catalyst. Regarding the obtained spectra, no peak related to the interaction NO-Pt was observed after HT-aging. Thus, the higher phosphates formation verified by TEM and XRD could block the active sites, hindering NO conversion.

IV. Conclusions

In this chapter, the hydrothermal aging influence was investigated on the physico-chemical, redox and catalytic activity of PtPd reference catalyst and modified with Na, K, Ca and P species.

The physico-chemical characterization results showed the sintering of the catalyst as well as the higher size of Pt-Pd bimetallic particles, which leads lower number of catalytic active sites. In addition, H_2-TPR results evidenced that the redox capacities of the catalyst also decreased.

Although CO and C_3H_6 complete conversions continued attained after HT-aging, higher T_{50} values were found related to the leaching of the metal. In addition, the leaching of alkali impurities, as well as the catalyst sintering, weakened the promoted adsorption of electron-accepting adsorbates, such as CO, NO and O_2. These results are in agreement with the lower intensity bands presented in obtained DRIFTS spectra, which evidenced the attenuation of alkali electronic promotion. Notwithstanding it had a positive effect on the CO oxidation by preventing the "self-inhibition" effect, it decreased the reaction rates of C_3H_6 and NO.

The sintering of the catalyst decreased the number of active sites on the catalytic surface, lowering NO reaction rate values. Nevertheless, the higher metallic state of PtPd particles evidenced by H_2-TPR enhanced NO to NO_2 conversion. Moreover, the bigger size of these particles also promoted NO conversion, as it is a well-known structure sensitive reaction [32].

The lower reaction rate obtained for CO and C_3H_6 in the case of HT-Ca-PtPd would be related to electronic effects, as no loss of impurities was detected. In addition, the high basicity of the Ca impurities increased the stability of adsorbed nitrates, decreasing the catalytic activity.

On the other hand, phosphorus species were forming phosphates on the catalyst surface according to XRD and TEM analyses. As verified by in-situ DRIFTS experiments, it inhibited the catalyst surface saturation, increasing CO and C_3H_6 reaction rates. However, NO oxidation was disfavored due to the presence of phosphates blocking the catalytic sites.

References:

[1] J. Andersson, M. Antonsson, L. Eurenius, E. Olsson, M. Skoglundh, Appl. Catal. B Environ. 72 (2007) 71–81.
[2] H. Jeong, J. Bae, J.W. Han, H. Lee, ACS Catal. (2017) 7097–7105.
[3] P. Munnik, P.E. De Jongh, K.P. De Jong, Chem. Rev. 115 (2015) 6687–6718.
[4] A. Kalantar Neyestanaki, F. Klingstedt, T. Salmi, D.Y. Murzin, Fuel 83 (2004) 395–408.
[5] B.C. Bunker, G.W. Arnold, E.K. Beauchamp, D.E. Day, J. Non. Cryst. Solids 58 (1983) 295–322.
[6] G. Leofanti, M. Padovan, G. Tozzola, B. Venturelli, Catal. Today 41 (1998) 207–219.
[7] M. Skoglundh, L.O. Löwendahl, J.E. Otterated, Appl. Catal. 77 (1991) 9–20.
[8] C.H. Bartholomew, Appl. Catal. A Gen. 212 (2001) 17–60.
[9] V. Kröger, M. Hietikko, U. Lassi, J. Ahola, K. Kallinen, R. Laitinen, R.L. Keiski, Top. Catal. 30–31 (2004) 469–474.
[10] B. Béguin, E. Garbowski, M. Primet, Appl. Catal. 75 (1991) 119–132.
[11] X. Chen, Y. Liu, G. Niu, Z. Yang, M. Bian, A. He, Appl. Catal. A Gen. 205 (2001) 159–172.
[12] A. Pfau, K.-D. Schierbaum, Surf. Sci. 6028 (1994).
[13] J.C.S. Dalton, B.P. Burroughs, A. Hamnett, A.F. Orchard, G. Thornton, (1975).
[14] C. Battistoni, V. Cantelli, M. Debenedetti, S. Kačiulis, G. Mattogno, A. Napoli, Appl. Surf. Sci. 144–145 (1999) 390–394.
[15] J. Gong, D. Wang, J. Li, K. Kamasamudram, N. Currier, A. Yezerets, Catal. Today (2018) 0–1.
[16] S. Ricote, G. Jacobs, M. Milling, Y. Ji, P.M. Patterson, B.H. Davis, Appl. Catal. A Gen. 303 (2006) 35–47.
[17] H.-W. Jen, G.. Graham, W. Chun, R.. McCabe, J.-P. Cuif, S.. Deutsch, O. Touret, Catal. Today 50 (1999) 309–328.
[18] F. Tao, M.E. Grass, Y. Zhang, D.R. Butcher, J.R. Renzas, Z. Liu, J.Y. Chung, B.S. Mun, M. Salmeron, G. a. Somorjai, Science (80-.). 322 (2008).
[19] E. Rogemond, R. Fréty, V. Perrichon, M. Primet, M. Chevrier, C. Gauthier, F. Mathis, Appl. Catal. A Gen. 156 (1997) 253–265.
[20] X. Auvray, L. Olsson, Appl. Catal. B Environ. 168–169 (2015) 342–352.
[21] M. Adamowska, V. Lauga, P. Da Costa, Top. Catal. 56 (2013) 267–272.
[22] Y. Xie, E. Rodrigues, N. Furtado, A. Matynia, T. Arlt, P. Rodatz, P. Da Costa, Top. Catal. 59 (2016) 1039–1043.
[23] C.A. Franchini, D. V. Cesar, M. Schmal, Catal. Letters 137 (2010) 45–54.
[24] Y. Yu Yao, J. Catal. 87 (1984) 152–162.
[25] J.R. González-velasco, J.A. Botas, R. Ferret, M.P. González-marcos, J. Marc, M.A. Gutiérrez-ortiz, 59 (2000) 395–402.
[26] N.D. Lang, S. Holloway, J.K. Nørskov, Surf. Sci. 150 (1985) 24–38.
[27] J.M. García-Cortés, J. Pérez-Ramírez, J.N. Rouzaud, A.R. Vaccaro, M.J. Illán-Gómez, C. Salinas-Martínez De Lecea, J. Catal. 218 (2003) 111–122.
[28] I. V. Yentekakis, V. Tellou, G. Botzolaki, I.A. Rapakousios, Appl. Catal. B Environ. 56 (2005) 229–239.
[29] S. Koukiou, M. Konsolakis, R.M. Lambert, I. V. Yentekakis, Appl. Catal. B Environ. 76 (2007) 101–106.
[30] Y. Minemura, M. Kuriyama, S. ichi Ito, K. Tomishige, K. Kunimori, Catal. Commun. 7 (2006) 623–626.
[31] H. Hattori, Chem. Rev. 95 (1995) 537–558.
[32] P.W. Davies, R.M. Lambert, Surf. Sci. 110 (1981) 227–249.

Chapter VI

CHAPTER VI: General conclusions

This chapter summarizes the main conclusions derived from the research of the influence of Na, K and Ca impurities related to the use of biodiesel, as well as P impurities coming from the automotive lubricants in the performance of Diesel Oxidation Catalysts (DOCs).

The continuously tightened European emission standards lead the introduction of an after-treatment system in order to reach the desired emission levels. The after-treatment system of current diesel exhaust consists on Diesel Oxidation Catalysts (DOCs) along with diesel particulate filters (DPF) and selective catalytic reduction catalysts (SCR). In addition, Euro VI established that the durability of the after treatment system has to be at least seven years or 700 000 km, requiring the use of more active and durable catalysts. Particularly, Diesel Oxidation Catalysts (DOCs) could efficiently eliminate the CO, unburned hydrocarbons and oxidize NO to NO_2, which plays a crucial role in the promotion of soot oxidation and the low-temperature activity for SCR. The DOC catalysts are mainly composed of noble metals (platinum, palladium) supported on high surface area compounds, as alumina. It is worth noting the addition of an oxygen storage phase, which would provide a better resistance to redox aging.

Moreover, the use of renewable energy sources has been gaining some attention during the last years. Biofuels, particularly biodiesel, has depicted as a promising alternative fuel to conventional diesel, as it presents similar calorific power and better carbon balance, which implies lower net emissions of CO_2. However, the use of biodiesel could influence in the activity and durability of the after-treatment system due to the presence of alkaline metals (Na, K, Ca) coming from its liquid-phase synthesis, as well as impurities coming from motor lubricants (P). As literature review has shown, these impurities can have an influence on the activity of Pt-Pd based catalysts. On the one hand, the presence of alkalis may influence the adsorption and strength of the bonds formed between the adsorbed species and the substrate. In addition, due to their highly basic properties they could provide a major contribution to the overall NO_x adsorption capacity of the catalyst. On the other hand, the accumulation of phosphorus species may modify the composition of the support by

reacting with it. Moreover, it could disturb the adsorption of reactants on the catalyst surface.

A reference DOC composed by $PtPd/CeZrO_2/La\text{-}Al_2O_3$ was synthesized by successive impregnations. In order to evaluate the catalytic behaviour of DOC at the end of its lifetime, Na, K, Ca and P impurities were added by impregnation in a percentage based on 35 L/km consumption during 700 000 km. The impact of alkali and alkaline earth metals (Na, K and Ca), phosphorus species (P) and its combinations, on the reference catalyst $PtPd/CeZrO_2/La\text{-}Al_2O_3$ diesel oxidation catalyst was evidenced by several characterization techniques like ICP, N_2 adsorption/desorption, XRD, TEM, XPS, H_2-TPR and NO-TPD. Finally, to evaluate the influence of these impurities on the catalytic performance of the catalyst, catalytic tests were carried out as described in Chapter II. To gain further insight into the detail of the modifications of the added impurities on the catalyst surface, in-situ DRIFTS experiments were also done.

The catalytic activity results showed that Na, K, Ca and P impurities have an influence on the CO, C_3H_6 and NO reaction rates. The electron-donor behaviour of alkali impurities enhanced the metal-electron acceptor adsorbates charge transfer in the case of CO, NO and O_2. Thus, in presence of Na and K impurities lower values of CO reaction rates were found, due to the "self-inhibition" effect, which would saturate the catalyst surface. Moreover, the high basicity of Ca made more difficult desorption of CO_2 produced by CO oxidation, decreasing the catalytic activity.

As the adsorption of oxygen was promoted, the redox capacities of the modified-catalysts decreased, as verified by H_2-TPR. However, it had a positive effect on propylene oxidation. Thus, it has been demonstrated that Na, K and Ca impurities increased C_3H_6 reaction rates due to its higher interaction with adsorbed oxygen (Chapter III).

The NO-TPD results evidenced that the addition of Na, K and Ca impurities modified the NO adsorption strength. The observed effects were due to the electronic properties of these impurities, which are related at the same time with the basicity: the higher basicity, the higher NO adsorption strength. Notwithstanding, it has been shown that the molar percentage of impurity contained on the catalyst played an important role. Thus, while Na and Ca impurities diminished the NO reaction rate, the lower amount of K increased the catalytic activity. Accordingly, it seems that it exists

a certain value at which the impurities would act as promoters instead of poisons as initially expected.

Higher amount of phosphorus impurities was incorporated to the catalyst. Characterization results evidenced the formation of phosphates, which could block the catalytic active sites. In addition, phosphorus species stabilized ceria phase on its reduced state, Ce^{3+}, which acted as an electron-donor under oxidizing atmospheres. Thus, it could inhibit the "self-poisoning" phenomenon of the catalyst surface produced by the excessive adsorption of CO and C_3H_6, increasing the reaction rates in presence of phosphorus. Nevertheless, the formation of phosphates blocked the adsorption sites in agreement with the significant decrease of NO adsorption showed by NO-TPD.

The results obtained by in-situ DRIFTS experiments were used to gain important insights into these catalytic results. The study of the catalyst surface has shown the formation of nitrites/nitrates as intermediates for NO oxidation, as well as formates/acetates for C_3H_6 and CO involved reactions. In some cases isocyanates and cyanides species were also observed, related with NO to N_2O reduction via SCR-C_3H_6.

The higher intensity of nitrites/nitrates corresponding bands evidenced the metal-NO interaction related with the electronic promotion of Na and K impurities. In addition to the lower molar percentage, the atomic weight of K also influenced its effect on the NO adsorption. The large valence shell of the K cations would increase the transferred charge. Thus, the greater electronic effect of K would favor NO adsorption, in agreement with the higher NO reaction rate. As well, the basicity of the catalyst increased after Ca incorporation, leading high nitrites/nitrates adsorption that were stable with the temperatures, in agreement with the lower reaction rate found previously.

In addition, the negative electrostatic potential around alkali impurities decreased the bonding energy of electron-accepting adsorbates like CO and O_2, promoting CO and C_3H_6 co-oxidations as already discussed. Otherwise, the strengthening of oxygen adsorption promoted the reaction with the adjacent adsorbed species, such as nitrates, which are also strong oxidants.

The blocking of adsorption sites due to phosphates formation have been evidenced by the few adsorption peaks observed on obtained P-PtPd catalyst DRIFT spectra.

In order to verify the durability of the DOC under harsh conditions, all the catalysts were hydrothermally aged at 850 ºC during 16 h. The physico-chemical characterization results evidenced the leaching and the sintering of noble metal particles, increasing the size of Pt-Pd bimetallic particles. In addition, the redox abilities of the catalyst were also diminished after the HT-aging.

In general, lower reaction rates were found after HT-aging when compared with the stabilized catalysts. The leaching of Na and K impurities as well as the catalyst sintering, attenuated the promoted adsorption of electron acceptor adsorbates, as verified by the lower intensity bands observed on DRIFT spectra. Nevertheless, as previously discussed, the amount of impurities played an important role on their effect. Thus, although it could promote CO oxidation by preventing the "self-inhibition effect", the C_3H_6 and NO reaction rates decreased.

The amount of Ca impurities found did not vary significantly after HT-aging, thus their effects continued in addition to the catalyst sintering, decreasing the catalytic activity.

It is worth noting that the metallic state and bigger size of Pt-Pd bimetallic particles enhanced NO oxidation. However, the sintering of the catalyst decreased the number of catalytic active sites, decreasing the NO reaction rates.

Finally, the adsorption sites were blocked again due to the presence phosphates. It would inhibit the catalyst surface saturation, which has a positive effect on CO and C_3H_6 reaction rates. Nevertheless, the redox capacities were diminished as verified by XPS and H_2-TPR analyses, decreasing catalytic activity in the case of NO oxidation.

Even if several conclusions were found during this study, further investigations would be advice:

- The study at similar percentage of impurities is advisable, in order to better compare the impact of each impurity.
- The kind of impurities employed could be extended, adding for example Zn impurities and combination with the already alkali and alkaline earth impurities here studied.

- The use of biodiesel is known to increase the oxygenated hydrocarbon emissions. Thus, it could be interesting to complete the research of Na, K, Ca and P impurities influence on a DOC catalyst adding oxygenated HC emissions to the reactant mixture.

Annexes

ANNEX I

The graphs AI-1 to AI-4 presented in this Annex correspond to supplementary results of the catalyst characterization by N_2 adsorption/desorption (Section Ia).

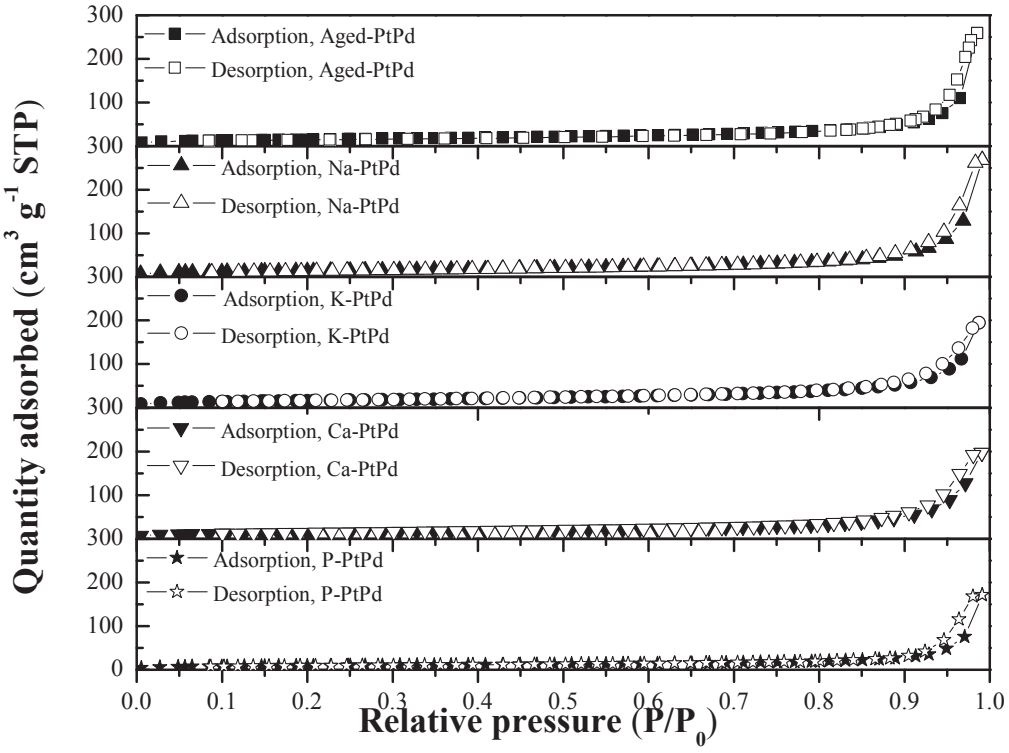

Figure AI-1. Adsorption/desorption isotherms of modified and aged catalysts.

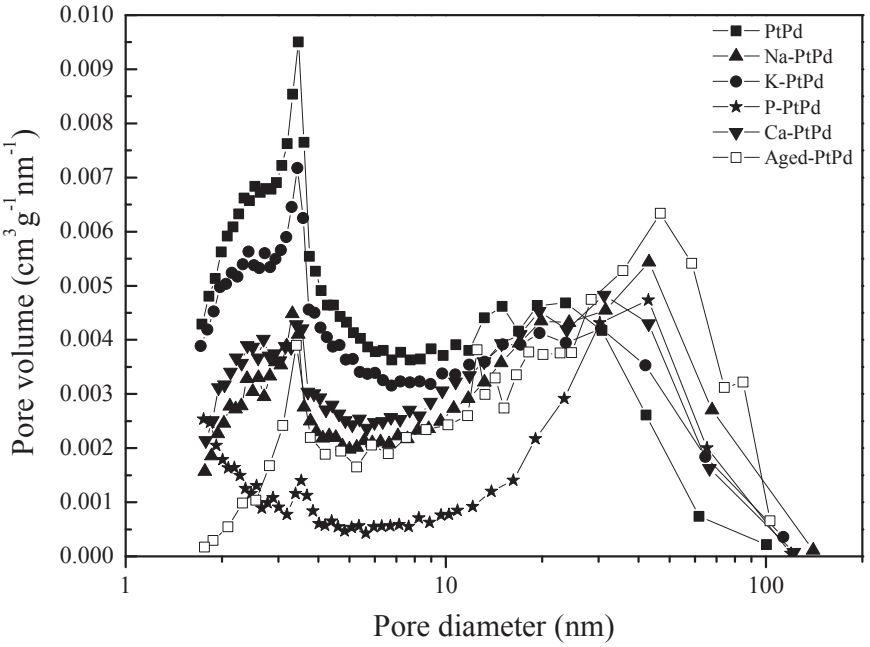

Figure AI-2. The BJH pore size distribution curves of the referenec, hydrothermally aged and modified catalysts.

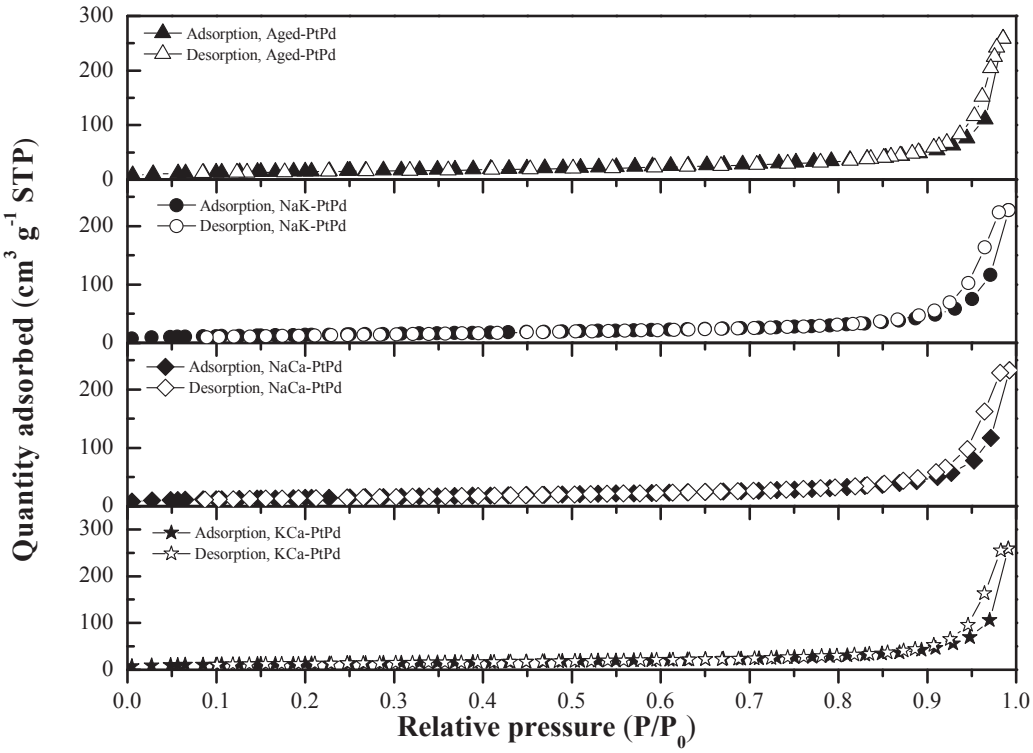

Figure AI-3. Adsorption/desorption isotherms of aged and combined Na, K and Ca couple modified catalysts.

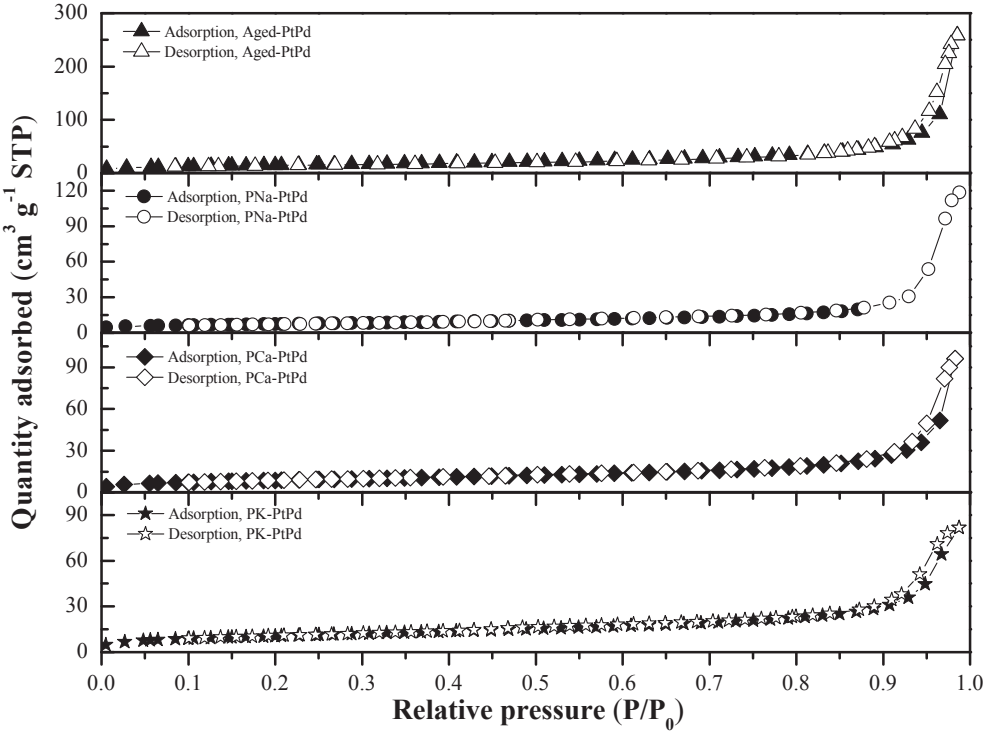

Figure AI-4. Adsorption/desorption isotherms of aged and phosphorus combination modified catalysts.

The results exposed in Figure AI-5 were related to the already discussed influence of the reaction between C_3H_6 and NO_2, which apparently decreases the NO conversion (section II-b-ii).

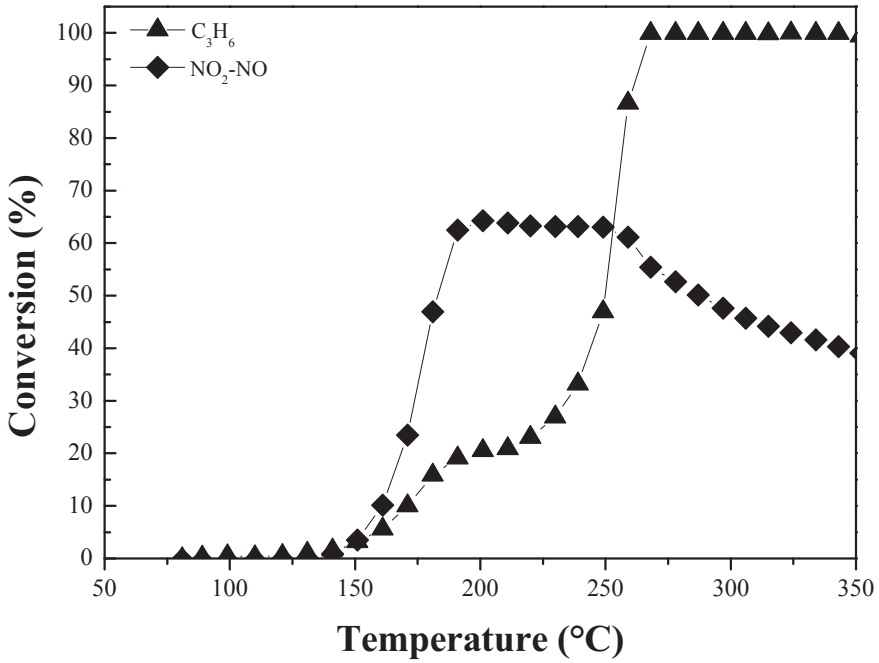

Figure AI-5. Propylene and NO_2-NO conversion in function of the temperature during the heating ramp of the first catalytic cycle. Mixture conditions: 300 ppm C_3H_6, 500 ppm NO_2, 10% O_2 and He as balance. Catalyst mass: 50 mg, 250 ml min^{-1}, GHSV = 135 000 h^{-1}.

In addition, in Figure AI-6 was shown the influence of water adsorption on the catalytic active sites, which increases the competition between the reactants (Section II-b-ii).

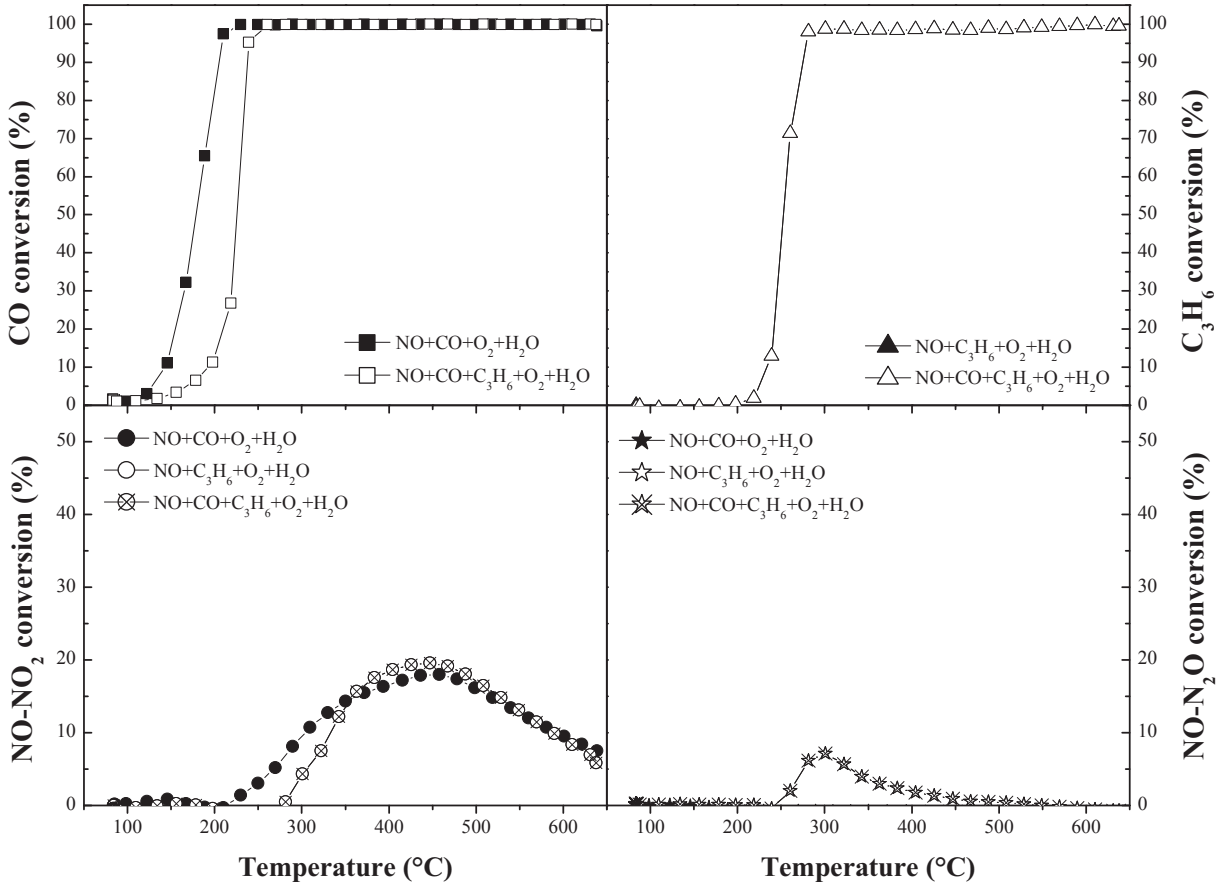

Figure AI-6. CO, C_3H_6, NO to NO_2 and NO to N_2O conversion obtained by different mixtures employed during the heating ramp of the first catalytic cycle. Operating conditions: 50 mg, 250 ml min^{-1}, GHSV = 135 000 h^{-1}; 300 ppm CO and/or 300 ppm C_3H_6, 500 ppm NO, 10% O_2, 5% CO_2, 3.5% H_2O and He as balance.

Finally, Figures AI-7 and 8 displayed the CO, C_3H_6, NO-NO_2 and NO-N_2O conversion values in function of the temperature after impurities combination (Section II-d).

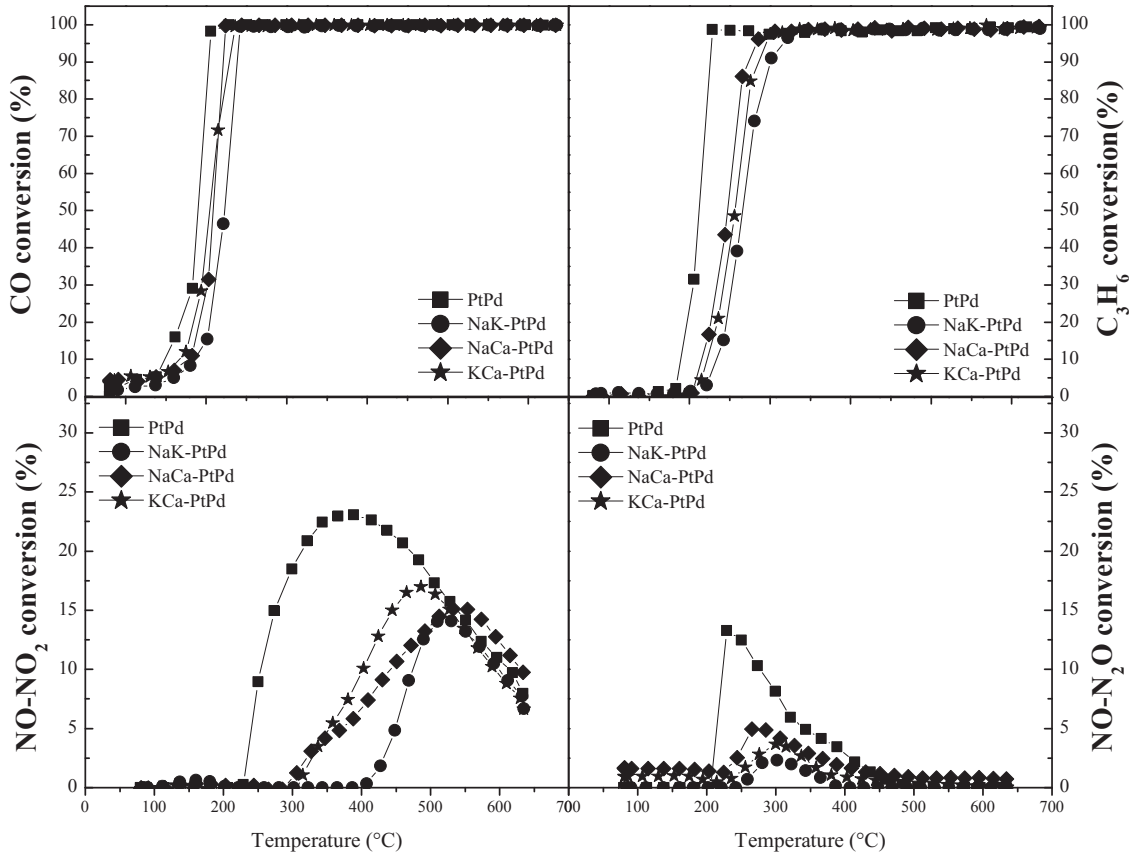

Figure AI-7. CO, C_3H_6, NO-NO_2 and NO-N_2O conversion after modification of reference with combination of alkali impurities during the heating ramp of the first catalytic cycle. Operating conditions: 50 mg, 250 ml min^{-1}, GHSV = 135 000 h^{-1}; 300 ppm CO, 300 ppm C_3H_6, 500 ppm NO, 10% O_2, 5% CO_2, 3.5% H_2O and He as balance.

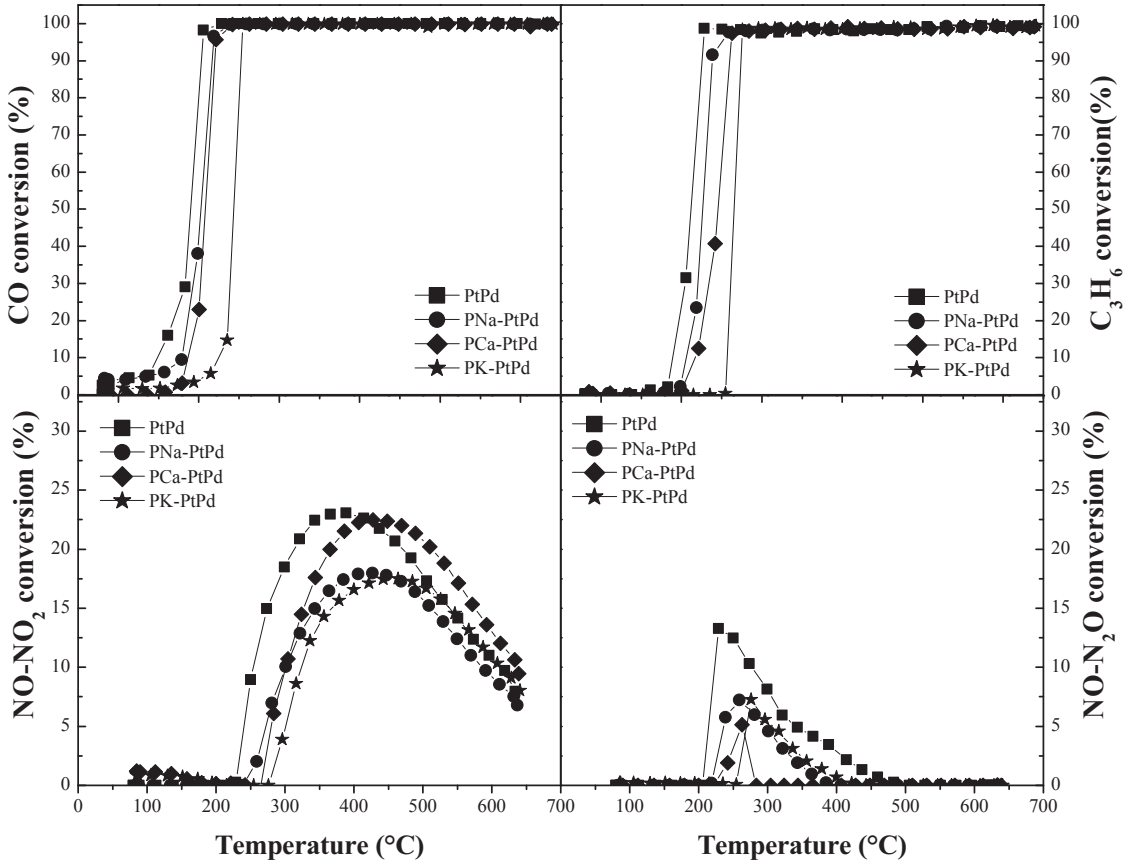

Figure AI-8. CO, C_3H_6, $NO-NO_2$ and $NO-N_2O$ conversion after modification of reference with combination of phosphorus-alkali impurities during the heating ramp of the first catalytic cycle. Operating conditions: 50 mg, 250 ml min^{-1}, GHSV = 135 000 h^{-1}; 300 ppm CO, 300 ppm C_3H_6, 500 ppm NO, 10% O_2, 5% CO_2, 3.5% H_2O and He as balance.

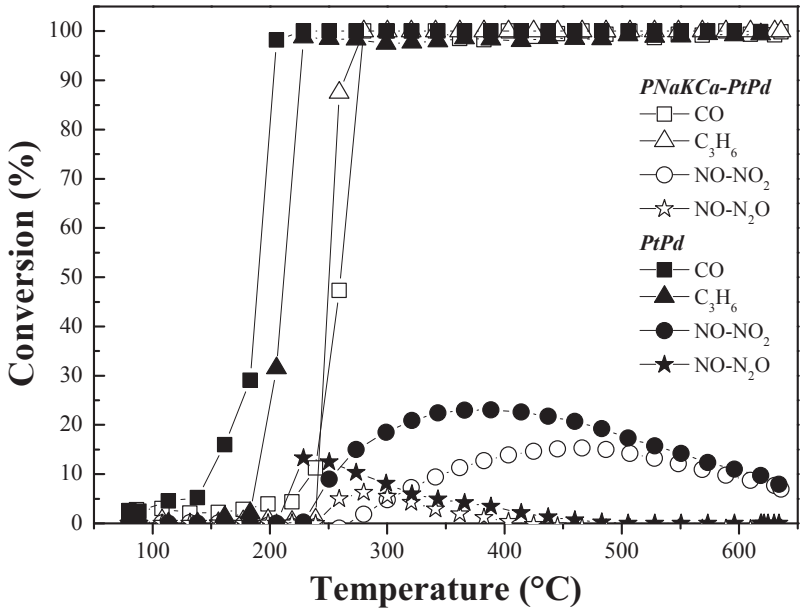

Figure AI-9. CO, C_3H_6, NO-NO_2 and NO-N_2O conversion obtained during the heating ramp of the first catalytic cycle for the reference and PNaKCa-PtPd catalysts. Operating conditions: 50 mg, 250 ml min^{-1}, GHSV = 135 000 h^{-1}; 300 ppm CO, 300 ppm C_3H_6, 500 ppm NO, 10% O_2, 5% CO_2, 3.5% H_2O and He as balance.

ANNEX II

Table AII-1. Bands position and the corresponding assignments of surface species in DRIFT spectra.

Surface species		Peak position (cm^{-1})	Infrared vibration	Reference
Bridging nitrites	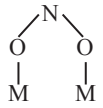	1314-1266	$\nu_{as}(NO_2)$	[5]
		1230-1276	$\nu_{s}(NO_2)$	
Monodentate nitrites	O-N-O-M	1470-1375	ν(N=O)	[6]
		1206-1065	ν(N-O)	
Bidentate nitrites	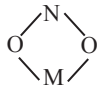	1375-1314	$\nu_{s}(NO_2)$	
		1203-1176	$\nu_{as}(NO_2)$	
Bridging nitrates	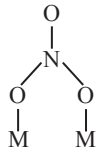	1600-1650	$\nu_{s}(NO_2)$	[4,6–11]
		1200-300	$\nu_{as}(NO_2)$	
Bidentate nitrates	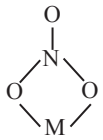	1590-1550	$\nu_{s}(NO_2)$	
		1200-1300	$\nu_{as}(NO_2)$	
Monodentate nitrates	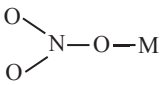	1510-1508	$\nu_{as}(NO_2)$	[2]
		1275-1250	$\nu_{s}(NO_2)$	
Linear or bent NO on Pt	$(NO)^-$	1680-1780	ν(N-O)	[5,7,12,13]
P-OH	$(HO)^-$	3670	ν(O-H)	[14]
Free OH	$(HO)^-$	3684		
Formates	$(HCOO)^-$	1373	$\nu_{s}(COO^-)$	[15–21]
		1410-1390	δ(CH)	
		1585	$\nu_{as}(COO^-)$	
Adsorbed hydrocarbon fragments	$(HC)^-$	2965, 2938	$\nu_{as}(CH)$	
		2910, 2908	$\nu_{s}(CH)$	
Acetates	$(CH_3\text{-}(C{=}O)\text{-}O)^-$	1460-1440	$\nu_{s}(COO^-)$	
		1555-1545	$\nu_{as}(COO^-)$	
Carbonates	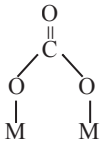	1645	$\nu_{as}(COO^-)$	[21–23]
		1350-1345	$\nu_{s}(COO^-)$	
Carbonyls on partially oxidized Pt	(>C=O)	2113, 2120	ν(CO)	[15,16,21,24]
Cyanide	$(N{+}C)^-$	2155 2141	ν(C+N)	[15,25,26]
Isocyanates	$(N{=}C{=}O)^-$	2205 2170	ν(N=C=O)	[21,27–29]

In order to verify the interaction of Na, K, Ca and P impurities with OH groups on Al_2O_3 surface, an ex-situ study under 40 ml min^{-1} of He at 35 ºC was made to PtPd reference and modified catalysts. Previous studies [28,29] identified five types of OH species depending mainly from number of Al^{3+} ions associated with OH groups, as well as the coordination between them. In Table AII-2 are resumed the corresponding assignments to principal bands observed on the 3900-3500 cm^{-1} region.

Table AII-2. Bands position and the corresponding assignments of OH groups on alumina surface on the 3900-3500 cm^{-1} region.

Surface species		Peak position (cm^{-1})	Infrared vibration
Type Ib (Al_{VI})OH		3800-3785	ν(OH)
Type Ia (Al_{IV})OH		3780-3760	ν(OH)
Type IIb (Al_{VI})$_2$OH	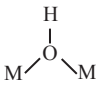	3745-3740	ν(OH)
Type IIa ($Al_{IV}Al_{VI}$) OH		3735-3720	ν(OH)
Type III (Al_{VI})$_3$OH	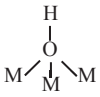	3710-3680	ν(OH)

As it can be seen in Figure AII-1, the bands at 3775, 3735 and 3670 cm^{-1} are associated with species type Ia, IIa and III. After addition of Na, K and Ca slightly modifications of OH bands were observed, probably due to the changes on the basicity of the catalysts. It is worth noting the spectra of P-PtPd catalyst, which showed an intense peak at 3670 cm^{-1}, associated with the P-OH interaction. This is in agreement with the already justified phosphates formation on catalyst surface.

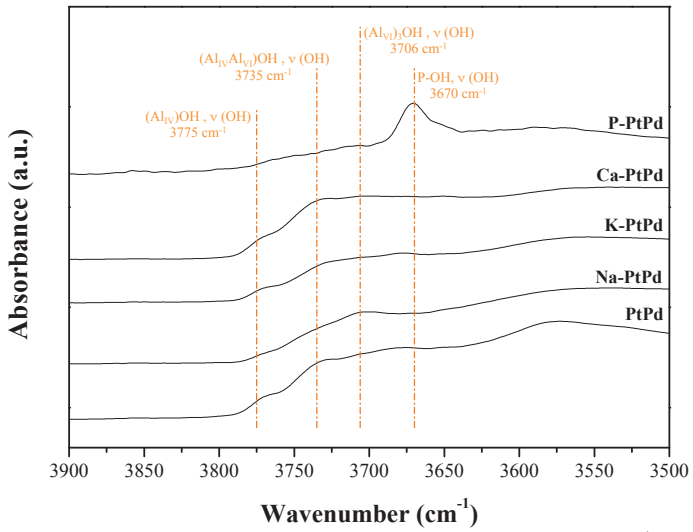

Figure AII-1. DRIFT spectra in the region 3900-3500 cm^{-1} of PtPd reference and Na-, K-, Ca- and P-modified catalysts under 40 ml min^{-1} of He at 35 ºC.

Figures AII-2, 3, 4 and 5 corresponds to the evolution of the NO adsorbed species on Na-, K-, Ca- and P-PtPd increasing the temperature (Chapter IV, section I-b). As discussed in Chapter IV, when the temperature reached higher values the nitrites to nitrates transformation was detected. In addition, at higher temperature values, nitrates decomposed to NO_2, which desorbed in form of NO due to the displaced thermodynamic equilibrium. The higher temperatures at which the variation of the intensity bands was produced (Figures AII-2, 3 and 4) corresponds with the desorption peaks found by NO-TPD in Chapter III, that was ascribed to the electronic effects produced by alkali impurities. At 500 ºC, any of the catalysts presented adsorbed species, in agreement with the total desorption showed by NO-TPD.

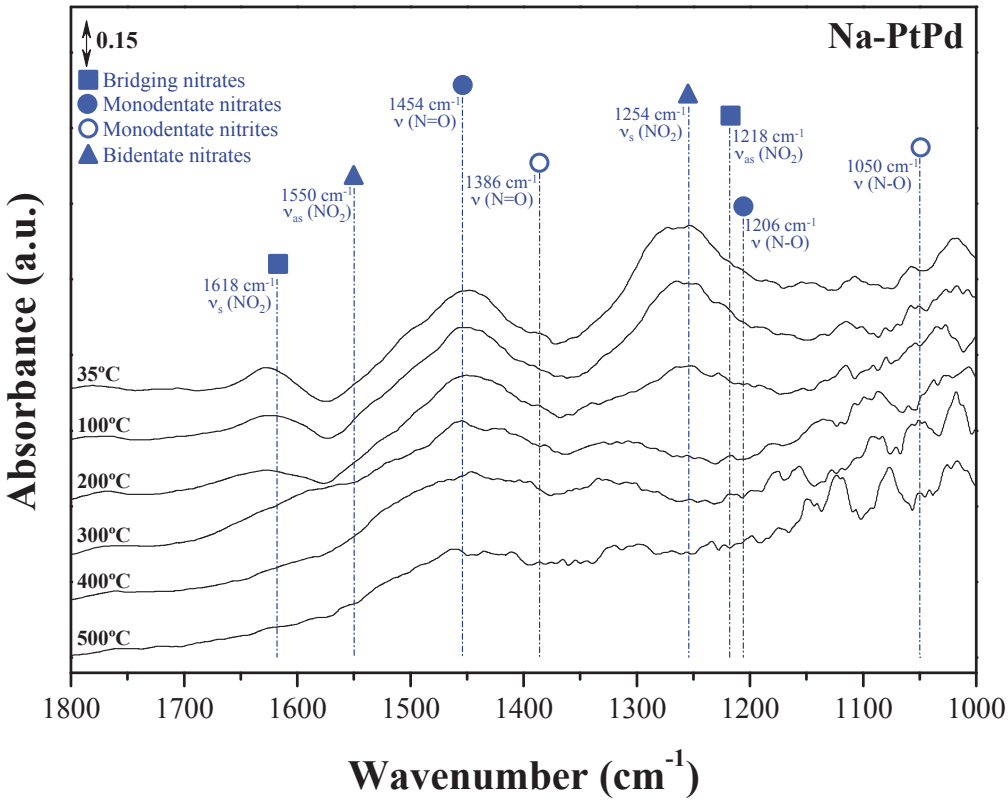

Figure AII-2. DRIFT spectra in the region 1800-1100 cm^{-1} of Na-PtPd catalyst during NO desorption at temperatures in the interval of 35-500°C. Operating conditions: 40 ml min^{-1} He; NO stored at 35 ºC until saturation and subsequently NO-TPD.

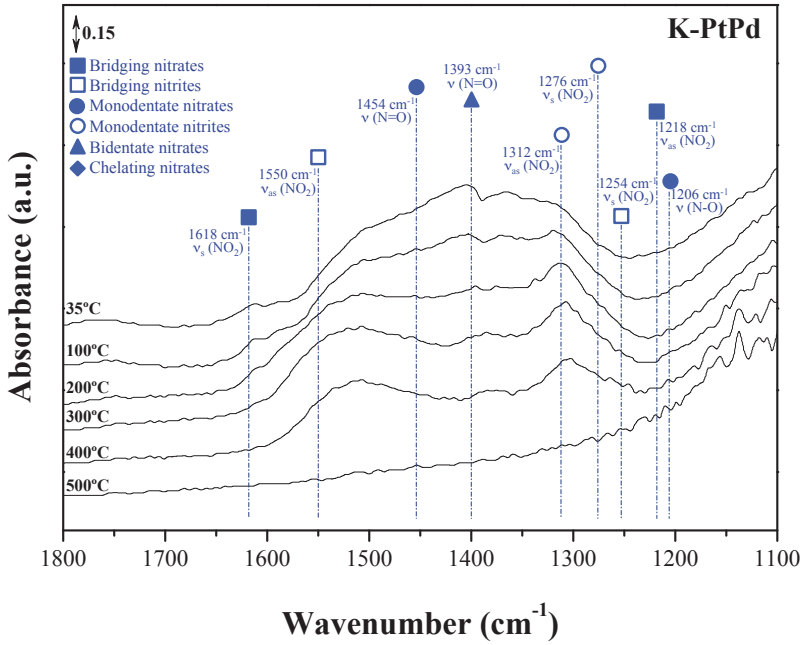

Figure AII-3. DRIFT spectra in the region 1800-1100 cm^{-1} of K-PtPd catalyst during NO desorption at temperatures in the interval of 35-500°C. Operating conditions: 40 ml min^{-1} He; NO stored at 35 ºC until saturation and subsequently NO-TPD.

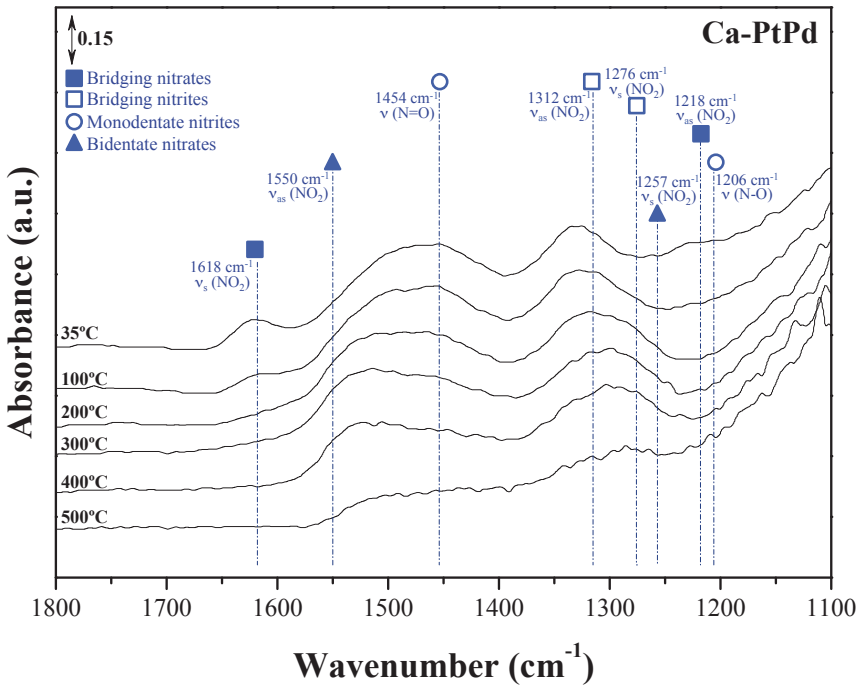

Figure AII-4. DRIFT spectra in the region 1800-1100 cm^{-1} of Ca-PtPd catalyst during NO desorption at temperatures in the interval of 35-500°C. Operating conditions: 40 ml min^{-1} He; NO stored at 35 ºC until saturation and subsequently NO-TPD.

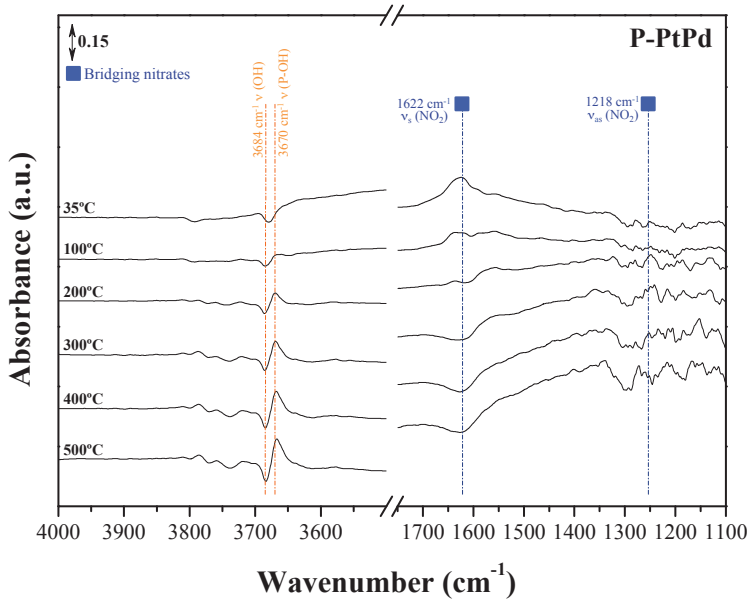

Figure AII-5. DRIFT spectra in the region 1800-1100 cm^{-1} of P-PtPd catalyst during NO desorption at temperatures in the interval of 35-500°C. Operating conditions: 40 ml min^{-1} He; NO stored at 35 ºC until saturation and subsequently NO-TPD.

Figures AII-6 and 7 corresponds to supplementary data of Chapter IV, section II-b. Figure AII-6 evidenced the adsorption of $NO+O_2$ by the higher intensity of nitrates species increasing the time.

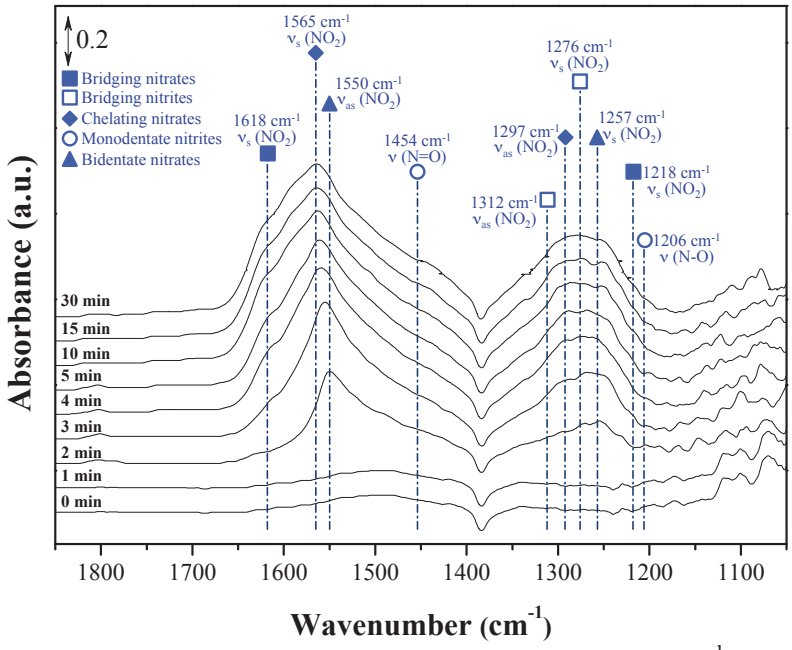

Figure AII-6. DRIFT spectra in the region 1800-1100 cm^{-1} of PtPd catalyst during $NO+O_2$/He adsorption at 35 ºC. Operating conditions: 40 ml min^{-1} He; 500 ppm NO, 10% O_2, He as balance.

Otherwise, in Figure AII-7 was evidenced the inhibition of NO adsorption in the case of P-PtPd catalyst due to the phosphates presence blocking the adsorption sites.

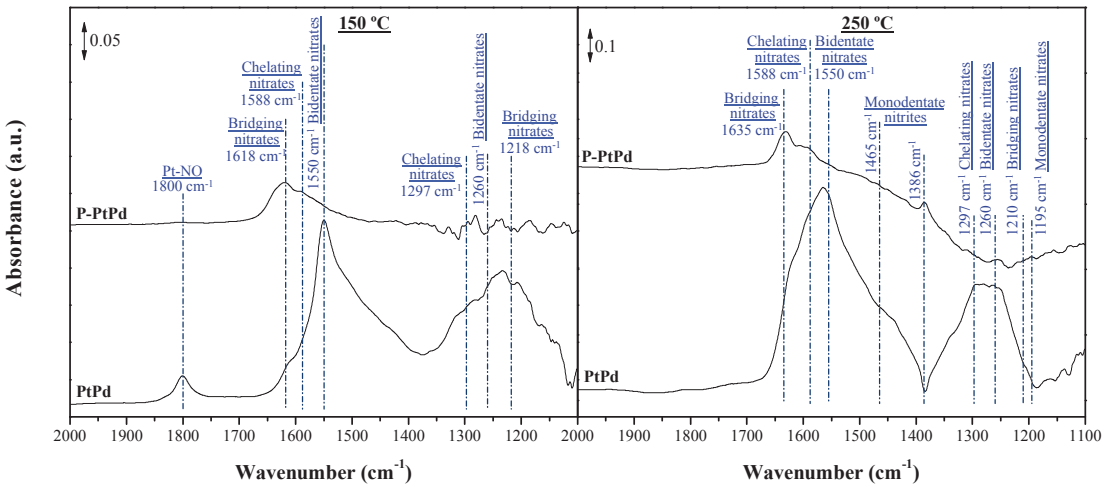

Figure AII-7. DRIFT spectra of PtPd-reference and P-PtPd catalysts at 150ºC (left) and 250ºC (right) after 60 min under simulated exhaust conditions. FT-IR chamber feed: 500 ppm NO, 10% O_2, He as balance; 40 ml min^{-1}.

Figures AII-8 and 9 present the results obtained switching from NO or NO + O_2 to C_3H_6 in function of the time for K- and Ca-PtPd catalysts (section III, Chapter IV). Similarly than in the case of reference and Na-PtPd catalysts, the reaction between nitroxy species and C_3H_6 is evidenced by the decrease of nitritres/nitrates bands intensities.

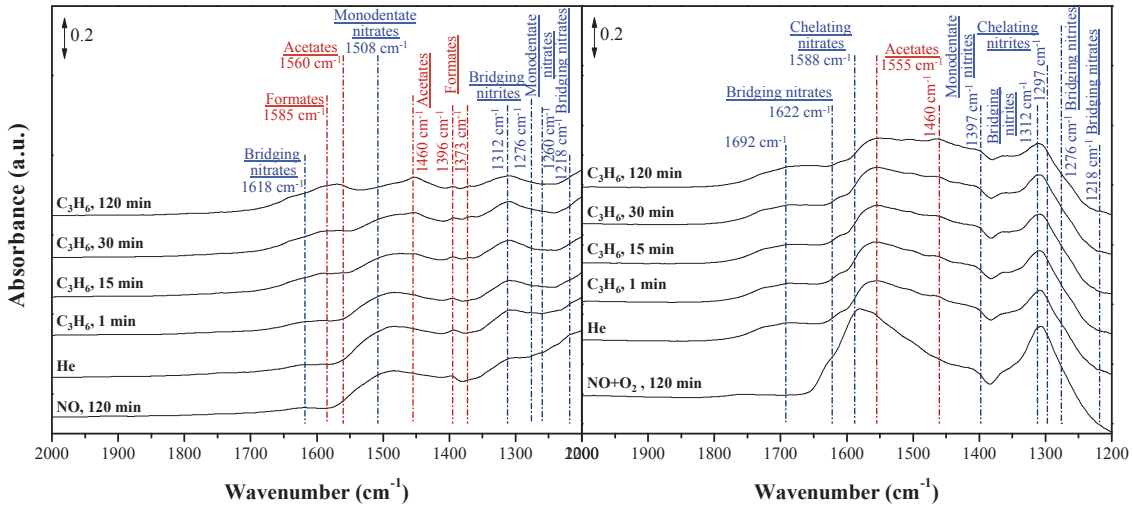

Figure AII-8. DRIFT spectra of K-PtPd at 250ºC under NO (left) or NO + O_2 (right) /He/C_3H_6 after 120 min. FT-IR chamber feed: 500 ppm NO, (10% O_2), He as balance; He purge; 300 ppm C_3H_6, He as balance; total flow 40 ml min^{-1}.

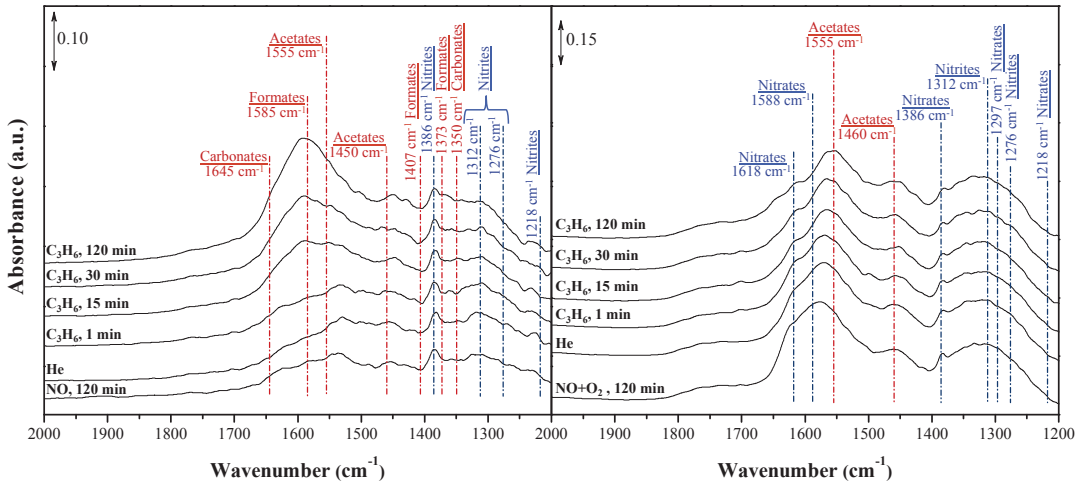

Figure AII-9. DRIFT spectra of Ca-PtPd at 250ºC under NO (left) and NO + O_2 (right)/He/C_3H_6 after 120 min. FT-IR chamber feed: 500 ppm NO, (10% O_2), He as balance; He purge; 300 ppm C_3H_6, He as balance; total flow 40 ml min^{-1}.

Finally, in Figures AII-9 to 12 are present the results obtained for K-, Ca- and P-PtPd catalysts after NO + O_2 exposition until saturation and subsequent exposition to CO. As explained in section III in Chapter IV when alkali impurities, such as K (Figure AII-11), were added to the catalyst, higher amount of nitrites/nitrates were formed due to the enhanced dissociation of NO, saturating the catalyst surface. The band attributed to Pt-NO interaction still presented after CO exposure, which proves the stability and high strength of Pt-NO interaction. Thus, less adsorption sites were available for CO adsorption, even if its dissociation is also improved in presence of alkalis.

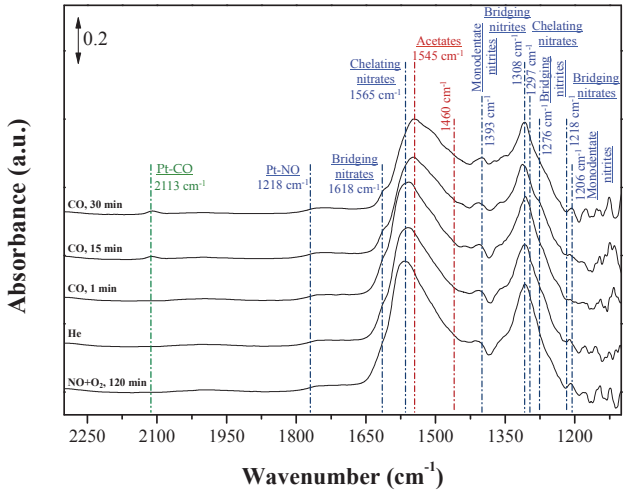

Figure AII-10. DRIFT spectra of K-PtPd at 250ºC under NO + O_2 /He/CO after 120 min. FT-IR chamber feed: 500 ppm NO, 10% O_2, He as balance; He purge; 300 ppm CO, He as balance; total flow 40 ml min^{-1}.

In the case of Ca-PtPd, the higher basicity of the catalyst was demonstrated by the presence of carbonates species (Figure AII-11).

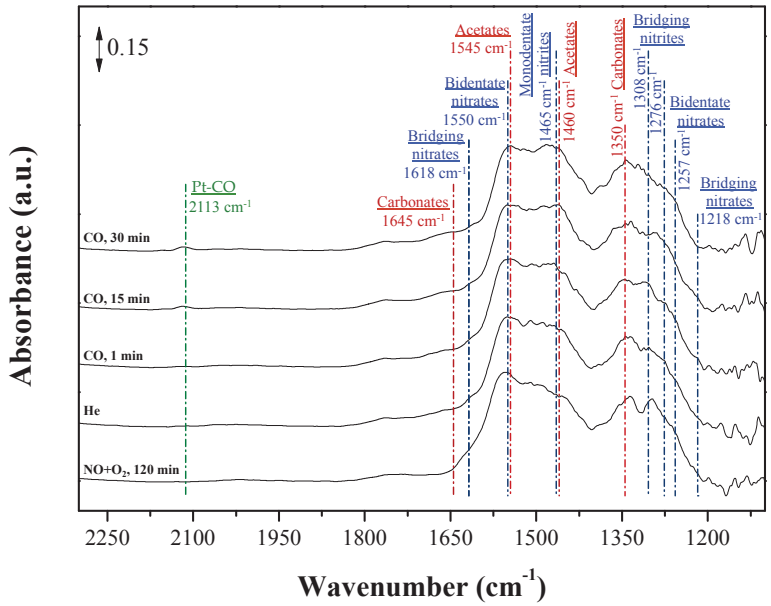

Figure AII-11. DRIFT spectra of Ca-PtPd at 250ºC under NO + O_2 /He/CO after 120 min. FT-IR chamber feed: 500 ppm NO, 10% O_2, He as balance; He purge; 300 ppm CO, He as balance; total flow 40 ml min^{-1}.

Similarly than when exposed to C_3H_6 instead of CO, the presence of phosphates avoided the adsorption on P-PtPd catalyst (Figure AII-12).

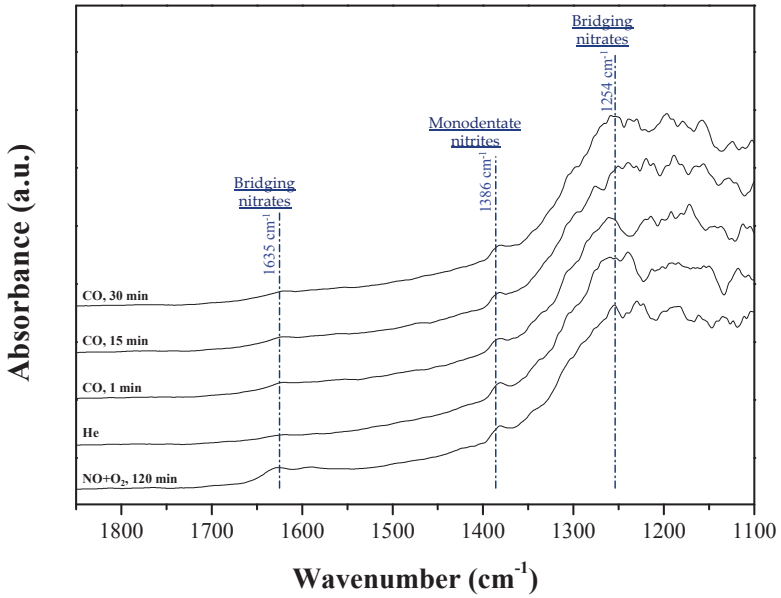

Figure AII-12. DRIFT spectra of P-PtPd at 250ºC under NO + O_2 /He/CO after 120 min. FT-IR chamber feed: 500 ppm NO, 10% O_2, He as balance; He purge; 300 ppm CO, He as balance; total flow 40 ml min^{-1}.

References:

[1] S. Koukiou, M. Konsolakis, R.M. Lambert, I. V. Yentekakis, Appl. Catal. B Environ. 76 (2007) 101–106.
[2] K.I. Hadjiivanov, Catal. Rev. Sci. Eng. 42 (2000) 71–144.
[3] A. Bourane, O. Dulaurent, S. Salasc, C. Sarda, C. Bouly, D. Bianchi, J. Catal. 204 (2001) 77–88.
[4] P. Granger, H. Praliaud, J. Billy, L. Leclercq, G. Leclercq, Surf. Interface Anal. 34 (2002) 92–96.
[5] S.J. Huang, A.B. Walters, M.A. Vannice, Appl. Catal. B Environ. 26 (2000) 101–118.
[6] Y. Su, M.D. Amiridis, Catal. Today 96 (2004) 31–41.
[7] B. Westerberg, E. Fridell, J. Mol. Catal. A Chem. 165 (2001) 249–263.
[8] A. Kotsifa, D.I. Kondarides, X.E. Verykios, Appl. Catal. B Environ. 72 (2007) 136–148.
[9] J.Y. Luo, W.S. Epling, G. Qi, W. Li, Catal. Letters 142 (2012) 946–958.
[10] R.F. Van Slooten, B.E. Nieuwenhuys, J. Catal. 122 (1990) 429–437.
[11] M. Primet, J.M. Basset, E. Garbowski, M. V Mathieu, J. Am. Chem. Soc. (1972) 3655–3659.
[12] G. Socrates, Infrared and Raman Characteristic Group Frequencies, 2004.
[13] D.K. Captain, M.D. Amiridis, 389 (1999) 377–389.
[14] W. Schießer, H. Vinek, A. Jentys, Appl. Catal. 33 (2001) 263–274.
[15] M. Haneda, N. Bion, M. Daturi, J. Saussey, J.C. Lavalley, D. Duprez, H. Hamada, J. Catal. 206 (2002) 114–124.
[16] G. Bamwenda, a Ogata, a Obuchi, J. Oi, K. Mizuno, J. Skrzypek, Appl. Catal. B Environ. 6 (1995) 311–323.
[17] M. Huuhtanen, T. Kolli, T. Maunula, R.L. Keiski, Catal. Today 75 (2002) 379–384.
[18] K. Shimizu, H. Kawabata, A. Satsuma, T. Hattori, J. Phys. Chem. B 103 (1999) 5240–5245.
[19] V. Matsouka, M. Konsolakis, R.M. Lambert, I. V. Yentekakis, Appl. Catal. B Environ. 84 (2008) 715–722.
[20] C. Morterra, G. Magnacca, Catal. Today 27 (1996) 497–532.
[21] K. ichi Shimizu, J. Shibata, H. Yoshida, A. Satsuma, T. Hattori, Appl. Catal. B Environ. 30 (2001) 151–162.
[22] O.S. Alexeev, S.Y. Chin, M.H. Engelhard, L. Ortiz-Soto, M.D. Amiridis, J. Phys. Chem. B 109 (2005) 23430–23443.
[23] F.C. Meunier, V. Zuzaniuk, J.P. Breen, M. Olsson, J.R.H. Ross, Catal. Today 59 (2000) 287–304.
[24] N. Bion, J. Saussey, M. Haneda, M. Daturi, J. Catal. 217 (2003) 47–58.
[25] X. Auvray, L. Olsson, Appl. Catal. B Environ. 168–169 (2015) 342–352.
[26] A.A. Davydov, S. Branch, 54 (1991) 287–291.
[27] H.Y. Huang, R.Q. Long, R.T. Yang, Energy & Fuels 15 (2001) 205–213.
[28] H. Knözinger, P. Ratnasamy, Catal. Rev. Sci. Eng. 17 (1978) 31–70.
[29] A.A. Tsyganenko, V.N. Filimonov, Spectrosc. Lett. (1972) 477–487.

ANNEX III

In Figure AIII-1 is presented the H_2-TPR results of HT-K-PtPd and HT-Ca-PtPd catalysts. In both cases similar results than to the others HT-aged catalysts were found, only a broad beak around 400 ºC corresponding to the reduction of superficial CeO_2 is visible.

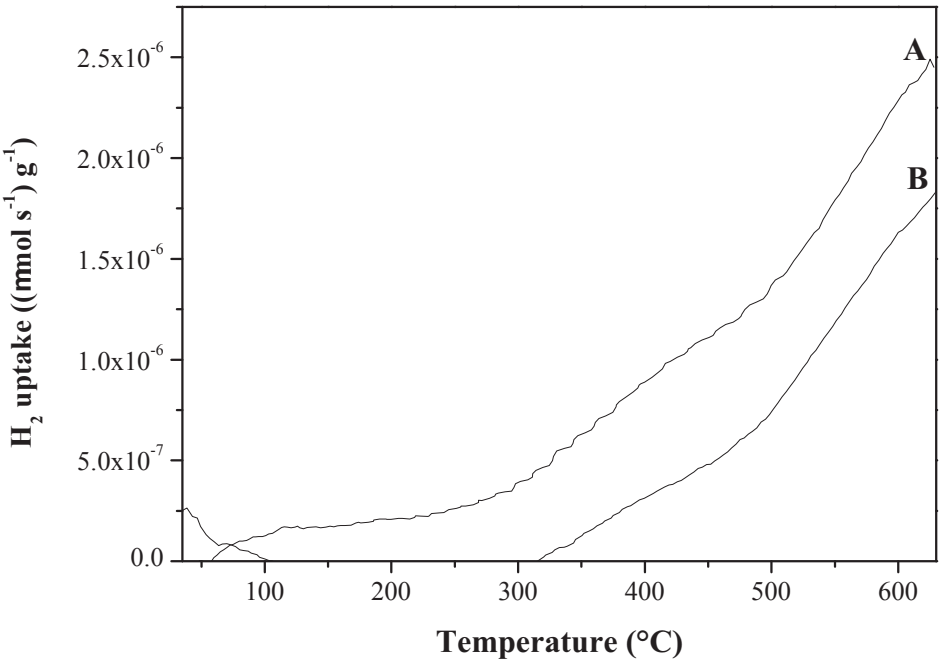

Figure AIII-2. H_2-TPR profiles of (A) HT-K-PtPd and (B) HT-Ca-PtPd catalysts.

ANNEX IV

Complementary information of the reference catalyst is present in this Annex.

Firstly, in order to evaluate the influence of the support on the catalytic activity, experiments with Al_2O_3, La-Al_2O_3 and $CeZrO_2$/La-Al_2O_3 were evaluated. As it can be seen in Figure AIV-1, the γ-Al_2O_3 calcined did not present any activity. However, when it was doped by lanthanum, CO, C_3H_6 and NO oxidation took place. The catalytic activity presented by La_2O_3-Al_2O_3 catalyst is related to its acid-base properties. Previous studies [1,2] have proved that the basic properties of lanthanum makes it catalytically active.

Once the cerium-zirconium was impregnated, the temperature at which 50% conversion of CO and C_3H_6 were attained decreased (Figure AIV-1). The catalytic activity of ceria-zirconia oxides has been already related with its high oxygen storage capacity (OSC). Adamowska et al. [3] proposed that oxygen vacancies in ceria-zirconia lattice leads to the so-called "coordinatively unsaturated sites" ("cus"), which allows reactive adsorption on cerium cation active sites. Furthermore, the ceria phase promotes NO adsorption and oxidation to nitrates, as verified by DRIFTS study (section I-a, Chapter IV). Thus, the oxidation of NO detected in absence of platinum-palladium can be related to the reaction on the oxygen vacancies formed upon the introduction of zirconium ions on the ceria structure [4,5].

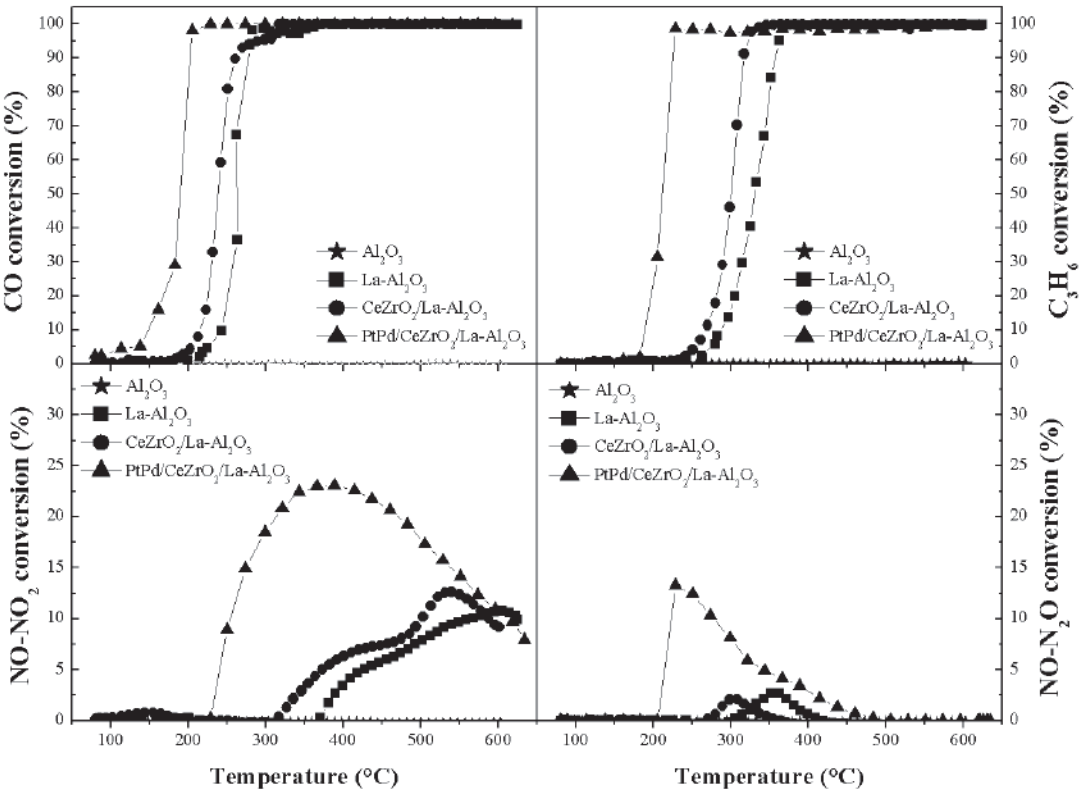

Figure AIV-1. CO, C_3H_6, NO-NO_2 and NO-N_2O conversion obtained for the different support phases during the heating ramp of the first catalytic cycle. Operating conditions: 50 mg, 250 ml min^{-1}, GHSV = 135 000 h^{-1}, 300 ppm CO, 300 ppm C_3H_6, 500 ppm NO, 10% O_2, 5% CO_2, 3.5% H_2O and He as balance.

Otherwise, the activity test procedure was carried out three times to evaluate the reproducibility of the results and the modification of the reference catalyst in operating conditions (Figure AIV-2). CO and C_3H_6 conversion cycles were reproducible when three cycles were tested, and did not present hysteresis in these cases, reaching total conversion on both cases at the same temperature.

On the contrary, when NO total conversion was evaluated it can be observed the presence of a light hysteresis on the conversion curves. PtPd catalyst was more active at low temperature during cooling although the top conversion was similar in both phases. One potential explanation of this behaviour is a reversible oxidation of the active phase. It is thus proposed that at high temperatures platinum is oxidized by NO_2 or O_2 to form an oxide that is less catalytically active than the metallic platinum particle. At lower temperatures the particle would be reduced back to its original state, most likely by NO [6]. It is known that, at low temperature, platinum oxide can form

due to the high oxygen concentration and the formation of NO_2 [7,8] and that platinum and palladium oxides are less active for NO oxidation than metallic phase.

Beside these results, very close superposition of the NO oxidation activity was found during cooling and heating steps respectively, and that therefore the observed hysteresis was entirely reversible.

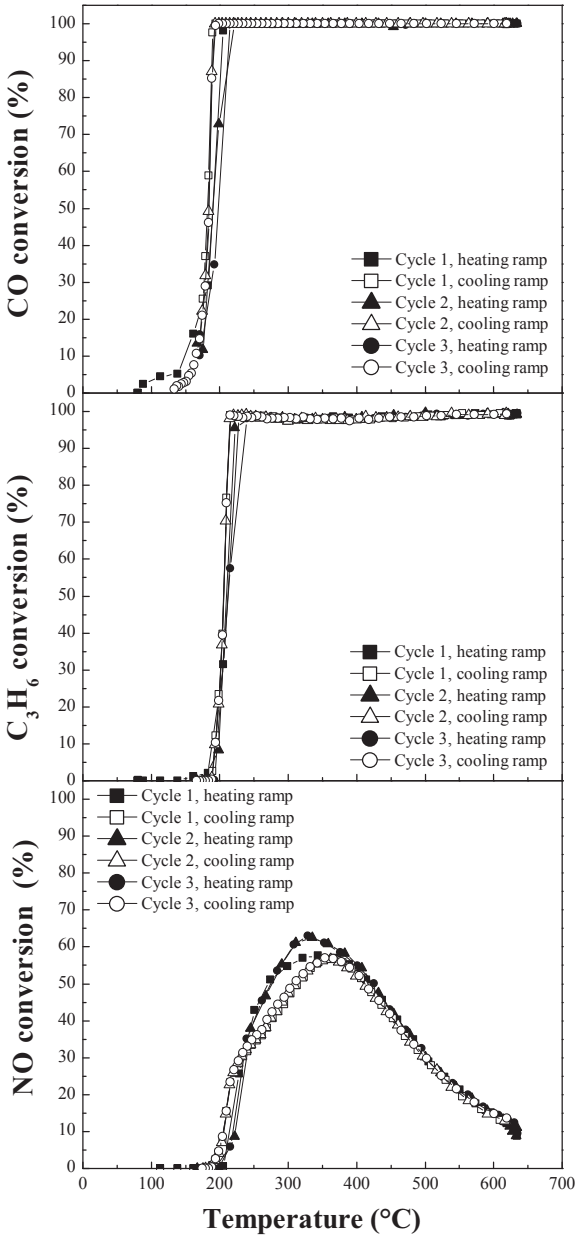

Figure AIV-2. CO, C_3H_6 and NO conversion obtained for the reference catalyst during the three catalytic reaction cycles. Operating conditions: 50 mg, 250 ml min^{-1}, GHSV = 135 000 h^{-1}, 300 ppm CO, 300 ppm C_3H_6, 500 ppm NO, 10% O_2, 5% CO_2, 3.5% H_2O and He as balance.

Finally, to complete the study of the stability of the reference catalyst, X-Ray Diffraction and N_2 adsorption/desorption were made to the sampler after reaction conditions. As it can be seen in Figure AIV-3, no significant changes were found in the crystallinity of the catalyst. As well as before the reaction, the peaks corresponding to support are again visible. In addition, it starts to depict the peak corresponding to Pt-Pd at 46.5º probably due to the sintering of the metal after exposition to higher temperature.

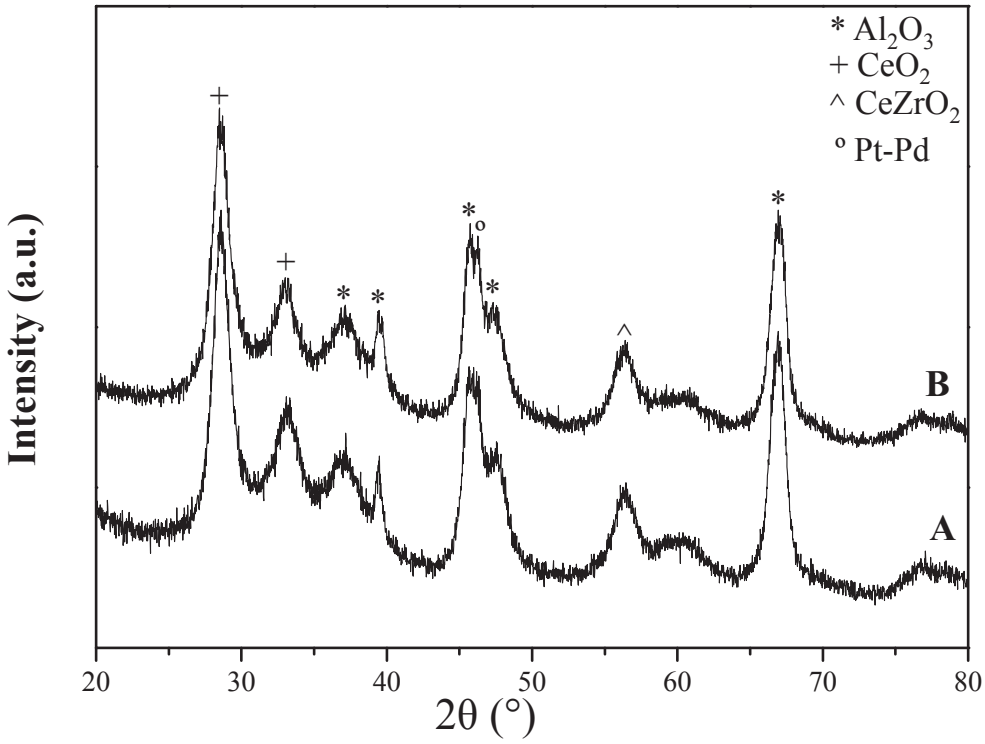

Figure AIV-3. X-ray diffraction patterns of PtPd reference catalyst before (A) and after (B) three catalytic reaction cycles. Operating conditions: 50 mg, 250 ml min^{-1}, GHSV = 135 000 h^{-1}, 300 ppm CO, 300 ppm C_3H_6, 500 ppm NO, 10% O_2, 5% CO_2, 3.5% H_2O and He as balance.

Moreover, significant decrease of the SSA was found, passing from 60 m^2 g^{-1} to 40 m^2 g^{-1} after reaction. Again, this could be ascribed to the exposition to high temperatures, producing the sintering of the catalyst.

References:

[1] S. Valange, A. Beauchaud, J. Barrault, Z. Gabelica, M. Daturi, F. Can, J. Catal. 251 (2007) 113–122.
[2] L. Wang, Y. Ma, Y. Wang, S. Liu, Y. Deng, Catal. Commun. 12 (2011) 1459–1462.
[3] M. Adamowska-Teyssier, A. Krztoń, P. Da Costa, G. Djéga-Mariadassou, Fuel 150 (2015) 21–28.
[4] Y. Ji, D. Xu, S. Bai, U. Graham, M. Crocker, B. Chen, C. Shi, D. Harris, D. Scapens, J. Darab, Ind. Eng. Chem. Res. 56 (2017) 111–125.
[5] A. Martínez Arias, J. Soria, J.C. Conesa, X.L. Seoane, A. Arcoya, R. Cataluña, J. Chem. Soc. Trans. 91 (1995) 1679–1687.
[6] W. Hauptmann, M. Votsmeier, J. Gieshoff, A. Drochner, H. Vogel, Appl. Catal. B Environ. 93 (2009) 22–29.
[7] K. Hauff, U. Tuttlies, G. Eigenberger, U. Nieken, Appl. Catal. B Environ. 123–124 (2012) 107–116.
[8] X. Auvray, L. Olsson, Appl. Catal. B Environ. 168–169 (2015) 342–352.